

HZDR-012

# ION BEAM PROCESSING OF SURFACES AND INTERFACES

– Modeling and atomistic simulations –

Bartosz Liedke

Wissenschaftlich-Technische Berichte  
HZDR-012 · ISSN 1437-322X

WISSENSCHAFTLICH-  
TECHNISCHE BERICHTE

**hzdr**



HELMHOLTZ  
ZENTRUM DRESDEN  
ROSSENDORF

Wissenschaftlich-Technische Berichte  
**HZDR-012**

Bartosz Liedke

## **Ion beam processing of surfaces and interfaces**

- Modeling and atomistic simulations -

**HZDR**

 **HELMHOLTZ**  
| ZENTRUM DRESDEN  
| ROSSENDORF

Druckausgabe: ISSN 2191-8708

Elektronische Ausgabe: ISSN 2191-8716

Die elektronische Ausgabe erscheint unter Creative Commons License (CC BY-NC-ND):

Qucosa: <http://fzd.gucosa.de/startseite/>

Die vorliegende Arbeit wurde sowohl als Dissertation an der Fakultät Mathematik und Naturwissenschaften der Technischen Universität Dresden sowie als Wissenschaftlich-Technischer Bericht des Helmholtz-Zentrum Dresden-Rossendorf mit der Berichtsnummer **HZDR-012** veröffentlicht.

2011

Herausgegeben vom

Helmholtz-Zentrum Dresden-Rossendorf e.V.

Postfach 51 01 19

D-01314 Dresden

Bundesrepublik Deutschland/Germany

**Ion beam processing of surfaces and interfaces**  
– Modeling and atomistic simulations –

D I S S E R T A T I O N

zur Erlangung des akademischen Grades

Doctor rerum naturalium  
(Dr. rer. nat.)

vorgelegt

der Fakultät Mathematik und Naturwissenschaften  
der Technischen Universität Dresden

von

Bartosz Liedke

geboren am 31. Juli 1982 in Białystok, Poland

Eingereicht am 24.03.2011



Gutachter:

1. Prof. Dr. W. Möller, Helmholtz-Zentrum Dresden-Rossendorf
2. Prof. Dr. E. Chason, Brown University



# Abstract

Self-organization of regular surface pattern under ion beam erosion was described in detail by Navez in 1962. Several years later in 1986 Bradley and Harper (BH) published the first self-consistent theory on this phenomenon based on the competition of surface roughening described by Sigmund's sputter theory and surface smoothing by Mullins-Herring diffusion. Many papers that followed BH theory introduced other processes responsible for the surface patterning e.g. viscous flow, redeposition, phase separation, preferential sputtering, etc. The present understanding is still not sufficient to specify the dominant driving forces responsible for self-organization. 3D atomistic simulations can improve the understanding by reproducing the pattern formation with the detailed microscopic description of the driving forces. 2D simulations published so far can contribute to this understanding only partially.

A novel program package for 3D atomistic simulations called TRIDER (TRansport of Ions in matter with DEfect Relaxation), which unifies full collision cascade simulation with atomistic relaxation processes, has been developed. The collision cascades are provided by simulations based on the Binary Collision Approximation, and the relaxation processes are simulated with the 3D lattice kinetic Monte-Carlo method. This allows, without any phenomenological model, a full 3D atomistic description on experimental spatiotemporal scales. Recently discussed new mechanisms of surface patterning like ballistic mass drift or the dependence of the local morphology on sputtering yield are inherently included in our atomistic approach.

The atomistic 3D simulations do not depend so much on experimental assumptions like reported 2D simulations or continuum theories. The 3D computer experiments can even be considered as 'cleanest' possible experiments for checking continuum theories. This work aims mainly at the methodology of a novel atomistic approach, showing that: (i) In general, *sputtering* is not the dominant driving force responsible for the ripple formation. Processes like bulk and surface defect kinetics dominate the surface morphology evolution. Only at grazing incidence the sputtering has been found to be a direct cause of the ripple formation. Bradley and Harper theory fails in explaining the ripple dynamics because it is based on the second-order-effect 'sputtering'. However, taking into account the new mechanisms, a 'Bradley-Harper equation' with redefined parameters can be derived, which describes pattern formation satisfactorily. (ii) Kinetics of (bulk) *defects* has been revealed as the dominating driving force of pattern formation. Constantly created defects within the collision cascade, are responsible for local surface topography fluctuation and cause surface mass currents. The mass currents smooth the surface at normal and close to normal ion incidence angles, while ripples appear first at  $\theta \geq 40^\circ$ .

The evolution of bimetallic interfaces under ion irradiation is another application of TRIDER described in this thesis. The collisional mixing is in competition with diffusion and phase separation. The irradiation with  $\text{He}^+$  ions is studied for two extreme cases of bimetals: (i) Irradiation of interfaces formed by *immiscible* elements, here Al and Pb. Ballistic interface mixing is accompanied by phase separation. Al and Pb nanoclusters show a self-ordering (banding) parallel to the interface. (ii) Irradiation of interfaces by *intermetallics* forming species, here Pt and Co. Well-ordered layers of phases of intermetallics appear in the sequence Pt/Pt<sub>3</sub>Co/PtCo/PtCo<sub>3</sub>/Co. The TRIDER program package has been proven to be an appropriate technique providing a complete picture of mixing mechanisms.





# Contents

<b>Abstract</b>	<b>v</b>
<b>Abbreviations</b>	<b>ix</b>
<b>1. Introduction</b>	<b>1</b>
1.1. Self-organization . . . . .	1
1.2. History of self-organization of surface pattern under ion irradiation . . . . .	3
1.3. Aim and structure of this work . . . . .	5
<b>2. Simulating ion-solid interactions</b>	<b>7</b>
2.1. Fundamentals of ion-solid interactions . . . . .	9
2.1.1. Interatomic potentials . . . . .	9
2.1.2. Cross sections . . . . .	10
Nuclear stopping . . . . .	12
Electronic stopping . . . . .	13
2.1.3. Theory of sputtering . . . . .	14
2.1.4. Ion-beam mixing . . . . .	17
2.2. Binary Collision Approximation . . . . .	20
2.2.1. TRIM . . . . .	21
2.2.2. TRIDYN . . . . .	24
2.2.3. Theoretical limits of BCA . . . . .	25
2.3. Kinetic Monte-Carlo . . . . .	27
2.3.1. Lattice gases . . . . .	28
2.3.2. KMC time step, ion flux and ion fluence . . . . .	30
2.3.3. Binary alloys . . . . .	31
2.3.4. Atom coordinates as binary arrays using bit coding technique . . . . .	32
2.4. The interface between BCA and KMC . . . . .	33
2.4.1. Major modifications in TRIM / TRIDYN . . . . .	35
2.4.2. Defect processing . . . . .	37
2.4.3. Recombination . . . . .	39
2.4.4. Data flow . . . . .	41
2.4.5. Demonstration of the simulation procedure . . . . .	42
2.4.6. CPU times . . . . .	43
<b>3. Ion-induced surface processes</b>	<b>45</b>
3.1. Defect evolution in Si . . . . .	49
3.1.1. Simulation parameters . . . . .	49
3.1.2. Results . . . . .	49
3.2. Crater formation by single ion incidence . . . . .	51
3.2.1. Simulation of single ion incidence . . . . .	53
3.2.2. Fitting function for crater formation . . . . .	57
3.3. Ripple evolution . . . . .	61
3.3.1. Constant flux per coordinate unit . . . . .	62
Surface morphology . . . . .	62
Spatial evolution of surfaces . . . . .	65
3.3.2. Simulation with ray tracing of ions . . . . .	70
Surface morphology . . . . .	70

## Contents

---

With or without sputtering . . . . .	72
Spatial evolution . . . . .	74
3.4. Surface mass currents . . . . .	77
3.4.1. Gibbs-Thomson relation . . . . .	79
3.4.2. Mullins-Herring diffusion of surface . . . . .	80
3.4.3. Surface mass currents under irradiation and diffusion . . . . .	83
<b>4. Interface mixing of bilayer interfaces</b>	<b>87</b>
4.1. Many-body interatomic potential for energies of Cellular Automata . . .	88
4.2. Gauging simulation parameters . . . . .	90
4.3. Simulation results . . . . .	93
4.3.1. Al/Pb bimetal mixing . . . . .	93
4.3.2. Pt/Co bimetal mixing . . . . .	96
4.4. Comparison of TRIDER with TRIDYN . . . . .	98
4.5. Conclusions . . . . .	101
<b>5. Summary</b>	<b>103</b>
<b>A. Nuclear stopping in Al/Pb bimetal</b>	<b>107</b>
<b>List of Figures</b>	<b>111</b>
<b>List of Tables</b>	<b>115</b>
<b>Bibliography</b>	<b>117</b>
<b>Acknowledgments</b>	<b>131</b>
<b>Curriculum Vitae</b>	<b>133</b>
<b>List of publications</b>	<b>135</b>

# Abbreviations

The list of acronyms presented below contains expressions frequently used within this work that are also common in scientific and technological literature.

BCA	Binary Collision Approximation
bcc	body-centered cubic
BH	Bradley and Harper
CA	Cellular Automata
CM	center of mass
DFT	density functional theory
DoG	difference of Gaussians
dpa	displacement per atom
EW	Edwards and Wilkinson
fcc	face-centered cubic
FPS	Frenkel pairs
IBS	ion beam sputtering
KMC	kinetic Monte-Carlo
KPZ	Kardar-Parisi-Zhang
Kr-C	krypton-carbon
KS	Kuramoto-Sivashinsky
MC	Monte-Carlo
MCs	Monte-Carlo steps
MD	molecular dynamics
MH	Mullins and Hearing
NN	nearest neighbor
SOS	solid-on-solid
RGL	Rosato Guillope Legrand
sc	simple cubic
SRIM	the stopping and range of ions in matter
TRIDER	transport of ions in matter with defect relaxation
TRIDYN	TRIM.SP dynamical
TRIM	transport of ions in matter
TRIM.SP	TRIM sputtering
ZBL	Ziegler-Biersack-Littmark



In all science,  
 error precedes the truth,  
 and it is better it should go first than last.  
 Hugh Walpole (1884 - 1941)

# 1

## Introduction

### 1.1 Self-organization

Self-organization is a process driving a system towards coherent structures by the system itself. Two types of self-organization mechanisms can classify systems from the thermodynamic point of view: (i) in **closed systems**, which evolve towards *thermodynamic equilibrium*, self-organization may reduce the entropy of sub-systems, however the entropy of the closed system as a whole will always rise; (ii) in **open systems**, which evolve towards a *steady-state*, high-quality energy of low entropy enters the system continuously delivered by an external source. If self-organization occurs during this process, the entropy of the open system will be lowered due to entropy export. Therefore, the low-quality energy that abandons the system will have higher entropy.

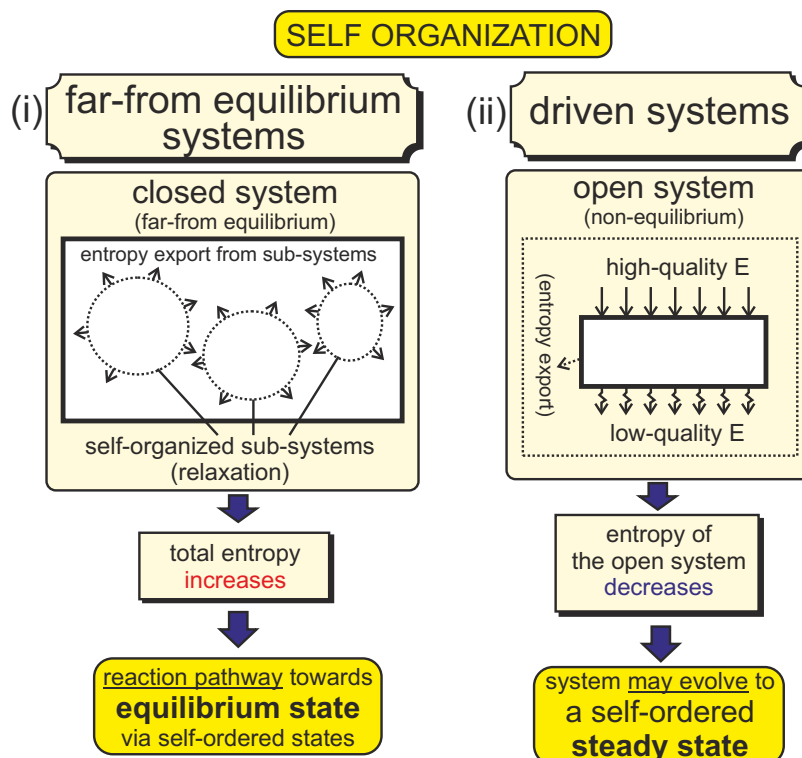


Figure 1.1.: Two types of self-organization.

In solid state physics self-organization can be found for mechanisms like phase transition, crystallization, percolation of random media, surface and interface energy minimization, epitaxial growth, etc. The first type (i) applies to all these mechanisms,

where self-organization occurs as an intermediate state providing an efficient way to reduce the free energy of the system. An example showing the reaction pathway of an ion-implanted, cylindrical Gaussian impurity atom distribution, thermally activated relaxing towards equilibrium is depicted in Fig. 1.2(i), starting with the as-implanted far-from-equilibrium state. Now, various processes drive the system towards equilibrium with a different speed. Phase separation, coarsening and interface smoothing are three subsequent mechanisms, which lead to the first ordering stage, where the system forms a nanowire. It exists relatively long due to a small driving force by a small energy gain coming from further surface area reduction. In the second stage the wire decays by Plateau-Rayleigh instability into a chain of spherical particles [1,2]. The particle chain is another stage of a relatively long lifetime, which lowers the surface energy further but even slower by coarsening to a single nanocluster via bulk diffusion. Finally, only one particle remains in the system creating the state closest to thermodynamical equilibrium.

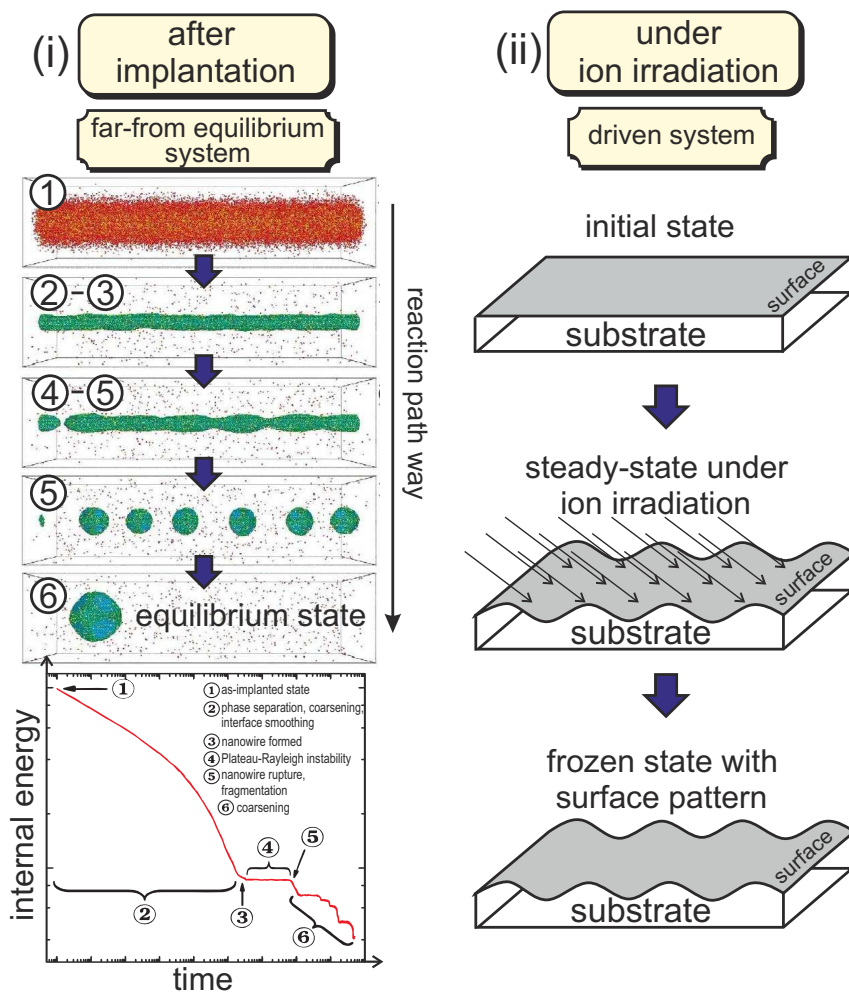


Figure 1.2.: Two examples of self-organizing processes. (i) **after implantation**, starting from a far-from-equilibrium state, Gaussian profile of particle distribution, the system evolves towards the equilibrium state through a sequence of separated stages: nanowire formation by phase separation, coarsening and interface smoothing; nanocluster chain formation by Plateau-Rayleigh instability; single nanocluster formation by total surface energy minimization. Internal energy reduction is plotted with indication of evolutionary states (from Ph.D. thesis of Röntzsch [2]). (ii) system **under ion irradiation** is driven towards ordered steady-state. Starting from initial flat surface the system evolves to an organized wavy morphology.

The second example in Fig. 1.2(ii) shows self-organization in a driven system. Here, steady state order can evolve under specific conditions. For instance, ion irradiation can modify surface topography and surface patterning can occur. Using proper conditions of ion beam sputtering (IBS), self-organization of ripples may appear. However, slightly different conditions during the sputtering may increase the surface roughness without creating any coherent structure or, on the other hand, can lead to smoothing of the surface. It is not trivial to understand under which conditions self-organization is expected during IBS and distinct approaches have been applied to study and explain experimental findings. It is the major objective of this thesis to improve the general understanding of the ripple formation mechanisms.

## 1.2 History of self-organization of surface pattern under ion irradiation

---

Although first experiments are dated back in the 1960s by Navez *et al.* [3], the first conclusive theory about self-organization of patterns under ion irradiation was proposed much later by Bradley and Harper (BH) [4] leading to a continuum model, the so-called BH equation. Their model of ion-eroded surface pattern is based on the competition between roughening processes by the ion sputtering and smoothing processes by surface diffusion. It became the dominating idea in the theories describing surface evolution under ion irradiation for many years. During these years mainly extensions of the BH model were proposed. At first the BH equation was extended to a non-linear equation [5], and then it was modified to an equation of the Kuramoto-Shivashinsky (KS) type [6] and to the anisotropic KS equation [7]. Finally by coupling KS equation to the "hydrodynamic" model it was possible to reproduce pattern coarsening [8]. It is mandatory to mention that all of the above-named models are rooted in the famous Sigmund theory of sputtering [9] established 9 years after the first experiment of the ripple formation [3]. The theory assumes that the local erosion rate is proportional to the intersection of the surface with a three-dimensional Gaussian distribution of energy deposited by a collision cascade.

Many atomistic approaches of modeling also favor the Sigmund theory as the source of a surface instability, i.e. surface roughness increase. Therefore, combination of the solid-on-solid (SOS) atomistic model with Sigmund's ellipsoid of the energy deposition results in BH type of surface evolution [10–12].

Also extensive atomistic simulations like molecular dynamics (MD), which follow the trajectory of atoms by integrating Newton's laws of motion, have been used to describe surface modification by ions. One of the investigation gives the first indication that ion bombardment is not always responsible for roughening, but can even very efficiently smooth surfaces depending on the initial conditions for bombardment [13]. This has been also observed experimentally [14]. Another MD study proves the existence of conditions where the surface roughness may increase under ion irradiation [15], however it is not clarified if the sputtering is the main cause. The most interesting conclusion provides Kalyanasundaram *et al.* [16] calculating with MD the crater function out of single ion impacts on Si (see scheme in Fig. 1.3). They show that the majority of the crater volume is caused by material rearrangement to the crater rims and the sputtering is not the only and not the dominant process during ion bombardment. It has been shown that inclusion of the crater function into continuum theory results in BH type continuum equations,



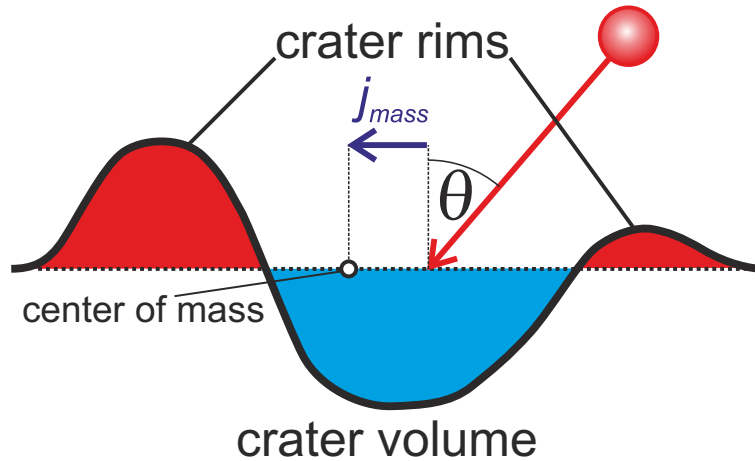


Figure 1.3.: Schematic plot of the one-dimensional crater topography after oblique impact. Strong asymmetry in the size of crater rims depending on the incidence angle decides about size and orientation of the mass current vector  $j_{mass}$ . The crater volume is the sum of the volume from removed atoms and the atoms relocated into the rims.

which can lead to pattern formation [17]. Also by superposition of the crater function on the surface for different ion impact, ripple formation can be expected [18].

The most convenient way to follow the kinetics of mass displacement after the collision cascade is to use computer simulation. With efficient computational methods it is possible to study both, the evolution of the system after single ion impact leading to crater formation and, after multiple impacts pattern formation. At present, it is necessary to use two different simulation techniques. With MD it is convenient to simulate single collision cascades. Such MD studies can be used to determine parameters of continuum equations. For instance, a convincing method about application of MD calculations into the continuum equation was provided by Norris *et al.* [17]. Taking this into account, they express the surface evolution in terms of moments of the crater function calculated with MD. An even more straightforward approach would be to use MD simulations to reproduce the surface pattern formation by multiple collision cascades, without calculating the energy deposition into the surface or the crater function after a single ion impact. Unfortunately, even in the next future it will not be possible to simulate these surface structures by MD. Modern computation techniques do not yet allow performing the simulations for needed time and length scales. An additional limitation is the difficulty in finding reliable atomistic potentials covering the whole range of atomic interactions.

Unlike atomistic modeling, continuum approaches are generally disregarding the influence of bulk defects on the surface morphology, considering only the local erosion rate proportional to the energy deposited locally on the surface. Recent models that introduce coupled fields of the mobile species [8] or the concentrations of elements for different compounds [19] provide a better description of surface diffusion processes and a more detailed picture of surface evolution under ion irradiation, but cannot fully describe bulk and surface kinetics. What is also missing is a direct link between continuum theory and atomistic simulations. The main disadvantage of the method of Norris *et al.* is the necessity to calculate the moments of a crater function rather than focusing on microscopic mechanisms, which are responsible for the crater formation. These mechanisms are producing the dynamics on the surface continuously during the ion bombardment and not only by a local height variation. A more detailed and straightforward approach was given

by Moseler *et al.* [13]. They suggest the existence of ion impact induced downhill currents as the driving force responsible for surface smoothing at normal incidence. Based on MD simulation of the collision cascade the downhill currents have been quantified and included into a linear continuum equation to study the transition between roughening and smoothing.

Crater function clearly contains much more information about the effect of the ion impact than the intersection of the deposited energy with the surface. Sputtering is described as the difference of the volume integral over the original surface and the crater function and the surface mass drift is related to the center of mass of the crater. The asymmetry in the crater formation due to ion impact under oblique local incidence angle induces a surface mass drift that can be described by the mass current vector  $j_{mass}$  shown in Fig. 1.3. There are two different sources that induce  $j_{mass}$  after single ion impact at the energies below thermal spike energy regime:

- (i) A *direct* formation of the crater is made, if the cascade produced by the ion has relatively high energy density [20] creating redistribution of the surface atoms and plastic deformation. The densest cascades are expected if the mass of the ion is much larger than the mass of target atoms (e.g. Xe<sup>+</sup> bombardment).
- (ii) An *indirect* crater formation is made, if the cascade energy density is low (the mass of ion is the same or smaller than the mass of target atom) and a single incidence causes a few atomic displacements at the surface's impact position only. However, averaging over hundreds of surface topographies created by single ion impacts crater formation with rims may appear [16].

For the both sources of  $j_{mass}$ , the atomic displacement induced by the collision cascade is orienting the mass current vector parallel to the ion trajectory. At present, it is possible to calculate the current vectors by simulations (e.g. with MD [13, 17]), but the quantitative relation between collision cascade and  $j_{mass}$  and its influence on the pattern formation remains unclear.

### 1.3 Aim and structure of this work

---

This work will not focus on further extensions of the BH theory but on the methodology of a novel atomistic approach named TRIDER (TRansport of Ions in matter with DEfect Relaxation) that is described in details in Chap. 2. The defect relaxation defined in the name TRIDER corresponds to the defects like: vacancies, interstitials, surface vacancies, ad-atoms, impurities and antisites. A description of patterning mechanisms starting from microscopic effects of defects migration and coming later to macroscopic processes like the evolution of ripple patterns will be supported by simulation results in Chap. 3, divided into four sections:

1. Kinetic of defects created within the collision cascade, and its influence on the crater structure is provided in Sec. 3.1. The role of processes like defect creation, recombination, accumulation and excess, is studied as time dependent variables.
2. The obtained crater formations are analyzed and compared for different irradiation conditions in Sec. 3.2. Analytical function to reproduce a crater-like surface morphology is proposed and the explanation of function arguments is provided.

3. In Sec. 3.3 mainly the results of the surface morphology after multiple ion impact are presented. The investigation focuses on the dominating driving force responsible for the ripple formation at non-grazing incidence angles. The complex role of processes like bulk and surface defect migration, recombination, bulk and surface diffusion during the evolution of surface patterns is taken into account. Here, the main objective is the surface erosion and its influence on the self-organization in the system. The qualitative picture of surface morphologies is then the basis of quantitative studies of the surface evolution using statistical variables of the surface like interface width and wavelength.
4. In Sec. 3.4 the mass current vectors are extracted from initially generated surfaces, which provide perfectly ordered wavy topography. At first smoothing conditions occurring due to the surface thermal diffusion is shown, and then the results after the irradiation and relaxation are given.

Finally, in Chap. 4 only the bulk processes are considered to study multicomponent systems, in particular intermetallic compounds. Self-organized structures can be obtained due to the competition between collisional mixing processes at the interface with defect relaxation and phase separation. As applications, two extreme cases of interface mixing in bimetal are presented: (i)  $\text{He}^+$  irradiation of bimetal formed by immiscible elements, here Al and Pb, causes ballistic interface mixing resulting in phase separation. Al and Pb clusters, which form in the interface region, show self-ordering. (ii)  $\text{He}^+$  irradiation of bimetal made by components which form intermetallics, here Pt and Co, causes the formation of step-like nanometric intermetallic layers with the phase sequence Pt/Pt<sub>3</sub>Co/PtCo/PtCo<sub>3</sub>/Co across the former interface.

Science is organized common sense,  
where many a beautiful theory,  
was killed by an ugly fact.

Thomas Huxley (1825 - 1895)

# 2

## Simulating ion-solid interactions

Nowadays there are many advanced and sophisticated simulation methods in solid state physics available. Starting from the fundamentals, *ab-initio* methods (also called first principles methods) are applied to describe electron states using quantum mechanical laws. They characterize electronic structure of solids and deliver fundamental background about basic properties of molecules and materials using numerical solution of the Schrödinger equation. The many-body interactions are usually approximated by single particles interacting with a self-consistent mean field based on the Hartree-Fock theory, which neglects electron-electron correlation. The problem of  $N$  interacting electrons in

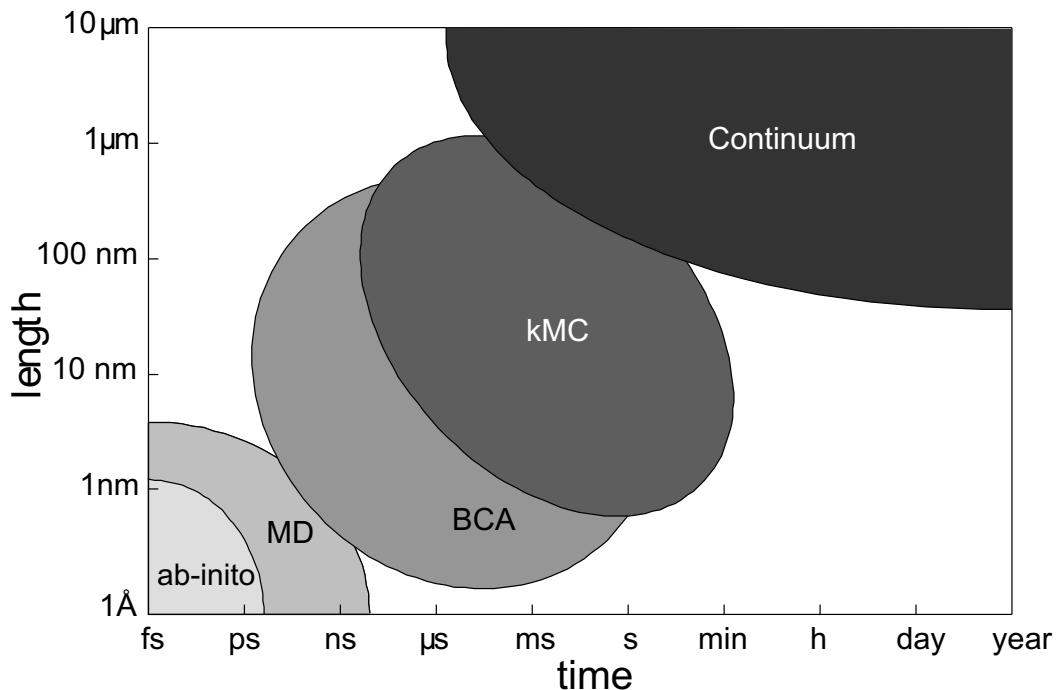


Figure 2.1.: Schematic diagram of time-space efficiency of solid state simulation methods.

an external potential is mapped onto a set of noninteracting electrons in an effective potential (mean field) [21, 22]. The density functional theory (DFT) is the most common and the most straightforward approach to describe the ground-state properties of solid materials and molecules [23–25]. It is based on another approximation, the negligence of Fermion character of electrons. To correct the two crucial approximations to a certain extent, correlation and exchange energies are added to the single particle Hamiltonian. DFT results are very often used as input parameters for classical atomistic simulations.

One of them is the MD method, which fulfills purely classical mechanical laws to describe the many-body interaction between atoms. The general aim is to reproduce the

dynamical behavior of systems of many particles by the calculation of atomic interactions and trajectories, by numerical integration of Newton's laws of motion (for detailed methodology see [26]):

$$\vec{F}_i(\vec{r}_i) = -\nabla u_i(\{\vec{r}_i\}) = m_i \frac{\partial}{\partial t} \vec{v}_i(t) = \frac{\partial}{\partial t} \vec{p}_i(t), \quad (2.1)$$

where for each atom  $i$ , atomic forces  $\vec{F}_i$  can be calculated only if the MD many-body potential function  $u_i$  is given.

The classical interatomic potential is the most important input deciding about the level of physical accuracy of the MD approach. Except classical interactions between the atoms, it describes also the electronic influence on the nuclei. Using first principles methods and experimental results semi-empirical and empirical potentials can be generated.

A practical calculation with the MD algorithm is the continuous updating of the velocity and the position vectors. Using  $\vec{F}_i$  and Newton's second law, velocity  $\vec{v}_i$  and atomic position vectors  $\vec{r}_i$  can be integrated with second order Taylor series to equations, e.g. by Verlet algorithm [27]:

$$\begin{aligned} \tilde{\vec{r}} &= \vec{r} + \vec{v}\Delta t + \frac{1}{2m}\vec{F}(\Delta t)^2 \\ \tilde{\vec{v}} &= \vec{v} + \frac{1}{2m}(\tilde{\vec{F}} + \vec{F})\Delta t \end{aligned} \quad (2.2)$$

Calculated trajectories are in the  $6N$ -dimensional phase space, with  $3N$ -dimensional space of positions  $\vec{r}_i$  and  $3N$ -dimensional momentum  $\vec{p}_i$  space. The time interval between two iteration steps  $\Delta t$  should be small enough to minimize the errors connected with the finite difference method of Taylor expansion and it should be smaller than the time of one vibration of atom on a lattice, which usually is in the femtoseconds range. This time discretization leads to the very serious restriction of MD simulation regarding time scale of simulation, which is in the order of picoseconds up to nanoseconds. Regarding the simulation cell sizes, MD has been applied up to nearly  $10^9$  atoms in condensed matter systems [28]. It is worth mentioning a recent publication of Samela and Nordlund about surface cratering using macroscopic projectiles (clusters) impacts on Au, where the total number of simulated atom was more than  $1 \times 10^7$  [29]. The largest calculation consumed in that case about 6 years of CPU time but the real time of the simulated physical process was followed only up to 50 ps.

Application of MD at the present time is not very practical concerning system sizes and irradiation times usually observed in the experiments, especially in terms of simulations of IBS. The average duration of a collision cascade is very short (sub-picosecond regime), therefore  $\Delta t$  used in MD has to be small enough to reproduce the trajectories. Because of this, the total simulation time increases. Moreover, for the simulation of atomic displacement during the cascade a special type of interatomic potential is used [30], which describes precisely the high energy regime of atomic collisions. The same type of interatomic potential is typically applied for Binary Collision Approximation (BCA) based methods, where it is possible to simulate very similar trajectories of projectiles like with MD, but with a heavily reduced computational time. Unfortunately the thermally activation of atoms that relaxes the system after the cascade is in BCA either completely neglected or simplified. This however, can handle kinetic Monte-Carlo (KMC) simulations. They are empirical methods, where the input parameters come often from the MD results. KMC can model a variety of kinetic processes of a solid state with rather large spatiotemporal scales, which can be compared with experimental results.

The unification of BCA and KMC should be able to reproduce full collision cascade with kinetic relaxation afterwards. Both of methods will be described in this chapter starting from the fundamentals, followed by the general methodology and its modifications. The major improvement however, applies to the interface between the methods, where the main programming challenge has been accomplished.

### 2.1 Fundamentals of ion-solid interactions

---

All the information provided in this section is only the brief review of the very broad subject of ion-solid interactions. All the formulas described here can be easily derived. However, only the final outcomes are presented in the subject areas, which are strictly connected with this work. More detailed insight into the field of ion-solid interactions bring fundamental reviews of Nastasi *et al.* [31], Sigmund [32], Smith [33] or Was [34].

The collision attempt and the trajectory in a center of mass (CM) system is shown in figure 2.2. Assuming that the projectile has the energy  $E$  and the scattering angle between two particles in a CM system is given by  $\theta_c$ , the elastic energy transferred to the target atom during every collision is given by,

$$T_{el} = \gamma E \sin^2 \frac{\theta_c}{2}, \quad (2.3)$$

where  $\gamma$  denotes the energy transfer factor between projectile of a mass  $m_1$  and target atom of a mass  $m_2$

$$\gamma = \frac{4m_1m_2}{(m_1 + m_2)^2}. \quad (2.4)$$

According to Eq. (2.3), the maximum of elastic energy transfer  $T_{max}$  occur, if the relative angle between atomic trajectories is  $\theta_c = 180^\circ$  that is equivalent to a head-on collision. Moreover, the energy transfer factor (2.4) suggests that another condition to increase  $T_{el}$  is to equalize the masses of projectile and the target atom ( $m_1 = m_2$ ).

#### 2.1.1. Interatomic potentials

To describe the interaction between atoms it is necessary to develop the proper potential function. Using binary collision approach it is possible to reduce the problem to only two particles interacting via Coulomb forces, separated by a distance  $r$  with the atomic numbers  $Z_1$  and  $Z_2$

$$V_c(r) = \frac{Z_1Z_2e^2}{4\pi\epsilon_0r}. \quad (2.5)$$

However, the existence of electrons has to bring some modifications based on shielding effects, especially active for the intermediate distance  $a_0 < r < r_0$  (where  $a_0=0.053$  nm, is the Bohr radius of the hydrogen atom and  $r_0$  is the nearest neighbor (NN) atomic distance). Due to the reduction of Coulomb potential by the repulsive force, caused by inelastic interactions between the electron shells, the screened Coulomb interaction potential has been developed

$$V(r) = V_c(r) \Phi\left(\frac{r}{a}\right), \quad (2.6)$$

where  $\Phi$  and  $a$  are the screening function and the screening length, respectively. There have been many variations of  $\Phi$  in the past, to describe  $V(r)$  that does not depending on

a specific electronic configuration. Based on experimental data and calculations of solid state interatomic potentials of about 500 ion-target combinations, Ziegler, Biersack and Littmark [30], have created the generalized version of screening function, the so-called “universal screening function”,

$$\Phi_U(y) = 0.182e^{-3.2y} + 0.51e^{-0.942y} + 0.28e^{-0.403y} + 0.0282e^{-0.202y}, \quad (2.7)$$

with universal screening length,

$$a_U = \frac{0.8853a_0}{Z_1^{0.23} + Z_2^{0.23}}. \quad (2.8)$$

The interatomic potential (2.6) calculated using the universal function is called after the names of creators: Ziegler, Biersack and Littmark (ZBL). It has been derived by calculations of total interaction energy, which take into account such parameters like: electrostatic potential energy between nuclei, electrostatic interaction energy between electron distributions, interaction energy between nucleus and electron distribution, kinetic energy increase of electrons due to Pauli excitation, and increase of exchange energy of electrons.

ZBL is the most often used potential in models based on BCA, mainly because it is employed for the widely spread SRIM package [30]. Not very far from ZBL lies the Kr-C potential [35], which has been proven to be a good mean potential, especially combined with the Firsov screening length [36]:

$$a_F = 0.8853a_0 \left( Z_1^{1/2} + Z_2^{1/2} \right)^{-2/3} \quad (2.9)$$

$$\Phi_{\text{Kr-C}}(y) = 0.19e^{-0.278y} + 0.47e^{-0.637y} + 0.34e^{-1.919y}.$$

This potential has been successfully used in many simulation techniques [37–39], in particular describing the sputtering yield with good experimental agreement.

### 2.1.2. Cross sections

To quantify a large number of atomic interactions during a collision cascade it is necessary to examine the probability of ion-solid scattering events. This can be done by introducing

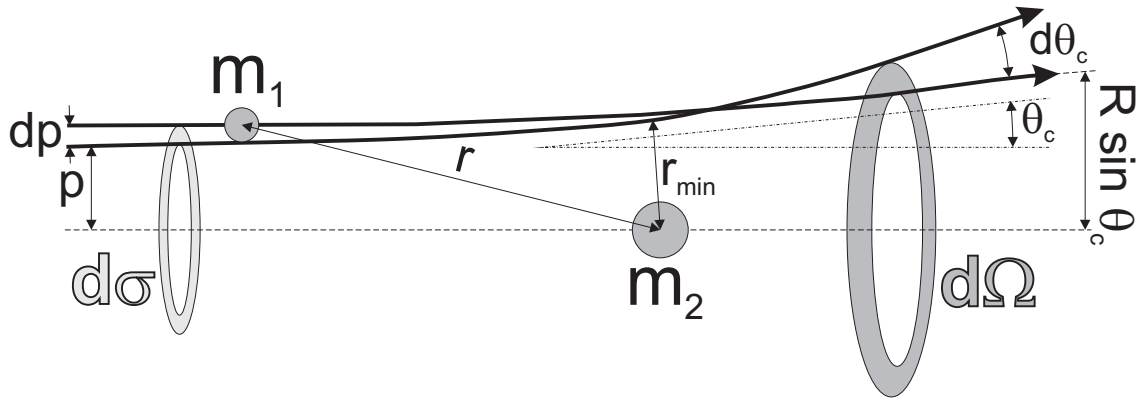


Figure 2.2.: Scattering cross section ( $d\sigma/d\Omega$ ) of a particle of mass  $m_1$  approaching the nucleus of mass  $m_2$  with an impact parameter  $p$ , reflected at a solid angle  $\theta_c$ .

a **cross section**, which is defined as the probability that between approaching particle

and target projectile a particular interaction occurs. Two types of cross sections can be distinguished:

1. *Scattering cross section* ( $d\sigma/d\Omega$ ) (Fig. 2.2) - is the probability of projectile scattering in the defined angle  $\theta_c$ . The relation of differential rings before ( $d\sigma$ ) and after ( $d\Omega$ )<sup>1</sup> the impact is a function dependent on the impact parameter  $p$  and the scattering angle  $\theta_c$ , expressed by the formula

$$\frac{d\sigma}{d\Omega} = \left| \frac{2\pi p dp}{2\pi \sin \theta_c d\theta_c} \right| = \frac{p}{\sin \theta_c} \left| \frac{dp}{d\theta_c} \right| \quad (2.10)$$

Equation (2.10) is derived using the ratio between ring's area before and after collision. The relation between scattering angle and energy is given by the so-called 'trajectory integral'<sup>2</sup>

$$\theta_c = \pi - 2p \int_0^{r_{min}^{-1}} \frac{dr^{-1}}{\sqrt{1 - \frac{V(r)}{E} - \frac{p^2}{r^2}}}, \quad (2.11)$$

where  $r_{min}$  denotes the minimal distance between two projectiles, and  $V(r)$  is the potential function used for the calculation. Using the Eqs. (2.10) and (2.11) combined with the potential function given by (2.6), the scattering cross section and preferential scattering angles for different projectiles can be studied analytically.

2. *Stopping cross section* ( $S(E)$ ) - in contrary to the scattering cross section, stopping cross section describes multiple collisions that follow the energy loss per unit length due to the nuclear ( $nu$  - by the collisions) and electronic ( $el$ ) interaction effects in the target with atomic density  $n$

$$S(E) = -\frac{1}{n} \left( \frac{dE}{dx} \right) = -\frac{1}{n} \left( \frac{dE}{dx} \Big|_{nu} + \frac{dE}{dx} \Big|_{el} \right). \quad (2.12)$$

Multiplying  $S(E)$  by  $n$  gives a *stopping power*, which describes the energy loss per unit of pathlength. The stopping cross section can be divided into two types of interactions, which are the nuclear ( $S_{nu}(E) = n^{-1} |dE/dx|_{nu}$ ) and the electronic ( $S_{el}(E) = n^{-1} |dE/dx|_{el}$ ) stopping.

Both scattering and stopping cross sections determine the trajectory of atoms. Starting from the 'primary' ion, slowing down process is induced by the energy transfer to the primary recoils. If the energy transferred is sufficiently large, the recoils will follow the trajectory that is similar to the trajectory evoked by the ion, possibly generating further recoils ('secondary' recoils). The secondary recoils may also repeat nuclear collisions with other atoms transferring the nuclear energy until they will come to the rest and finalize the 'collision cascade'. The schematic picture of atomic trajectories is shown in Fig. 2.3.

In the right part of Fig. 2.3 two types of stopping mechanisms are indicated: (i) nuclear stopping activated by a binary collision, is a kinetic transfer of energy between atoms and (ii) electronic stopping, is an inelastic energy loss induced by a 'friction' at electrons of the medium.

<sup>1</sup> $\sigma$  is simply the differential area before the collision and  $\Omega$  a relative solid angle after the collision.

<sup>2</sup>The classical trajectory integral is a method to calculate a scattering angle in CM systems based on the kinetic and potential interaction between two particles only. It is derived using classical laws of energy and momentum conservation [31].



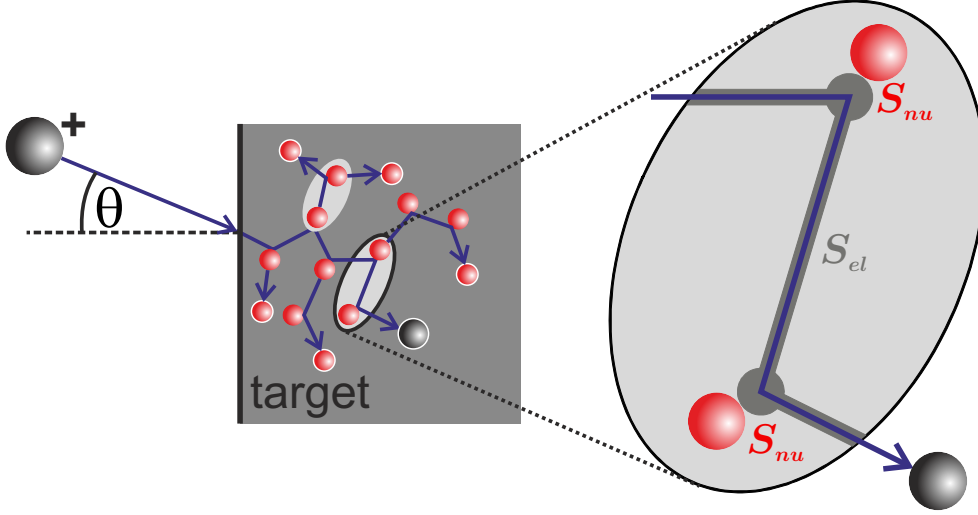


Figure 2.3.: Schematic of a collision cascade showing primary ion and recoils trajectory. Final positions of projectiles are indicated with white contour.

### Nuclear stopping

A nuclear stopping power can be derived directly by integration over all possible values of the energy transfer  $T$  from Eq. (2.3),

$$S_{nu}(E) = \int_{T_{min}}^{T_{max}} T d\sigma(T). \quad (2.13)$$

The lower limit of the integration  $T_{min}$  is the minimal energy needed to displace an atom from its lattice position and is usually in the range of few eV, however for calculation of the nuclear stopping it can be set as 0.  $\sigma(T)$  is the scattering cross section that is calculated by (2.10). To solve (2.13) it is convenient to introduce ‘reduced’ dimensionless quantities for the energy and path length, which have been defined by Lindhard *et al.* [40]. With the distance of closest approach  $r_{min}(E)$  in a head-on collision, they are given by:

$$\varepsilon = \frac{a}{r_{min}(E)} = \frac{4\pi\varepsilon_0 a m_2}{Z_1 Z_2 e^2 (m_1 + m_2)} E \quad \text{and} \quad \rho = \pi a^2 n \frac{4m_1 m_2}{(m_1 + m_2)^2} x. \quad (2.14)$$

Based on a fitting procedure to experimental sputtering yield data Matsunami *et al.* [41] calculated  $S_{nu}(\varepsilon)$  as a semiempirical approximation for the Thomas-Fermi screening function  $a_{tf}$ , yielding

$$S_{nu}(\varepsilon) = \left. \frac{d\varepsilon}{d\rho} \right|_{nu} = \frac{3.44\sqrt{\varepsilon} \ln(\varepsilon + 2.718)}{1 + 6.35\sqrt{\varepsilon} + \varepsilon(6.882\sqrt{\varepsilon} - 1.708)}. \quad (2.15)$$

Another fitting function describing nuclear stopping has been proposed by Ziegler *et al.* [30], where the best results can be obtained using the universal screening function (2.7)

$$S_{nu}(\varepsilon) = \left. \frac{d\varepsilon}{d\rho} \right|_{nu} = \frac{0.5 \ln(1 + 1.2288\varepsilon)}{\varepsilon + 0.1728\sqrt{\varepsilon} + 0.0008\varepsilon^{0.1504}}. \quad (2.16)$$

The comparison between Eqs. (2.15) and (2.16) is plotted in Fig. 2.4. The plots overlap for the all values except for  $\varepsilon > 0.1$  and  $\varepsilon < 10$ .

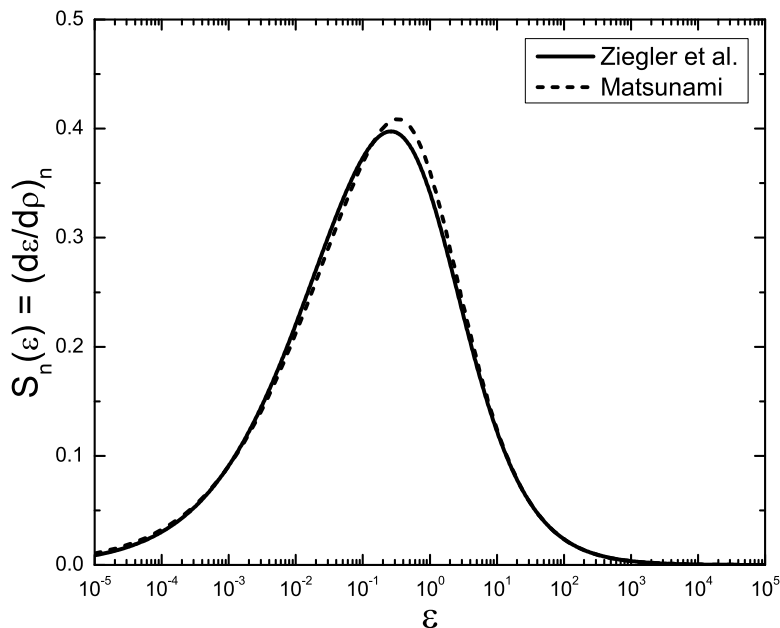


Figure 2.4.: Nuclear stopping power plotted in reduced coordinates.

### Electronic stopping

The second type of energy transfer from fast moving atoms, delivered to the electrons of the medium is called electronic stopping or inelastic energy loss. To describe this type of particle interaction, it is important to realize that electronic stopping is always velocity dependent and therefore also energy dependent. Two types of electronic excitations can be distinguished according to the initial velocity  $v$ :

- a)  $v > v_0 Z_1^{2/3}$ , corresponding to high-energetic collisions, where the projectile is significantly faster than the mean orbital velocity of electrons (where  $v_0 = \hbar/m_e e^2 \approx 2.188 \times 10^8$  cm/s denotes Bohr velocity of atomic electrons). For these conditions, ions almost immediately lose their electrons straight after and can be treated as a bare nucleus with a positive charge  $Z_1$ . The energy loss can then be calculated for purely Coulombic interactions with the electrons, according to the Bethe formula [42]

$$S_{el}^>(E) = \left. \frac{dE}{dx} \right|_{el}^> = \frac{2\pi Z_1^2 Z_2 e^4 m_1}{(4\pi\epsilon_0)^2} \frac{1}{m_e E} \log \left( \frac{4m_e E}{m_1 I} \right). \quad (2.17)$$

In Eq. (2.17)  $I$  denotes the average excitation energy of an electron in the medium ('mean ionization potential'), which has been roughly approximated by Bloch [43] as a linear function of the atomic number of medium,  $I \cong 10Z_2$ .

- b)  $v < v_0 Z_1^{2/3}$ , for low particle energies, positively charged ions tend to be neutralized by electrons captured from target atoms. In the work of Firsov [36] the assumption of creating a quasi-molecule is used. It explains the loss of

the momentum by the projectile during the collision, due to the electron exchange in an overlap region of the transient quasi-molecule. This leads to the a following formula

$$S_{el}^<(E) = \left. \frac{dE}{dx} \right|_{el}^< = 3.309 \times 10^{15} (Z_1 + Z_2) \left( \frac{E}{m_1} \right)^{1/2} \text{ eV cm}^2. \quad (2.18)$$

An alternative expression has been derived by Lindhard and Scharff by integrating the ion-electron interactions over radial shells of the target atom<sup>3</sup>. In reduced units their result is given by the formula

$$S_{el}^<(\varepsilon) = \left. \frac{d\varepsilon}{d\rho} \right|_{el}^< = \frac{Z_1^{2/3} Z_2^{1/2} (1 + m_2/m_1) \varepsilon^{1/2}}{12.6 \left( Z_1^{2/3} + Z_2^{2/3} \right)^{2/3} m_2^{1/2}}. \quad (2.19)$$

Both formulas show that low-energy electronic stopping is proportional to the velocity of the moving atom. The difference of Eqs. (2.18) and (2.19) results from different interatomic potentials used for the integration. In comparison with experimental data, the Firsov formula fits better if the ratio between  $Z_1$  and  $Z_2$  does not exceed 4. However, the Lindhard-Scharff equation is more universal concerning the full range of atomic number combinations.

Fig. 2.5 shows the stopping cross section calculated for two different systems. The main plot is valid for light ion bombardment (i.e. He<sup>+</sup>), where the electronic stopping is dominant and the nuclear stopping is always lower than  $S_{el}$ . It is easy to realize that at low energies  $S_{el}$  is proportional to  $\varepsilon^{0.5}$ , like in Eqs. (2.18) and (2.19), whereas at high energies, in accordance with Eq. (2.17), the dependence is becoming  $\varepsilon^{-1} \log \varepsilon$ . The intermediate energy regime of the electronic stopping around  $v = v_0 Z_1^{2/3}$  is usually approximated using inverse interpolation

$$\frac{1}{S_e} \approx \frac{1}{S_e^<(\varepsilon)} + \frac{1}{S_e^>(\varepsilon)}. \quad (2.20)$$

Using heavier ions (e.g. Ar<sup>+</sup>) the nuclear stopping is much more significant at the lower energies. However, when the energy increases,  $S_{nu}$  goes down proportionally to  $\varepsilon^{-1} \log \varepsilon$ , in accordance to the Eq. (2.15), while  $S_{el}$  starts to become the dominant stopping power.

### 2.1.3. Theory of sputtering

If a collision cascade intersects the surface boundary it transfers energy to the surface atoms. If transferred energy overcomes their binding energy the surface atoms will be removed from the target. This kind of event is named as sputtering or surface erosion.

The rate of surface erosion is described by the factor called sputtering yield  $Y_s$ , which determines the average number of removed atoms per incidence ion. Analytical cascade transport theory is generally applied to find an approximation of  $Y_s$ . It is based on an analytical solution of so-called ‘forward’ transport equation to obtain distribution function of beam properties like deflection angle or particle energy over depth [45]. The

<sup>3</sup>Lindhard and Sharff have never published their derivation although it has been used worldwide. In the work of Sugiyama (see Ref. [44]), the Lindhard-Scharff equation has been derived using the Firsov approach

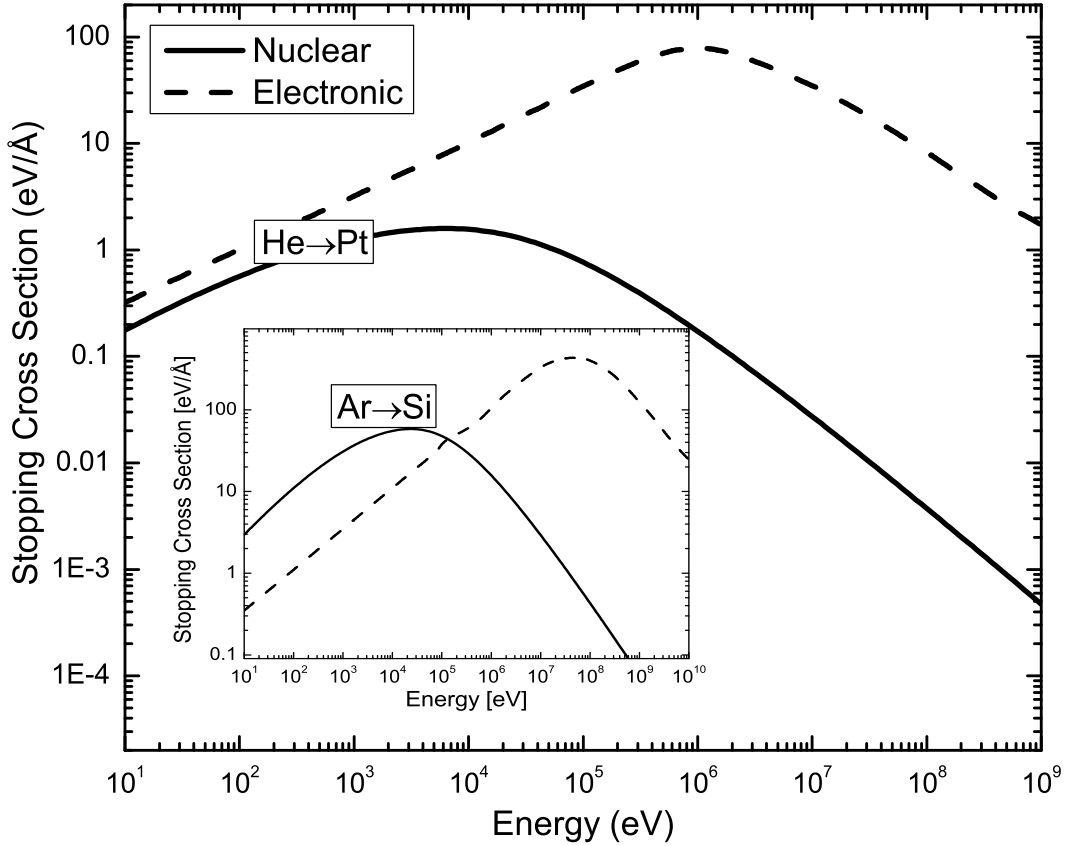


Figure 2.5.: Stopping cross sections ( $dE/dx$ ) of nuclear (solid lines) and electronic (dashed lines) energy loss for Pt irradiated with  $\text{He}^+$  ions. The inset plot shows corresponding functions for heavy ion irradiation ( $\text{Ar}^+$  ion sputtering of Si target). The data are generated using the SRIM-2008 package [30]

sputtering yield is there calculated using the isotropic distribution of recoil energies cut at the surface. The usual range of  $Y_s$  values is 0.5-20. It scales with the total amount of energy deposited by nuclear collision at the surface. The sputtering yield is proportional to the number of recoils generated in the near surface region, thus being proportional to the nuclear stopping cross section. If the fraction of deposited energy density is low enough, the sputtering can be described in the linear cascade regime using Sigmund's theory [9] with a fundamental formula  $Y_s = \Lambda F_D(E_0)$ , where  $\Lambda$  is a factor containing material properties and  $F_D$  is the nuclear energy deposition at the surface<sup>4</sup>. The transport theory assumes infinite medium, where ions start the trajectory internally and the surface boundary is included artificially. These assumptions overestimate  $Y_s$  especially, if the scattering angles become larger and large fraction of collision cascade forms beyond the surface in the infinite medium. To reduce created error correction factor  $\alpha$  is applied. The  $\alpha$  is a function of the mass ratio  $m_2/m_1$ , ranging between 0.1 and 0.6. It is usually interpolated from experimental yields. In a more detailed formulation  $Y_s$  looks as follows,

$$Y_s(E_0, \theta) = \frac{4.2 \times 10^{14} \text{cm}^2}{NU_0} \alpha \left( \frac{m_2}{m_1} \right) S_n(E_0) \cos^{-f} \theta. \quad (2.21)$$

$U_0$  is a surface binding energy that for one component materials is equal to the sub-

<sup>4</sup>Deposited energy is proportional to nuclear energy-loss rate  $N \times S_n(E_0)$

limation energy. The dependence on the incidence angle is included as an additional term  $\cos^{-f} \theta$ . Here, the exponent  $f$ , is according to the Sigmund theory equal  $5/3$ , if  $m_2/m_1 \leq 3$ , however it can only reproduce the sputtering yield for angles close to normal incidence ( $\theta \cong 0^\circ$ ). At the grazing incidence, ion reflection from the surface lowers  $Y_s$  significantly towards zero. In Fig. 2.6a, the sputtering yield dependence on the energy is presented. The Sigmund theory overestimates the sputtering yield in comparison with the experimental data, especially at low ion energies, as the threshold effects at the surface are neglected. At sufficiently low ion energies the energy transfer to recoils becomes lower than the surface binding energy, so that sputtering is completely suppressed.

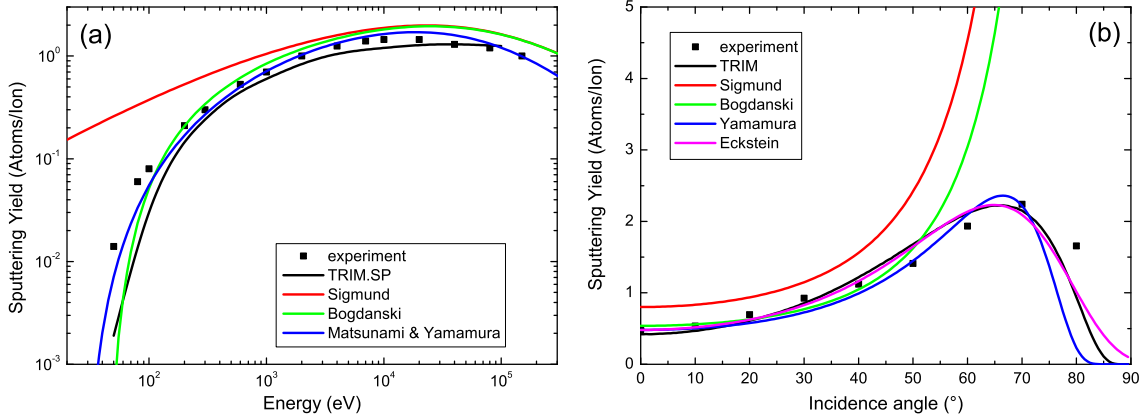


Figure 2.6.: Sputtering yields for Ar bombardment of Si as a function of: (a) energy at normal incidence angle, (b) incidence angle at 500 eV ion energy. The experimental data are taken from [46] and [47] (black squares). Solid color lines are solution of different analytical formulas. Black solid lines are TRIM simulations.

A semi-empirical correction in the sputtering formula, including a threshold energy  $E_{thr}$  selection has been introduced by Bohdanský [48] according to

$$Y_s^{thr}(E_0) = Y(E_0) \left( 1 - \left( \frac{E_{thr}}{E_0} \right)^{2/3} \right) \left( 1 - \frac{E_{thr}}{E_0} \right)^2, \quad (2.22)$$

where  $E_{thr}$  depends on the mass ratio  $m_1/m_2$  as

$$E_{thr} = \begin{cases} \frac{E_s}{\gamma(1-\gamma)} & \text{for } \frac{m_1}{m_2} < 0.2, \\ 8E_s \left( \frac{m_1}{m_2} \right)^{2/5} & \text{for } \frac{m_1}{m_2} > 0.2, \end{cases} \quad (2.23)$$

with  $\gamma$  calculated by Eq. (2.4).

For larger energies Eqs. (2.21) and (2.22) lead to the same results, without taking into account electronic processes. Depending on the electronic stopping power, the total sputtering yield will be reduced at the energy range of a few 100 keV. For this purpose, Lindhard-Scharff electronic stopping cross-section is used (2.19) and  $Y_s$  becomes,

$$Y_s^{thr}(E_0) = \frac{0.42 \alpha_{ex} S_n(E_0)}{U_0 (1 + 0.35 U_0 S_e(\varepsilon))} \left\{ 1 - \left( \frac{E_{thr}}{E_0} \right)^{1/2} \right\}^{2.8}, \quad (2.24)$$

where  $\alpha_{ex}$  is empirical parameter determined from the experiments. The equation above has been introduced and evaluated by Matsunami *et al.* [49] and Yamamura and Itoh [50].

Again, threshold energy is considered, similarly like for (2.22), separately for the light and the heavy ions:

$$E_{thr} = \begin{cases} \left(\frac{4}{3}\right)^6 \frac{U_0}{\gamma} & \text{for } m_1 > m_2, \\ \left(\frac{2m_1+2m_2}{m_1+2m_2}\right)^6 \frac{U_0}{\gamma} & \text{for } m_1 < m_2. \end{cases} \quad (2.25)$$

A recent publication proves the existence of a fully analytical description of sputtering yield at normal ion incidence, derived for the energy range of 50 eV - 540 keV by Wittmaack [47].

Angular dependence of sputtering yield proposed by Sigmund, has been corrected by Yamamura [51] based on the reflection tendency for oblique ion incidence angles. However, a very similar although less empirical formula was recently proposed by Eckstein *et al.* [52]:

$$Y_s(E_0, \theta) = Y_s(E_0, 0) \left(\cos(\tilde{\theta}^c)\right)^{-f} \exp\left\{b\left(1 - \cos^{-1}(\tilde{\theta}^c)\right)\right\}, \quad (2.26)$$

with  $\tilde{\theta}$  as a corrected incidence angle that takes into account the low ion energy regime and self-ion bombardment, unlike the equation of Yamamura (Ref. [51]),

$$\tilde{\theta} = \theta \frac{\pi}{2} \left\{ \pi - \arccos \sqrt{\frac{1}{1 + E_0/U_0}} \right\}^{-1}. \quad (2.27)$$

The only difference from Yamamura's approach is the correction factor (2.27) and additional fitting parameter  $c$  ( $c = 1$  in Ref. [51]).

Calculated sputtering yield for Ar<sup>+</sup> ion bombardment of Si at the energy  $E_0 = 500$  eV using all presented approaches is given in Fig. 2.6b. For comparison, the experimental data [46] and TRIM calculation are included. The data taken from the experiment, which has been done with 1.05 keV Ar<sup>+</sup> ion energy, have been rescaled to 500 eV ion energy. Therefore, TRIM simulation is expected to be a more reliable indicator and the experiment provides a qualitative description.

Every analytical approach is an approximation of the reality. Each effort of finding correct formula tends to increase the total confidence. Unfortunately the number of necessary parameters increases and applications of such formulas, for instance in continuum theories describing the surface evolution under ion irradiation, may become very inefficient.

#### 2.1.4. Ion-beam mixing

Kinetic energy transfer to the recoils results in the displacement of atoms in the target. Additionally, if more than one component is present in the target a change of local concentrations will occur due to so-called ion-beam mixing. The observation of mixing processes are usually based on controlled experiments of bilayer materials, like for instance investigation of interface mechanisms of Pd/Si interface [53], or marker ion mixing experiments, for example in amorphous Si [54].

Both configurations of the target are illustrated by Fig. 2.7. The solid gray lines represent the concentration profile after a certain irradiation time. To describe time

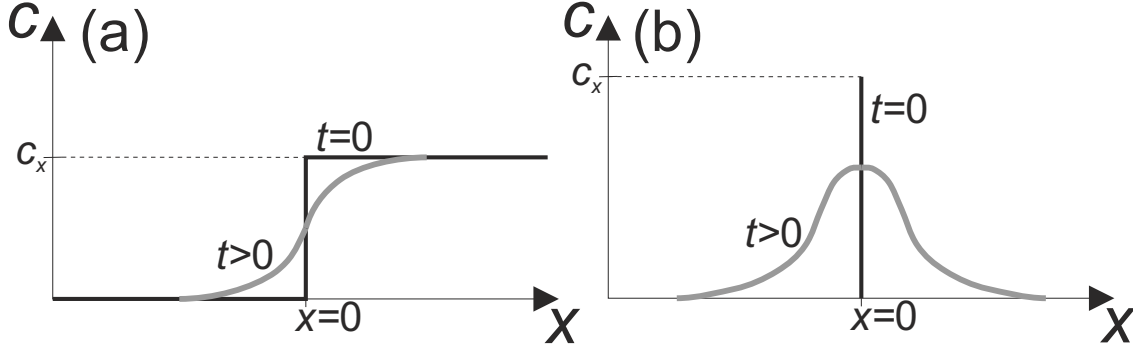


Figure 2.7.: Schematic of ion-beam mixing processes on (a) bilayer materials (interface) and (b) a thin film (marker)

evolution of the concentration profile, the fundamental **2nd Fick's law of diffusion** can be used:

$$\frac{\partial c}{\partial t} = -D\nabla^2 c \quad (2.28)$$

where  $c$  is the concentration,  $D$  is concentration independent interdiffusion coefficient and  $\nabla$  is a divergence operator. The 2nd Fick's law can be derived from the **1st Fick's law** describing the diffusion flux  $j$  in relation with the concentration

$$j = -D\nabla c. \quad (2.29)$$

Simple one-dimensional solutions of the diffusion equation (2.28) following Fig. 2.7 can be given under the assumption of an infinite medium, as follows:

- (a) Interface mixing for bilayer materials for the initial conditions  $\{c(x < 0, t = 0) = 0; c(x \geq 0, t = 0) = c_x\}$ ,

$$c(x, t) = \frac{c_x}{2} \left\{ 1 + \operatorname{erf} \left( \frac{x}{\sqrt{4Dt}} \right) \right\}, \quad (2.30)$$

where  $c_x$  denotes the initial constant concentration of the material at the surface and  $\operatorname{erf}$  the error function.

- (b) Ion irradiation of a thin film marker for the initial condition  $\{c(x < 0, t = 0) = 0; c(x = 0, t = 0) = c_x; c(x > 0, t = 0) = 0\}$ ,

$$c(x, t) = \frac{c_x}{\sqrt{4\pi Dt}} \exp \left( \frac{-x^2}{4Dt} \right). \quad (2.31)$$

Here,  $c_x$  denoted the concentration of the mater solute in the target.

Similarly like for sputtering yield, also here the transport theory can be applied for estimation of mixing, where the infinite medium assumption is a good approximation for bulk cascades. The mixing will be described using the assumption of the isotropic collision cascades [55] by the formula

$$D_{\text{bal}} t = \frac{N_{\text{dpa}}(x) \langle r^2 \rangle}{6} = \frac{S_n(E_0) \langle r^2 \rangle}{12E_m N} \phi, \quad (2.32)$$

where  $N_{\text{dpa}}$  is the number of displacements per atom of the material at depth  $x$ ,  $\phi$  the ion fluence,  $S_n$  nuclear stopping cross-section at the ion energy  $E_0$ ,  $E_m$  threshold

energy below which no relocation occurs and  $N$  the atomic density.  $\langle r^2 \rangle$  is the mean squared range of the displaced atoms. The time  $t$  is here the irradiation time, which is proportional to the fluence of the ion beam.

Eq. (2.32) describes purely collisional effects and neglects any chemical driving forces between the atoms of the material. The latter might induce phase ordering or at the other extreme, phase separation. The chemical driving forces can be quantified by the **heat of mixing**  $\Delta H_{mix}$ , which denotes the concentration dependent energy difference between energetic state of the system after ( $H_2$ ) and before ( $H_1$ ) the reaction (therefore  $\Delta H_{mix} = H_2 - H_1$ ). If  $\Delta H_{mix}$  is positive,  $H_2$  is larger than  $H_1$ , which means  $H_2$  is not the preferential state and heat is absorbed<sup>5</sup>. If  $\Delta H_{mix}$  is negative, the total energy of the system after the reaction is lowered and the heat is released<sup>6</sup>. In a regular solution model the concentration dependent heat of mixing for components A and B is defined as [56]

$$\Delta H_{mix} = X_A X_B \eta_l N_A \left\{ \varepsilon_{AB} - \frac{1}{2} (\varepsilon_{AA} + \varepsilon_{BB}) \right\} \quad (2.33)$$

where  $X_A$  and  $X_B$  are mole fraction of elements A and B respectively,  $\eta_l$  is a lattice coordination number and  $N_A$  Avogadro's number.  $\varepsilon_{ij}$  are the mean bond energies between atomic pairs.

Introduction of the chemical driving force into the interdiffusion coefficient, leads to a modification of the diffusion equation (2.28) due to the dependency of potential the energy on local configuration, which has been originally discussed by Darken [57]. Therefore, the mixing diffusion coefficient follows

$$Dt = D_{bal} t \left( 1 - \frac{2\Delta H_{mix}}{k_B T} \right), \quad (2.34)$$

where  $k_B$  is Boltzmann's constant and the temperature  $T$  refers to an effective temperature of the collision cascade during its thermalization phase.

Similarly, a dependence of the mixing rate on the cohesive energy  $\Delta H_{coh}$  has been proven by experiments by van Rossum *et al.* [58]. It was shown that systems with lower  $\Delta H_{coh}$  exhibit higher mixing rate. Because  $\Delta H_{coh}$  is a measure of rigid lattice strength, due to the presence of tighter atomic bounds, the diffusion in the lattice will be suppressed, and therefore mixing will be lower as well. A direct connection between the cohesive energy and the enthalpy of mixing is provided by regular solution theory according to

$$\Delta H_{coh}^{AB} = (X_A \Delta H_{coh}^A + X_B \Delta H_{coh}^B) + \Delta H_{mix}. \quad (2.35)$$

Eqs. (2.33) and (2.35) show that both,  $\Delta H_{mix}$  and  $\Delta H_{coh}$  are concentration dependent. Attempts of the analytical solution to describe the interdiffusion via atomic migration under ion irradiation become very complicated, even for binary systems at low temperatures. The effect of thermal spikes on the mixing rate has been treated by Rossi and Nastasi [59] resulting in a semi-empirical formula, where the ratio of  $\Delta H_{mix}/\Delta H_{coh}$  plays the most significant role. Another investigation shows the separation between thermal mixing and ion induced mixing by existence of specific activation thresholds induced by increasing the temperature of a sample [60]. The presence of ion irradiation during thermally activated mixing lowers the activation energy of atoms  $E_A$  and increases

---

<sup>5</sup>if  $\Delta H_{mix} > 0$ , reaction is endothermic, and the substances are immiscible (for instance: W/Cu, Al/Pb, Pt/Ti)

<sup>6</sup>if  $\Delta H_{mix} < 0$ , reaction is exothermic and the substances are miscible (Au/Co, Pt/Co, Hf/Ni)



bulk kinetics. At high temperatures, the interdiffusion coefficient follows Arrhenius behavior  $D_{rad}t \exp(-E_A^{rad}/k_B T)$ , whereas if the temperature is lower, ballistic mixing is dominating according to Eq. (2.32).

There are many driving forces, which are contributing to mixing during ion irradiation, e.g. relaxation of collision cascade, chemical driving forces, activation energy of lattice atoms, etc. Most of them cannot be described sufficiently based on the analytical treatment only. At present only the atomistic simulations (e.g. MD), where all the driving forces are included, are able to reproduce ion-induced-mixing correctly. Additionally, microscopic processes like phase formation, nucleation, phase ordering or recrystallization are included into atomistic modeling.

## 2.2 Binary Collision Approximation

---

In the last section it has been shown that analytical transport theory can describe various properties of collision cascades, e.g. sputtering yield or ion beam mixing. It has been also shown that a major disadvantage of that theory comes from the surface treatment in the *ad hoc* infinite medium. The infinite initial conditions in the transport calculations allow recoils for a multiple crossing of an arbitrary plane of a material. In reality, the particle is lost straight after it crosses the surface. Therefore, the sputtering yield is often overestimated by analytical formula. On the other hand, ion beam mixing will be usually underestimated in the transport calculation (see Sec. 2.1.4), mainly because of the assumption of isotropic cascade mixing.

An alternative approach is using computer simulations to follow the full collision cascades and study sputtering or mixing processes. As it has been shown, integration of the equation of motion used by MD is very time consuming, mainly because of necessary fine time discretization. Especially in simulations including ion irradiation, the MD approach seems to be not always obligatory and several approximations can be applied. One very successful method simulating the radiation damage in solids is called Binary Collision Approximation. It takes many advantages from ion-solid interaction theory of ion beam sputtering [31, 34, 61], which have been introduced in the previous section. In order to reduce the simulation time and increase the simulated system size, a number of assumptions are necessary:

1. The many-body interactions are reduced to the binary interactions, which appears sequentially along the trajectory of the projectile.
2. During each collision kinetic energy is transferred using classical momentum conservation law. This process is called elastic energy transfer (see Sec. 2.1.2).
3. Electronic energy loss is treated separately and the method of calculation depends on the energy of the projectile (see Sec. 2.1.2).
4. Two methods of material distribution in the target have been proposed up to now: (i) suited for amorphous targets, where the target atoms are chosen randomly (according to MC sampling rules). This method enables the introduction of mean free path, which is fixed and strictly related to the volume density  $\lambda = n^{-1/3}$  [30, 38, 62]. (ii) including the crystal structure, where the binary interactions appear as the next nearest-neighbor projections on the projectile trajectory. The stochastic

distribution of target atoms is replaced by static rigid lattice and  $\lambda$  is now equal the nearest projected neighbor distance [63,64].

5. Interactions between projectiles and surface atoms are approximated by introduction of surface binding energies. Atoms with energy higher than the surface binding energy are removed from the target, i.e. these atoms are sputtered.

Based on these assumptions, several modeling strategies using BCA technique have been developed. The first version called TRIM (TRansport of Ions in Matter) [62] is a Monte-Carlo algorithm that describes the trajectory of projectiles represented by a binary collision sequence. It assumes a complete independence of subsequent ion impacts in amorphous solid and allows computer experiments of low computational costs. Originally TRIM handled only the incident ion trajectories, neglecting the full collision cascade including all recoil trajectories. Later on many extensions have been introduced. The most popular version of TRIM is contained in the SRIM package<sup>7</sup> (The Stopping and Range of Ions in Matter), and was developed originally by Biersack and Haggmark [62]. However, more detailed studies on stopping powers and ranges have been done by Ziegler, Biersack and Littmark [30]. Further extensions focus on the surface phenomena like sputtering [30,38] (TRIM.SP), or including the crystal structure instead of an amorphous target for the investigation of channeling effects [63,64] (CRYSTAL TRIM). Later on Möller and Eckstein developed the TRIDYN [39] (TRIM.SP DYNaMical), which includes fluence dependent target changes and changes of local concentration distribution of multicomponent targets in 1 dimension (along the depth). Furthermore, recent studies present an important actualization of TRIM.SP, by addition of a lateral dimension and allow surface profile modification [65–67]. Unfortunately also additional free parameters had to be introduced there (like anisotropy coefficients), responsible for the horizontal and perpendicular volume changes induced by atomic displacement and implanted impurity atoms.

Sec. 2.2 provides an introduction into the two BCA type models mentioned in the previous paragraph, TRIM and TRIDYN. Both are valid for amorphous material study.

### 2.2.1. TRIM

In TRIM ions and recoils are treated as so called ‘pseudoprojectiles’<sup>8</sup>. This means that a single projectile is considered as a group of atoms (or a certain unit of fluence) and all the parameters are scaled accordingly to the number of particles in the group. Any thermal vibrations of the matrix atoms around their equilibrium positions are neglected. The vibrational frequency of lattice atoms is usually of the order of  $10^{12} \text{ s}^{-1}$ , whereas the duration of the collision cascade, as measured by MD simulations, is in the range  $10^{-14} - 10^{-13} \text{ s}$ . Therefore, the assumption of fixed atomic position and independent collision cascades provides a very good theoretical approximation. The scattering angles of the collisions are calculated for all impact parameters below a maximal impact parameter

$$p_{max} = (\lambda\pi N)^{-1/2}, \quad (2.36)$$

---

<sup>7</sup>SRIM - the stopping and range of ions in matter - can be downloaded from [www.srim.org](http://www.srim.org). It is freeware software updated almost each year. For the biggest attention deserve a huge collection of stopping power experimental data together with analytical fits.

<sup>8</sup>The interval of fluence, corresponding to the one pseudoprojectile is calculated as  $\Delta\phi = \phi_{tot}/N_H$ , where  $\phi_{tot}$  is the total simulated fluence and  $N_H$  denotes the number of incident pseudoprojectile histories

where  $N$  represents atomic density and  $\lambda$  is a mean free path denoting the distance between two subsequent collisions. In the simulated algorithm, separately for each collision, impact parameter is selected according to the random number and afterward it is used for calculation of deflection angle in so-called ‘Magic’ formula [62]. The computation relies on scattering cross section calculation of trajectory integral (2.11).

In TRIM the colliding partner is selected randomly to provide quasi-random distribution of atoms in the system and to simulate amorphous materials. Even for crystalline materials, spatial randomness is usually a good approximation, especially if effects connected with the channeling are not dominating in the system.

In the present version of program used for simulations in this work, the mean free path is fixed and strictly related to the volume density  $\lambda = N^{-1/3}$ . Atomic interaction is described by universal two body potential is based on so-called ‘Kr-C’ potential approximation [35] with the Firsov [36] screening length (2.9). The target atom for each collision is chosen within a disk of a radius  $p_{max}$  (2.36). Reduced energy and length is introduced according to Lindhard equations (2.14). For the elastic energy transfer to the target atom is used Eq. (2.3). Electronic energy loss is divided into:

- Nonlocal ( $\Delta E_{nloc}$ ) - projectiles lose the energy within the straight path between the collisions and the energy cross section  $S_{el}(\varepsilon)$  is calculated using the Eqs. (2.19) for low ion energies and (2.17) for high energies

$$\Delta E_{nloc} = (\lambda - \lambda_t) N S_e(\varepsilon). \quad (2.37)$$

Here,  $\lambda_t$  denotes the offset of deflection point in an hard-sphere approximation given by

$$\lambda_t = r_{min} \sin \frac{\theta}{2} \quad (2.38)$$

- Local ( $\Delta E_{loc}$ ) - inelastic energy loss is directly connected with the collision itself, where local energy loss was given by Oen and Robinson [68], with the formula

$$\Delta E_{loc} = \frac{c_6^2}{2\pi a^2} S_{el}(\varepsilon) e^{-c_6 r_{min}/a} \quad (2.39)$$

where  $c_6$  is a fitting parameter and  $a$  a screening length for given interaction potential (2.9).

To increase the underestimated energy loss of binary collision, additional subsequent ‘weak’ collisions with more distant atoms are performed with impact parameter larger than  $p_{max}$ :

$$p_{weak} = p_{max} \sqrt{k + R_u}, \quad k = 1, 2, 3, \dots \quad (2.40)$$

where  $R_u$  is an uniform random number.

In order to reproduce experimental values of sputtering yield ions starts the cascade at ‘atomically rough’ surface, where the surface roughness is equal  $\lambda$ . Above the height of 0, no atoms are expected, however the collisions with surface atoms are possible up to the height of  $2p_{max}$ , which is the initial position of ions and also the threshold height of sputtered atoms. Although the maximal impact parameter is only  $p_{max}$  the ‘weak’ interactions are possible even for larger distances.

Several material specific input energies have to be defined at the beginning of the simulation. Here is a review of each of them:

## 2.2. BINARY COLLISION APPROXIMATION

1. Surface binding energy ( $U_0$ ) - is a factor that determine the sputtering yield. There is an inverse linear dependence between  $U_0$  and the sputtering yield, which has been analytically derived with Eq. (2.21). For monoatomic targets it is sufficient to use sublimation enthalpy for  $U_0$ , however if several compounds are present, the additional dependence on an enthalpy of formation and a dissociation enthalpy (for diatomic gases) may play an important role.
2. Displacement threshold energy ( $E_d$ ) - is a minimum energy transferred to the recoil, necessary to permanently displace an atom from its lattice site. It is not the same as threshold energy  $E_m$  used in ion beam mixing defined in Eq. (2.32) and usually  $E_d > E_m$ , as defect recombination can influence Frenkel-Pair much less than relocation. The values of  $E_d$  in crystalline targets can be in range even of 20-50 eV (see Refs. [69–71]), however high fluence simulations consider usually highly damaged, amorphous targets, where the displacement energy is significantly lower and the value of 15 eV is mostly used.
3. Cutoff energy ( $E_{cut}$ ) defines the threshold for particle termination. This means, if the atom's energy drops below  $E_{cut}$ , it is considered as stopped and can be treated as interstitial. Generally in TRIM it is common to reduce the computation time using this parameter, by putting it as high as possible. Nevertheless to preserve proper values of sputtering yield it should be lower than  $U_0$  and as low as possible to preserve ion and recoil ranges.
4. Bulk binding energy ( $E_b$ ) is subtracted from nuclear energy transfer within each collision.  $E_b$  is also interpreted as the vacancy activation energy. No general procedure for determination of  $E_b$  has been reported in the literature. Usually it is simply set by 0, otherwise the sputtering yield tends to be underestimated [38, 72].

Also the target parameters have to be defined. The most important are (for both TRIM and TRIDYN): atomic and volume density, number of implanted projectiles, ion energy and incidence angle, target composition, etc.

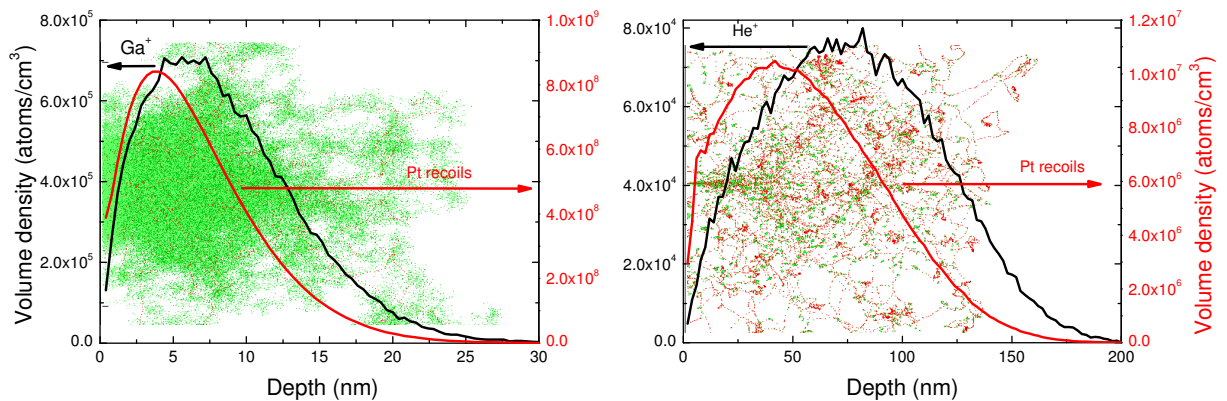


Figure 2.8.: Ranges distributions of  $\text{Ga}^+$  (left) and  $\text{He}^+$  (right) at 30 keV ion bombardment of Pt. Simulations have been performed with SRIM package using 100000 ions and recalculated for volume density units at the ion fluence of  $10^{16} \text{ cm}^{-2}$ . Black and red curves denotes ion and recoils distributions respectively. In the background, the atomic trajectories for corresponding simulations are inserted after 100 ions, implanted from the left direction.

On a Fig. 2.8, ion and recoil ranges distributions are presented after bombardment with heavy Ga and light He ions with 30 keV of ion energy. It is a typical output of

TRIM simulation that provides several important insights of collision cascade evolution. Due to the low nuclear energy loss with light He ions, its range (80 nm) is one order of magnitude larger than Ga ions (8 nm). Also in displacement rates there is a huge difference. For the fluence of  $10^{16} \text{ cm}^{-2}$  maximum value for  $\text{Ga}^+$  is  $\text{dpa}=11.2$  and for  $\text{He}^+$   $\text{dpa}=0.14$ , which can be confirmed from the background trajectories of Fig. 2.8.

### 2.2.2. TRIDYN

Local composition changes and a dependence of the atomic concentration on the fluence (often called ‘dynamic’ effects of collision cascade) are introduced in TRIDYN. It is well known, that most of the equations that control TRIM functionality, are dependent on the local concentration of components at the different locations in the target. This concentration will change together with the fluence, which is the time factor of every simulation. Major influence on composition changes has an ion induced ballistic displacement of the bulk atoms that induces defect creation and defect dynamics.

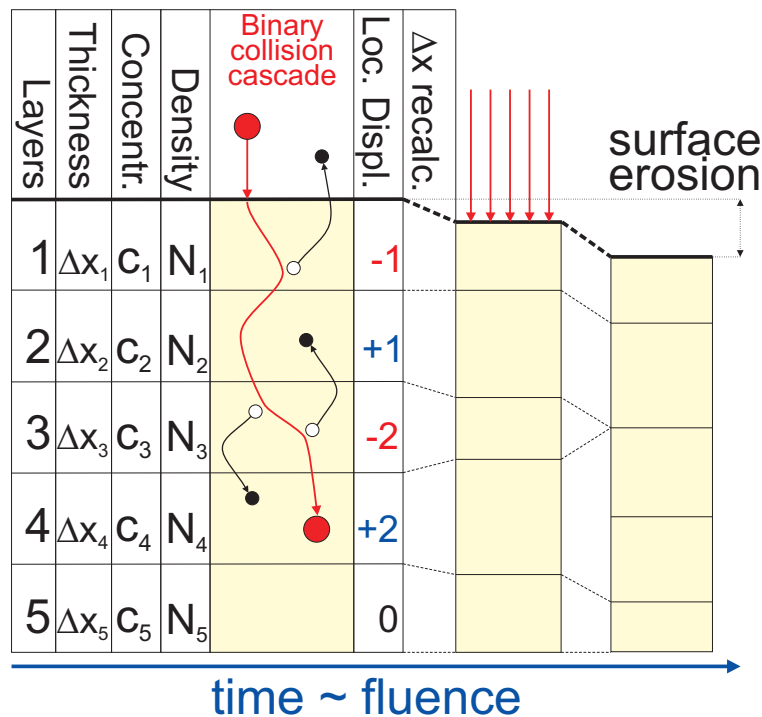


Figure 2.9.: Schematic representation of simulation procedure followed in TRIDYN. Except the ballistic part of the binary collision, the recalculation of layer properties such as, thickness, concentration and atomic density is completed after each collision cascade. Emphasized erosion process is usually induced by higher sputtering yield than implantation rate during the bombardment.

Very schematic evolution of the system under ion irradiation is presented in Fig. 2.9. It shows that the whole target is subdivided into a certain number of slabs of initially constant thicknesses  $\Delta x_i = \Delta x_0$ . This depth intervals evolve in time and the thickness varied proportional to the number and the type of relocated atoms into or out of the layer  $i$ . If  $i$  is the number of depth interval (layer) and  $j$  is a type of the component, the

thickness of the slabs can be expressed by

$$\Delta x_i = \sum_j \frac{A_{ij}}{N_{0j}}. \quad (2.41)$$

Here,  $N_{0j}$  is the atomic density of a pure component  $j$ .  $A_{ij}$  denotes the atomic areal density of component  $j$  in the layer  $i$  and its change ( $\Delta A_{ij}$ ) is described by the relation

$$\Delta A_{ij} = \Delta n_{ij} \Delta \phi, \quad (2.42)$$

where  $\Delta n_{ij}$  denotes the change in the number of pseudoprojectiles type  $j$  in layer  $i$ .  $\Delta A_{ij}$  provides the information about the local displacement. The local concentration is then given by,

$$c_{ij} = \frac{A_{ij}}{\sum_k A_{ik}} \quad (2.43)$$

and atomic density of each layer is calculated with the equation

$$N_i = \left( \sum_j \frac{c_{ij}}{N_{0j}} \right)^{-1}. \quad (2.44)$$

The thickness of each layer should not exceed 50 percent of initial thickness  $\Delta x_0$  during the simulation. If it happens however, the total number of depth intervals have to be increased by one, if  $\Delta x_i < 0.5\Delta x_0$  or decreased by one, if  $\Delta x_i > 1.5\Delta x_0$ . Finally, output of the simulation is calculated for equidistant intervals by interpolation.

The introduction of dynamic effects for bulk composition changes is a powerful advantage of TRIDYN. However, it is very restricted by one-dimensional calculation of the composition as a function of depth only, whereas the two lateral directions are neglected. It was mentioned before that the extension of this method exists and Mutzke, Bizyukov and Schneider provided two-dimensional evolution of composition by Refs. [66, 67, 73]. The main advantages of this approach are investigation of the surface topography modified by ions, influence of the surface morphology on sputtering yield, local surface composition analysis or local deviations of the composition of different components in the bulk. However, what is still missing is full atomistic, three dimensional view, where all chemical interaction are included. The major aim of this thesis is such an extension, where the methodology of two different simulation techniques i.e. BCA and KMC are unified into a new program package named TRIDER, which is the abbreviation from TRansport of Ions in matter with DEfect Relaxation. The defect relaxation contained in the abbreviation denotes the defects like: vacancies, interstitials, surface vacancies, ad-atoms, impurities and antisites.

### 2.2.3. Theoretical limits of BCA

The limitation of BCA based models is even today not completely clarified. The major argument that determines the limitation is the thesis that binary approximations breaks down, if many-body effects become significant. This means, that at a low energy of collision the projectiles cannot reach their trajectory asymptotes within the time necessary to interact with the next collision partner. Very extensive review about the theoretical restrictions concerning hard-sphere approximation of BCA was provided by Eckstein [61] with the conclusion that the break down energy is in the order of few eV even for unequal

masses of colliding atoms. Therefore, in cases of atomic trajectory studies the energy regime of a few eV is too low to reproduce exact trajectories of a collision cascade. In case of sputtering however, very low energy tends to provide still very accurate, experimental results.

Many approaches of direct comparison between BCA and MD type of simulation have been proposed in the past. Most of them however, consider only crystalline materials, very often with incorporation of channeling effects during implantation. The most famous effort of investigation of a huge number of numerical algorithms is the ‘round robin’ simulation of the ion transmission through crystalline  $\langle 100 \rangle$  Si and Cu. It was described in the work of Gärtner *et al.* [74]. The final conclusion was a very good agreement between MD and BCA even for energies around 100 eV.

Another parallel work [75] suggest that the small differences in concentration profiles can be observed at  $E_0 = 500$  eV in case of self-sputtering in Si, where MD results tend to provide significantly lower ion projected ranges ( $R_p$ ). At the energy of 250 eV and below the difference becomes significant. Later on, MD study [76] confirms this tendency using the comparison with amorphous targets of TRIM simulation.

On the other hand Hobler and Betz [77] provide an extensive study about the consistency between MD and BCA with crystalline Si target of  $\langle 110 \rangle$  surface, comparing most carefully the projected ranges using different types of ion. They derive the empirical formula describing the lower limit of ion energy  $E_{min}^{BCA}$ , where the error is still acceptable (i.e. lower than 5%):

$$E_{min1}^{BCA} = 30M_1^{0.55} \text{ eV} \quad (2.45)$$

where  $M_1$  is the mass of the ion. Additionally, if the mass ratio between target and ion is close to 1, the  $E_{min}^{BCA}$  can be even lower (in case of Si bombardment for the ions with atomic weight between the mass of Si and Ar,  $E_{min}^{BCA} \approx 70\text{eV}$ ).

The most recent comparison by Chan *et al.* (see Ref. [78]), includes a large database of experimental results made with secondary ion mass spectroscopy, to study implantation of dopants into Si in low ion energy regime, as well as the MD results. They propose new formula of ion energy ‘breakdown’, based on DFT calculation of pair potentials regardless of crystal orientation and neighboring effects:

$$E_{min2}^{BCA} = 0.0565M_1^{0.907} \text{ keV} \quad (2.46)$$

It results in significant increase of the minimal ion energy up to keV regime, especially in case of heavier projectiles (e.g. for Si  $E_{min2}^{BCA} = 1.202$  keV, for  $\text{Ar}^+$   $E_{min2}^{BCA} = 1.6$  keV). Nevertheless, the same comparison for phosphorous (with the atomic mass almost the same like Si) does not show any significant deviation of concentration curve even at 500 eV energy of ion implantation.

Table 2.1.: Comparison between TRIM and CRYSTAL-TRIM at low energies

$E_0$ (eV)	TRIM			CRYSTAL-TRIM		
	$R_p$ (Å)	$\Delta R_p$ (Å)	$N_{coll}$	$R_p$ (Å)	$\Delta R_p$ (Å)	$N_{coll}$
100	9.00	4.97	6.27	6.45	2.74	12.8
500	22.8	12.7	14.4	21.1	10.2	33.2
1000	35.1	19.4	21.3	35.4	19.5	53.7

In case of the low energy ion bombardment of amorphous Si, the general picture is not fully understood due to the lack of experimental and theoretical data. However, the

comparison of two types of BCA models, which are TRIM [62] and CRYSTAL-TRIM [64], provided in Tab. 2.1 shows that amorphous-like BCA generates slightly higher values of  $R_p$  and  $\Delta R_p$  (straggling<sup>9</sup>) than the crystal-like and the difference diminish for higher energies. But still, at  $E_0 = 100$  eV the deviation in  $\Delta R_p$  rises up to 28%. The simulations have been performed using 10000 ion impacts, with the volume densities  $N_{a-Si} = 49.76$  nm<sup>-3</sup> and  $N_{c-Si} = 49.94$  nm<sup>-3</sup>. Ion trajectories have been initially tilted by 7° to reduce channeling effects in CRYSTAL-TRIM at higher energies. The only variable that deviates more than 100% is the average number of collisions per ion  $N_{coll}$ . Since crystalline version of BCA does not consider average path length  $\lambda$  as a constant distance between two independent collisions, selecting the collision partner to be the first atom located perpendicular to the trajectory of projectile within a previously defined maximal radius, the number of ‘weak’ interactions increases strongly. This has a significant influence on  $N_{coll}$ , whereas  $R_p$  and  $\Delta R_p$  are affected only at very low energies.

## 2.3 Kinetic Monte-Carlo

A fairly good approach for fast calculation of thermally activated processes is provided by KMC methods [79–81]. There are several applications of these types of algorithms especially in studies of atomistic description of phase separation [82–84] or chemical ordering of metal alloys [85–88]. In both cases systems are driven by thermal relaxation towards equilibrium. The simulation of the driving forces with the KMC leads to a better understanding of interactions between the atoms in compounds due to effects like nucleation or ordering. It is well known that Monte-Carlo simulation can also describe driven steady-states, which occur in open systems e.g. during ion irradiation [89, 90]. Thus, it cannot be a tool, which provides information about the collision cascade. Therefore, to study ion-induced kinetic processes with the KMC, a statistical input obtained using different computer experiments (usually MD or BCA) of the defect distribution or deposited energy distribution has to be included.

In contrary to MD simulations, equilibrium Monte-Carlo (MC) considers an existence of a well-defined statistical probability for the system to change the state from a configuration  $\nu$  to  $\tilde{\nu}$ . This probability is called transition probability  $P(\nu \rightarrow \tilde{\nu})$  and the mechanism that generates a new state is based on the Markov process [91]. In the conditions close equilibrium the transition of *detailed balance* ensures that the rates for the system to make the transition from  $\nu$  to  $\tilde{\nu}$  and opposite are equal and follow the equation,

$$\sum_{\nu} p_{\tilde{\nu}} P(\tilde{\nu} \rightarrow \nu) = \sum_{\nu} p_{\nu} P(\nu \rightarrow \tilde{\nu}) \quad (2.47)$$

where  $p_{\nu}$  and  $p_{\tilde{\nu}}$  are the probabilities of occurrence of the states  $\nu$  and  $\tilde{\nu}$  respectively. They can be written based on Boltzmann’s probability distribution as,

$$p_{\nu} = \frac{1}{Z} \exp \{-E_{\nu}/k_B T\}. \quad (2.48)$$

Here  $Z$  is the partition function,  $E_{\nu}$  is the energy at the state  $\nu$  for the temperature  $T$ .  $k_B$  is the Boltzmann’s constant. To save the continuity of the Markov chain, any set of

<sup>9</sup>Straggling is the standard deviation of a range distribution. If  $r_p$  is a projected range of an ion,  $\Delta R_p = \langle r_p^2 \rangle - \langle r_p \rangle^2$ , where  $\langle \cdot \rangle$  denotes spatial averaging.



transition probabilities that satisfy equation (2.47) is allowed. Now using the probability distribution (Eq. (2.48)) it is enough to write

$$\frac{p_\nu}{p_{\tilde{\nu}}} = \frac{P(\tilde{\nu} \rightarrow \nu)}{P(\nu \rightarrow \tilde{\nu})} = \exp\{-\beta(E_\nu - E_{\tilde{\nu}})\}, \quad (2.49)$$

where  $\beta = 1/k_B T$ . Knowing the configuration energies allows for describing statistical processes close to equilibrium on the atomic scale. Its advantage on MC brings the fact that not all of the intermediate states have to be followed and the number of possible configuration can be drastically decreased.

All types MC models, which describe only the equilibrium state do not consider dynamics in the system, therefore each state has energy  $E_\nu$ . In case of kinetic models out-of-equilibrium such as KMC, the transition from one state to another describes the reaction pathway and is defined by the transition energy barrier. From atomistic point of view, the time interval used in the KMC simulations does not have to be vibrational frequency around the equilibrium, but it is enough to use the frequency of the jump attempt from one position to another. It is common to discretize the position phase space, following only the crystal lattice locations and therefore decreasing the number of possible system configurations.

Generally, kinetic Monte-Carlo models allow for a direct comparison with experiments on spatio-temporal scales. KMC method used in this work, is a 3D lattice kinetic Monte Carlo algorithm, based on a Cellular Automata (CA) approach [92], which allows the projection of many-body potential of MD onto atomic configurations used by KMC. It was also a scientific tool in many Ph.D. theses for investigation of shape evolution and growth [2, 93], ripening [94] or in modeling the synthesis of nanocrystals [95]. KMC approach is used here to study defect relaxation kinetics at the presence of ion-induced processes.

### 2.3.1. Lattice gases

Ising model [96] has been originally proposed to study phase transition from a paramagnetic to a ferromagnetic behavior. It considers a system in a canonical ensemble containing  $N$  lattice sites and assume that each site  $i$  is associated with spin projections on the orientation  $s_i = \pm 1$ . Because of only two possible spin projection, the total number of states in the system will be  $2^N$  and the energy of any particular state can be expressed by the Ising Hamiltonian

$$\mathcal{H} = -J \sum_{\langle i, j \rangle_{NN}} s_i s_j - B \sum_i s_i, \quad (2.50)$$

where  $J$  is the interaction energy between NN spins  $\langle i, j \rangle_{NN}$  (the exchange integral) and  $B$  is proportional to the uniform external magnetic field. If  $J$  is positive spin alignment is favored and the system becomes *ferromagnetic*. For negative exchange constant ( $J < 0$ ), anti-alignment of spins is favored and the system becomes *antiferromagnetic*.

The transition from magnetic spin to atomic lattice configuration is done by redefinition of spin orientation as the occupation number of a single lattice site

$$c_i = \frac{1}{2}(s_i + 1). \quad (2.51)$$

The occupation number of  $c_i$  is then 0, if the lattice site is empty, or 1 if, the lattice site is occupied. Substituting  $s_i$  and  $s_j$  in Eq. (2.50) and neglecting any external interactions ( $B = 0$ ) results

$$\mathcal{H} = -4J \sum_{\langle i,j \rangle_{NN}} c_i c_j + \text{const.} = -\varepsilon_{NN} \sum_{\langle i,j \rangle_{NN}} c_i c_j + \text{const.} \quad (2.52)$$

with NN bond energy  $\varepsilon_{NN}$ . Moreover, the total binding energy of a fully coordinated bulk atom (cohesive energy) is expressed by

$$E_b = \frac{1}{2} \eta_l \varepsilon_{NN}. \quad (2.53)$$

$\eta_l$  is a coordination number of a given lattice structure (for fcc lattices  $\eta_l = 12$ ). The total potential energy of bulk atom is divided by 2, because every bond is always shared between two neighbor atoms.

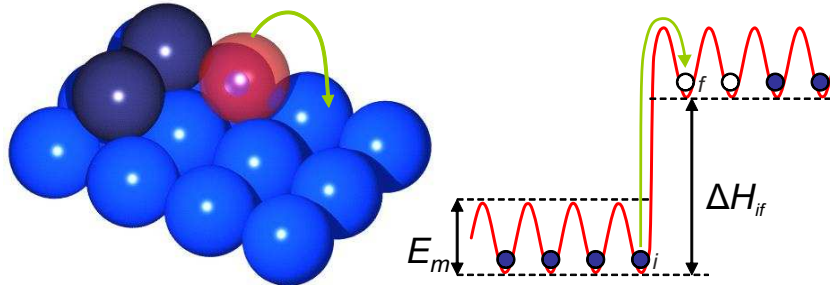


Figure 2.10.: Scheme of simple reaction pathway. The total energy necessary to relocate the atom due to the thermal reaction is a sum of migration energy  $E_m$ , specifying the frequency of migration on the lattice, and the energy barrier  $\Delta H_{if}$ , as a transition in the state of the system to be overcome, depending on the local atomic configuration. On the left, corresponding lattice representation is shown, where the energy state of the system will be increased, because of the one bond to be broken during the jump attempt ( $\Delta H = 1 \cdot \varepsilon_{NN}$ )

The main concept of KMC is to reproduce atomic jumps of atoms in the lattice through the jump probabilities between neighbor atomic positions described by Metropolis method [97],

$$P_{i,j} = \begin{cases} \Gamma_0 \exp \{ -E_m / (k_B T) \} & , n_f \geq n_i \\ \Gamma_0 \exp \{ -(E_m + \Delta H_{if}) / (k_B T) \} & , n_f < n_i \end{cases} \quad (2.54)$$

where  $n_i$  and  $n_f$  are number of occupied NN lattice sites in the initial ( $i$ ) and final ( $f$ ) state respectively,  $\Gamma_0$  is a frequency of a jump attempt.  $E_m$  is migration energy barrier and  $\Delta H$  is an energetic difference between initial and final site,  $k_B$  is a Boltzmann constant and  $T$  the temperature. In Fig. 2.10 schematic representation of one atom transition, together with energy levels for a reaction pathway is shown.  $\Gamma_0$  is a constant value that scales the time of simulation according to Debye frequency (that is in the range of  $10^{-12} \text{s}^{-1}$ ). For simplification reasons it is convenient to assume  $E_m$  to be constant for the matrix diffusion of a free monomer or a vacancy and the surface diffusion of an ad-atom, independent on a local configuration. Using the Vineyard method [98] of discrete lattice representation by saddle points, lattice vibration will not alter, if the constant effective mass of the system does not change (for instance in vacancy driven

diffusion system). Therefore, the time of the simulation can be calibrated by the vibrational frequency. Additionally, in order to reduce further the simulation time, the jump probability  $P_{i,j}$  can be normalized by the constant migration energy  $E_m$  [81]. Division by a factor  $\Gamma_0 \exp\{-E_m/(k_B T)\}$  results in scaled probability of the Ising model

$$\tilde{P}_{i,j} = \begin{cases} 1 & , n_f \geq n_i \\ \exp\{-(n_i - n_f)\epsilon\} & , n_f < n_i \end{cases} \quad (2.55)$$

where  $\epsilon$  is a reduced, dimensionless bond energy defined by

$$\epsilon = \frac{\varepsilon_{NN}}{k_B T}. \quad (2.56)$$

Using this assumption  $E_m$  will directly correspond to the jump frequency at a given temperature. A jump attempt according to eq. (2.55) of every atom in the system will be called 1 Monte-Carlo step (MCs).

Experimentally, ripple formation do not depend on the temperature in wide range around room temperature. This implies that the activation of jumps described above is caused by ion bombardment through a local increase of the kinetic energy of the atoms in the volume of each collision cascade. In this view the above formalism assumes an average increase of temperature to some amount, which is difficult to quantify. On the other hand, assuming room temperature in (2.56) for the bond energy expected for Si, would lead to an unacceptably inefficient MC procedure, as the jump rate would be prohibitively low. For the present simulations quite arbitrarily  $\epsilon = 1.7$  was chosen, which would correspond to an artificial  $T = 5350$  K according to (2.56).

### 2.3.2. KMC time step, ion flux and ion fluence

As discussed above, the MC simulation time step is defined by the mean time between atomistic diffusional jumps in the undisturbed lattice. According to the random walk model of diffusion, the diffusion coefficient is given by

$$D = \frac{a_{lat}^2}{\eta_l} \Gamma \quad (2.57)$$

for a lattice with the lattice constant  $a_{lat}$ .  $\Gamma$  denotes the average frequency of successful diffusional jump per atom (see eq. (2.54)) and the KMC time step is set as

$$\tau = \frac{1}{\Gamma} \quad (2.58)$$

or according to eq. (2.57) as

$$\tau = \frac{a_{lat}^2}{\eta_l D}. \quad (2.59)$$

The temperature, which determines the diffusion coefficient  $D$ , is subject to the same uncertainty as discussed above for the jump frequency. Therefore, a realistic correlation between the MC time step and a characteristic time of the system cannot be given.

The ion flux is defined as the number of incident ions per unit of time and irradiated area. A typical order of magnitude in experiments is  $10^{15} \text{ cm}^{-2}\text{s}^{-1}$  [99]. The number of incident ions per MC time step is then for a simulation with an ion flux  $j_{sim}$

$$N_i(\tau) = j_{sim} \tau A_{sim}, \quad (2.60)$$

where  $A_{sim}$  denotes the total surface area of the simulation cell. In the combined collisional/KMC simulation,  $N_i$  is the number of collisional simulations being performed between the KMC simulation steps, with ions of random incidence on  $A_{sim}$ . Depending on the ion flux, it may be smaller or larger than one. As the combined simulation is conveniently accomplished with an integer number of collisional simulation events per MCs (or vice versa), the simulations cover only a discrete set of ion fluxes. The results shown below have typically been obtained with 0.125 to 4 collisional simulations per MC time step.

With the uncertainties associated with definition of temperature as described above the simulated ion flux cannot be reasonably connected to the experimental ion flux. Therefore, for convenient comparison of the simulation results, a dimensionless normalized ion flux is introduced according to

$$j_{norm} = j_{sim} \frac{a_{lat}^2 \tau}{2}, \quad (2.61)$$

where the divisor 2 accounts for the fact that the fcc surface contains two atoms per unit cell.

By multiplying the  $j_{sim}$  by the time  $\tau$  ion fluence  $\phi$  is obtained. By the definition  $\phi$  is the number of incidence ions per surface area, i.e.  $\phi = N_i/A_{sim}$  (with the unit  $\text{cm}^{-2}$ ).

### 2.3.3. Binary alloys

For a binary alloy of a completely occupied lattice with the components  $a$  and  $b$  the mapping procedure on the Ising Hamiltonian (2.50) is similar to unary lattice gas case, according to the Eq. (2.52). Here, the pairwise interactions are calculated by a linear combination of  $\varepsilon_{NN}$  (for review see [88]) with the relation

$$\varepsilon_{NN} = \frac{1}{2} (\varepsilon_{aa} + \varepsilon_{bb} - 2\varepsilon_{ab}), \quad (2.62)$$

where the kinetics of the system is based on the Kawasaki dynamics [100] between the NN occupied lattice sites. The Kawasaki dynamics consider a pair of NN atoms of a different component that attempt to exchange the position and the exchange attempt probability is calculated with Metropolis method [97] (Eq. (2.54)).

In a simplest case of two phase system (the atomic phase and the vapor phase), it is enough to use single binary lattice to store atomic positions [81]. It is necessary to include several modifications into the simple lattice gas algorithm, if more than 1 atomic species are present in the system. System of three components has to be extended into two components: (i) atomic species  $a$ , (ii) atomic species  $b$  and (iii) empty sites<sup>10</sup>. That changes energy difference calculation used in equation (2.54) and the new Hamiltonian is given by  $\mathcal{H}$ ,

$$\mathcal{H} = -\frac{1}{2} \left\{ \sum_{\langle i,j \rangle} (\varepsilon_{aa} c_i^a c_j^a + \varepsilon_{bb} c_i^b c_j^b - 2\varepsilon_{ab} c_i^a c_j^b) \right\} \quad (2.63)$$

where  $\varepsilon_{ab}$  is a bond strength between components  $a$  and  $b$ , and  $c_i^a$  is the occupancy number of a lattice position  $i$  for the component  $a$ .

<sup>10</sup>In lattice gas approach the two existing phases are the gas and the vapor phase, however only the gas phase exhibits chemical interactions. Binary alloy case is fully equivalent to gas phase if no vapor phase exists, following simply the Eq. (2.62)

### 2.3.4. Atom coordinates as binary arrays using bit coding technique

The simulations with KMC algorithm used in this work consider perfectly arranged discrete crystal lattices, on which atomic positions are stored as binary numbers in the computer memory.

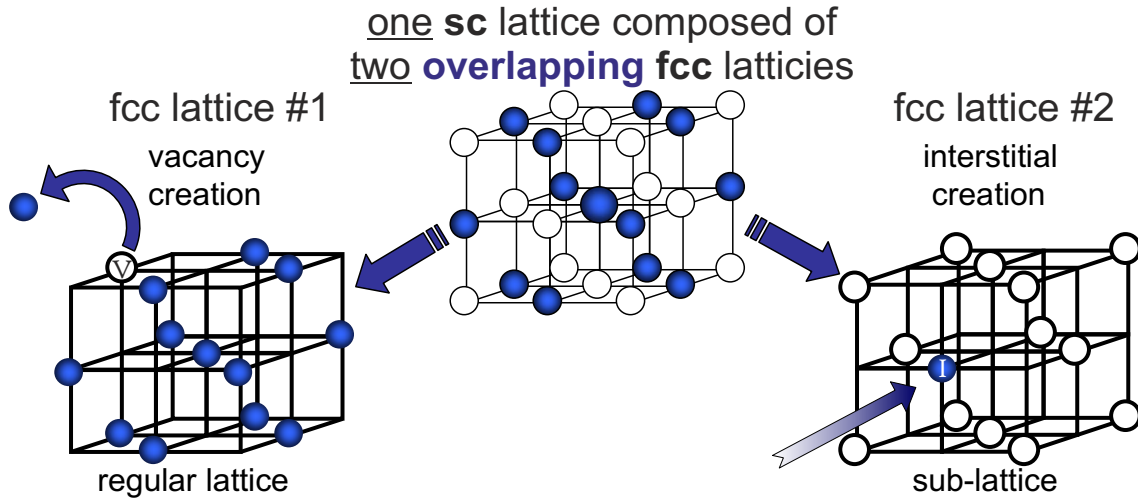


Figure 2.11.: Schematic diagram showing the lattice representation used in KMC simulations in one component systems. The `sc` lattice is divided by two `fcc` sub-lattices. Interstitial atoms can be stored in non-regular sub-lattice (right), vacancies belong to regular lattice (left).

For the simulations of two components, the system is represented by so-called binary lattice space, where the occupancy state of one atom is stored using a single bit memory unit (one bit for each lattice location). It is possible to simulate every cubic crystal structures (`sc`, `bcc`, `fcc`, `diamond`) with discrete atomic positions. The information is stored as an occupancy number in the `sc` lattice (see Fig. 2.11), which is the basis structure for all cubic lattices. In case of `fcc` lattice, only half of the possible atomic configurations are occupied. The second half (sub-lattice) originally stays empty. The regular lattice is used to store vacancies created during the cascade and sub-lattice contains interstitials. This type of lattice configuration is applied in the simulation of ion bombardment of Si surfaces described in Chap. 3.

To simulate 3-component systems (i.e. atomic species  $a$  and  $b$ , and empty sites) an extended description of binary lattice has been introduced. Here, two binary `sc` lattices, which are overlapping in the address space, store the information about the occupation of the lattice sites and the atomic species that occupy these sites. In Fig. 2.12 the `sc` lattice #1 defines, if a lattice site contains an atom independent on atomic species. It is composed of two overlapping `fcc` lattices described in the previous paragraph (Fig. 2.11), therefore it defines the positions of vacancies in the regular lattice and interstitials in sub-lattice. The `sc` lattice #2 (specification lattice) is used define species of atom, which occupation number has been provided by the `sc` lattice #1. Because the lattices are binary only 2 components ( $a$  and  $b$ ) can be defined by 1 specification lattice. The information about species of `fcc` lattice atoms is stored the the regular lattice sites of binary lattice #2, whereas the sub-lattice sites of binary lattice #2 define the species of interstitials. This procedure is universal and can describe multi-component systems by increasing the number of specification lattices. Therefore, to study  $n$ -component systems it is necessary to create in total  $\lfloor \log_2 n \rfloor + 1$  binary lattices. The lattice configuration of

3-component system is used in Chap. 4 to simulate two bilayer targets irradiated with  $\text{He}^+$  ions: Al/Pb and Co/Pt.

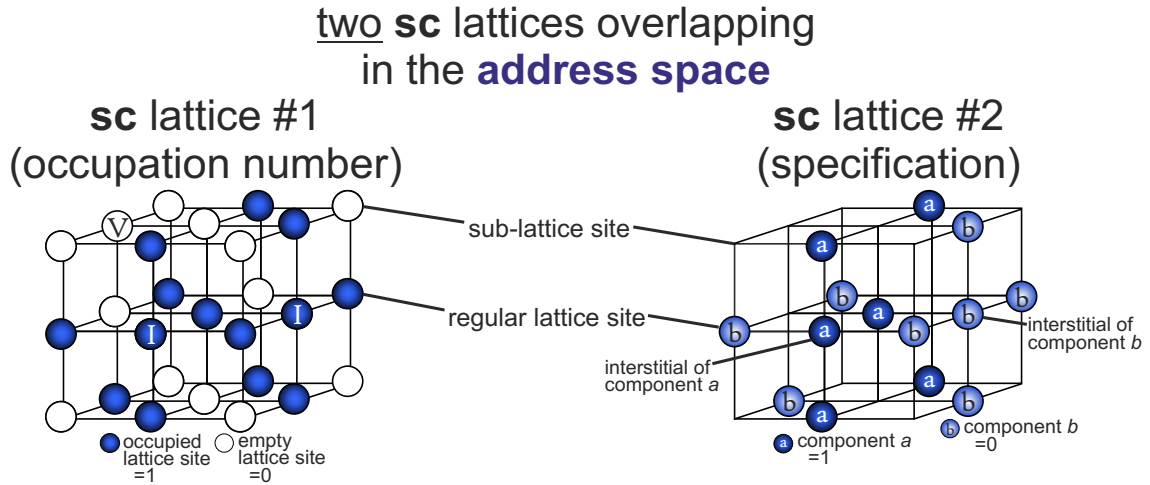


Figure 2.12.: Scheme showing the lattice representation used in KMC simulations in 2 component systems. To store location of atoms  $a$  and  $b$  as well as vacancies and interstitials in the computer memory two sc binary lattices overlapping in the address space are necessary: (left) sc binary lattice space #1 defines the lattice occupation not specifying atom types (it is equal 1 or 0, if the lattice site is occupied or empty, respectively); (right) sc binary lattice space #2 specifies an atom type (it is equal 1 or 0, if the occupied lattice site contains an atom of the component  $a$  or  $b$  respectively).

## 2.4 The interface between BCA and KMC

Within the last few years it became very popular to combine various types of simulation methods to solve more complicated physical problems, where very often different scales of simulation are involved. This computation approach is known as ‘multi-physics modeling’. Multiphysics usually combines different kinds of continuum theories, by solving partial differential equations via finite element analysis, coupling several phase fields like electric, thermal, magnetic, acoustic, structural, etc.<sup>11</sup>

In recent publications, several approaches of coupling computation methods like MD and KMC, can be found [102,103]. Usually MD is employed as a tool for finding input parameters of energy barriers, or migration energies for Monte-Carlo simulations, although there exists an “on the fly” combination, where collisional and defect relaxation parts are invoked sequentially [104]. Moreover, combinations of BCA and KMC approaches have been proposed in the past. In the work of Koponen *et al.* they focus mainly on surfaces modification restricting to two-dimensional simulation of SOS model, where sputtered atoms are constantly removed from a 2 + 1 dimensional surface [105]. Kellerman *et al.* use a binary collision model to generate bulk defects and afterwards simplified KMC algorithm is applied to simulate bulk diffusion and phase separation [106].

The method proposed in this thesis, is a full three-dimensional atomistic treatment based on many-body interactions, which can be applied to very large systems (areas larger than  $1000 \times 1000$  lattice sites). The main reasons for that is a very fast code based

<sup>11</sup>There are several packages available on the market, which are mainly applied by engineering and design industry [101]

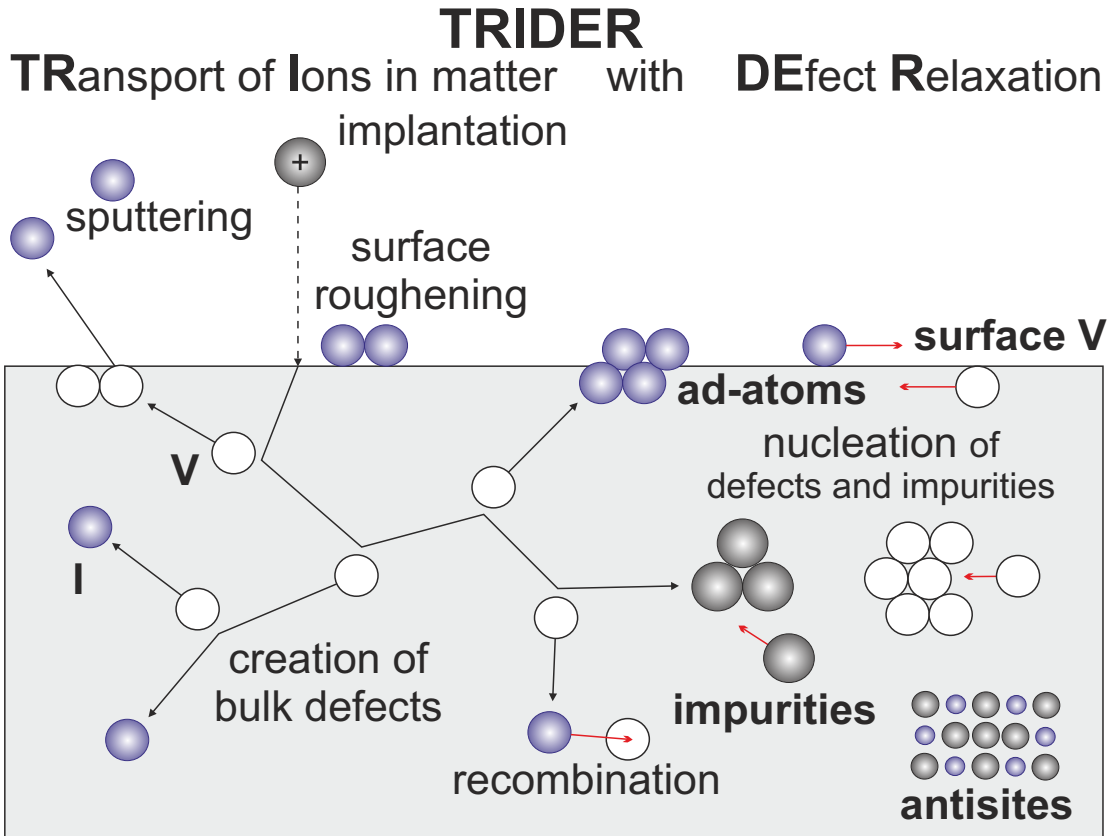


Figure 2.13.: Variety of processes present during ion-induced irradiation. Black arrows describe bombardment induced mechanisms, red arrows defect relaxation mechanisms.

on BCA unified with a bit-coded CA [92]. The latter one is used for KMC simulations. Bit-coding provides maximal usage of random access memory.

A simultaneous description of the formation of ion-induced collision cascades and the immediately following recombination of defects, phase separation etc. can be inherently performed by molecular dynamics simulations. However, for this kind of description MD suffers so far from two unresolved problems: (i) it is very difficult to find reliable atomistic potentials covering the whole range from eV (thermally activation) to keV (close collisions), (ii) even with modern fast computers it is not yet feasible to perform MD simulations for practical ion fluences at experimental spatiotemporal scales.

In the computer program named TRIDER, processes like a *damage formation* and a *defect relaxation* have been connected via an interchangeable interface. The damage formation refers to processes like: vacancy and interstitial creation, sputtering, impurity implantation, surface roughening. The defect relaxation refers to the defects like: vacancies, interstitials, surface vacancies, ad-atoms, impurities and antisites. As the result of the simulation, the information about the atomistic features, i.e. vacancies and defect creation and annihilation, sputtering yield distribution, bulk and surface diffusion, ion-induced or thermal inter-mixing and concentration profiles, can be obtained (see Fig. 2.13).

This section focuses mainly on methodology concerning the simulation procedures, which build the interface between BCA based algorithm and KMC simulation. Several assumptions are needed that provide the description of defect processing, surface treatment and recombination mechanisms. Next, the flow diagram of simulation sequence will

provide the information about the memory management and the data transfer between stages of the simulation. Finally, a small scale demonstration of simulation including all major processes will be presented.

### 2.4.1. Major modifications in TRIM / TRIDYN

The current version of the program is based on multicomponent TRIDYN simulation of Möller and Eckstein [39], where ‘dynamic’ part has been replaced by KMC algorithm of Strobel and Heinig [81]. Therefore, the algorithm based on BCA is almost identical to the Biersack code TRIM and a brief description of all the aspects of algorithm have been provided in Sec. 2.2. Moreover the detailed specification can be found elsewhere as well [62].

In the new version, treatment of ion bombardment has been extended in the way that every impact position is selected randomly on the surface of bombarded target of requested system sizes. The surface has to be extracted from the three-dimensional lattice system used during the KMC calculation. The normalization of pseudoprojectiles, used previously in TRIDYN to accelerate the computation of fluence, is not valid here anymore, since the atomistic picture of the bulk is applied in KMC. The methodology regarding extraction of the surface from the regular lattice space is an important issue and has to be explained in details. There are four steps of algorithm developed especially for fcc lattices:

- (i) The system is scanned to find and select the lower-coordinated atoms (here the atoms with less than 12 NN).
- (ii) The previous choice is now restricted only to surface coordinates due to recursive selection of atoms mutually connected through the bounds. This point might not work in case of large vacancy clusters occurrence, therefore the decision is restricted only to the set of atoms of the number higher or equal than the number of atoms covering a surface plane.
- (iii) The three-dimensional output is converted to  $2 + 1$  dimensional surface plane where every position is representing the height.
- (iv) The Gaussian smoothing algorithm is applied (so-called blur filter [107]) to reduce step edges differences of heights between the neighboring sites. The matrix size of the Gaussian filter is equal 5 and the standard deviation equals 1.

This procedure is demonstrated in Fig. 2.14 and the final output, a smooth polynomial surface, can be directly applied into the BCA calculations. The stage of the simulation responsible for the displacement cascade considers an amorphous distribution of atoms. Therefore, the final smoothing procedure provides a quasi-amorphous interface. An additional advantage of smoothing is the reduction of strong surface slopes, related with existence of step edges on the surface. Strong slopes affect the calculation of projectile energy threshold for sputtering that depends on a local surface slope. For a microscopically rough surface the smoothing procedure provides a better estimation of sputtering yield especially at oblique ion incidence angles, whereas without smoothing the sputtering yield is underestimated even by 25%.

Obtained  $2 + 1$  dimensional surface of a height  $h(x, y)$ , with coordinates  $x$  and  $y$ , is now updated with the initially defined period of time. As mentioned before every ion



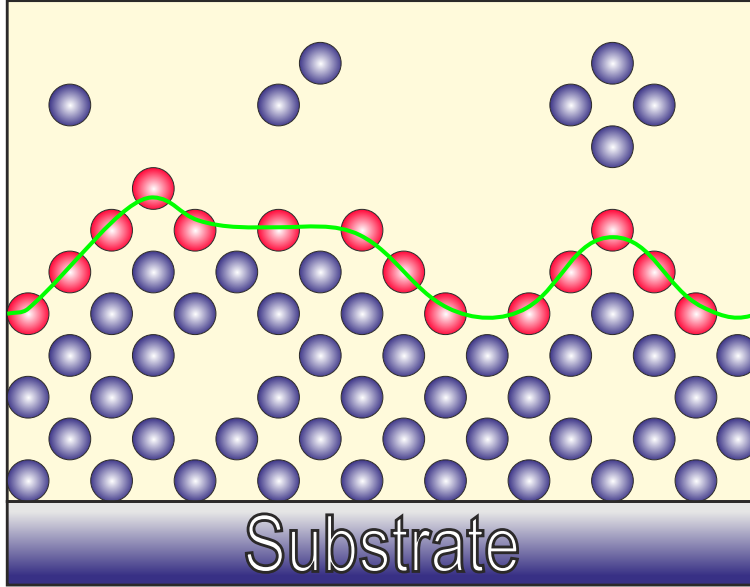


Figure 2.14.: Schematic of the surface treatment. Four stages of the surface extraction procedure are described in text. Here, the red atoms are the extracted surface atoms. The green curve is the final surface, smoothed with the Gaussian filter.

trajectory starts externally at the surface  $h(u_x, u_y)$ , where  $u_x$  and  $u_y$  are random numbers uniformly distributed between 0 and the system size in the lateral  $x$  and  $y$  directions, respectively. However, the distribution of ions approaching the surface is not uniform along lateral directions. In order to correct the local flux distribution<sup>12</sup> the acceptance condition for incoming ions is applied according to

$$R_u \geq \cos \alpha_{in}, \quad (2.64)$$

where  $\alpha_{in}$  is the local incidence angle and  $R_u$  is a random number uniformly distributed between 0 and 1. Using the condition in (2.64) randomly selected ions are discarded from further computation and only for accepted ions the KMC stage is considered.

The height of a collision is determined also randomly  $h(u_x, u_y) + x_c + \lambda R_u$ , with a constant  $x_c = -2N_s^{-1/3}/\sqrt{\pi}$  defining the maximal interaction distance over the surface (Fig. 2.15) [38], where  $N_s$  is atomic density at the surface (see Ref. [38]). Periodic boundary condition is assumed in lateral directions of the system. In longitudinal direction, an atom is considered either as sputtered, if its height is larger than  $h(x, y) + x_c$  or transmitted, if its height is lower than zero.

The surface morphology may change during the simulation. Therefore, it is necessary to modify the method of calculation of sputtered particles. The corrected angle of sputtering  $\alpha_c$  (see Fig. 2.15) will be now the angle between vector normal to the surface  $\nabla h$  and the direction *unity* vector  $\vec{D}$  of an atom according to,

$$\begin{aligned} \nabla h &= \left( \frac{\partial h}{\partial x}, \frac{\partial h}{\partial y}, -1 \right)^T \\ \cos \alpha_c &= \frac{\nabla h \cdot \vec{D}}{|\nabla h|}. \end{aligned} \quad (2.65)$$

<sup>12</sup>In this work also the case without flux correction is studied to show the sensitivity of surface pattern propagation on the local slope approximation.

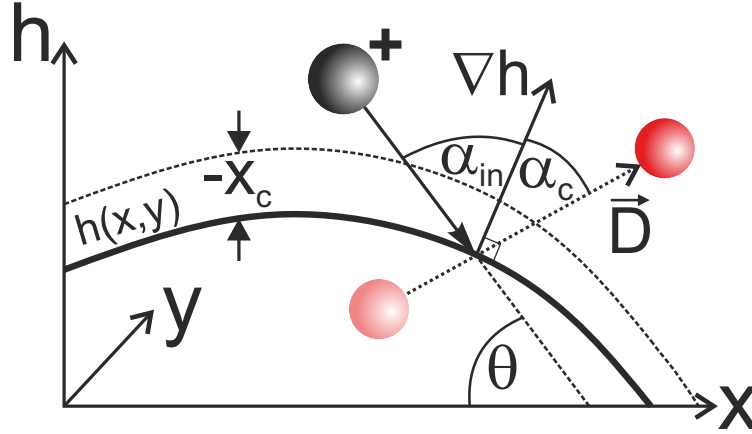


Figure 2.15.: Surface representation for estimation of angle of sputtering  $\alpha_c$  and local incidence angle  $\alpha_{in}$ .

The position of a target atom during the collision event is not completely stochastic anymore. Although TRIM considers only the constant concentration of the components, specified before the simulation, TRIDYN was able to handle ‘dynamically’ transitions in concentration profiles [39] due to the collisional displacement, by one-dimensional description. In present version this treatment has been extended into three-dimensional lattice. During every collision event the projectile chooses the species of collision partner according to the closest lattice atom, inside a sphere of the radius  $\lambda + x_c$ . Such an approach corrects the energy transfer in the systems with high concentration of voids. In case of presumptive collision inside the volume filled by vacancies, there is no energy loss and the trajectory of the projectile does not change until the next collision with one of the system components.

The calculation of volume density has been modified and now strictly depends on the local position of the projectile. Although in TRIDYN the volume density is also localized, it considers only depth dependence, neglecting actual position in space and influence of the neighborhood. In the present version, the estimation of the local partial density of the projectile  $N_{loc}^{-1}$ , takes into account the closest environment according to the equation,

$$N_{loc}^{-1} = \sum_{i=1}^q \frac{c_i}{N^{(j)}} = \frac{1}{\eta_l} \sum_{i=1}^q \frac{1}{N^{(i)}} [n_{lat}^{(i)} + n_{int}^{(i)}] \quad (2.66)$$

where  $N^{(i)}$  is a global volume density of component  $i$ ,  $n_{lat}^{(i)}$  is a number of occupied nearest neighbor (NN) lattice sites of component  $i$ ,  $n_{int}^{(i)}$  is a number of NN interstitials of  $i$ ,  $q$  is the number of components in the system and  $\eta_l$  is the coordination number of fully occupied with atoms lattice (for fcc lattice this number is 12). For a fully occupied lattice system, the local concentration  $c_i$ , fulfill the condition  $\sum_{i=1}^q c_i = 1$ . However, if additionally interstitials are present locally, the sum  $\sum_{i=1}^q c_i$  will be higher than 1 and therefore the local density will be higher than  $N^{(i)}$ .

### 2.4.2. Defect processing

An important feature of the atomistic simulation presented in this chapter is the treatment of defects. Collisional displacement of atoms causes series of rearrangements in

originally rigid lattice of KMC simulation (for possible processes see Fig. 2.16). Two types of defects are simulated:

- (i) Every relocated atom (the transferred energy should be higher than the relocation threshold energy [62]) creates a **vacancy**. The atom closest to the position of the displacement is removed from the regular lattice space.
- (ii) Slow-downed projectile with the energy lower than cut-off energy [62] becomes an **interstitial** and is included into the sub-lattice space.

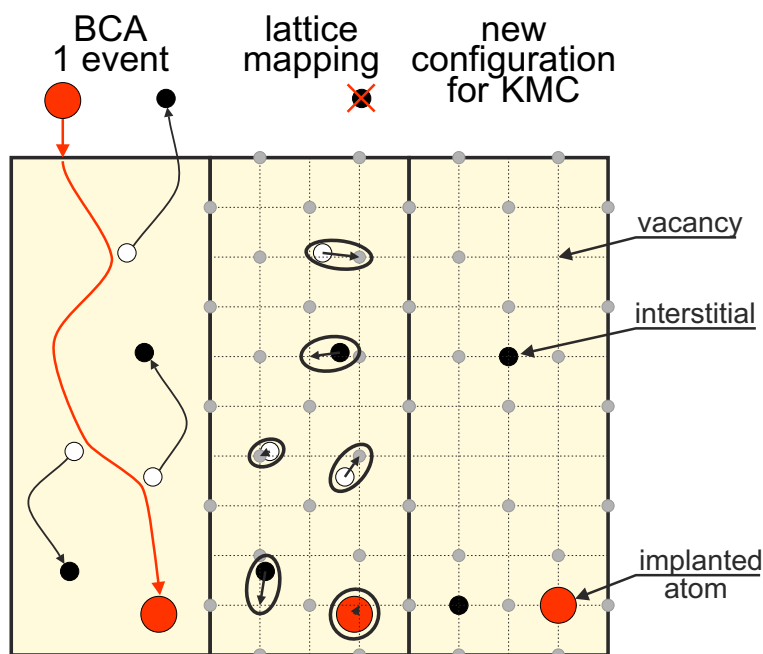


Figure 2.16.: Schematic diagram describing the mapping from continuous defect distribution created in BCA simulation stage onto discrete lattice space used in KMC simulation stage.

The defect creation after one collision event of BCA algorithm and then mapping on discrete lattice space of KMC simulation is schematically presented in Fig. 2.16. It shows the functionality of algorithm divided into three stages:

- (i) Due to the collision cascade made by a single event of the BCA algorithm the positions of defects like vacancies and interstitials are given in the continuous coordinates.
- (ii) During the collision cascade, the nearest regular lattice sites to the positions of the vacancies and the nearest sub lattice sites to the positions of interstitials are localized, respectively<sup>13</sup>.
- (iii) The vacancies are created by removal of atom from the regular lattice sites and the interstitials are created by inclusion of atoms into the sub lattice sites, respectively.

<sup>13</sup>sc lattice is made out of two overlapping fcc lattices. Therefore it is convenient to distinguished between regular and sub-lattice positions of fcc (sc lattice positions are marked in Fig. 2.16 by crossing points of dashed lines)

### 2.4.3. Recombination

Defects, created by ballistic displacement can recombine during or straight after the collision cascade. The different approaches to study the recombination mechanisms have been introduced in the literature before. There are BCA based methods to study implantation processes and point defect creation in Si using modified MARLOWE model incorporated with transient enhanced diffusion of defects [108,109]. Moreover, MD simulations provide very precise information about such parameters like recombination radius, local configuration or temperature influence [110]. In nuclear research, neutron irradiation continuum models provide rate theory simulations to follow ballistic and chemical processes in nuclear reactors. Defect recombination is an important process, which conserves the mass balance in the system [111,112].

In fcc lattice representation, every interstitial atom located in the sub lattice space is surrounded by 6 NN atoms from the regular lattice space. If any of NN regular lattice sites is empty (i.e. filled by a vacancy), the annihilation process is performed (interstitial will recombine immediately with vacancy depending on the maximal recombination radius  $r_{thr}^{max}$ <sup>14</sup>. The recombination radius can vary and the correct values of this parameter are not easy to define. However, the usual distances are in the range between  $0.22a_{lat}$  and  $0.85a_{lat}$  [108], where  $a_{lat}$  is a lattice parameter. Moreover, the recombination radius it is very often temperature dependent especially for very low temperatures [113].

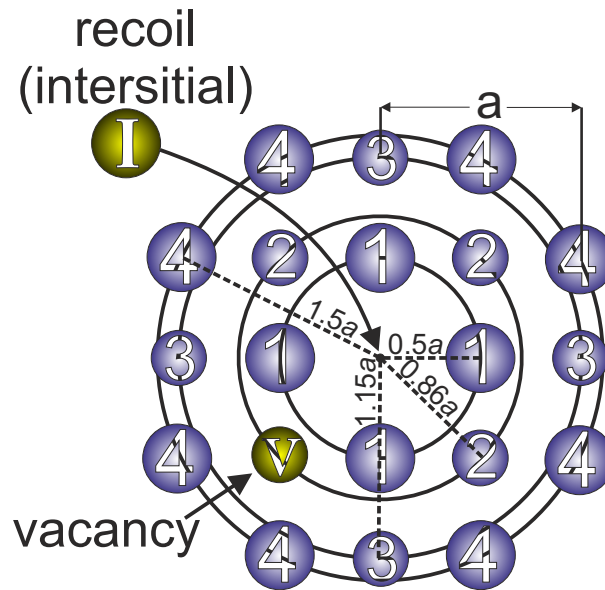


Figure 2.17.: Schematic of a recombination procedure. It searches for an empty lattice position (vacancy  $V$ ) with respect to the interstitial ( $I$ ) position of an atom. The recombination radius is a parameter described by NN distance between  $V$  and  $I$  (for fcc the radius corresponds to 1st NN=  $0.5a_{lat}$ , 2nd NN=  $0.88a_{lat}$ , 3rd NN=  $1.15a_{lat}$ , 4th NN=  $1.5a_{lat}$ , etc...).

The simulation framework considers generation of FPs by BCA stage and their annihilation in KMC stage. The defect recombination during the collision cascade is not allowed. Even if the vacancy appears straight next to the interstitial it will wait until the end of the collision cascade to be annihilated in the KMC stage. Every randomly selected

<sup>14</sup>In the simplest case only NN atoms are qualified for recombination, however in reality the recombination radius may be higher, therefore an extended annihilation procedure has been introduced in Sec. 2.17

interstitial recombines immediately as long as it finds the vacancy within the maximal recombination radius. The decision procedure for recombination considers several rules schematically shown in Fig. 2.17:

- (i) During the KMC stage, one randomly chosen interstitial ( $I$ ) atom, examine its neighborhood for an existence of vacancies ( $V$ ).
- (ii) Maximal recombination radius ( $r_{thr}^{max}$ ) is a free, constant parameter of the simulation that provides the information about the maximal range, with the possibility for annihilation:  $r_{thr}^1 = 0.5a_{lat}$  - 1st NN distance,  $r_{thr}^2 = 0.88a_{lat}$  - 2nd NN distance, etc.
- (iii) For each NN distance  $r_{thr}^i$ , the  $i$  lists of positions with the same radius are created. Starting from the 1st NN distance ( $i=1$ ), the position within the list are sampled randomly and examined for the occurrence of  $V$ . This procedure is repeated for each list  $i$  starting from  $i=1$ , as long as the radius  $r_{thr}^i \leq r_{thr}^{max}$ .
- (iv) If the vacancy appears, the recombination  $I \leftrightarrow V$  is performed.

If there is no possibility to recombine, interstitials performs a ‘random walk’ as a free lattice gas. In a present code, there is no real mechanism of interstitial kinetics included. That means, clustering or creation of dislocation loops in the sub-lattice is not present. Nevertheless, there exist KMC models, which can deal with this problem [114, 115].

Possible kinetic reactions of defects, derived from the assumptions described in Sec. 2.4, can be formulated mathematically:

1. **Clustering.** Vacancies are the only type of defects capable to create clusters (voids). Creation of voids is possible due to the bulk kinetics realized by reduction of free energy of the system by interface energy minimization. Free energy is reduced by clustering of vacancies, which decreases the total number of free interatomic bonds. Interstitials, due to the very complicated nature are treated as free particles without a direct influence on the free energy.

$V^n + V^m \Rightarrow V^{n+m}$	Voids collapse (general rule)
$V + V \Rightarrow V^2$	$V$ clustering (results: di-vacancy)
$I^n \Rightarrow nI$	No interactions between $I$
$I^2 \Rightarrow I + I$	Release of $I$

2. **Point defect recombination.** The most typical process of recombination is a FPs annihilation. In case of existence of a bigger vacancy cluster, the recombination results only in the size reduction of the cluster.

$I + V^n \Rightarrow V^{n-1}$	Reduced cluster size (general rule)
$I + V \Rightarrow 0$	$I/V$ annihilation
$V + I^n \Rightarrow (n - 1)I$	No interactions between $I$

3. **Surface recombination.** Each type of defects can approach the surface region due to the diffusion mechanism. It induces the surface modification that changes the local height  $h$ , and the surface curvature, increasing or decreasing the height depending on the type of the defect, respectively.

$V + h \Rightarrow h - 1$	local height $h$ decreased by 1 ( $V$ )
$I + h \Rightarrow h + 1$	$h$ increased by 1 ( $I$ )

## 2.4.4. Data flow

The Fig. 2.18 presents a flow diagram of the simulation sequence. The simulation starts

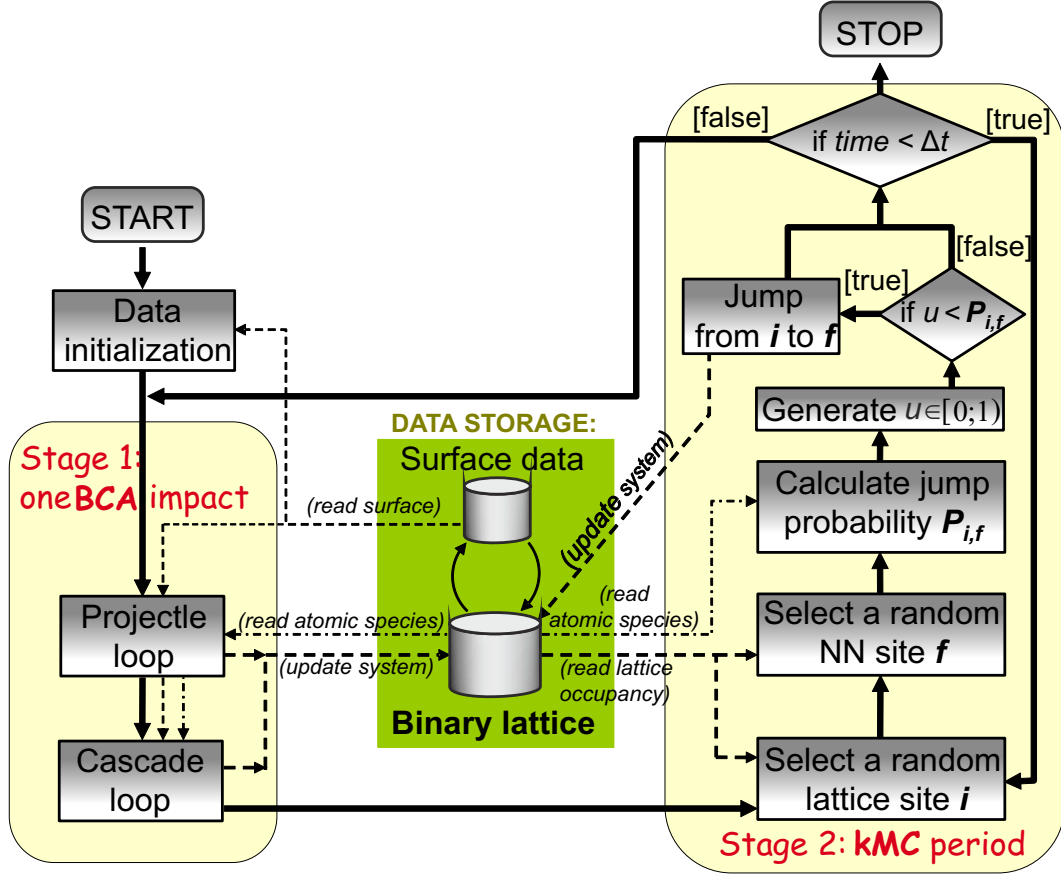


Figure 2.18.: Schematic flow diagram of simulation sequence divided by two stages. The  $time$  variable denotes a current state of Monte-Carlo period and  $\Delta t$  is the total number of MCs performed per ion impact, multiplied by irradiated area  $L^2$ . Stage 1 represents ballistic displacement of ion and recoils; stage 2 performs defect relaxation kinetics during  $\Delta t$  relaxation time. Dashed arrows denote the references to the global memory calls.

with a data initialization, where all input parameters are imported and the information about the surface configuration is extracted from the binary state of the system, for the first time. Afterwards a single BCA impact is executed in the 1st stage. Ion and recoil displacement loops are handled separately. Therefore, cascade damage made by recoils may be neglected during the impact, for instance to study the mechanisms caused by ions only (e.g. defect creation, ion implantation, backspattering). Each collision is followed by the update of binary lattice data. Depending on the type of ballistic process, the binary lattice system is updated with a vacancy, if an atomic displacement occurred or with an interstitial, if the atom is slowed-down, respectively.

In the 2nd stage, defect relaxation is treated. At first, random lattice site  $i$  and NN site  $j$  is selected. Second, jump probability between chosen sites  $P_{i,j}$  is calculated (see Eq. (2.54)). The information about the lattice occupancy and the atomic species has to be imported from the data storage. Next random number  $r$  has to be generated to decide whether jump is succeeded or not. The success will follow updating of the binary lattice by moving the atom from the location  $i$  to  $j$ .

To specify the length of KMC period, the new parameter  $\Delta t$  has been defined. It is correlated to the experimental flux and diffusion coefficient used during the simulation, and is independent on system size. The  $\Delta t$  determines a number of MCs per incidence ion multiplied by  $L^2$ . Such relation keeps the flux and the diffusivity constant, whereas system size and fluence may alter. More detailed physical description of the terms like flux and time in the simulation and its relation to the experimental measured parameters was provided in Sec. 2.3.2. Straight after the KMC period, the BCA collision sequence starts again closing the loop. The total number of generated ions is defined via input parameters providing the condition for terminating the simulation.

### 2.4.5. Demonstration of the simulation procedure

Presentation of the model has been shown in Fig. 2.19 and it follows the data flow arrangement from Sec. 2.4.4. In a given example the system size  $2^5 \times 2^5 \times 2^5$ , partially filled with Si atoms and bombarded with a single  $\text{Ar}^+$  ion at 600 eV ion energy. Simulation can be divided into 2 stages.

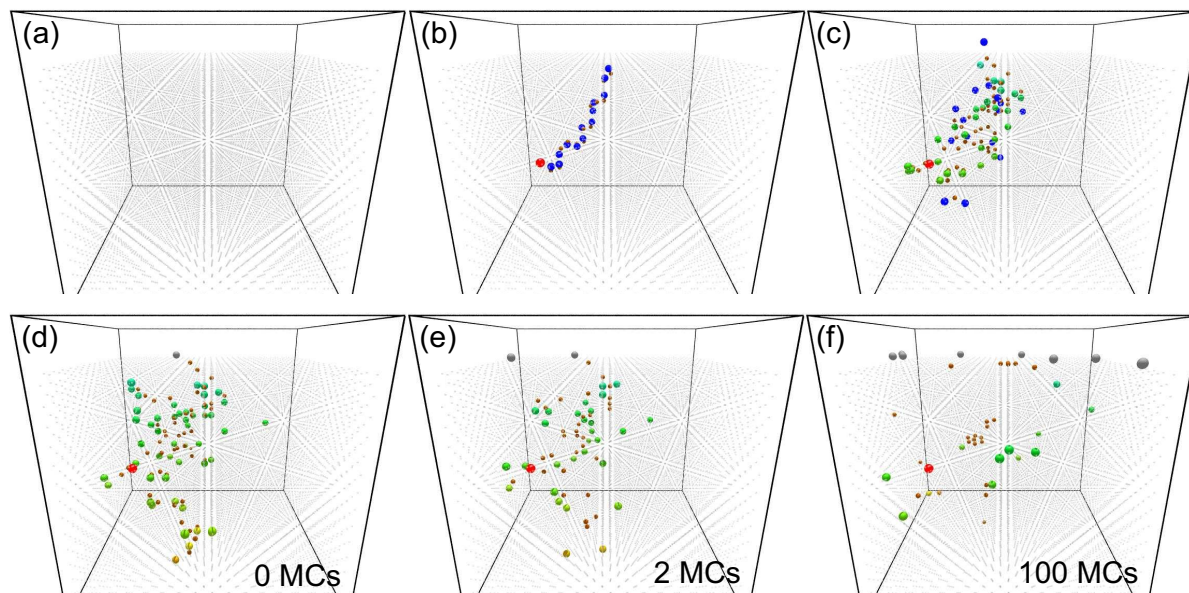


Figure 2.19.: Demonstration of simulation stages (600 eV  $\text{Ar}^+$  impact into Si (100) fcc lattice, simulation cell size is  $2^5 \times 2^5 \times 2^5$ ): (a) initial system configuration, BCA stage starts (b) ion trajectory and collision partners (recoils), (c) ballistic recoil displacement, (d) initial configuration for KMC stage - defect relaxation, (e) relaxation by mainly I-V recombination (f) asymptotic state of the system. Color interpretation: red -  $\text{Ar}^+$  ion, blue - energetic recoils, brown - vacancies, green - bulk interstitials, grey - Si lattice atoms, dark grey - ad-atoms.

Stage 1 - BCA:

- Ballistic ion displacement.  $\text{Ar}^+$  ion transfers its kinetic energy to the Si target atoms and creates energetic recoils. Atoms relocated from their original lattice positions create empty lattice sites - vacancies (Fig. 2.19b).
- Ballistic recoil displacement. Energetic recoils continue the collision cascade until the energy is low enough to stop. The final position of all recoils is mapped on the sub-lattice system, which defines positions of interstitial atoms (in Fig. 2.19c

stopping of recoils is presented, additionally removal of a surface atom can be observed).

Stage 2 - KMC:

- Annihilation. Vacancies and interstitials recombine rapidly within the first steps of the KMC stage (1-2 MCs, Fig. 2.19d,e)
- Thermally activated migration of atoms and defects. Two types of migration mechanisms: for atoms and vacancies the jump probability is depending the interatomic potential and the jump frequency is proportional to the migration energy barrier  $E_m$  (see Eq. (2.54)), whereas interstitials migrate freely in the sub-lattice with the constant migration energy barrier  $E_m$ ;

The final state of the system (see Fig. 2.19e) release ad-atoms created by interstitial migration to the surface. Moreover, energetic configuration favors the creation of small vacancy clusters in the bulk and on the surface. The total number of defects in the final state is strongly reduced.

The simulation architecture proposed in Sec. 2.4, which is applied to simulate IBS provides many advantages over the classical simulations like MD, but it has also some disadvantages. The most important benefit comes from the system size restrictions in MD. The binary representation of atoms used in KMC reduces the amount random access memory necessary to store a simulation cell. It also enables usage of very fast binary operations to describe the system kinetics [2,94]. Using the binary architecture the system sizes up to few  $\mu m$  can be simulated. The second benefit comes from the limitation of the simulation time in MD. All BCA based models are extremely fast and the most ‘expensive’ stage of the algorithm is the KMC period. The lattice discretization decrease the simulation time significantly however, it may reduce accuracy of the simulation, which is the major disadvantage. The error evoked from the lattice approximation in KMC model can be reduced for instance by using better interatomic potentials for energies in Cellular Automata. One possible approach will be described in Sec. 4.1. One minor disadvantage comes from the limitations of BCA based models breaking-down at the low energies. The theoretical limits of BCA have been defined in Sec. 2.2.3. Additionally, the KMC model requires properly assigned migration energy, which defines the duration of MCs (see Sec. 2.3.2). In reality the migration energy is not the constant value and depends on the local configuration of atoms, impurity concentration, temperature, etc. Therefore, the migration energy for KMC is usually chosen empirically based on experimental results.

### 2.4.6. CPU times

CPU times of the simulation presented in this work vary depending on the system size, applied fluence, flux and the number of defects created by a collision cascade. Also the type of simulation matters so that the calculation of the crater formation (Sec. 3.2) or the defect evolution (Sec. 3.1) is much less computationally demanding than the simulation of ripple evolution (Sec. 3.3) or the interface mixing (Chap. 4).

For instance the typical calculation of the crater formation averaged out of 50000 ion impacts at the system size<sup>15</sup>  $2^7 \times 2^7 \times 2^7$  lattice units, and  $j_{norm} = 2^{-17}$  (i.e. 2 MCs relaxation time) on AMD Opteron<sup>TM</sup>2.6 GHz processor (HZDR cluster *Hydra*) takes

<sup>15</sup>For the simulation cell size  $s_x \times s_y \times s_z$  the surface size is  $s_y \times s_z$ .



about 14 hours. On the other hand the full TRIDER simulation of  $10^8$  ion impacts with 500 eV energy at  $\theta = 0^\circ$  that corresponds to the ion fluence of  $10^{18} \text{ cm}^{-2}$  (i.e. system size is  $2^7 \times 2^9 \times 2^9$ ) with the flux of  $j_{norm} = 2^{-17}$  takes about 11 days. A typical calculation of interface mixing provided in Chap. 4 for the system size of  $2^8 \times 2^6 \times 2^6$ , the relaxation time of 200 MCs and  $10^6$  ion impacts takes about 15 days. The KMC stage is generally significantly longer than the BCA stage mainly because the collision cascade occurs only locally, whereas the thermally activated kinetics is considered for every atom in the system. Additionally the simulations of two-component materials are much more time consuming than of single-component materials due to more complicated calculation of jump probability during the KMC stage (see Sec. 2.3.4).

*Science can purify religion  
from error and superstition.  
Religion can purify science  
from idolatry and false absolutes.*

Pope John Paul II (1920 - 2005)

# 3

## Ion-induced surface processes

Ion beam modification of surface morphologies proved to be a promising technique to fabricate various topographies by using for instance ion beam sputtering (IBS). The major advantage of IBS are capability to obtain very regular, self-organizing surface patterns of a few nm wavelength with the possibility to predict the wavelength depending on the irradiation parameters.

Different periodic dots and ripple patterns on various types of substrates have been observed in IBS experiments. The formation of well ordered dot patterns was reported on GaSb [116], InSb [117] and on Si [118]. Also randomly ordered dots have been observed on Ge [119] at normal ion incidence angle. A strong variety of ripple patterns were observed on Si [14, 120–122], SiO<sub>2</sub> [123, 124], Ge [119], C [125, 126] or GaAs [127]. Metallic substrates are responsive on patterning as well, e.g.: Pt [128], Cu [129], Au [130] or Ag [131]. Many different parameters can be varied to reveal their influence on the pattern formation. To the most important system parameters are:

- Ion mass and species - mainly noble gases, self-bombardment, O<sub>2</sub><sup>+</sup>, Cs<sup>+</sup>
- Ion energy - from few hundreds eV [122] to few dozen keV [126]
- Incidence angle - dots are mainly expected at normal ion incidence angle and ripples at oblique incidence angle (relating on the value of the angle, ripples can be oriented parallel or perpendicular to the ion beam)
- Fluence (time factor describing the number of ions per unit area) - patterns may change their properties like wavelength, amplitude, regularity, orientation with irradiation time
- Temperature - surface morphology vary strongly for different irradiation temperatures [132, 133]
- Flux - is the number of ions per unit area and time and describes the time between two independent ion impacts. Usually the significant influence of a very high flux is visible for focus ion beam experiments [134]. In case of the simulation, the flux is related strongly with  $\Delta t$  parameter, which describes the period of time, expressed in MCs units, between two independent collision cascades.

The first extensive experiment, where periodic pattern formation has been observed, is dated at the beginning of 60s by Naves *et al.* [3]. Ripples have been observed on glass with wavelengths less than 100 nm oriented either parallel or perpendicular to the ion beam. Ripples orientation has been determined ion beam direction. Parallel orientation

was expected at grazing incidence [128], whereas at close to normal ion incidence angle ripples were rotated by  $90^\circ$  [14, 135].

Physical processes present during ion bombardment are schematically presented in Fig. 3.1. Nowadays it is still difficult to identify the dominant mechanisms to the specified system using only experimental techniques. The general tendency was to claim that **surface erosion** was the primary reason for the patterning or at least the reason for the roughening [4, 7]. The **surface diffusion** is mainly responsible for the surface smoothing [4, 136]. For metal surfaces however, additional effects contribute to the surface diffusion, e.g. **Ehrlich-Schwoebel barriers** [137, 138] or **Villain instability** [139] that can even act as a temperature dependent driving force for patterning [131]. **Ion-induced diffusion** is usually responsible for the mixing mechanism in the bulk during bombardment [53, 54]. Considering the rough surfaces, ballistic diffusion tends to provide an additional smoothing force, which is curvature dependent [13, 14]. The displacement of the atoms by the ion beam introduces enough energy to relocate the surface atoms but not enough to sputter them away. However, even if they are sputtered, reattachment is still possible under certain conditions of projectile orientation and energy. This process is explained as **redeposition** and can be prominent at grazing incidences [140] or for high surface amplitude/periodicity ratios. For instance, importance of redeposition has been confirmed by one-dimensional SOS modeling [141]. Finally, **viscous flow** is an additional smoothing mechanism that leads to relaxation of surface corrugations with the rate proportional to the viscosity and the wave vector [142]. In the presence of ion beam this effect is called **radiation-induced viscous flow** and is caused by the bulk damage mainly at the medium ion energies (keV to MeV range) [124, 136, 143].

There are several good quality reviews in the literature that present very broad sight on IBS topic and for the interested reader it is suggested to follow the references [131, 143–145].

Theoretical understanding of ion-induced ripple formation process is still missing in many cases [16, 146, 147]. Sigmund theory of sputtering [9] became an origin to create several models for investigation of IBS. The most spread is the continuum equation, where surface patterns have been successfully described by the competition between roughening processes of the ion sputtering and smoothing processes of the surface diffusion by Bradley and Harper (BH) [4]. However, instability of ripple amplitude in long time sputtering requires a non-linear extension in BH equation [5, 6] and furthermore its generalization to Kuramoto-Sivashinsky (KS) equation in anisotropic systems [6, 7]. Similar behavior of amplitude saturation has been observed in non-linear regime [148].

In addition, ripple coarsening is present in many experiments [99, 128, 129, 148]. In case of ripples oriented parallel to the ion beam the wavelength increase process can be explained through annihilation reaction of the mobile defects on the surface [128, 129]. Additionally coarsening of hillocks formation during ion bombardment, can be reproduced by Ostwald ripening mechanism [129]. Coarsening of ripples oriented perpendicular to the beam direction can be described by the newly proposed “coupled two-field equation”, which has been derived in analogy with the kinetics of aeolian sand dunes [8].

Another approach incorporates scaling concepts of non-equilibrium statistical physics [150–152] to study the surface evolution of finite systems. If the nonlinear equations used in the continuum model cannot be solved analytically, the asymptotic behavior of the numerical solution of the equation [153–155] can be used or even the equivalent kinetic model [156, 157] can be applied that follows the same power law scaling tendency using the same scaling exponents. In addition such parameters like interface width, wavelength

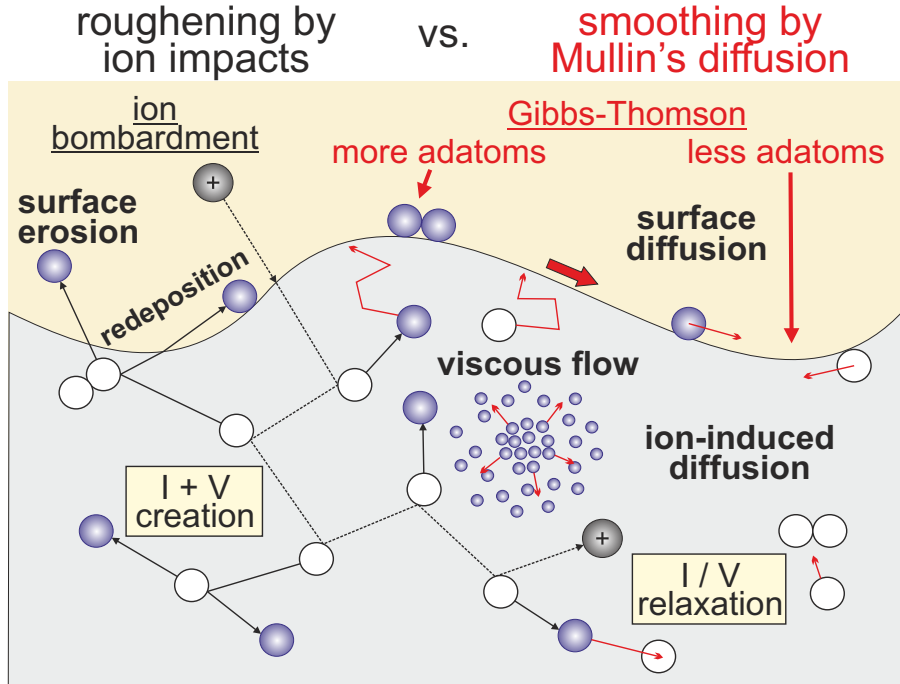


Figure 3.1.: Variety of processes present during ion irradiation and their influence on the surface morphology. Black arrows describe ion-induced mechanisms, red arrows - kinetic mechanisms. The diagram shows the competition between ballistic (defect and sputtering induced surface roughening) and thermally activated (Mullins-Herring surface diffusion [142, 149]) processes. The thick, red arrow denotes the surface mass current vector oriented into the valley due to the difference in the local ad-atom number between the hill and the vale.

or correlation length are easily calculated out of experimental surfaces, providing an opportunity of a quantitative comparison with the theory [99, 126, 143].

An alternative group of models, couple energy deposition profile from Sigmund's approximation, for simulating surface erosion, with KMC simulations of solid-on-solid (SOS) model [151], responsible for the surface diffusion [10–12, 121, 158]. This type of coupling technique boils down to nothing else than the type of mapping of the continuum equation of BH on numerical kinetic model. It has been shown by Chason *et al.* [11] that simulation of ripple formation at the early-stage instability regime gives very good agreement to linear continuum theory. KMC approach has been very successful to reproduce surface topographies of experiments at low fluences and for ripples oriented perpendicular to the ion beam direction [121]. Moreover, normal and grazing incidences have been quantitatively investigated [129].

Well known inaccuracy concerning Sigmund theory-based models is a restriction to the erosion processes only, without concerning defect kinetics<sup>1</sup>. Different profiles of the deposited energy have been proposed based on BCA simulations [159]. Nevertheless, MD simulations show clearly that ion bombardment modifies the surface preferentially more by rearrangement of atoms than due to the sputtering [16], especially for low ion energies. This inspired recent studies on combining single ion impacts with continuum equations through the crater function by Norris *et al.* [17]. It leads to a better understanding of additional smoothing mechanism, like an effective mass 'downhill' current induced

<sup>1</sup>Distribution of the energy deposited on the surface is approximated by Gaussian ellipsoid-shaped profile without considering surface defects like ad-atoms or surface vacancies created by the collision cascade [9]

by a ballistic atomic drift [13, 14]. Absence of ripple patterns for low incidence angles has been partially explained using multiscale modeling of MD combined with continuum rate equation approach [160]. However, recent study on ion bombardment of Si brings into consideration novel effects of inducing formation of ripples with at low ion incidence angles ( $10^\circ$ - $20^\circ$ ), which at present cannot be reproduced by any modeling technique [147].

Finally, atomistic models that include more than the surface erosion to simulate ion irradiation are least developed within the last years. Ballistic interactions are usually simplified by a random removal of atoms from the surface [161] or by surface defect creation around the ion incidence [81]. Moreover, BCA simulations have been exploited to extract positions of sputtered atoms and handle redeposition [162], as well as bulk defects, created during the collision cascade [106]. All these simulations use KMC treatment of diffusion either restricted to SOS model [161, 162] or three-dimensional lattice KMC [81, 106]. However, Kellerman *et al.* simplified it neglecting NN interactions.

In this work, a new atomistic approach called TRIDER combining collision cascade simulations of BCA, with KMC method of thermally activated defect movement is investigated. Ballistic displacement of atoms due to the ion bombardment is handled by modified dynamical TRIM model, where one-dimensional evolution of bulk concentration profiles, is replaced by on-lattice three-dimensional KMC method of bulk/surface diffusion. This approach is based on the assumption of defect creation in the target during the collision cascade and further thermally activated defect movement period. Briefly it can be described as a cycle consisting of 2 stages:

- (i) BCA of ions and recoils trajectories create vacancies and interstitials. Additionally, the sputtering yield decreases the total number of atoms in the target by removing them from the system. This depends on the local curvature of the surface and on the spatial distribution of the deposited energy of a projectile.
- (ii) The cascade defects created in stage (i) modify the state of the system due to the defect relaxation, which considers kinetic of such defects like: vacancies, interstitials, surface vacancies, ad-atoms, impurities and antisites.

Two types of processes can be distinguished: interstitials diffuse randomly as long as they are in the initially defined range from a vacancy (vapor phase is equivalent to the volume filled with the vacancies), lattice atoms move according to a jump probability, depending on NN atomic configuration [81].

In order to verify correctness of proposed algorithms, several simple theoretical examples concerning surface processes are investigated mainly related with defect analysis and the statistical investigation of a single ion incidence. Following these studies the ripple formation on Si will be presented based on different simulation parameters like energy, incidence angle, fluence and ion flux. Finally, the surface mass current investigation will be proposed in Sec. 3.4. As it is shown in Fig. 3.1, the surface mass current is the curvature dependent force assigned to the surface (marked with the red arrow at the arbitrary position), which is an effect of the varying number of ad-atoms between the hill and the vale.

## 3.1 Defect evolution in Si

It is usually very convenient to simulate first systems, which have been widely studied in the past using much more detailed methods. Low energy self-bombardment of Si has been analyzed with MD simulations by Tarus *et al.* [163] in review of defect creation and evolution in bulk after the collision cascade. Here, the first attempt of modeling using TRIDER simulation was applied. The MD calculation provides the opportunity to investigate a physical conformity of the model and to determine the parameters for future simulations.

### 3.1.1. Simulation parameters

In this work, the simulations were done with 100 eV Si<sup>+</sup> single ion bombardment into (100) Si lattice. The evolution of defect during the collision cascade is analyzed with respect to creation and annihilation processes. Due to simplification and symmetry reasons, only fcc lattices have been used. After every ion impact, a constant relaxation period of 30 MCs is applied, at the constant temperature represented by a dimensionless factor  $\epsilon = \epsilon_{Si}/k_B T = 1.7$ , which was used in jump probability function (2.54) ( $\epsilon_{Si}$  is a NN bond energy of Si atoms). The surface binding energy used in BCA is set to be equal to the atomization energy of Si of 4.7 eV. The initial condition of every ion impact considers a rigid lattice of a flat surface. Data evaluation starts straight after collisional processes and is averaged over 1000 of ion incidences for each run.

### 3.1.2. Results

Fig. 3.2 shows the time evolution of defects created by self-bombardment of Si at 100 eV ion energy. Ballistic part of the simulation does not include time dependence during the collision cascade. Therefore, only the thermally activated part can be analyzed, starting from higher initial number of defects in comparison with MD simulations. There are at average 16.7 vacancies and 23.3 interstitials created initially. This significant difference between the values is related to the low ion incidence energy  $E_0$ . Most of the vacancies are created in the surface layer. Therefore, they cannot be counted as bulk defects and belong rather to the surface. Interstitials in contrary fill the volume between the lattice atoms and may recombine with holes immediately within the first steps of KMC period. Three cases are compared, where a free parameter has been chosen as recombination radius  $r_{thr}^{max}$  that determine the asymptotic behaviors for applied  $r_{thr}^{max} = 1NN, 2NN, 3NN$  (see Sec. 2.4.3), decreasing the saturation time respectively.

MD calculations show the maximum number of defects at around 4. However, one should take into account that in the present model the thermally activated processes start directly after defect generation by the collision cascade, and therefore the number of defects increases rapidly at first. That is unlike to MD, where bulk diffusion is suppressing collisional damage relaxing the defects also within the first 0.2 ps. The comparison of relaxation curves between MD and TRIDER provides Fig. 3.2. Following the number of defects from the maximum number 4 at 0.2 ps to the asymptotic value of 2.3 at 1.5 ps, the best fit indicates the recombination radius  $r_{thr}^{max} = 2NN$ , the closest to MD simulations.

Additional feature of the simulations is a difference between the number of vacancies and interstitials, which is initially positive. However, for  $t > 5$  MCs, this difference is becoming negative unlike for MD, where the average number of vacancies is always

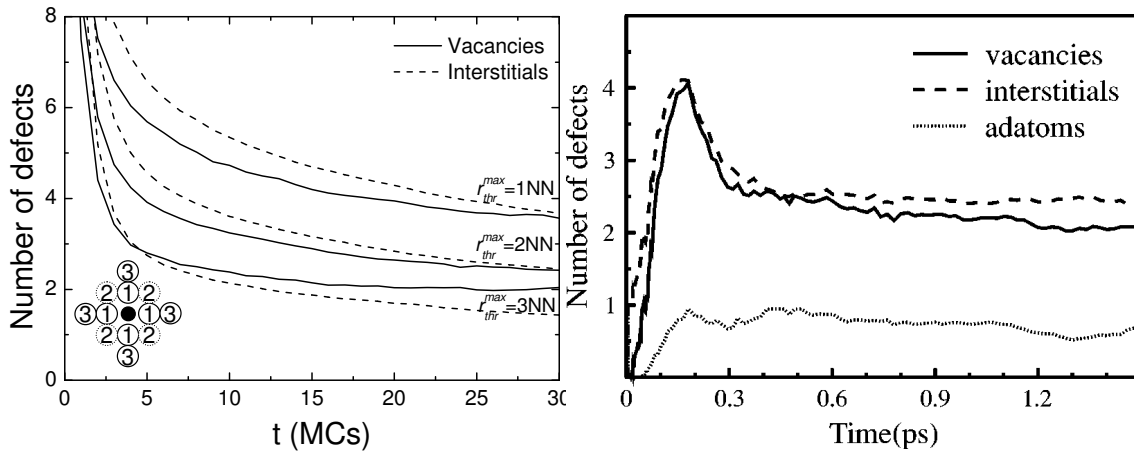


Figure 3.2.: Time evolution of the average number of defects created by single Si ion impacts into Si (100) target calculated with TRIDER method (left) and MD simulation of Tarus *et al.* [163] (right). Solid and dashed lines represent vacancies and interstitials respectively. Three different curves correspond to different annihilation distances,  $r_{thr}^{max}$  of 1NN, 2NN and 3NN (from the top to the bottom) respectively. Inset shows atoms on a (100) plane of fcc lattice included into annihilation procedure. The maximal recombination radius  $r_{thr}^{max}$  is an input parameter, represented by the numbers in circles.

higher. The reason for this is a large mobility of interstitials that is kept constant, whereas vacancy mobility is suppressed due to their tendency of clustering. This behavior reduces the number of interstitials that may diffuse at the surface and create ad-atoms.

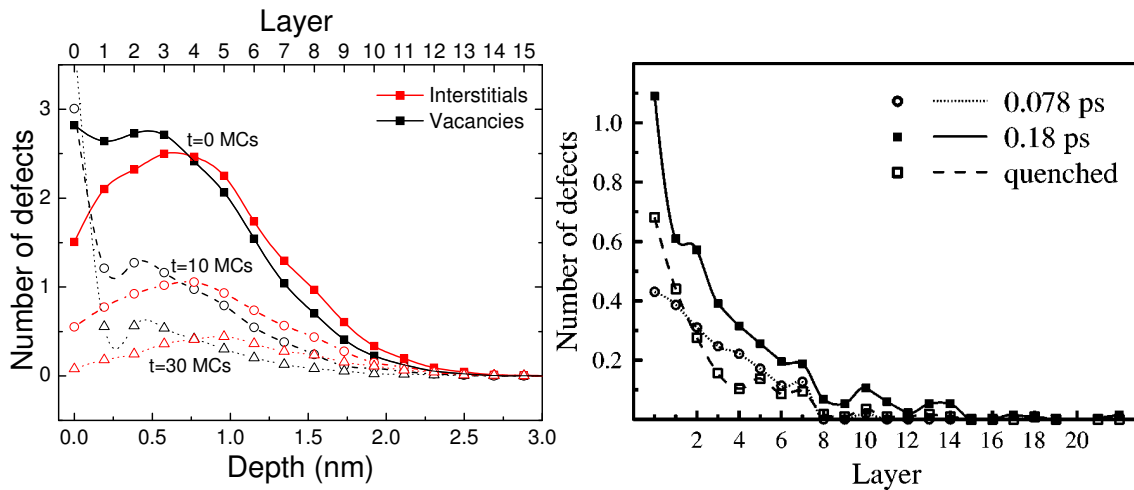


Figure 3.3.: Averaged defect distributions over depth/layers calculated with TRIDER method (left) and MD simulation of Tarus *et al.* [163] (right). Plots present the number of defects at different times ( $t=0, 10, 30$  MCs). Interstitials are always shifted to the right with respect to the vacancy distributions. The lines are guide to the eye.

The average defect distributions as a function of depth are shown in Fig. 3.3. Straight after the collision cascade ( $t = 0$  MCs) the number of defects is much higher than the values predicted by MD. These types of distributions provide a typical result obtained by TRIM simulations. At  $t = 0$  MCs a separation between I and V depth profile creates I/V excess (see Fig. 3.4). The distribution of I/V excess is independent on relaxation time and only the magnitude of the distribution decreases. The maximum of interstitial excess

### 3.2. CRATER FORMATION BY SINGLE ION INCIDENCE

is reached at 1.5 nm depth, which is more than the ion penetration depth ( $R_p = 1.1$  nm). After longer relaxation times ( $t = 10$  MCs and  $t = 30$  MCs) the number of defects is strongly reduced. The vacancies accumulate at the surface, whereas interstitial peak is shifted in the direction of deeper layers (see Fig. 3.3). The calculation of vacancy distribution takes into account all empty lattice positions integrated across the depth. Because of the low penetration depth, the relaxed vacancies create clusters at the surface and overestimate the number of vacancies generated at the surface region.

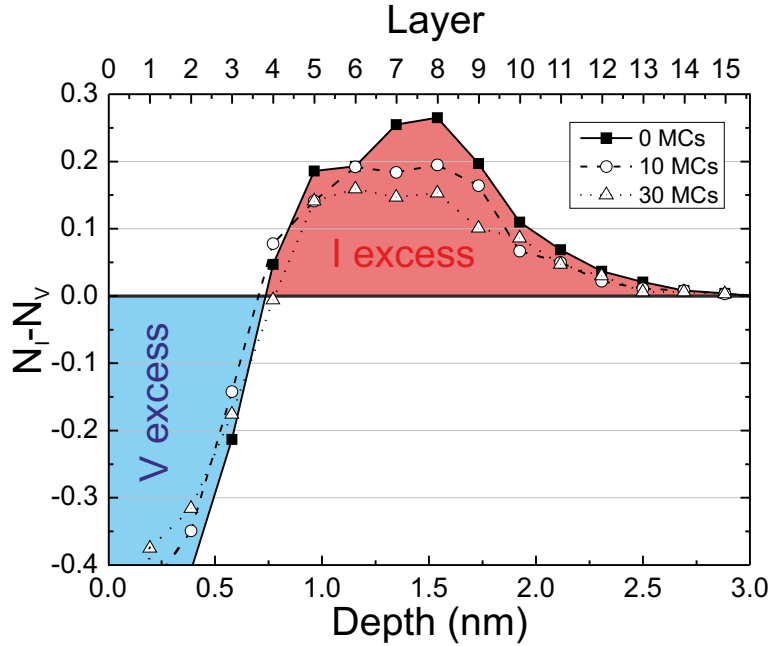


Figure 3.4.: I/V excess calculated for the results shown in Fig. 3.3. The curves show number of defects at different relaxation times ( $t=0, 10, 30$  MCs). With the blue background the vacancy excess is indicated, red background indicates interstitial excess.

Resuming both approaches of defect analysis, it is proven that the new modeling technique can reproduce MD results with a very good correspondence. In case of the evolution of the average defect number, the asymptotic behavior is reproduced especially for longer simulation times. Also widths of defect distributions are consistent with MD calculations, where the tendency of separation between vacancies and interstitials is conserved.

### 3.2 Crater formation by single ion incidence

Local change of the surface topography by a single particle impact is very often an important subject of investigation, especially in terms of cluster bombardment [164] that creates a characteristic crater with rims. Nevertheless, the surface modification can be also present after single-ion sputtering [20]. Depending on the kinetic energy transferred to the target during the impact, the type of a crater can be classified by two categories with a different type of surface morphology. First, at the **high energy density** of a cascade, a *direct* formation of the *crater* made mainly by heavy projectiles impact, is a very interesting process, investigated especially intensively with MD simulations [20, 29, 164]. Kinetic energy transfer made by cluster bombardment is usually large enough to relocate the surface atoms, forming the structure comparable with the crater



formation made by meteorite impact [29]. Also single ion incidence may provide direct craters at the favorable ion parameters, which are: low energy, large mass, oblique incidence [20]. Second, the *indirect crater* is formed, if the cascade has the **low energy density**. A single ion incidence causes only a minor rearrangement of atoms at the impact position followed by creation of ad-atoms up to few nanometers away. However, after averaging out of hundreds of surface topologies created by single ion impact the crater formation with rims may appear. To create the indirect crater, the mass of the ion should be much smaller than the mass of the target atoms and the ion energy should be high enough to displace atoms in the bulk. Moreover, relaxation and kinetics of bulk defects straight after the collision cascade are necessary (see Fig. 3.5).

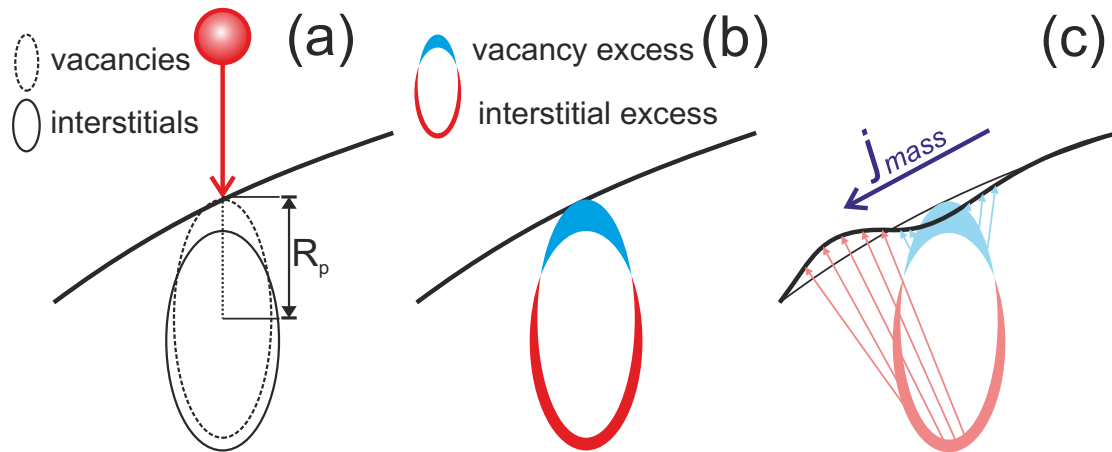


Figure 3.5.: Scheme of surface crater formation by bulk defects relaxation: (a) creation of vacancy and interstitial distributions, (b) recombination of defects, V+I vacancy and interstitial excess remaining, (c) defect migration towards the surface.

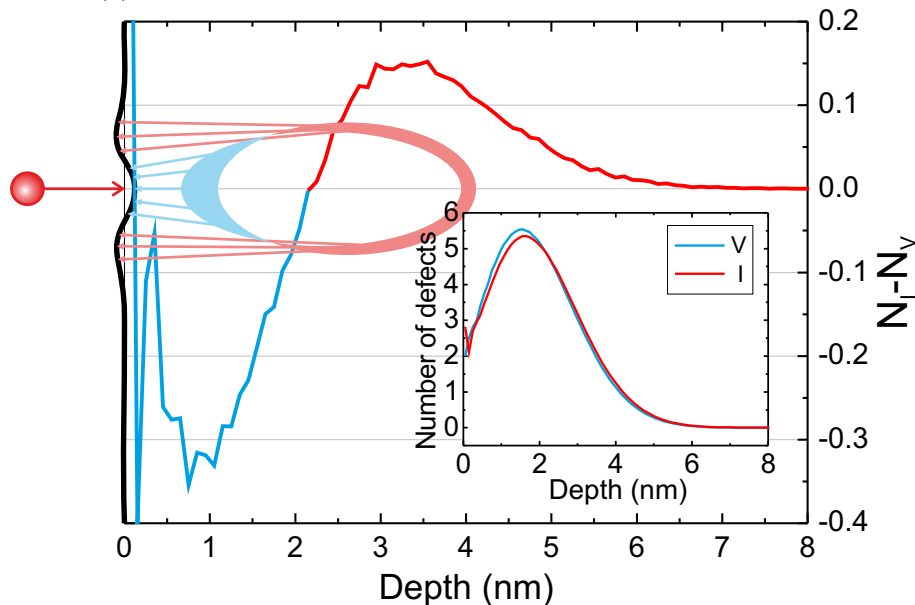


Figure 3.6.: Defect excess by ion irradiation (TRIM simulation) and I/V distributions (inset). Schematically, the surface modification by defect migration after ion impact is marked. Blue and red arrows follow the migration paths of vacancies (V) and interstitials (I) respectively.

Ion impact it is not only responsible for a removal of atoms from the surface, but mainly for the creation of the huge amount of Frenkel pairs (FPs) left in the bulk due

to the atomic displacement. Kinetic movement of FPs recombines most of the defects, nevertheless, in the steady state up to 10% of defects may accumulate in the target [165]. In Fig. 3.5a the most likely positions of defects are selected. Before the steady state however, vacancy (V) and interstitial (I) depth profiles will separate resulting in I/V excesses [166, 167] (Fig. 3.5b). A simplified model can be applied, e.g. to study ion implantation, where the point defects annihilate almost completely in the bulk, leaving only one interstitial atom remaining in the crystal per implanted ion. This so-called ‘+1’ model [168] neglects the recombination between the vacancies and the surface, as well as any thermally activated processes, although it can be a good approximation of defect evolution, if a low radiation damage is expected. The I/V excess has been studied with simulations for impurity gattering in Si by ion implantation and subsequent relaxation of point defects during annealing [169]. It was confirmed using mainly the TRIM simulations, that the impurities are gattered in the vacancy excess at half of the projected range  $R_p/2$ .

Subsequent kinetics of defects relaxes the bulk strains by recombination of I/V excess at the surface (Fig. 3.5c). In the simplest case, with point-defects only, the recombination distance follow the ‘random walk’ diffusion length  $\Delta x$  according the equation

$$\Delta x = \sqrt{2Dt}, \quad (3.1)$$

where  $D$  is the diffusivity and  $t$  is the time. Therefore, based on I/V excess plot (Fig. 3.6), surface modification will be proportional to the number of defects relaxed at the surface: interstitials will evoke local, positive change of the height; vacancies, local and negative, respectively. It has been proven experimentally that bulk defect relaxation enhances defect production rate on the surface by low-energy ion bombardment of Ge(001) even at low temperatures (-100 °C) [170].

In this section the change of topography by single ion irradiation of Si targets is analyzed using different incidence angles and ion energies. The results are the crater functions, which are qualitatively compared with MD data from Ref. [16]. Moreover, analytical fitting function is provided to reproduce simulated crater formation.

### 3.2.1. Simulation of single ion incidence

The simulation parameters used to reconstruct the crater function are the same as for the simulations in Sec. 3.1, however from now on, till the end of this chapter, the recombination radius  $r_{thr}^{max} = 2$  NN. Additionally, the relaxation time of collision cascade is  $\Delta t = 2$  or 30 MCs and the system size  $L = 2^7$  lattice units. It corresponds to a system size of  $245.76 \times 245.76$  Å. The calculation has been performed for different incidence angles of Ar<sup>+</sup> ions on Si target:  $\theta = 0^\circ, 30^\circ, 67^\circ$  and  $85^\circ$  respectively. Three different ion energies have been applied:  $E_0 = 250, 500$  and  $1000$  eV. The ion impact location has the coordinates (x,y)=(0,0) and the height distribution are extracted, averaged over 50000 independent collision cascades.

A significant difference in the shape of the craters was obtained at normal incidence angle (Fig. 3.7). The sizes of the crater rims increase with the energy. In contrary, the deepest crater is obtained at lower ion energies. This effect is related to the smaller penetration depth of ions, defect creation near the surface boundary and possible recombination of vacancies with the surface atoms. It is interesting to observe that the major mass displacement results in the positive variation of height, by the ad-atoms created around the ion impact location. Height reduction occurs only at the impact position and is induced by the sputtering yield and by the surface vacancies. After single ion

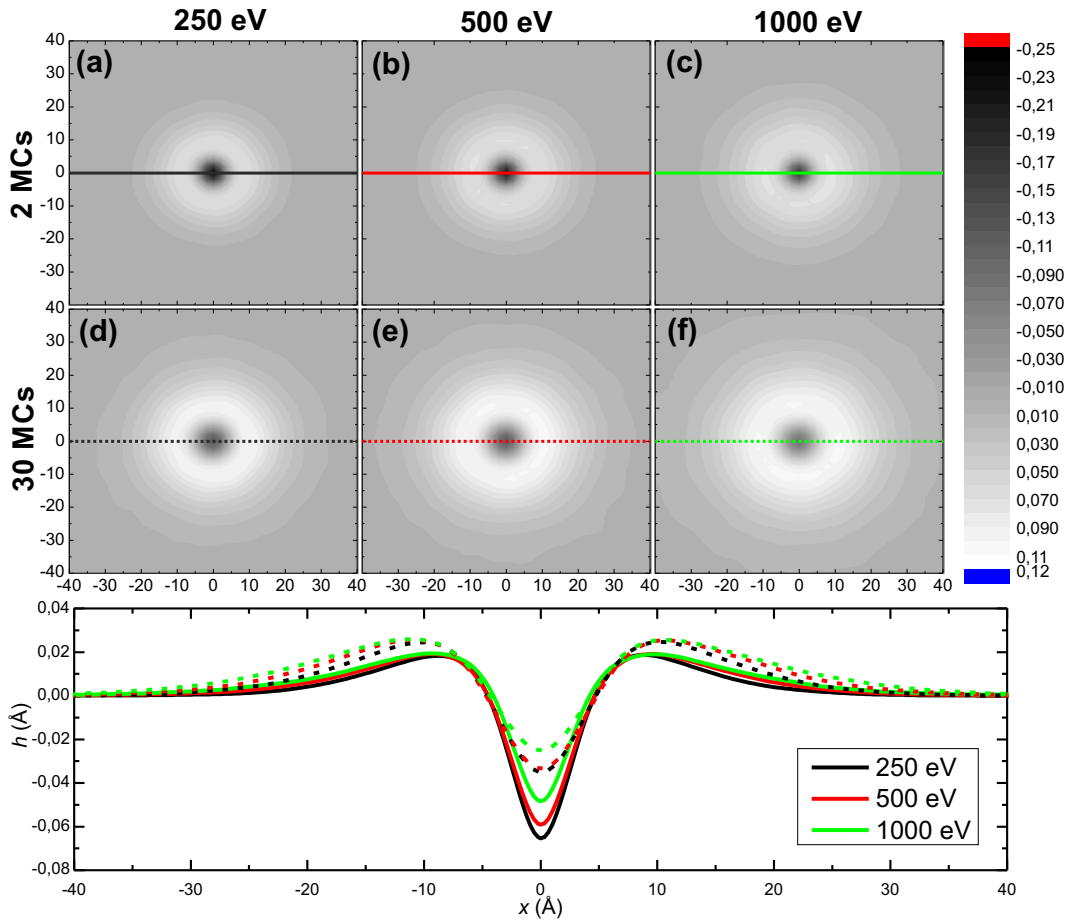


Figure 3.7.: Crater distributions obtained with the simulation, after defect relaxation stage of 2 MCs (upper row) and 30 MCs (lower row), with  $\text{Ar}^+$  ion impact on Si at the incidence angle  $\theta = 0^\circ$  for ion energies: (a),(d)  $E_0 = 250$  eV, (b),(e)  $E_0 = 500$  eV and (c),(f)  $E_0 = 1000$  eV. All dimensions are in angstrom. Curves in the bottom plot show the line profiles along the impact positions. Solid and dashed lines correspond to 2 MCs and 30 MCs relaxation times respectively.

### 3.2. CRATER FORMATION BY SINGLE ION INCIDENCE

impact more ad-atoms than surface vacancies are observed. Higher number of ad-atoms is caused by the higher mobility of bulk interstitials. The interstitials recombine with the surface faster than the vacancies, whereas bulk vacancies can create clusters. The cluster creation slows down recombination of vacancies with the surface. The comparison between 2 and 30 MCs shows that both height and width of the crater rims increase with relaxation time, however the crater depth tends to decrease. This is again the effect of a faster interstitial diffusion.

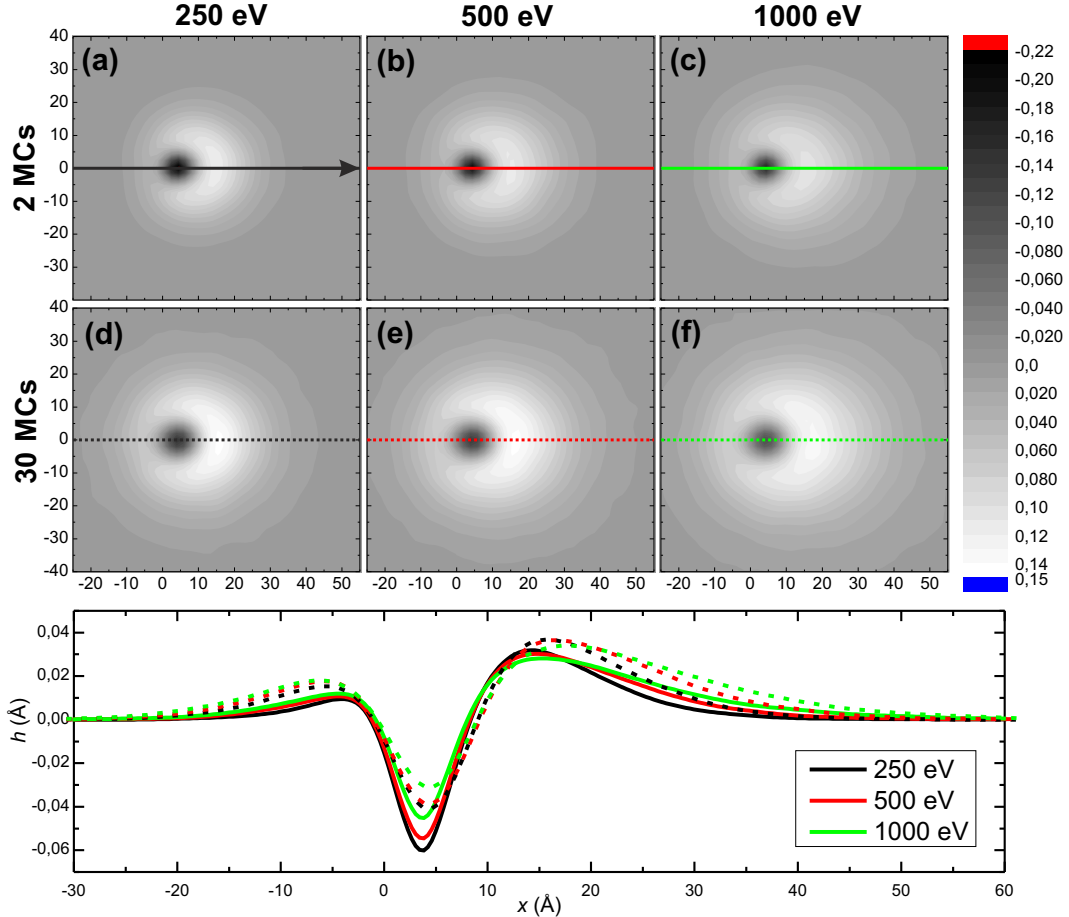


Figure 3.8.: Crater distributions obtained with the simulation, after defect relaxation stage of 2 MCs (upper row) and 30 MCs (lower row), with  $\text{Ar}^+$  ion impact on Si at the incidence angle  $\theta = 30^\circ$  for ion energies: (a),(d)  $E_0 = 250$  eV, (b),(e)  $E_0 = 500$  eV and (c),(f)  $E_0 = 1000$  eV. The trajectory of the  $\text{Ar}^+$  ion before hitting the surface is marked in (a) by the black arrow. Curves in the bottom plot show the line profiles along the ion trajectory. Solid and dashed lines correspond to 2 MCs and 30 MCs relaxation times respectively.

After increasing the incidence angle up to  $30^\circ$  (see Fig. 3.8), an asymmetric distribution of the crater occurs. The asymmetry is related with the mass transport from the region next to the impact position, along the trajectory of  $\text{Ar}^+$  ion. Another reason of the asymmetry is a different concentration of interstitial and vacancies at the different bulk positions. Typically, due to a kinetic displacement of atoms, self-interstitial's distribution is always shifted by several angstroms towards larger depths, with respect to the distribution of the vacancies (see Fig. 3.3). After defect relaxation process I/V distributions separate to I/V excess even up to several tens of nm. This process has been often seen experimentally, especially for doped Si targets [167] and has been confirmed by simulations using BCA-type methods in Ref. [166, 169] and in this work in Fig. 3.4.

There is no significant difference between each crater distribution, expect the influence of the ion energy on the rise of the crater rims magnitude. Moreover, for longer relaxation times (Fig. 3.8 30 MCs) the final crater is much more circular and the total crater width increase significantly. Analogically to the normal incidence, the crater depth decreases.

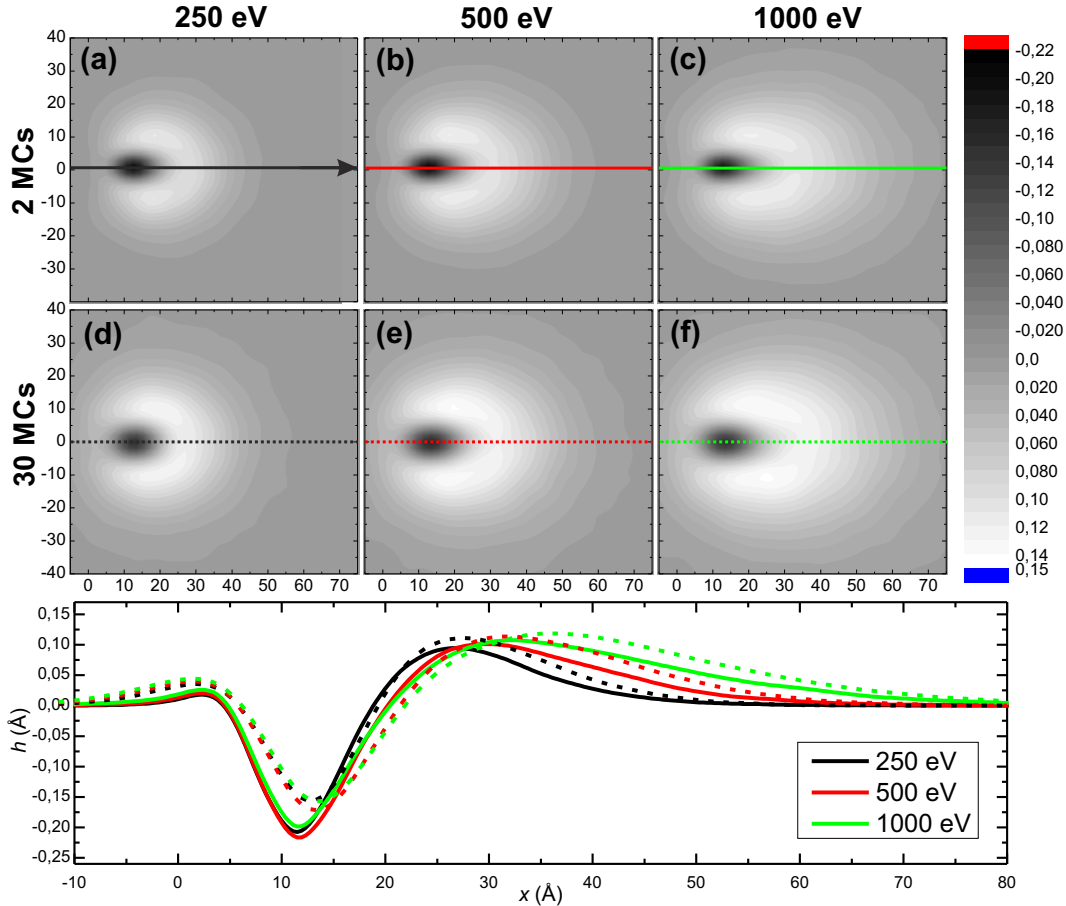


Figure 3.9.: Crater distributions obtained with the simulation, after defect relaxation stage of 2 MCs (upper row) and 30 MCs (lower row), with  $\text{Ar}^+$  ion impact on Si at the incidence angle  $\theta = 67^\circ$  for ion energies: (a),(d)  $E_0 = 250$  eV, (b),(e)  $E_0 = 500$  eV and (c),(f)  $E_0 = 1000$  eV. All dimensions are in angstrom. The trajectory of the  $\text{Ar}^+$  ion before hitting the surface is marked in (a) by the black arrow. Curves in the bottom plot show the line profiles along the ion trajectory. Solid and dashed lines correspond to 2 MCs and 30 MCs relaxation times respectively.

At  $67^\circ$  ion incidence angle (Fig. 3.9), much more spatial anisotropy of the crater shape appears, which increases with the ion energy. The crater rims are shifted and elongated in the longitudinal direction with respect to the ion trajectory. Moreover, two peaks in the height distribution can be distinguished, located at the two sides, next to the eroded area. The crater size is clearly the largest in comparison to the previous simulations ( $\theta = 0^\circ$  and  $\theta = 30^\circ$ ). The volume with negative crater height is the largest at this angle. It is the result of the maximum sputtering yield at  $\theta = 67^\circ$  ion incidence angle (see Fig. 2.6). Again, no significant difference in terms of thermal relaxation of defects after 30 MCs is observed, expect of the crater height increase and the reduction in the shape anisotropies (see Fig. 3.9 30 MCs).

The last example shows  $85^\circ$  ion incidence angle at 3 different energies (see Fig. 3.10). Here, the height scale is almost one order of magnitude lower than in previous cases

### 3.2. CRATER FORMATION BY SINGLE ION INCIDENCE

due to a strong ion reflection, typical for the grazing ion impacts. The sputtering yield for ion incidences close to  $90^\circ$  drops almost to 0. Therefore, the crater depth closes at  $-0.035 \text{ \AA}$ , whereas the height peak rises to the value of  $0.065 \text{ \AA}$ . The asymmetry is much stronger than for  $67^\circ$  impact and obtained distributions have not the shape of the crater with rims. Two peaks in height are located at the sides to the eroded area, while almost no mass relocation occurs in the front. This strong shape anisotropy and the transverse mass transport with respect to the impact position provides a good explanation for the appearance of ripples oriented parallel to the ion beam direction at the grazing ion impacts [128, 147].

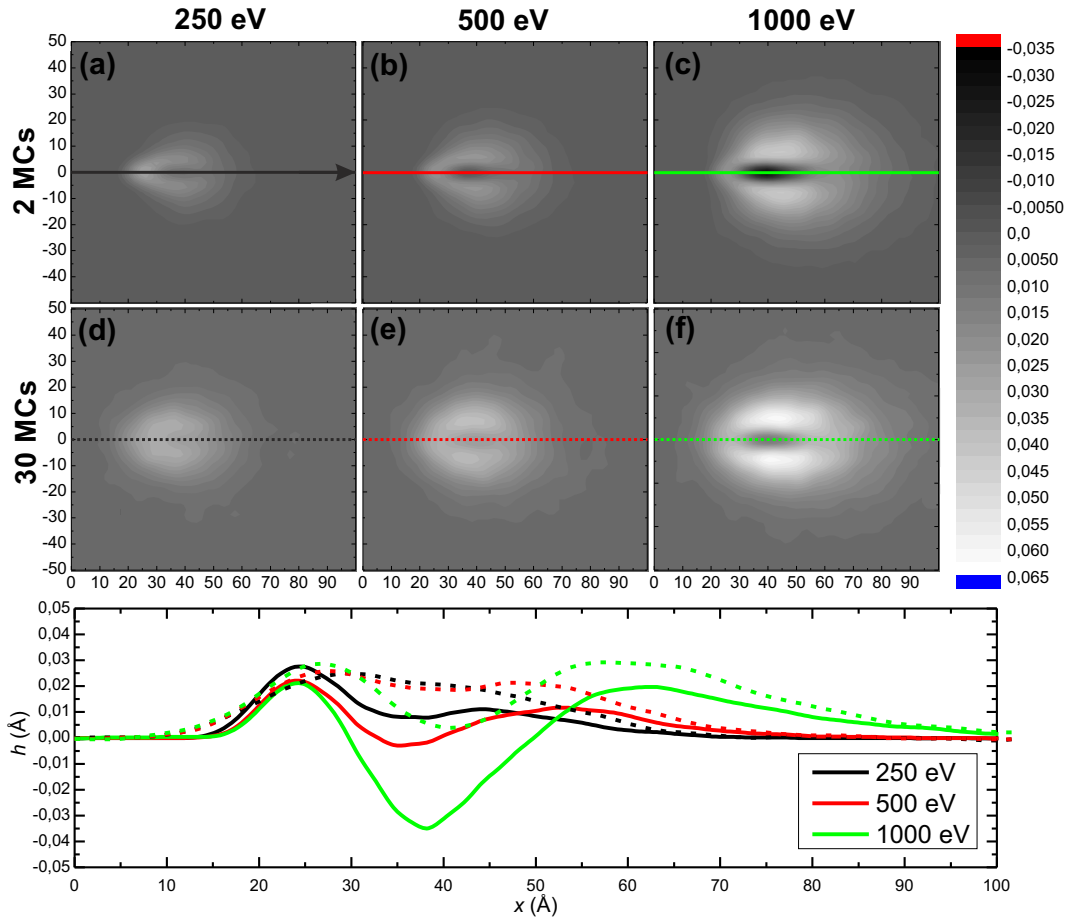


Figure 3.10.: Crater distributions obtained with the simulation, after defect relaxation stage of 2 MCs (upper row) and 30 MCs (lower row), with  $\text{Ar}^+$  ion impact on Si at grazing incidence angle  $\theta = 85^\circ$  for ion energies: (a),(d)  $E_0 = 250 \text{ eV}$ , (b),(e)  $E_0 = 500 \text{ eV}$  and (c),(f)  $E_0 = 1000 \text{ eV}$ . All dimensions are in angstrom. The trajectory of the  $\text{Ar}^+$  ion before hitting the surface is marked in (a) by the black arrow. Curves in the bottom plot show the line profiles along the ion trajectory. Solid and dashed lines correspond to 2 MCs and 30 MCs relaxation times respectively.

#### 3.2.2. Fitting function for crater formation

The shape of the height distribution at non-grazing incidences is a crater like, with pronounce rims. Therefore, the empirical function used to reproduce this structure is

similar to the one reported in Ref. [16]

$$h(\mathbf{x}, \mathbf{y}) = A_1 \exp(-B_1 [D_1 \mathbf{x}^2 + (\mathbf{y} - C_1)^2]) - A_2 \exp(-B_2 [D_2 \mathbf{x}^2 + (\mathbf{y} - C_2)^2]) \quad (3.2)$$

where  $A_1, A_2, B_1, B_2, C_1, C_2, D_1, D_2$  are 8 free parameters fitted for two independent variables  $\mathbf{x}$  and  $\mathbf{y}$ . In case of completely symmetric distributions ( $\theta = 0^\circ$ ), the equation

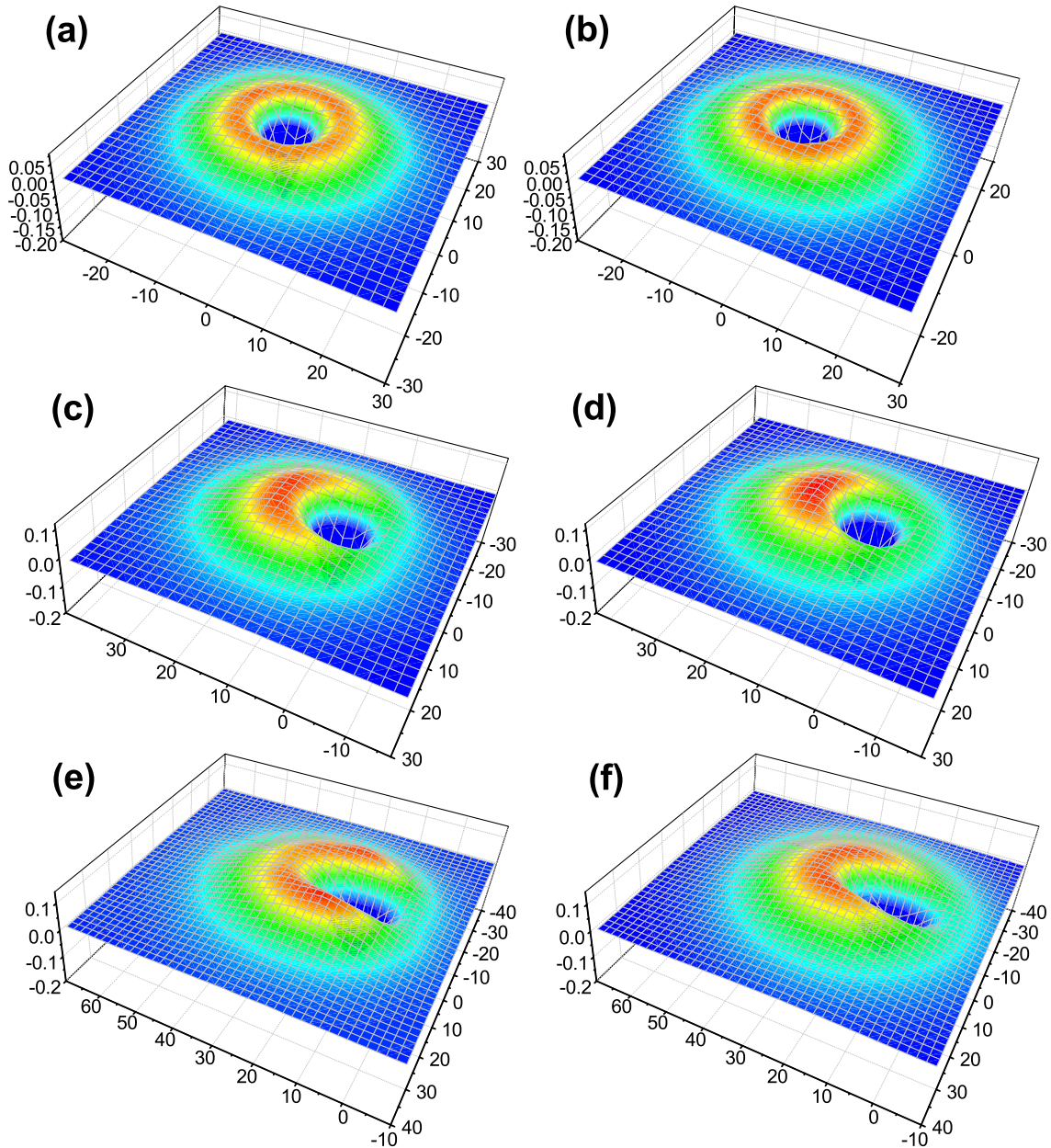


Figure 3.11.: Comparison between the simulated crater distributions (left column) and the fitted crater functions Eq. (3.2) (right column) at  $\theta = 0^\circ$  (a),(b);  $\theta = 30^\circ$  (c),(d);  $\theta = 67^\circ$  (e),(f) ion incidence angle and 500 eV ion energy. The number of free fitting parameters are: (b) 4 -  $A_1, A_2, B_1$  and  $B_2$ , (d) 6 - additionally  $C_1$  and  $C_2$ , (f) 8 - additionally  $D_1$  and  $D_2$ . All dimensions are in angstrom.

is reduced, because  $C_1, C_2$  are equal 0. Also for small incidence angles ( $\theta = 0^\circ..30^\circ$ ), the factors that elongate the crater in the direction along the ion movement ( $D_1$  and  $D_2$ ) are close to 1, otherwise a strong asymmetry can be seen in the shape of the rims,

### 3.2. CRATER FORMATION BY SINGLE ION INCIDENCE

as well as the crater itself (see Figs. 3.9, 3.10 and 3.11). For  $\theta = 67^\circ$  the fitting is still reasonable (Fig. 3.11f), however, due to even stronger asymmetry it cannot be fitted for even larger ion incidence angles close to the grazing impact. The equation itself is obtained from modified two-dimensional Difference of Gaussians (DoG) function, mainly applied in image processing methods.

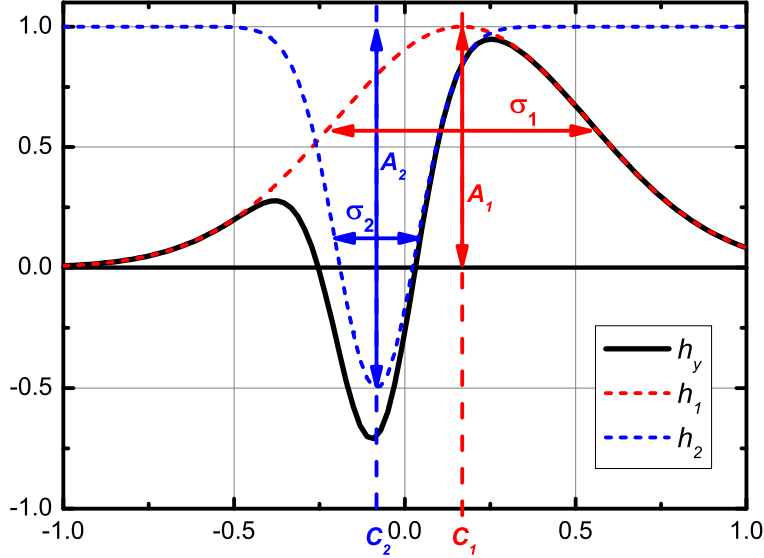


Figure 3.12.: Reconstruction of two-dimensional DoG function  $h_y$  (black curve) from two Gaussian functions: positive  $h_1$  (red-dashed) and negative  $h_2$  (blue-dashed). The parameters representing the amplitude  $A_1$  and  $A_2$ , width  $\sigma_1 = (2B_1)^{-0.5}$  and  $\sigma_2 = (2B_2)^{-0.5}$ , and mean value  $\mu_1 = C_1$  and  $\mu_2 = C_2$ .

The crater function used in this section has been derived from the difference of 2 Gaussian functions  $h_1$  and  $h_2$ :

$$h(\mathbf{x}, \mathbf{y}) = h_1 - h_2 = A_1 \exp\left(-\frac{\mathbf{x}^2 + (\mathbf{y} - \mu_1)^2}{2\sigma_1^2}\right) - A_2 \exp\left(-\frac{\mathbf{x}^2 + (\mathbf{y} - \mu_2)^2}{2\sigma_2^2}\right), \quad (3.3)$$

where  $A_1$  and  $A_2$  determine the magnitude,  $\sigma_1$  and  $\sigma_2$  are widths,  $\mu_1$  and  $\mu_2$  are mean values of the positive and the negative Gaussian respectively. The two-dimensional version of this equation is plotted in Fig. 3.12. It shows how the parameters of a Gaussian distribution can be understood in terms of the crater function.

Fitting values for the different ion energies and incidence angles have been collected in the table 3.1, together with the reference values obtained with MD simulation (for details see [16]). The exact meaning of parameters is difficult to express, however  $A_1$  and  $A_2$  are clearly proportional to the height of relocated mass to the crater rims and to the depth of the crater respectively.  $B_1$  is proportional to the width of the crater, whereas  $B_2$  is proportional to the width of the crater rim.  $C_1$  and  $C_2$  describe the shift of the crater in horizontal direction and the difference between these parameters gives the material pileup in the projected ion direction, as well as the opening of the rim in the opposite direction. The relation of fitting parameters to the Gaussian characteristic is shown in Fig. 3.12 and can be expressed by,

$$\begin{aligned} B_i &= \frac{1}{2\sigma_i^2} \\ C_i &= \mu_i \end{aligned} \quad (3.4)$$

Although the fitting values differ from MD calculations (Tab. 3.1), the tendency of the crater shape is the same according to several assumptions: (i) Parameter  $A_2$  is always



greater than  $A_1$  because cratered depth is always larger than height of the crater rims. (ii)  $B_2$  is about one order of magnitude larger than  $B_1$ , because the width of the crater rims, i.e.  $\sigma_1 = (2B_1)^{-1/2}$ , is always larger than the width of the crater. (iii) Finally,  $C_2 > C_1$  due to the asymmetry in the crater shape for oblique ion incidence angles.

The comparison of different simulation conditions given in the Tab. 3.1 shows that the mass relocation peak ( $A_1$ ) is the highest at  $E_0 = 250$  eV and  $\theta = 30^\circ$  (see Fig. 3.8). Also the crater depths ( $A_2$ ) are the largest for the lowest energies and small incidence angles. On the other hand  $A_1$  and  $A_2$  are minimal for the highest energy 1 keV and low relaxation times 2 MCs. This is related to the highest ion penetration depth. Increasing the recombination distance of defects with the surface, the majority of defects will be annihilated by FPs recombination.

Table 3.1.: Fitting parameters obtained by three-dimensional fitting to the Eq. (3.2)

		$A_1$ (Å)	$A_2$ (Å)	$B_1$ (Å <sup>-2</sup> )	$B_2$ (Å <sup>-2</sup> )	$C_1$ (Å)	$C_2$ (Å)	$D_1$	$D_2$
250 eV (2 MCs)	0°	0.104	0.327	0.0047	0.0578	0.0	0.0	1.0	1.0
	30°	0.140	0.335	0.0046	0.0486	10.46	5.04	1.0	1.0
	67°	0.125	0.32	0.0034	0.0442	20.57	13.44	0.81	2.91
250 eV (30 MCs)	0°	0.131	0.257	0.0027	0.0357	0.0	0.0	1.0	1.0
	30°	0.160	0.291	0.0028	0.0322	9.62	4.49	1.0	1.0
	67°	0.147	0.286	0.0024	0.029	19.78	13.42	0.86	2.13
500 eV (2 MCs)	0°	0.101	0.297	0.0036	0.0541	0.0	0.0	1.0	1.0
	30°	0.126	0.306	0.0034	0.0499	11.49	5.0	1.0	1.0
	67°	0.124	0.33	0.0023	0.0417	24.06	13.98	0.98	3.65
500 eV (30 MCs)	0°	0.134	0.251	0.0022	0.033	0.0	0.0	1.0	1.0
	30°	0.154	0.278	0.0022	0.0313	10.79	4.64	1.0	1.0
	67°	0.149	0.292	0.0017	0.0267	23.34	14.44	1.02	3.05
500 eV (MD [16])	0°	0.205	0.805	0.00553	0.0351	0.0	0.0	...	...
	16°	0.169	0.788	0.0052	0.0325	...	1.2	...	...
	28°	0.201	0.891	0.00531	0.0357	7.46	1.48	...	...
1000 eV (2 MCs)	0°	0.094	0.253	0.0029	0.0587	0.0	0.0	1.0	1.0
	30°	0.109	0.26	0.0025	0.0507	12.69	4.93	1.0	1.0
	67°	0.12	0.292	0.0016	0.0456	28.9	13.93	1.22	4.29
1000 eV (30 MCs)	0°	0.124	0.213	0.0017	0.0336	0.0	0.0	1.0	1.0
	30°	0.136	0.234	0.0016	0.0328	12.44	4.63	1.0	1.0
	67°	0.14	0.265	0.0011	0.0284	28.69	14.78	1.2	3.56

The widths of the craters or crater rims increase always with energy independently on incidence angle or relaxation time. However, after 30 MCs wider craters occur in comparison to the 2 MCs simulation. It is confirmed by the high values of  $B_1$  and  $B_2$ , which are clearly correlated and rather close the MD results<sup>2</sup>.

$C_1$  and  $C_2$  describe the average position of a crater function on the surface plane, or the mean values of positive and negative Gaussian functions ( $\mu_1$  and  $\mu_2$ ). The difference between them decide about the asymmetry between the lower and the upper peak of the

<sup>2</sup>Although  $B_2$  is almost exact with MD data,  $B_1$  still deviates by a small factor, resulting in wider crater distributions.

crater rims. The scale of the mean values as well as the difference is clearly proportional to the incidence angle with the maximum obtained for the highest energies of 1 keV and  $67^\circ$  incidence angle. Nevertheless, even higher values are expected for grazing incidence of  $85^\circ$ . Due to the difficulties in finding a proper fitting function parameters this angle has not been evaluated.

$D_1$  and  $D_2$  factors have only been fitted for  $\theta = 67^\circ$  due to the elongated crater distributions. It is interesting to observe that crater rims are realized in contracted shape with respect to the ion orientation, especially at the energy of 250 eV ( $D_1 = 0.81$ ).  $D_2$  is always higher than 1, resulting in elongated shape of eroded area.

The simulation of a single ion impact shows that the height of the surface should increase rather than decrease due to the ion irradiation, even under consideration of sputtering. This will not be the true if multiple ions are considered and the relaxation time of a single collision cascade is the sum of the collective relaxation times of subsequent collisions. Therefore, at the constant simulation temperature, the total relaxation time of a collision cascade will be longer in comparison to the single ion impact, sufficient for all of the defect to reach the surface region and the total average height of the surface will drop due to the sputtering.

The most significant difference between MD results constitutes the crater depth (parameter  $A_2$ ), which is even three times smaller at  $\theta = 30^\circ$ . This is strongly related to the absence of bulk tension in TRIDER simulations that lowers the atomic concentration in the volume around the impact position. However, for a longer time scales this effect may not play an important role due to the continuous bulk relaxation of defects accumulated by subsequent ion impacts. The second work of Kalyanasundaram *et al.* [18] provides a multiscale simulation, where MD fitting function of crater formation is used to integrate two-dimensional surface at random positions with respect to the incidence angle calculated according to the local slope of modified surface. It is surprising that at  $15^\circ$  ion incidence angle ripples are formed, perpendicular to the incoming ions, whereas it is never the case for ‘clean’ experiments of IBS on Si [147, 171], where the ripple formation starts at  $\theta \geq 50^\circ$ .

### 3.3 Ripple evolution

One of the major purposes of this work is to create the atomistic model for simulating surface morphology under ion irradiation, in order to provide a better understanding for the processes inducing the topography evolution to the ripple structure. All of the atomistic models available in the literature that are applied to study pattern formation suffer from the assumptions of SOS approach: (i) the two-dimensional surface treatment using KMC technique, (ii) Sigmund’s ellipsoid of energy loss is applied to calculate erosion rate of surface atoms. At present, only the qualitative correspondence with experiments has been provided [10–12, 158], except the last reference, where the experiments can be reproduced for ripples oriented parallel to the ion beam direction quantitatively. The SOS model allows only for the surface diffusion, excluding completely all bulk effects, which tend to be crucial, especially according to the results in the last section. Moreover, SOS assumes two-dimensional surface, with two spatial dimensions ( $x, y$ ) and additional dimension representing the height at given coordinates  $h(x, y)$ . It eliminates existence of overhangs, shadowing effect and energy barriers in the out-of-plane direction (e.g. Ehrlich-Schwöbel barrier [137, 138]). To overcome these problems the TRIDER model

has been applied for multiple ion impact simulations. This section focuses on long time calculations up to  $10^{18}$  cm<sup>-2</sup> of periodic pattern formation where the time and length scales are comparable with experiments. Moreover, the quantitative analysis of ripple evolution will be presented based on the investigation of interface width and ripple wavelength evolution.

### 3.3.1. Constant flux per coordinate unit

Initially TRIDER simulations have been performed with a constant ion impact rate for unit of the  $x$  coordinate. Due to the small amplitude ( $\sim 5\%$  of wavelength) of patterns on Si for  $E_0 \leq 1$  keV, this approximation has been assumed to be justified. It has been proved that it is indeed justified for almost normal ion incidence and grazing incidence (because in the lateral case ripples are aligned with ion beam). However, in the intermediate range (at  $\theta = 45^\circ$ ) the results have to be considered with some caution as a few simulations taking into account some deviations. This section reports the simulation results with a constant ion impact rate per coordinate unit, following the dependence of simulation flux  $j_{sim}$ , ion incidence angle  $\theta$ , energy  $E_0$  and fluence  $\phi$ .

#### Surface morphology

The phase diagram of a pattern formation occurrence versus incidence angle and energy, for the first time under clean conditions, has been reported by Madi *et al.* [122] for Ar<sup>+</sup> ions, which has been confirmed later also for different projectiles, like Kr<sup>+</sup> by Macko *et al.* [171]. They demonstrated that the pattern formation is not expected at incidence angles below  $45^\circ$  with respect to the surface normal. In addition, the switch in *ripple mode* of ripple orientation with respect to the ion beam direction from *perpendicular* to *parallel* appears at a grazing incidence around  $\theta = 80^\circ$ . The experiments show that the wavelength of the ripples is relatively small at low energies, i.e. less or equal 1 keV, and stays around 20-30 nm [99].

The simulation results of pattern topography concerning ripple appearance and switching are shown in Fig. 3.13. A strong variety of structures can be distinguished. However, the general tendencies can be restricted to four statements concerning the range of  $\theta$ :

1. ( $0^\circ$ - $30^\circ$ ) - no or very irregular pattern formation
2. ( $40^\circ$ - $50^\circ$ ) - low wavelength of ripples (up to  $l = 7$  nm), with very high regularity, oriented perpendicular to the ion beam direction
3. ( $60^\circ$ - $70^\circ$ ) - increase of ripple wavelength (up to 25 nm), with very pronounced structures and strong asymmetry (highest at  $\theta = 70^\circ$ )
4. ( $80^\circ$ - $85^\circ$ ) - grazing incidence with ripples oriented parallel to the ion beam direction.

The simulation fluxes corresponding to the examples shown in Fig. 3.13 are usually  $j_{norm} = 2^{-20}$ . However at incidence angles  $\theta < 45^\circ$  a higher flux, of about  $2^{-15}$ , has been chosen to reduce computational time. Nevertheless test simulation with a lower flux did not provide any regular pattern formation as well.

There is a strong correspondence between the simulation and the phase diagram of Madi *et. al* [147], except the ripple occurrence around  $\theta = 45^\circ$ . However, very small wavelength and amplitude in this regime suggests the existence of a limitation of measurement techniques, where a very small surface undulations cannot be detected. Moreover,

experiments show the existence of additional perpendicular ripple mode at  $\theta \approx 10^\circ$ . This, particular case is not relevant in the framework of present simulation due to the limitation in the system size, that is about  $100 \times 100 \text{ nm}^2$  of the surface dimensions, whereas the experimental ripple wavelength is expected to be  $l \approx 75 \text{ nm}$ .

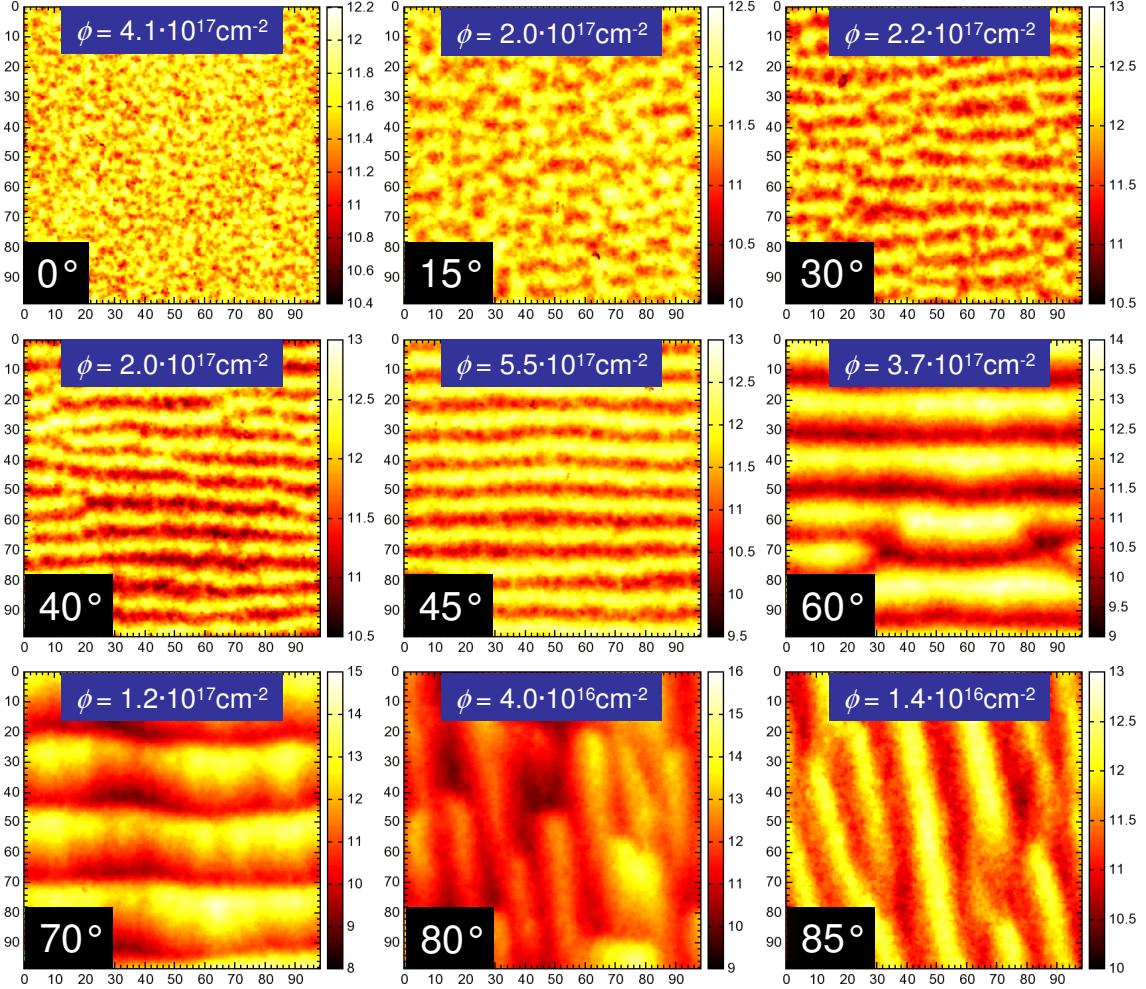


Figure 3.13.: Simulated surface pattern topographies after 0.8-1 keV  $\text{Ar}^+$  irradiation of (001) Si for different  $\phi$  and  $\theta$ . The normalized bond energy is  $\epsilon=1.7$ . All axis units are in nm. Ion orientation is always from the top.  $\theta$  is given at the bottom left corner of each simulation surface and  $\phi$  at the top of each surface.

Pattern topography dependency on  $\text{Ar}^+$  ion energy is shown in Fig. 3.14. Here, the  $j_{norm}$  is kept constant at  $2^{-15}$  for  $60^\circ$  ion incidence angle and the energy varies from 50 eV to 3.2 keV. Simulations show a strong difference of the structure shapes, however, the intermediate energy regime provides only variation of the interface width and the wavelength. Here, three energy regimes can be proposed:

1.  $E_0 < 200 \text{ eV}$  - static type of ripples (no ripple movement), only wavelength increase - very irregular patterns
2.  $200 \text{ eV} \leq E_0 \leq 1.6 \text{ keV}$  - saturation of the interface width and the ripple wavelength, both increase with the ion energy
3.  $E_0 > 1.6 \text{ keV}$  - irregular ripples, appearance of overhangs and very high amplitude/wavelength ratio (close to 1).

## CHAPTER 3. ION-INDUCED SURFACE PROCESSES

The most interesting is the intermediate ion energy range between 200 eV and 1.6 keV. Irradiation of surfaces at intermediate energies results in well-ordered ripples oriented perpendicular to the ion beam direction.

At very low energies (50 eV and 100 eV) the number of defects created by the collision cascade is reduced and the sputtering yield is almost zero. Nevertheless, patterns are forming even without influence of the surface erosion mechanism. In these cases, the defects are clearly responsible for self-organization of the surfaces. Ripple movement is strongly suppressed due to small number of defects. However, ripple coarsening is always present. The wavelength increases very inhomogeneously as a stochastic process, decreasing regularity of the pattern formation.

On the other hand,  $E_0 = 3.2$  keV tends to be too high energy and due to the relatively high flux the smoothing mechanism is too low in comparison to the damage created by energetic  $\text{Ar}^+$  ions. It is followed by the significant increase of ripples amplitude up to 15 nm with the wavelength at the same order of magnitude.

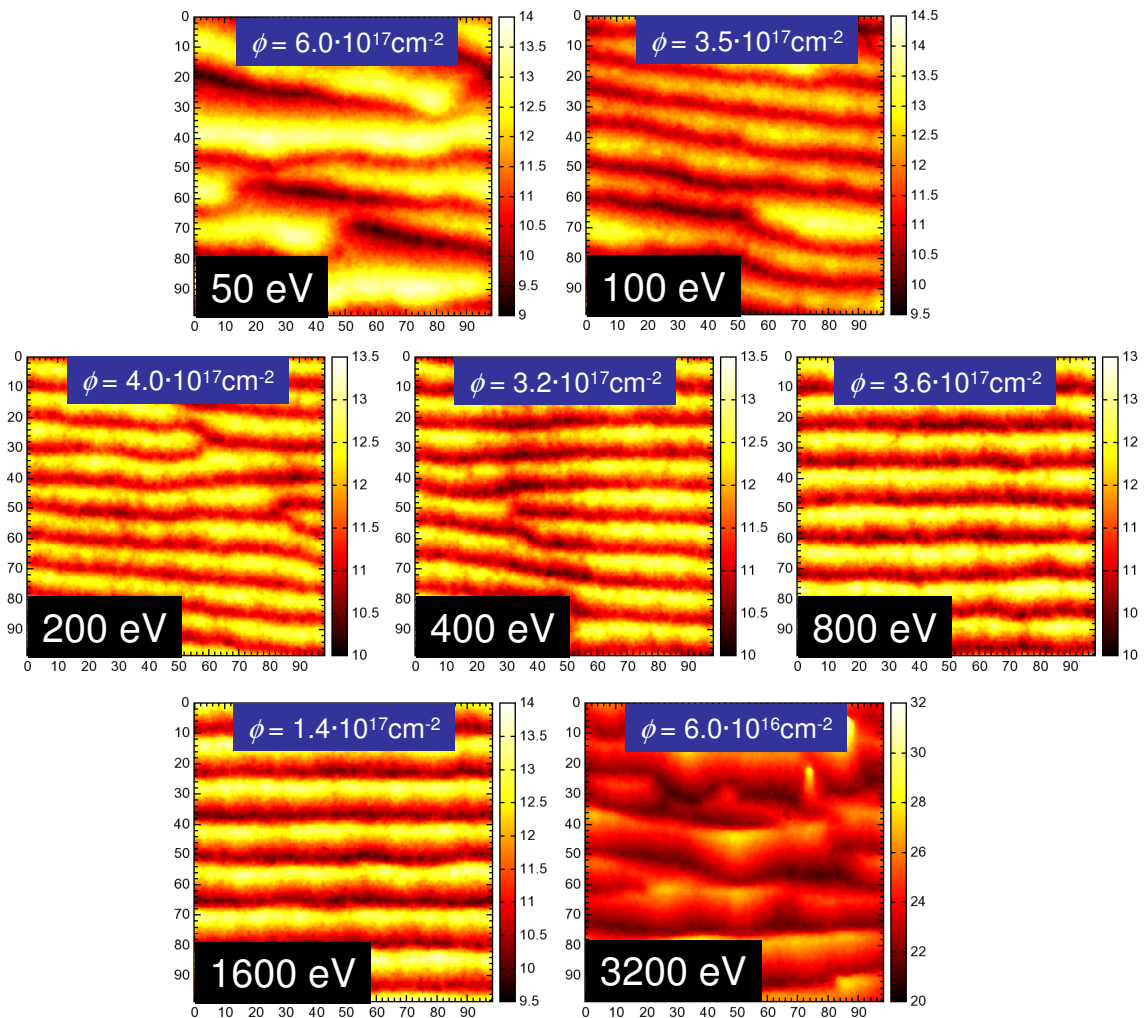


Figure 3.14.: Simulated surface pattern topographies after  $60^\circ$   $\text{Ar}^+$  irradiation of (001) Si for different  $\phi$  and  $E_0$ . Normalized bond energy is  $\epsilon=1.7$ . All axis units are in nm. Ion orientation is always from the top.  $E_0$  is given at the bottom left corner of each simulation surface and  $\phi$  at the top of each surface.

### Spatial evolution of surfaces

All the surfaces presented in the previous section are some types of discrete rough surfaces with deterministic properties. It means that it is possible to find a deterministic function of a surface position that can describe the most important characteristics of the surface height fluctuation. The most important first-order characteristic is the probability distribution function  $p(h)$  of height  $h$ , which in most general case can be expressed as the Gaussian height distribution,

$$p(h) = \frac{1}{\sqrt{2\pi}w} \exp\left(-\frac{h^2}{2w^2}\right). \quad (3.5)$$

Here,  $w$  is the width of the distribution, which is also called the surface roughness, however in this work, the term interface width, is used. The interface width accounts for the 2nd order moment of  $h$ , whereas the 1st order moment is the average surface height. The interface width of a system with the size  $L$  at the time  $t$  is given by the equation,

$$w(L, t) = \sqrt{\langle h^2 \rangle - \langle h \rangle^2} = \left[ \frac{1}{L^2} \sum_{x,y}^L h_{x,y}^2(t) - \left( \frac{1}{L^2} \sum_{x,y}^L h_{x,y}(t) \right)^2 \right]^{1/2}, \quad (3.6)$$

where  $\langle \cdot \rangle$  denotes spatial averaging, and  $h$  is the surface height at coordinates  $x$  and  $y$ .

Height distribution function can only describe the statistical properties of surfaces at individual positions. However, the connection between the surfaces at different positions can only be characterized using second-order statistics, in particular with the joint probability distribution function  $p_j(h_1, h_2, \vec{r}_1, \vec{r}_2)$  of heights  $[h_1, h_2]$ , where  $\vec{r}_1$  and  $\vec{r}_2$  are different positions on the surfaces

$$p_j(h_1, h_2, \vec{r}_1, \vec{r}_2) = p(h_1)p(h_2). \quad (3.7)$$

Joint probability distribution can be characterized by different types of correlation functions, which are mathematically equivalent. One of the most common is autocorrelation function with the discrete form given by the equation,

$$R(r) = \frac{1}{w^2} \langle \hat{h} \check{h} \rangle = \frac{1}{L(L-r)w^2} \sum_y^L \sum_x^{L-r} h_{x+r,y} h_{x,y}. \quad (3.8)$$

Here,  $\hat{h}$  and  $\check{h}$  are heights at different locations, and  $r$  is the distance between these locations. Using autocorrelation function it is possible to define the lateral correlation length  $\xi$ , being the distance  $r$  at which the  $R(r)$  drops to the value of  $1/e$

$$R(\xi) = 1/e \quad (3.9)$$

It is possible to study the spatial evolution of the statistical properties (like interface width, correlation length, etc.) of a random fields. In the absence of any characteristic length, growth and erosion processes are expected to follow a power-law behavior of the correlation functions in space and height and the surface evolution is described by the Family-Vicsek scaling [150] of the interface width  $w$

$$w(L, t) \propto \begin{cases} t^\beta, & \text{if } t_0 \ll t \ll t_s \\ L^\alpha, & \text{if } t \gg t_s \end{cases} \quad (3.10)$$

Here  $\alpha$  is the *roughness exponent* and characterizes the deviation from a flat surface in the stationary regime ( $t \gg t_s$ );  $t_s$  is the saturation time, above which the correlation length has exceeded the linear system size  $L$ .  $\beta$  is the *surface growth exponent*, which describes the time evolution for earlier times ( $t \gg t_0$ , where  $t_0$  is a ‘crossover’ time, see Fig. 3.15). The dynamical exponent  $z$  can be expressed by the ratio

$$z = \frac{\alpha}{\beta} \quad (3.11)$$

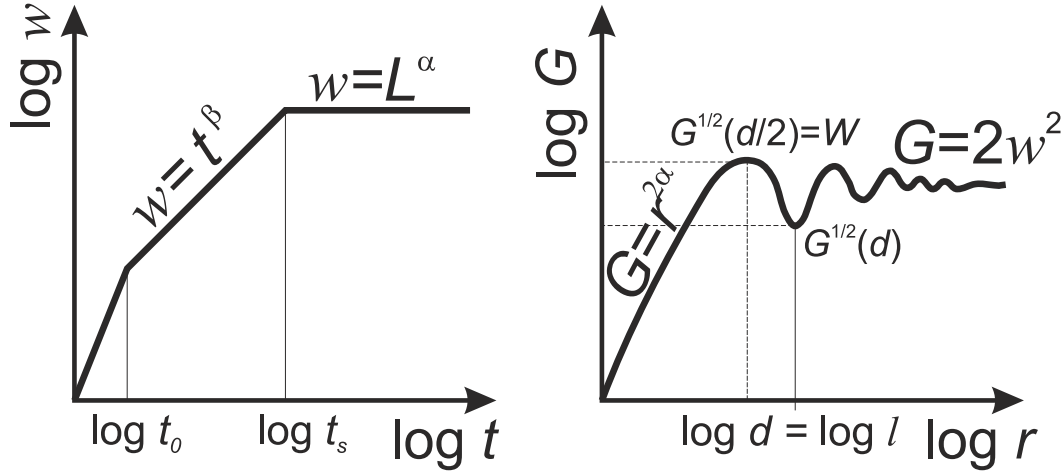


Figure 3.15.: Schematic plot of interface width  $w$  as a function of time  $t$  (left) and square root of the height-height correlation function  $G$  as a function of a spatial separation between the two points  $r$  (right). Evolution of  $w$  follows the equation (3.10) starting from  $t_0$ . In the early times random deposition behavior is expected, where the correction to the Family-Vicsek scaling is needed. In the late times ( $t \gg t_s$ ) saturation is expected.  $G^{1/2}(r)$  evolution (3.13) shows the typical curve for the Height-Height Correlation Function applied on the wavy surface perpendicular to the ripple orientation. The first local minimum is a rough measure of the ripple wavelength  $l$  at  $r = d$ , whereas the first local maximum is so-called roughness amplitude  $W$  (see Ref. [126]) at  $r = d/2$ .

However, if a characteristic length is present, it is necessary to provide a method to evaluate this information, for instance, by extraction of a surface wavelength  $l$ .  $l$  can be obtained by the Height-Height Correlation Function  $G(r)$  [126, 143]

$$G(r) = \left\langle (\hat{h} - \check{h})^2 \right\rangle = \frac{1}{L(L-r)} \sum_y^L \sum_x^{L-r} (h_{x+r,y} - h_{x,y})^2. \quad (3.12)$$

Again,  $G(r)$  can be described, with the scaling exponents for a random rough surface by,

$$G(r) \propto \begin{cases} r^{2\alpha}, & \text{if } r \ll \xi \\ 2w^2, & \text{if } r \gg \xi \end{cases}, \quad (3.13)$$

The lateral correlation length can be defined as a minimal lateral distance between two points, where the height is correlated. In this work, the ripple wavelength  $l$  is obtained from the first local minimum of the distance  $r$ , which tends to be a rather good approximation of a real value [126]. The way of estimation of scaling exponents, as well as, the wavelength of a ripple pattern is given in Fig. 3.15.

As mentioned before, the different types of correlation functions are equivalent, e.g. the height-height correlation function can be derived using the autocorrelation function according to

$$G(\vec{r}) = 2w^2 \{1 - R(\vec{r})\}. \quad (3.14)$$

Moreover, the Fourier transform  $\mathcal{F}$  of an autocorrelation function represents the power spectra density function of a random field. In contrary to the real-space characteristics like  $w$ ,  $\xi$  or  $l$ , in reciprocal space (or in Fourier space) it is more convenient to use the power spectrum  $P(\vec{k})$  for description of surfaces

$$P(\vec{k}) = \mathcal{F}(R(\vec{r})) = \frac{1}{2\pi} \int_{-\infty}^{\infty} R(\vec{r}) e^{-i\vec{k}\vec{r}} d\vec{r}, \quad (3.15)$$

where,  $\vec{k}$  is a wave vector in the reciprocal space.

To describe the evolution of periodic pattern formation only ion incidence angles  $\theta \geq 45^\circ$  of pattern evolution will be studied quantitatively. The reason for calculating the interface width and the ripple wavelength is to evaluate accuracy of proposed model and a comparison with available experimental and theoretical data. The evolution of first and second-order statistical parameters is an additional measure that characterizes the surface morphology.

The influence of simulation flux  $j_{sim}$  on a pattern evolution is an important and open question. Therefore, two ripple modes are analyzed separately following  $60^\circ$  and  $85^\circ$  ion incidence angles corresponding to Fig. 3.16 and Fig. 3.17 respectively.

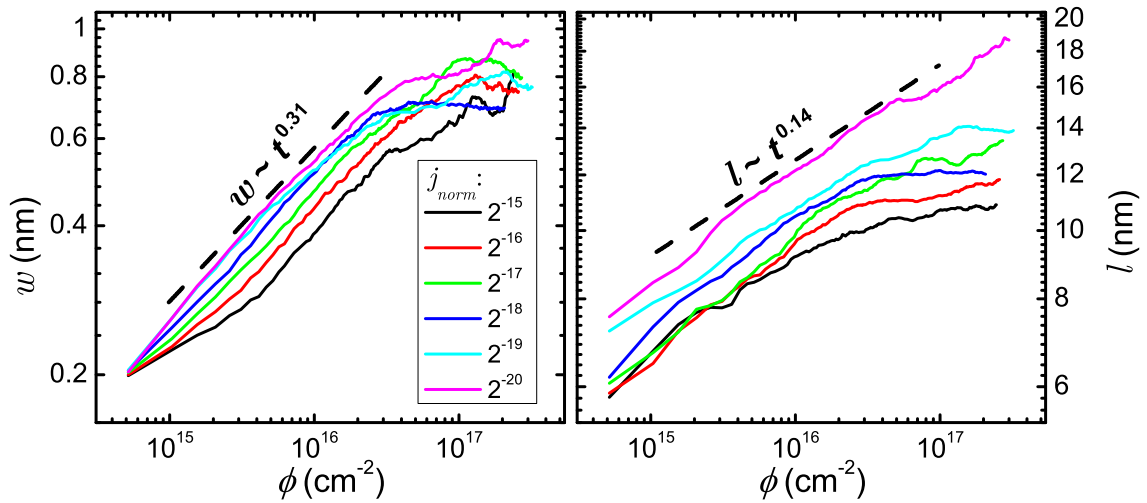


Figure 3.16.: Log-log plots of interface width  $w$  (left) and ripple wavelength  $l$  (right) evolution for different fluxes  $j_{norm}$  (see legend) at  $\theta = 60^\circ$  and the 1 keV ion energy. The dashed lines are the exponential fitting functions, with the growth exponent  $\beta = 0.31$  and the coarsening exponent of wavelength increase  $n = 0.14$ .

The parallel ripple mode exhibits a power law dependence for each  $j_{sim}$ , following the same type of asymptotic behavior with a growth exponent  $\beta = 0.31$  (see Fig. 3.16). The steady state amplitude is strongly fluctuating and the exact saturation value is difficult to specify. However, at the fluences  $\phi < 3 \times 10^{16} \text{ cm}^{-2}$  before the saturation, the interface widths  $w$  is inverse proportional to the applied flux  $j_{norm}$ , i.e. is proportional to the duration of defect relaxation stage after the collision cascades according to Sec. 2.3.2. Due to very demanding type of computations, only one simulation has been performed per



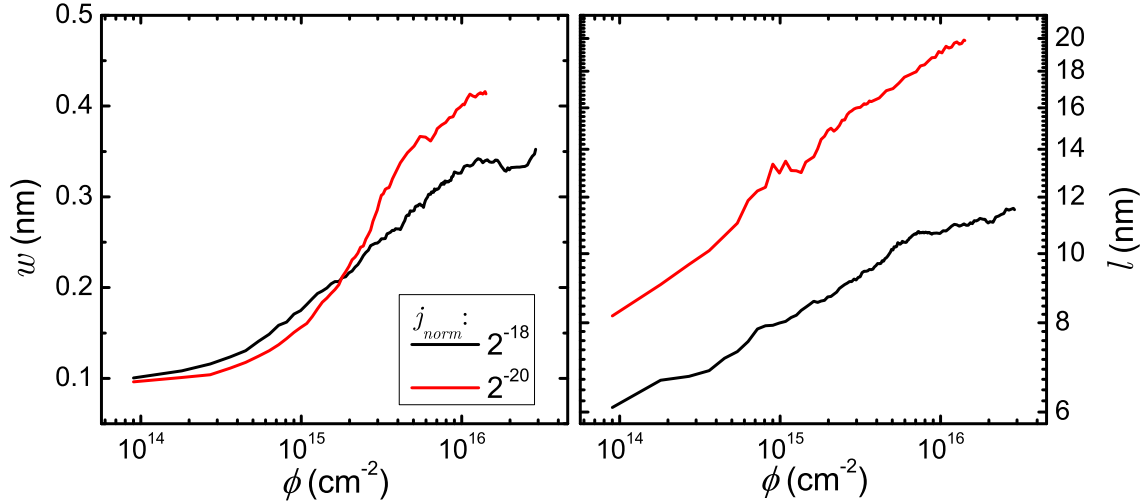


Figure 3.17.: Logarithmic plots ( $w$  scale is **linear**,  $l$  scale is **logarithmic**) of interface width  $w$  (left) and ripple wavelength  $l$  (right) evolution for different fluxes  $j_{norm}$  (see legend) at  $\theta = 85^\circ$  and  $E_0 = 1$  keV.

simulation flux. This explains the fluctuation of  $w$  or  $l$  after the saturation. Wavelength of ripples created by  $60^\circ$  ion irradiation is given on the right side of Fig. 3.16. It shows existence of coarsening behavior described by the effective power law  $l \sim t^{0.14}$ . This value is very close to results of continuum two-field model of Munoz-Garcia *et al.* [8] ( $n = 0.12$ ) and is not far from experimental results of Keller *et al.* [99] ( $n = 0.085$  and  $\beta = 0.28$ ). The evolutions of pattern wavelength are also inverse proportional to the applied flux (see right side of Fig. 3.16). The asymptotic behavior has been observed, where the saturation fluence of  $l$  is correlated with the saturation fluence of  $w$ . At the lowest flux  $j_{norm} = 2^{-20}$  however, the saturation does not occur within applied simulation fluence for both  $w$  and  $l$  evolution. A dependence of the saturation fluence of  $l$  on the simulated surface size tends to be important especially for very well ordered pattern formation, where no more ripple defects are left at the surface (see Fig. 3.13). This suppresses the further increase of  $l$  and consequently suppresses increase of  $w$ .

At grazing ion irradiation, only two  $j_{sim}$  values have been analyzed (see Fig. 3.17), providing similar tendency of the flux dependence, described in the previous paragraph. Interface width increases rather with logarithmic type of growth, especially for  $j_{norm} = 2^{-18}$  (linear scale of  $w$  evolution in left plot of Fig. 3.17), although the wavelength exhibits power law behavior, where  $l$  rise up to 20 nm without achieving a saturation<sup>3</sup>. Exponents  $n$  describing the coarsening of ripples are  $n = 0.14$  and  $n = 0.17$  at  $j_{norm} = 2^{-18}$  and  $j_{norm} = 2^{-20}$  respectively.

The evolution of  $w$  and  $l$  with respect to the ion incidence angle is shown in Fig. 3.18. For ripples oriented the parallel to the incoming ions, the  $\beta$  exponent increases with the incidence angle from  $\beta = 0.31$  at  $60^\circ$  to  $\beta = 0.46$  at  $70^\circ$ . The coarsening exponent changes from  $n = 0.14$  at  $60^\circ$  to  $0.22$  at  $70^\circ$ . The wavelength at  $70^\circ$  ion incidence goes up to 23 nm, which is the largest periodicity obtained within this type of simulation. Power law behavior has been observed, both for the interface width and the wavelength evolution. If the ripples are oriented perpendicular to the ion beam ( $85^\circ$ ), logarithmic growth of  $w$  is preferred (see also Fig. 3.17). The different initial position of each curve

<sup>3</sup>In the experiment of Madi *et al.* the wavelength obtained was around 23 nm [147].

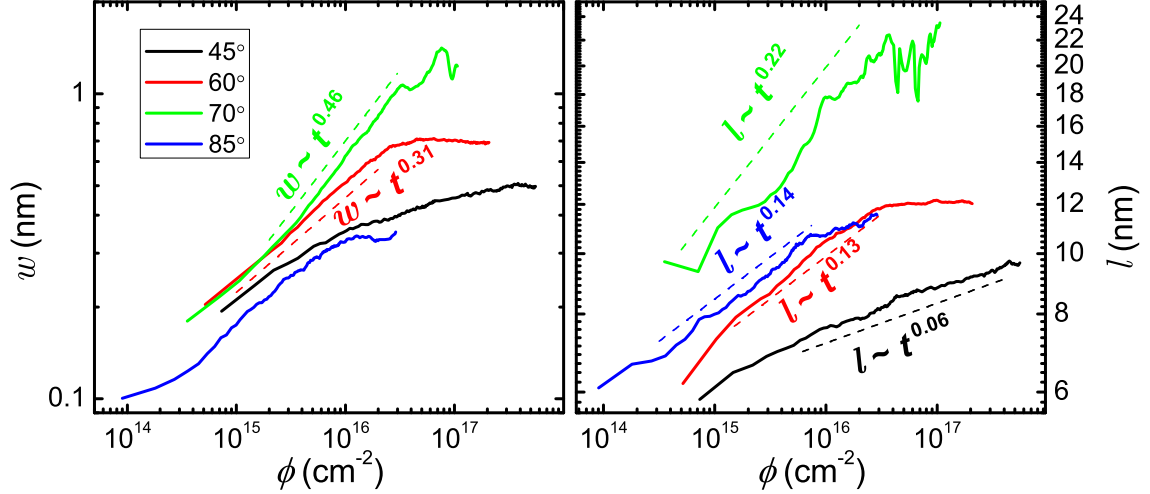


Figure 3.18.: Log-log plots of interface width  $w$  (left) and ripple wavelength  $l$  (right) evolution at the same fluxes ( $j_{norm} = 2^{-18}$ ) and different incidence angles:  $45^\circ$ ,  $60^\circ$ ,  $70^\circ$  and  $85^\circ$ , at ion energy  $E_0 = 1$  keV. Dashed lines represent power law fittings with the exponents defined in the plots description.

is due to rescaling of the fluence by a cosine of the impact angle (flux correction)

$$\phi_{new} = \phi \times \cos \theta. \quad (3.16)$$

Evolution of interface width and wavelength versus fluence at different ion energies is shown in Fig. 3.19. Previously mentioned physically irrelevant types of simulation are here marked with dashed lines, therefore only the energies of 200, 400, 800 and 1600 eV are investigated. Existence of an energy range shows an importance of a proper selection

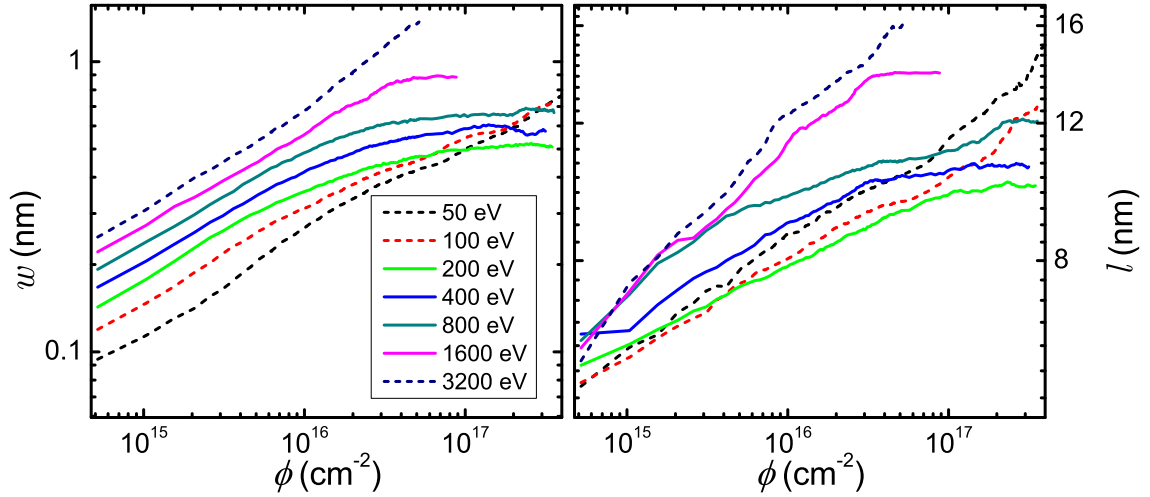


Figure 3.19.: Log-log plots of interface width  $w$  (left) and ripple wavelength  $l$  (right) evolution at the same fluxes ( $j_{norm} = 2^{-16}$ ) and incidence angle  $\theta = 60^\circ$ , but different ion energies: 50, 100, 200, 400, 800, 1600 and 3200 eV. Dashed curves denote the calculation, where the simulation conditions exclude asymptotic behavior within the evolution.

of the simulation flux (here  $j_{norm} = 2^{-16}$ ). It tends to be proportional to the ion energy and more specifically, to the total damage or to the average number of defects created within the collision cascade. More damage accumulated in the target leads to longer relaxation times applied for KMC simulation stage.

Interface width evolution in Fig. 3.19 clearly indicates no growth exponent variation ( $\beta = 0.31$ ) related to energy. However, the saturation width differs significantly, and is proportional to the ion energy. The evolution of  $l$  follows the dependence  $l \sim t^n$  with  $n$  starting from 0.1 at 200 eV to 0.18 at 1600 eV. The comparison of saturation times for  $w$  and  $l$  plots leads to the conclusion that both values are correlated and their asymptotic behavior is related with reduction of ripple defects, which suppresses further growth of ripple amplitude.

### 3.3.2. Simulation with ray tracing of ions

When the local incidence angles at the surface differ significantly from the global one the approximation used in the previous section, i.e. constant ion impact rate per coordinate unit cannot be applied. The approximation is justified at grazing incidences, where the ripples are aligned with the ion beam, and at normal and close to normal incidence angles, where the surface remains flat. On the other hand at oblique ion incidences relatively large amplitudes have been obtained ( $\sim 20\%$  of wavelength according to Fig. 3.13  $70^\circ$  and Fig. 3.14 1.6 keV), therefore, used approximation cannot be justified.

The ray tracing of ions, introduced by a correction of a local flux (2.64), provides a consistent description of the reality. In this section simulations with ray tracing of ions are presented. The phase diagram of pattern formation is again investigated followed by the analysis of spatial evolution of ripples. Moreover, the influence of the sputtering yield on the ripple formation will be analyzed by studying the surface morphology, the interface width and the wavelength evolution.

#### Surface morphology

Various initial conditions of the simulation concerning the ray tracing of ions provide various types of pattern formation, which are in a good correspondence with the phase diagram of Madi *et al.* [122]. The first results of the new simulation approach provided no pattern formation at an energy of 1 keV and above with the same initial conditions like for simulations from Sec. 3.3.1. Decreasing the energy below 500 eV showed the ripple patterns, what will be described in following.

Fig. 3.20 shows the full angular dependence of the pattern formation at an  $\text{Ar}^+$  ion energy of 250 eV, with a simulation flux of  $j_{norm} = 2^{-17}$ . The surface morphologies at incidence angles between  $0^\circ$  and  $50^\circ$  present the simulation surfaces already in the steady state, where interface width  $w$  and wavelength  $l$  are saturated, therefore no more morphological changes are expected. The first pronounced pattern formation can be recognized at the  $40^\circ$  incidence angle. The threshold for appearance of regular ripple structure with a periodicity larger than 10 nm is around  $\theta = 50^\circ$ . This result fits very well to the phase diagram of Madi *et al.*

In ripples oriented perpendicular to incoming ions between  $50^\circ$  and  $70^\circ$  there is a strong tendency of wavelength increase proportional to the incidence angle. This effect will be analyzed quantitatively in Sec 3.3.2 providing the evolution of wavelength at various incidence angles. At  $\theta = 70^\circ$  the wavelength exceeds 20 nm. Ripples oriented parallel to the trajectory of ions are obtained at  $80^\circ$  and  $85^\circ$  ion incidence angle and the wavelength is larger at the larger values of  $\theta$ . At  $\theta = 70^\circ$  and  $\theta = 80^\circ$ , both ripple types (parallel and perpendicular) can be distinguished simultaneously. Whereas, at  $70^\circ$  perpendicular ripples dominate, at  $80^\circ$  mainly parallel ripples are visible. Similar behavior, however,

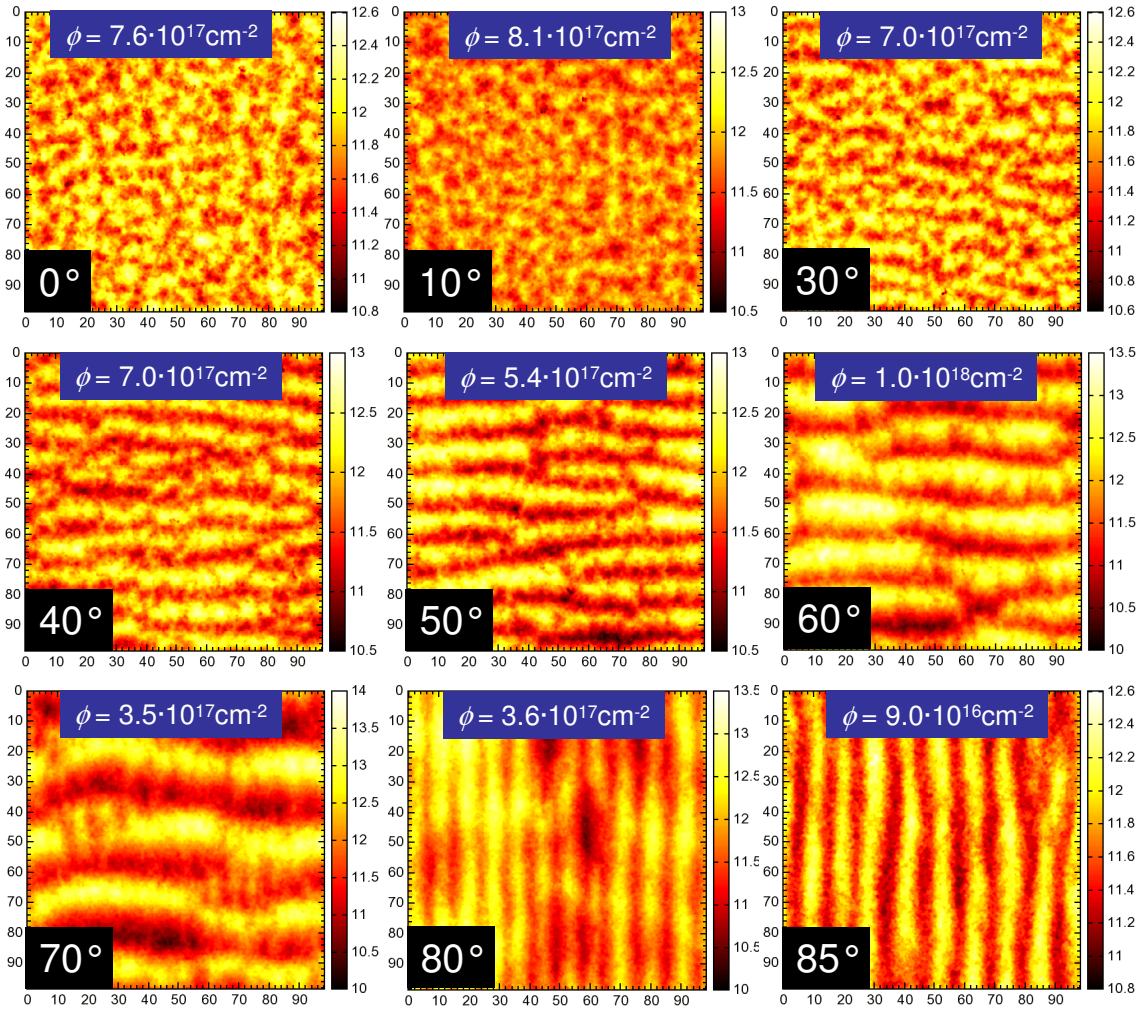


Figure 3.20.: Simulated surface pattern topographies at 250 eV Ar<sup>+</sup> irradiation of (001) Si for different ion fluences and incidence angles. Normalized bond energy is  $\epsilon=1.7$ . All axis units are in nm. Ion orientation is always from the top to the bottom. The incidence angle is given in the bottom left corner of each simulation surface. The fluence is denoted by  $\phi$  at the top of each surface.

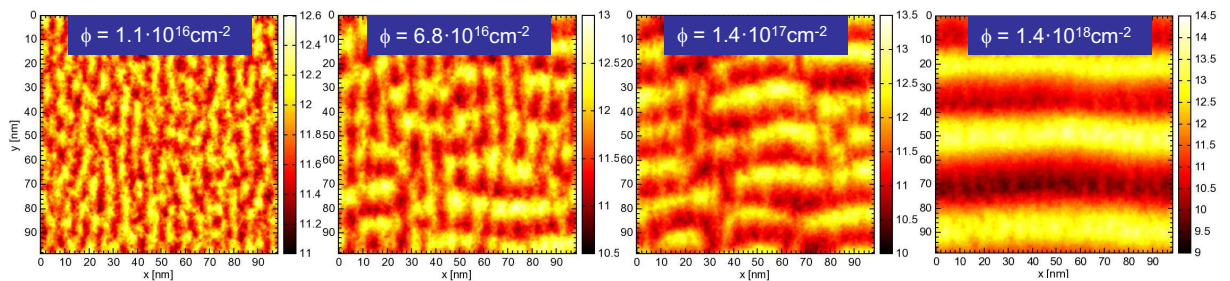


Figure 3.21.: Surface morphology evolution with fluence at 70° Ar<sup>+</sup> irradiation of (001) Si. Normalized bond energy is  $\epsilon=1.7$ . All axis units are in nm. Ion orientation is always from the top to the bottom, the fluence is denoted by  $\phi$  at the top of each surface.

for a much larger system size has been seen experimentally by Keller *et al.* [99] described as a co-existence of two ripple modes at  $67^\circ$  Ar<sup>+</sup> bombardment of Si.

Fig. 3.21 presents the evolution of surface at different ion fluences  $\phi$ . Ripples oriented parallel to the ion beam occur initially for very short irradiation times below  $6 \times 10^{16}$  cm<sup>-2</sup>. Later on, the structures perpendicular the ion trajectory are formed and become dominating for fluences above  $1.4 \times 10^{17}$  cm<sup>-2</sup>. This is followed by a significant rise of the surface roughness, as well as the ripple wavelength.

### With or without sputtering

BH theory [4] and related continuum models describing the pattern formation [6–8], explain the local topography modification by the different erosion rate depending on the local slope and shape of the surface. It results in a general statement that surface erosion in valleys should be higher than on hills. Therefore the local sputtering yield tends to be the major driving force determining the local surface erosion rate variations and therefore creating the ripple patterns.

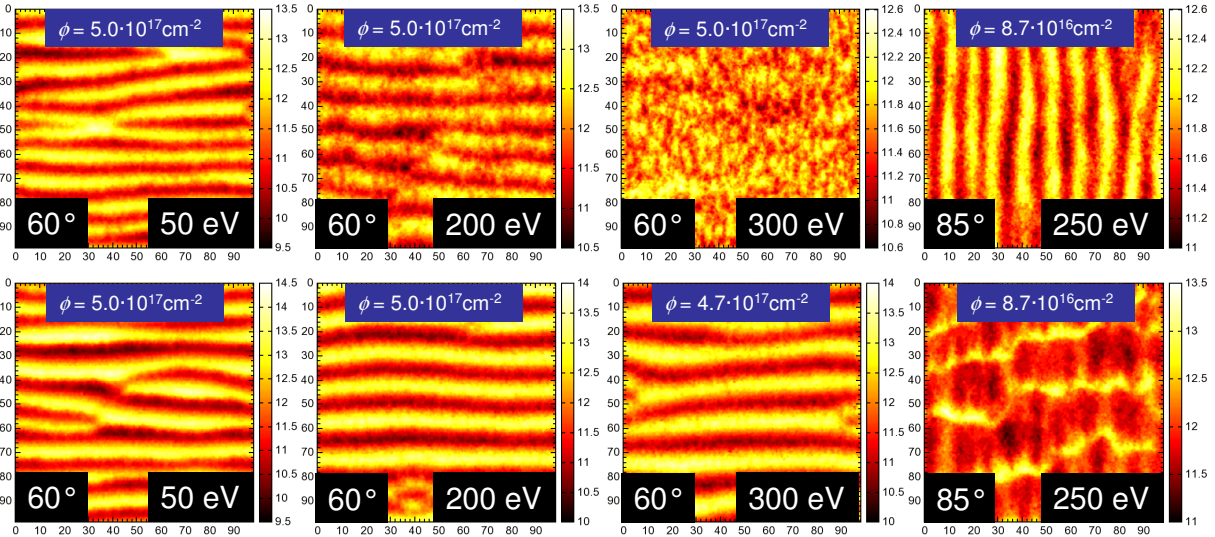


Figure 3.22.: Simulated surface pattern topographies with (top row) and without (bottom row) sputtering effect, after  $60^\circ$  (first, second and third column) and  $85^\circ$  (fourth column) Ar<sup>+</sup> irradiation of (001) Si at different ion fluences. Normalized bond energy is  $\epsilon=1.7$ . All axis units are in nm. Ion orientation is always from the top, the incidence angle is given in the bottom left corner of each simulation surface, and the fluence is denoted by  $\phi$  at the top and the ion energy at the bottom right corner.

BCA algorithm used in this work includes all sputtering effects and predicts the sputtering yield very precisely in comparison to the experiments [46, 49, 61]. However, it is not clear if the surface erosion is the dominant rippling mechanism in reality. Many other factors have to be taken into account additionally, like bulk/surface defect kinetics, surface diffusion, ion flux, etc. Atomistic type of modeling provides the possibility to manipulate the implemented physical mechanisms, turning some of them *on* or *off* if necessary. To investigate the role of surface sputtering, it is convenient to ‘artificially’ neglect sputtering, by turning it *off*, and to compare the results with the full simulation.

To exclude sputtering from the TRIDER simulation, the collision cascade is followed like originally (see Sec. 2.4.2) with additional condition. The initial lattice location of every atom is registered, and if the atom abandons the target is immediately filled again.

Therefore, no vacancies are expected made by the sputtered atoms and the mass balance in the system is conserved.

Fig. 3.22 provides the results of the simulation, where the sputtering is included in the upper row, and where this effect is excluded in the bottom row. Additionally, the energy dependence on the pattern formation at  $60^\circ$  of ion incidence is studied. The simulation fluxes are  $j_{norm} = 2^{-16}$  at  $60^\circ$  and  $j_{norm} = 2^{-17}$  at  $85^\circ$ .

By increasing the ion energy also the ripple wavelength increases. However, if the sputtering is included, the patterns became less pronounced and vanish almost completely at 300 eV. It is clearly not the case if sputtering is excluded, because the ripples tend to be always well ordered with the wavelength proportional to the ion energy.

The last column of Fig. 3.22 shows the grazing incidence simulations where the ripples oriented parallel to the ion beam direction are generally expected. Exclusion of sputtering, suppresses the switching behavior from parallel to perpendicular ripple mode in the range of  $70^\circ$ - $80^\circ$  ion incidence angle. Therefore it can be concluded that at the grazing incidences the sputtering is the dominant driving force of ripple formation.

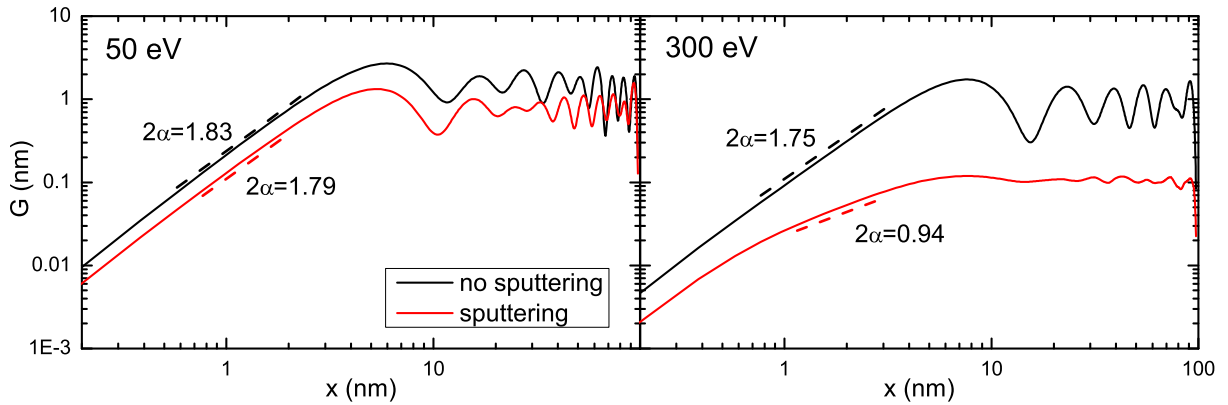


Figure 3.23.: Height-height correlation functions of a surface with (red curves) and without (black curves) sputtering, applied along ion trajectory at different ion energies: left 50 eV, right 300 eV. For both  $\theta = 60^\circ$ . The dashed lines are the exponential fitting functions, where the roughness exponent  $\alpha$  has been compared. Plots correspond to the morphologies shown in Fig. 3.22

The qualitative investigation of the influence of the sputtering yield on the ripple formation provides huge distinctions in the final surface topographies at oblique ion incidences at the ion energies larger than 50 eV. Ripples created by the full collision cascade with sputtering are visually much noisier and less ordered, even though the interface width is slightly higher if the sputtering is excluded. This type of height fluctuation cannot be described using interface width or wavelength parameters only. It is much more convenient to use the roughness exponent  $\alpha$  provided in Sec. 3.3.1, which can be extracted for instance from a height-height correlation function (3.13). The smaller  $\alpha$ , the rougher the surface becomes locally [172].

Fig. 3.23 shows height-height correlation of the morphologies presented in Fig. 3.22 at the energies  $E_0 = 50$  eV and  $E_0 = 300$  eV. At the very low energies the influence of sputtering on the statistical characteristic of the system tends to be almost negligible. The interface widths are almost identical ( $G(x)$  saturates to almost the same values) and  $\alpha$  equal 0.89 and 0.91 for the simulations with and without sputtering respectively. However, if the energy is higher the difference in the correlation functions becomes significant. If the sputtering is excluded the roughness exponent ( $\alpha=0.87$ ) at  $E_0 = 300$  eV

does not vary a lot, being only slightly smaller than at  $E_0 = 50$  eV. Though, if the sputtering is active, the roughness exponent drops to the value of 0.47. It suggests that ion induced surface erosion is responsible for lowering the roughness exponent, which is proportional to the total sputtering yield. The value of sputtering yield registered at the latest simulation time for wavy surface at the energy 50 eV was  $Y_s = 0.098$ , whereas at 300 eV,  $Y_s = 1.36$ . Exclusion of sputtering clearly preserves the ripple formation, which are rather induced by the bulk defects approaching the surface with the different rate depending on the local topography, i.e. defect relaxation. The driving force of the pattern formation and  $\theta = 70^\circ$  will be study in Sec. 3.4 in more details.

Increase of the ion energy increases also the total erosion rate, therefore already at the energy of 300 eV, the ripples vanish due to relatively high ion flux used for the simulation. Moreover, ripples oriented parallel to incoming at the grazing incidence are suppressed if no sputtering is included. In general, surface erosion is close to zero at  $85^\circ$  due to very large number of reflected atoms. However, only the projectiles, which are not reflected, cause bulk damage, as well as sputtering. TRIM simulation shows that only 1.6 %  $\text{Ar}^+$  ions arrive at the target and create the collision cascade in Si. Counting only non-reflected ions for the sputtering yield calculation provides a value of 23.6 sputtered atoms per collision cascade.

The significant difference of surface topographies, with and without sputtering, points out the very important role of the surface erosion. The studies provided in this section prove that sputtering is not the dominant driving force inducing self-organization of ripples at the incidence angles  $\sim 60^\circ$  and suggest that defect relaxation can have a strong influence on the pattern formation. On the other hand at the grazing incidence the sputtering yield by non-reflected ions is the largest. Therefore, the ripples oriented parallel to the incoming ions are formed mainly due to the sputtering.

### Spatial evolution

Surface topography evolution over fluence is again represented by power law dependence of interface width  $w$  and wavelength  $l$ . The influence of simulation flux  $j_{sim}$ , incidence angle  $\theta$  and ion energy  $E_0$  is analyzed this time for the simulations with ray tracing of ions (see Figs. 3.24, 3.25 and 3.26) regarding the two cases:

- Full collision cascade with sputtering (**solid** curves)
- Collision cascade, where the sputtering has been ‘artificially’ suppressed, as described in Sec. 3.3.2 (**dotted** curves)

For different simulation fluxes  $j_{norm}$ , the evolution of  $w$  differs significantly (see Fig. 3.24). Initially, where no correlation of surface structures is expected,  $w$  is proportional to the ion flux. At the low irradiation fluences, the collision cascade does not induce any self-organization, acting as a random noise that roughens the surface. Therefore, increasing  $j_{norm}$  at low fluences, the relaxation time of the collision cascade will be lower and the interface width will be higher. Around  $\phi = 3 \times 10^{15}$   $\text{cm}^{-2}$  a threshold point in the evolution of  $w$  is observed (see Fig. 3.24). From now on, the ripple formation becomes more pronounced and the periodic behavior triggers  $w$  increase. Moreover, the roughness exponents<sup>4</sup> are getting larger at lower fluxes starting from  $\alpha = 0.72$  at  $j_{norm} = 2^{-17}$  to  $\alpha = 0.84$  at  $j_{norm} = 2^{-20}$ . Thus, if the flux is low enough the patterns

---

<sup>4</sup>All the roughness exponents has been obtained at  $\phi = 10^{17}$   $\text{cm}^{-2}$  using the formula 3.13

become well-ordered and local height fluctuations are reduced. The well-ordered pattern formation can grow faster, because the surface noise induced by ion damage is lowered. Obtained growth exponents  $\beta = 0.38$  at  $\theta = 67^\circ$  and  $\beta = 0.31$  at  $\theta = 60^\circ$  suggest faster growth at larger incidence angles (see also Fig. 3.25). Additionally, if the sputtering effects are disregarded, the total interface width is higher within the whole range of the fluence, however  $\beta$  exponent does not differ. It can be explained using Fig. 3.22, where the images showing the simulations excluding sputtering provide much more regular pattern, which can form faster than the simulations with included sputtering, therefore also the values of  $w$  are higher, whereas the growth exponent is the same.

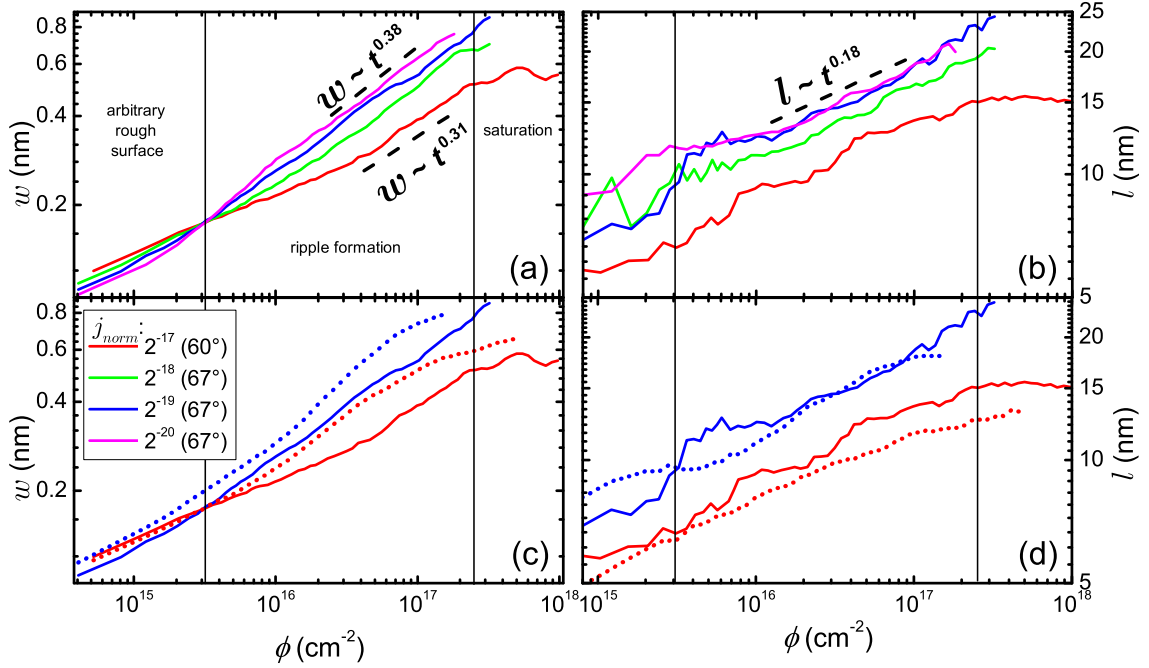


Figure 3.24.: Log-log plots of interface width  $w$  (left) and ripple wavelength  $l$  (right) evolution at different fluxes  $j_{norm}$  and ion incidence angles  $\theta$  (labeled in the legend),  $E_0 = 250$  eV. Plots (a) and (b) consider sputtering during the simulations, whereas (c) and (d) are selected comparisons with simulations, where the sputtering was suppressed (dotted curves). The dashed lines are the exponential fitting functions, where the growth exponent is between  $\beta = 0.31$  and  $\beta = 0.38$ . The coarsening exponent of wavelength increase is  $n = 0.18$ . Three different fluence ranges have been indicated: initial - arbitrary rough surface, middle - evolution of pattern formation, and final - saturation.

The evolution wavelength (see right side of Fig. 3.24) suggests power law dependence of coarsening with the same exponent  $n = 0.18$  for every  $j_{norm}$ . The magnitude of wavelength is inverse proportional to the  $j_{norm}$  within the whole range of fluence and at the  $j_{norm} = 2^{-19}$ ,  $l$  rise up to 25 nm. If the sputtering is excluded values of  $l$  are lower at the corresponding time points, however the coarsening exponent  $n = 0.18$  is preserved.

The evolutions of  $w$  and  $l$  at different incidence angles are shown in Fig. 3.25. Each curve represents evolution of a single simulation until about  $10^8$  ion impacts. Slopes of the interface width as well as the saturation point of the curves tend to rise if the incidence angle increases. This is also the case for the wavelength growth, where  $n$  exponent oscillates between 0.08 and 0.18, proportional to  $\theta$ . Suppression of the sputtering results in increase of  $w$  and decrease of  $l$  for the corresponding simulations. Evolution of the wavelength at  $\theta = 70^\circ$  is in agreement with the experiments [99,122], where the typical



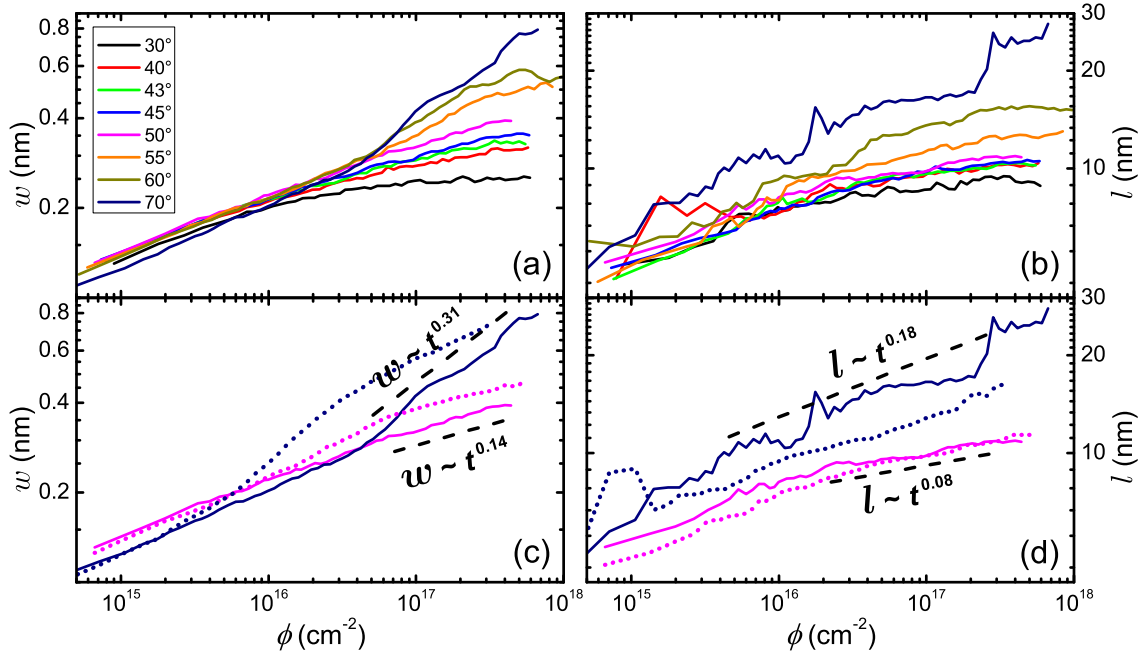


Figure 3.25.: Log-log plots of interface width  $w$  (left) and ripple wavelength  $l$  (right) evolution at the same flux  $j_{norm} = 2^{-18}$  and the ion energy  $E_0 = 250$  eV, but different incidence angles  $\theta$ :  $30^\circ$ ,  $40^\circ$ ,  $43^\circ$ ,  $45^\circ$ ,  $50^\circ$ ,  $55^\circ$ ,  $60^\circ$  and  $70^\circ$ , starting from the bottom solid lines. Plots (a) and (b) consider sputtering during the simulations, whereas (c) and (d) are selected comparisons with simulations, where the sputtering was suppressed (dotted curves). The dashed lines are the exponential fitting functions. The growth exponent is between  $\beta = 0.14$  and  $\beta = 0.38$ . The coarsening exponent of wavelength ranges from  $n = 0.08$  to  $n = 0.18$ .

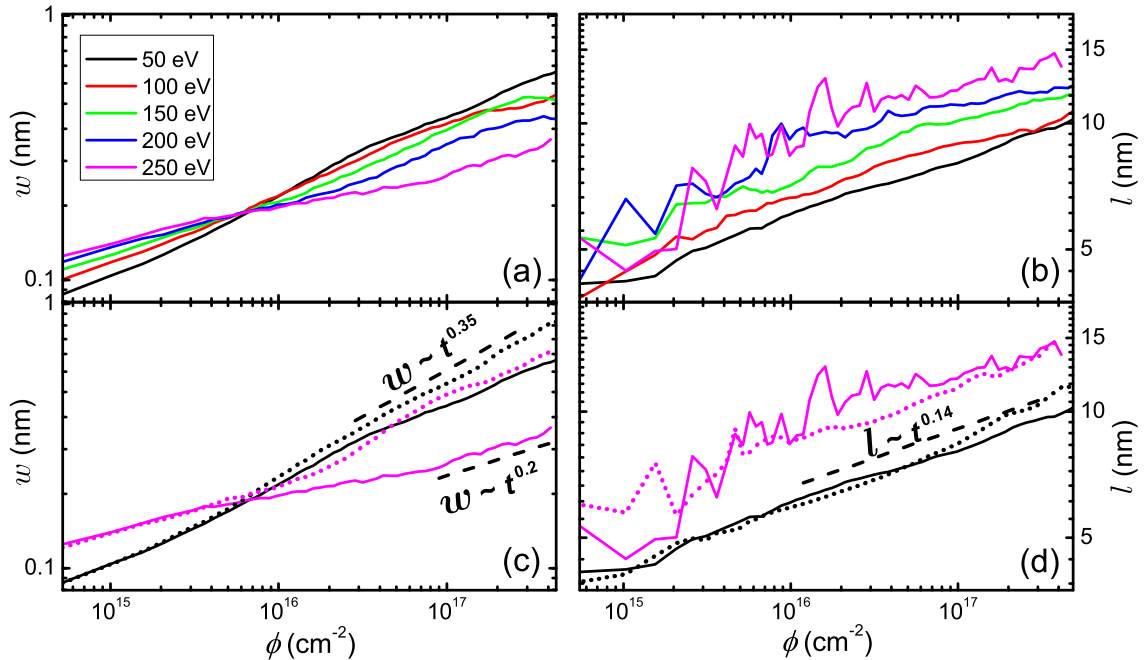


Figure 3.26.: Log-log plots of interface width  $w$  (left) and ripple wavelength  $l$  (right) evolution at the same flux  $j_{norm} = 2^{-16}$  and incidence angle  $\theta = 60^\circ$ , but different ion energies  $E_0$ : 50, 100, 150, 200 and 250 eV. Plots (a) and (b) consider sputtering during the simulations, whereas (c) and (d) are selected comparisons with simulations, where the sputtering was suppressed (dotted curves). The dashed line is the exponential fitting function, where the growth exponent is between  $\beta = 0.29$  and  $\beta = 0.35$ . The coarsening exponent of wavelength increase ranges from  $n = 0.14$  to  $n = 0.18$ .

range of  $l$  is from 20 to 30 nm.

Finally, the evolution of  $w$  and  $l$  is given at different ion incidence energies in Fig. 3.26. The results suggest correlation between the growth exponent and the ion energy, i.e.  $\beta$  decreases with increasing  $E_0$  from 0.35 at 50 eV to 0.29 at 250 eV simulated for a rather high flux of  $j_{norm} = 2^{-16}$ . If the sputtering is suppressed,  $\beta$  is energy independent. The power law exponent  $n$  fit to wavelength tends to be proportional to the ion energy with the values between 0.14 and 0.18 at the energies between 50 and 250 eV respectively.

The investigation of  $w$  and  $l$  evolution during ion beam irradiation of Si targets suggests a rather complex pattern formation and dynamics, also seen in experiments of IBS with  $\text{Ar}^+$ . The major conclusions are the ripple appearance above  $50^\circ$  incidence angle in the parallel mode and its rotation into ion beam direction at  $80^\circ$  also detected by Madi *et al.* [147], Macko *et al.* [171] and the others. Both the interface width and the wavelength evolution obey a power law dependence on fluence. Coarsening is present for every type of input parameters and its exponent tends to be rather independent on all simulation parameters, except the ion energy. The value of growth exponent  $\beta$  is not correlated with simulation flux, however it is strongly sensitive on the incidence angle and the ion energy, being proportional and inverse proportional, respectively. Suppression of sputtering does not significantly change formation of ripples (wavelength is almost exactly the same) except for higher energies, as shown in Fig. 3.26, where two different values of  $\beta$  can be obtained at the same ion energy 250 eV. To be able to understand better the reason of the differences in the simulations with and without sputtering, more detailed, atomistic investigation of surface kinetics is necessary. One possibility of the problem treatment will be presented in the next section.

### 3.4 Surface mass currents

The variety of ballistic and kinetic processes active during IBS, presented in Fig. 3.1, determine surface evolution by so-called **surface mass current**  $\vec{j}$ . It has been already shown in Sec. 3.2 that a single ion impact leads to the formation of a crater in the neighborhood of the impact point, which can result in an increase of the local curvature of a flat surface. It is possible to determine the mass current vectors, by the asymmetry of the crater due to ion impact under oblique local incidence angle, as has been shown in Figs. 1.3 and 3.5. Depending on the direction of mass current vectors on the surface, final surface will be modified by an increase or a decrease of its width. Atomistic computer simulation provides the unique opportunity to determine the local mass currents by registration of all atomic jumps. The surface mass current as an irradiation-driven downhill current has been already studied using MD simulation by Moseler *et al.* [13], at close to normal incidence angles. To extract a lateral surface mass current they calculate the lateral atomic displacement

$$\delta = \left\langle \sum_{I=1}^N d^{(I)} \right\rangle, \quad (3.17)$$

averaged between  $N$  numbers of displaced atoms during the impact. The  $d^{(I)}$  is a distance of a displacement projected on the surface plane. Now, the correction of  $\delta$  by the average flux  $r$  (number of atoms per unit area per unit time) gives the strength of the lateral current  $|\vec{j}| = r\delta$ . In case of higher values of incidence angle  $\theta$  Süle *et al.* [15] published MD studies with stability analysis of the mean height deviation from an initial

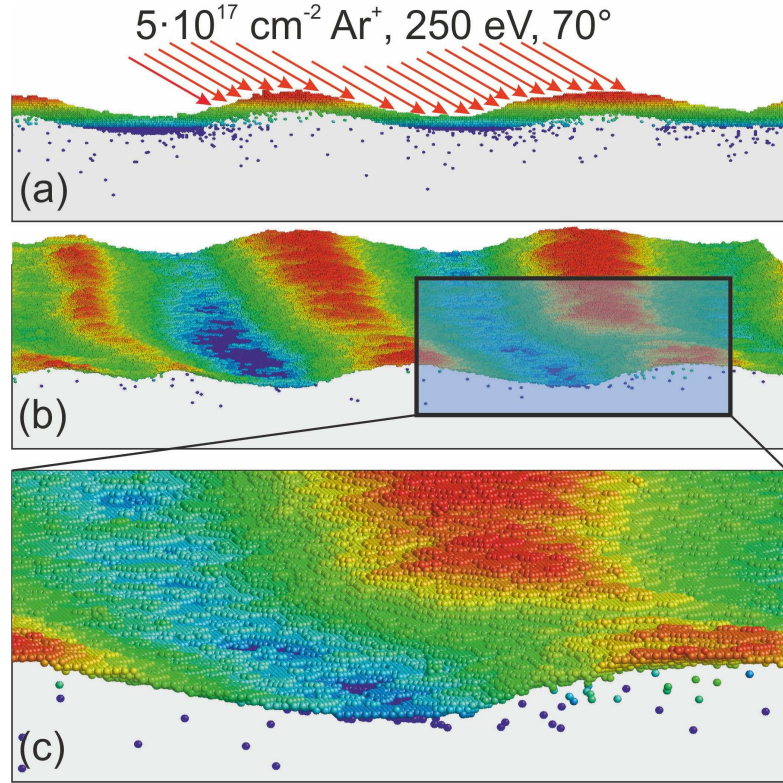


Figure 3.27: TRIDER simulation of (100) Si irradiation with  $5 \times 10^{17} \text{ cm}^{-2} \text{ Ar}^+$  of 250 eV  $70^\circ$  incidence angle. In order to see atomistic details, only the surface atoms and vacancies are plotted, fully coordinated atoms are made transparent: (a) side view in  $\langle 010 \rangle$  direction; bulk vacancies are seen at the leeward side of the ripples, (b) perspective view of (a), (c) zoomed part. Atoms are colored according to their height.

sinusoidal surface profile. According to their results the ripple formation is developed for wavelengths  $l < 35 \text{ nm}$ , whereas the stable structure, where the wavelength does not increase any more is expected if  $l > 35 \text{ nm}$ . A direct link between atomistic simulation and continuum theory was proposed by Norris *et al.* [17], where a possible way to apply MD calculations of a crater functions into the continuum equation was proposed. The conversion from the crater function  $g$  to the local change of surface height  $\partial h / \partial t$ , used in continuum models, has been done by means of effective moments of  $g$ . The crater function can be divided into two parts: (i) originating from surface erosion and (ii) redistribution. Projected positions of atoms were provided by the MD simulation. The disadvantage of the MD simulation is the limited number of ion impacts that are used to average of the localized surface movement.

Here, using TRIDER simulation, the evolution of the system can be calculated in order to describe creation of local defects, mass transport, ripple growth, ion impact rate, etc. An example of a ripple profile is shown in Fig. 3.27 to emphasize capabilities of the atomistic approach. Here, vacancies accumulate with regard of the ion wind at the leeward side of the patterns, which may suggest that also the surface erosion will be higher at this region. All MD approaches described in the last paragraph represent the link between atomistic simulations and the continuum description. The variety of parameters extracted from the simulation (e.g. sputtering yield, defect concentration, local flux, etc.) often depend directly on the local surface curvature  $\kappa$ . If  $\kappa$  can be derived from the atomistic simulation, the direct comparison with continuum equations of pattern propagation will be possible. For example the Kuramoto-Sivashinsky equation [173,174] with an additional damping term  $d_0$ , which stabilizes the pattern and prevents kinetic roughening [175].

$$\frac{\partial h}{\partial t} = -v_0 - d_0(h - \langle h \rangle) + \nu_x \frac{\partial h}{\partial x} + \gamma_2 \nabla^2 h + \xi_2 (\nabla h)^2 - K \nabla^4 h + \eta \quad (3.18)$$

Here,  $v_0$  is erosion velocity of a planar surface,  $\nu_x$  induces a lateral movement of the structures, the roughening surface tension coefficient  $\gamma_2$  is negative, the nonlinear term  $\xi_2$  defines the tilt dependent erosion rate and  $K$  is the positive surface diffusion coefficient. The Gaussian noise term  $\eta$  roughens the surface. Both  $h(\mathbf{x}, t)$  and  $\eta(\mathbf{x}, t)$  vary in space and time.

In order to be able to understand intrinsic physical processes of the interface region with or without ion irradiation, in the next sections major terms of the continuum equation describing the surface evolution are discussed.

### 3.4.1. Gibbs-Thomson relation

According to Lord Kelvin, formerly William Thomson, the saturated vapor pressure  $p$  and, as the consequence, also the surface tension  $\gamma_2$  is proportional to the surface curvature ( $\kappa = 1/R$ ). Thus, structures with convex surface will have higher vapor pressure than those of the concave shape (negative radius). This statement has been mathematically described in the so-called Gibbs-Thomson relation (also called Kelvin equation) [176, 177] for spherical particles with the radius  $R$ ,

$$\frac{p(R)}{p_0} = \exp\left(\frac{R_c}{R}\right) \quad (3.19)$$

where  $p_0$  is the vapor pressure at a flat ( $R \rightarrow \infty$ ) surface and  $R_c$  is the capillary length

$$R_c = \frac{\gamma_2 \Omega}{k_B T}. \quad (3.20)$$

Here  $\Omega$  is the atomic volume and  $T$  is the absolute temperature. Replacing the vapor pressure by the impurity concentration or the solubility over the flat surface  $c_0$  of the spherical particle  $c(\kappa)$  one can write more general form, valid for arbitrarily curved interfaces

$$\ln \frac{c(\kappa)}{c_0} = \frac{2\gamma_2 \Omega}{k_B T} \kappa, \quad \text{with } \kappa = \frac{\kappa_1 + \kappa_2}{2}, \quad (3.21)$$

where the mean local curvature of the surface  $\kappa$  is the sum of principal curvatures  $\kappa_1$  and  $\kappa_2$ . For the spheres  $\kappa_1 = \kappa_2$ , and therefore  $\kappa = R^{-1}$ . Now, if the average surrounding concentration is higher than the solubility of the curved surface ( $\langle c \rangle > c(\kappa)$ ), the surrounding atoms will condensate at the surface, the surface will grow. For the opposite case  $\langle c \rangle < c(\kappa)$ , the surface will lose particles, evaporate.

For the large radius  $R \gg R_c$ , Eq. (3.21) can be simplified to the first order Taylor expansion to

$$c(R) \approx c_0 \left(1 + \frac{R_c}{R}\right). \quad (3.22)$$

Finally, the equilibrium solubility will obey Arrhenius law, which has for an Ising system the simple form

$$c_0^{\text{fcc}}(\epsilon) = 4 \exp(-6\epsilon), \quad (3.23)$$

valid for fcc structures with normalized bond energy  $\epsilon = \varepsilon/k_B T$ , which is the relation between concentration and the temperature for a binary system in the equilibrium state [81].

A detailed derivation of the Gibbs-Thomson equation can be found for instance in Ref. [178]. Moreover, the comparison of the kinetic theory with the atomistic modeling application of lattice KMC simulation was proposed in Refs. [2, 94].

### 3.4.2. Mullins-Herring diffusion of surface

Surface diffusion can be understood in terms of local changes of the surface height  $h$ . If the total number of particles is conserved during the diffusion process, this local change is the result of mass currents at the surface and can be represented by the continuum equation

$$\frac{\partial h(\vec{x}, t)}{\partial t} = -\nabla \vec{j}(\vec{x}, t), \quad (3.24)$$

which is the equivalent of the 2nd Fick's law (Eq. (2.28)).

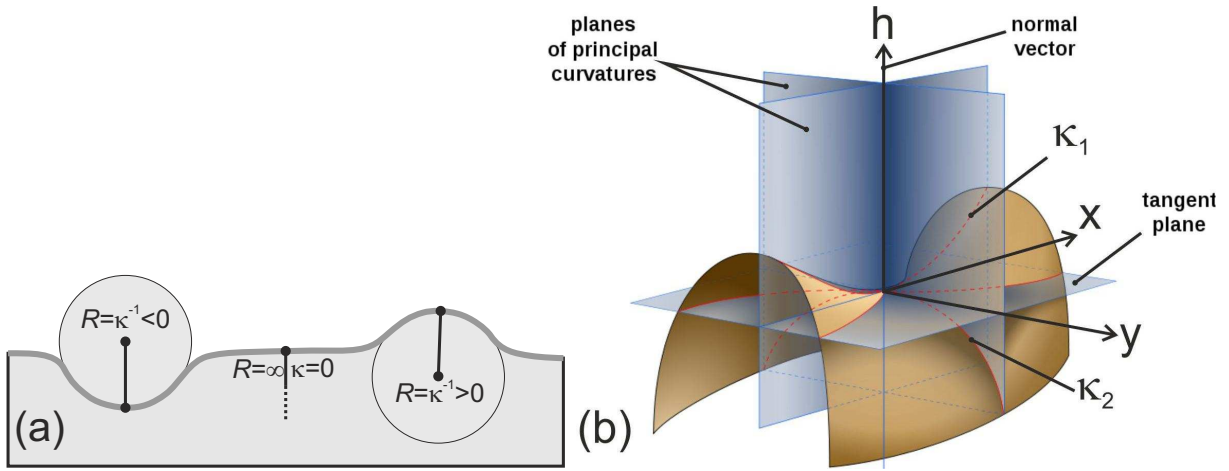


Figure 3.28.: Representation of the surface curvature  $\kappa$  at the 1 + 1 dimensional boundary (a), and at the 2 + 1 dimensional phase boundary (surface) (b). The image in (b) is taken from WIKIPEDIA [179]

The Gibbs-Thomson relation (3.21) provides the dependence of the concentration  $c(\kappa)$  on the local curvature  $\kappa(x)$

$$c(\kappa) = c_0 \exp \left\{ \frac{2\gamma_2\Omega}{k_B T} \kappa(x) \right\} \approx c_0 \left\{ 1 + \frac{2\gamma_2\Omega}{k_B T} \kappa(x) \right\}. \quad (3.25)$$

The curvature of a one-dimensional function, i.e the surface with one dimension coordinate  $x$  and one height coordinate  $h$ , is defined by

$$\kappa_{1d} = \frac{-h''}{\{1 + h'^2\}^{3/2}}, \quad (3.26)$$

where  $h'$  and  $h''$  are the 1st and the 2nd derivative of  $h$ , respectively. In Fig. 3.28a  $\kappa$  can be obtained for any point of the surface. If  $\kappa < 0$  the surface is convex for  $\kappa > 0$  the surface is concave. For flat surfaces  $\kappa = 0$ , since the radius  $R = \infty$ .

Assuming that the curvature of a two-dimensional function (height  $h$  over  $x$ - $y$ -plane), given in Fig. 3.28b, is represented by two orthogonal cut planes along the principle

direction<sup>5</sup>, according to the equation

$$\begin{aligned}\kappa_{2d} &= -\frac{1}{2}\nabla\left(\frac{\nabla h}{\sqrt{1+(\nabla h)^2}}\right) = \\ &= -\frac{(1+(\partial_x h)^2)\partial_{yy}h - 2\partial_x h\partial_y h\partial_{xy}h + (1+(\partial_y h)^2)\partial_{xx}h}{2(1+(\partial_x h)^2 + (\partial_y h)^2)^{3/2}},\end{aligned}\quad (3.27)$$

the value of  $\kappa$  at any point of the surface will be the average curvature of orthogonal, equally spaced normal cut planes. Using the small slope approximation (i.e.  $|\nabla h| \ll 1$  and therefore  $|\partial_x h| \ll 1$  and  $|\partial_y h| \ll 1$ ) on Eq. (3.27) results in

$$\kappa_{2d} \approx -\frac{1}{2}\nabla^2 h = -\frac{1}{2}(\partial_{xx}h + \partial_{yy}h), \quad (3.28)$$

and from Eq. (3.25) in

$$c(\mathbf{x}, t) \approx c_0 \left\{ 1 - \frac{\gamma_2 \Omega}{k_B T} \nabla^2 h(\mathbf{x}, t) \right\}. \quad (3.29)$$

Now from the 1st Fick's law (Eq. (2.29)) and Eqs. (3.24), (3.29) the general form of surface diffusion equation of MH is given by

$$\frac{\partial h(\mathbf{x}, t)}{\partial t} = D\nabla^2 c(\mathbf{x}, t) = -\frac{Dc_0\gamma_2\Omega}{k_B T}\nabla^4 h(\mathbf{x}, t), \quad (3.30)$$

where  $D$  is the surface diffusion coefficient. More detailed approach deriving MH equation can be found directly in Refs. [142, 149], where analytical solutions for specified initial conditions are presented.

To find the transition between atomistic view of the KMC simulation and continuum surface diffusion of MH very specialized methods of data interpretation is necessary.

Fig. 3.29 shows the initial simulation cell used, a pre-patterned structure with a sinus type of a ripple of a wavelength  $l$  and an amplitude  $a$ . Such a pattern is usually obtained out of the IBS experiments (i.e.  $l = 24$  nm,  $a = 3.1$  nm). Independently on the simulation conditions, four types of atomic movements have been always registered and described by the jump rates  $\nu$  with different orientations and locations. Here, " $l/r$ " gives the left and the right jump direction, with respect to the  $x$ -axis into decreasing and increasing values of the  $x$ -axis, respectively. " $i/o$ " denotes input into or out of the indicated atomic line. The relation between the jump rates, the surface current  $\vec{j}$ , looks as follows

$$\begin{aligned}\vec{j} &= (j_x, j_y, j_h)^T \\ j_q &= \frac{V_m}{c_y} \{ (\nu_q^{r,i} + \nu_q^{r,o}) - (\nu_q^{l,i} + \nu_q^{l,o}) \}, \quad (q = h, x, y)\end{aligned}\quad (3.31)$$

and the height evolution  $\partial_t h = -\nabla \cdot \vec{j}$  is given, according to the definition by a divergence  $\nabla$  of a vector field  $\vec{j}$ , i.e. a sum of partial derivatives of  $x$ ,  $y$  and  $z$  coordinates of  $\vec{j}$ :

$$-\nabla \cdot \vec{j} = -\partial_x j_x - \partial_y j_y - \partial_h j_h = \frac{V_m}{c_y} \sum_{q=x,y,h} \{ (\nu_q^{r,i} + \nu_q^{l,i}) - (\nu_q^{r,o} + \nu_q^{l,o}) \}, \quad (3.32)$$

<sup>5</sup>In Fig. 3.28b the minimal curvature is expected along the  $x$  axis, whereas the maximal along the  $y$  axis.

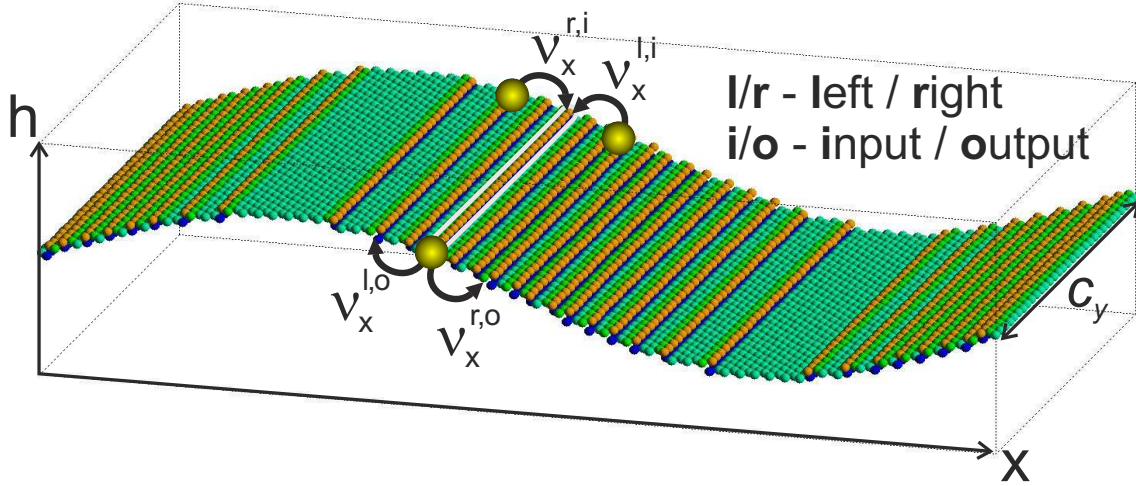


Figure 3.29.: Initial configuration of the simulation cell in the Si target during investigation of the surface current is a sinus function along the  $x$  axis of the 24 nm wavelength and 3.1 nm amplitude. Different colors represent different NN occupation numbers of the surface atoms. Three selected atoms are the candidates for a jump with different jump rates:  $\nu_i^r$ ,  $\nu_i^l$ ,  $\nu_f^r$  and  $\nu_f^l$ , are connected with the region marked with the white line, where the mass balance is analyzed.

where  $V_m$  is the molar volume of an atom and  $c_y$  is the system size in the  $y$  direction. To obtain the full vector  $\vec{j}$  of coordinates  $(x, y, h)$  it is necessary to integrate the atomic rates along every possible axis, therefore, except  $\nu_x$ , also  $\nu_h$  and  $\nu_y$  are locally calculated, as shown above. However, due to the symmetry reasons  $\nu_y$  is always equal to 0 and only  $\nu_h$  is evaluated additionally.

The surface mass currents of Eqs. (3.31) for a KMC simulation of a sinusoidal surface (without ion irradiation) are plotted in Fig. 3.30. According to the MH diffusion theory the surface height changes with respect to the current vectors along the surface boundary. The result of the simulation is in full agreement with the theory of MH diffusion. The red arrows in Fig. 3.30a are oriented parallel to the surface in the direction pointing down to the valleys that results in the mass transport into the region of a concave phase boundary with energetically favorable states. Investigation of the  $j_x$  component shows the maximum of the surface current at regions with the maximum slope according to the equation derived using (2.29) and (3.29)

$$\vec{j} = -\frac{Dc_0\gamma_2\Omega}{k_B T} \nabla^3 h(\mathbf{x}, t). \quad (3.33)$$

Because of  $h \sim \sin x$  used as the initial condition of the surface, the result  $j \sim \nabla^3 h$  leads to  $\vec{j} \sim -\cos x$ . Similarly in Fig. 3.30b  $\nabla \vec{j} \sim -\nabla^4 h$  therefore, the plotted curve is realized by  $\nabla \vec{j} \sim \sin x$ . These results agree with predictions of MH diffusion theory. The surface height evolution  $\nabla \vec{j}$  is the result of the driving force, which is maximal at the minimal slope values of  $h$ . This driving force leads to the smoothing behavior due to surface diffusion.

The normalized temperature  $1/\epsilon = k_B T/\varepsilon$  varies from  $\epsilon = 2.0$  to  $\epsilon = 1.0$ . Obviously, for high temperatures the movement at the surface is the highest and the amplitude of  $\nabla \vec{j}$  function increases that is in accordance with Eqs. (3.30) and (3.33). At lower temperatures, i.e.  $\epsilon = 2.0$  and  $\epsilon = 1.8$ , both functions  $j_x$  and  $\nabla \vec{j}$  show small discrepancy from sinusoidal shape, prominent for large slopes of the surface. This effect is caused by the

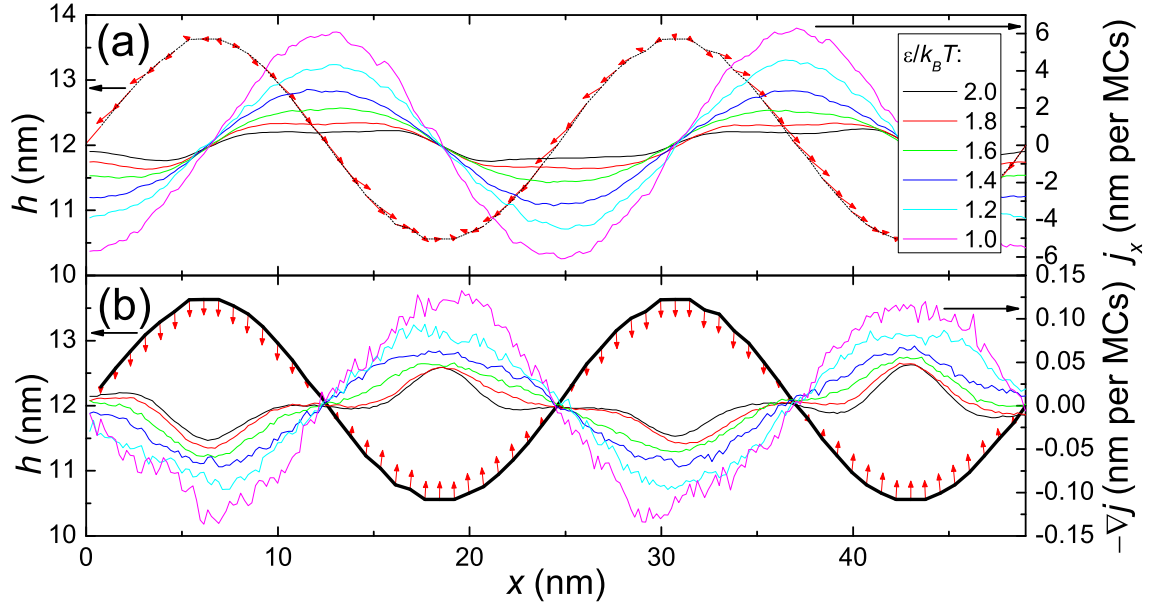


Figure 3.30.: Simulated plots of  $\vec{j}$  (a) and  $-\nabla\vec{j}$  (b), with respect to the  $x$  component of  $h$ . Calculation has been averaged out of  $10^6$  independent KMC runs **without including ion bombardment**. The arrows at the surface boundary (black line) correspond to the current vectors in (a) and direction of the height change in (b). Thin colored lines are the  $x$  component of  $\vec{j}$  and  $-\nabla\vec{j}$  in (a) and (b),s respectively. Different colors denote simulation temperatures, for  $\epsilon = 1.0, 1.2, 1.4, 1.6, 1.8$  and  $2.0$ .

Ehrlich-Schwöbel effect [137,138], which slows down the surface kinetics at surface edges, and is especially significant at low temperatures. The competition between the surface relaxation and the Ehrlich-Schwöbel effect was studied in the framework of continuum theory [180].

The data presented in this section is a direct comparison of the computer experiment with the continuum theory of MH diffusion. The mass currents obtained with TRIDER simulations can decide about the important terms in continuum equations, as will be considered in the next section.

### 3.4.3. Surface mass currents under irradiation and diffusion

The external driving force ‘ion irradiation’ modifies surface mass currents of the former section, i.e. pure MH diffusion, which can be the main reason for self-organization. This driving force has been observed in the ion induced phase transition [86,181], segregation [89], Ostwald ripening [2,94], ripple propagation by IBS [31,145,157], etc.

In this work, ion beam irradiation is an external driving force understood as the ballistic displacement of atoms and as removal of atoms due to sputtering, which is described appropriate by TRIDER. Defect relaxation processes are acting sequentially. In the framework of the continuum equation (3.18) (damped KS), the  $K\nabla^4 h$  term is the MH diffusion that has been studies in detail in the previous section. However, in addition to that, the origin of the linear  $\nabla^2 h$  and nonlinear term  $(\nabla h)^2$  is not yet clearly revealed in a unique manner. The presented method of data evaluation of KMC simulations performed by the extraction of  $\vec{j}$  and  $-\nabla\vec{j}$  (3.31), provides a possibility of a direct comparison between atomistic computer simulations and continuum theories. Eventually it allows even the computation of the unknown parameters (e.g. in the



equation (3.18)). The results presented in this section are preliminary, and give only an outlook for further studies. More detailed investigations have been started at the Helmholtz-Zentrum Dresden-Rossendorf in the framework of a new project founded by the Deutsche Forschungsgemeinschaft (DFG).

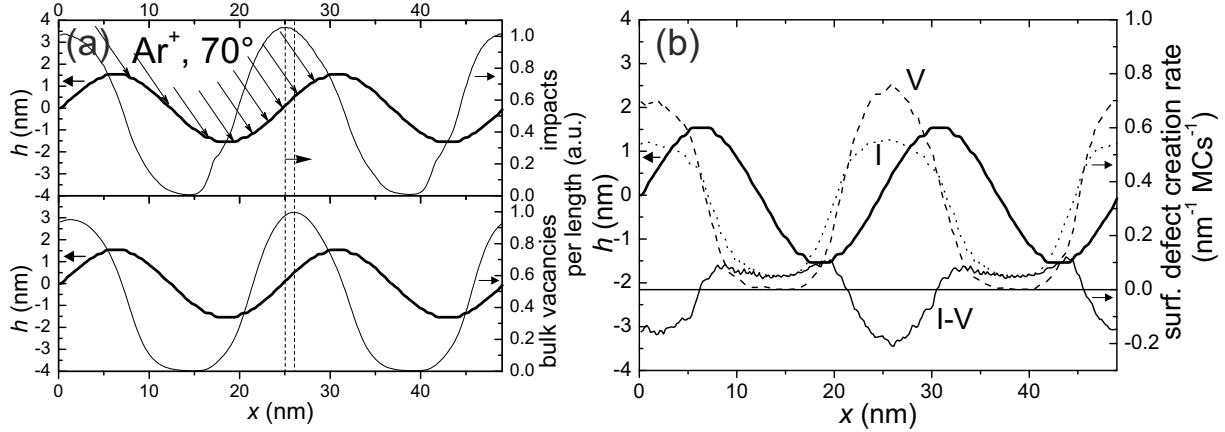


Figure 3.31.: Plots of defects on rippled surface ( $250 \text{ eV Ar}^+$ ,  $70^\circ$  ion incidence). In (a), the thin line denotes real ion flux due to surface undulation (upper plot), and the steady-state bulk vacancy density projected on the  $x$ -coordinate (lower plot). The orientation of the ion beam is given by arrows that end at the surface curve (thick line). In (b), recombination rates of interstitials (I - dotted line) and vacancies (V - dashed line) are plotted for simulation flux  $j_{sim} = 2^{-18}$ , which are the ad-atoms and surface vacancy generation rates, as well as their difference (I-V - solid line).

At first, it is important to understand the defect kinetics on surfaces under irradiation with ions that create surface pattern, i.e. the ion energy and the incidence angle have to be defined properly, as described in Sec. 3.3. Here,  $250 \text{ eV Ar}^+$  ions at  $\theta = 70^\circ$  were used, which results in the steady-state pattern of the wavelength  $24 \text{ nm}$  and the amplitude  $3.1 \text{ nm}$ . Fig. 3.31 shows the density of ion impacts and resulting vacancies over the rippled Si surface. Both, the ion impact and the vacancy densities are clearly correlated. However, the distribution of vacancies is shifted along the projection of the ion incident direction as it is indicated by dashed, vertical lines. Due to the oblique angle of ion incidence, there are almost no V's at the leeward side of the 'ion wind' on the ripples and the maximum V density is localized at the windward side (see also Fig. 3.27). The arrows in Fig. 3.31a show the real orientation of incoming ions preserving the aspect ratio between  $x$  and  $h$  axis. It confirms that no complete shadowing is present, although a pronounced reflection of ions at the leeward side is expected. The surface defect generation rate, which originates from recombination of bulk defects per MCs at the surface<sup>6</sup> is given in Fig. 3.31b. There are more surface defects created by surface recombination of bulk defects than surface defects formed directly by the collision cascade. I and V generation rate at the surface follow the same trend with respect to the surface morphology like bulk I and V. However, in an ion impact region the number of vacancies that recombine at the surface after the impact at the windward side on the ripples is larger than the number of interstitials. On the other hand, at the leeward side on the ripples recombine more interstitials. This difference is due to the I/V separation discussed in Sec. 3.2.1, i.e. the

<sup>6</sup>Vacancies (V) recombine with the with the surface forming surface vacancies, whereas interstitials (I) become ad-atoms.

ion impact crater formation. The vacancy excess is located closer to the windward side of the ripples surface than the interstitial excess, which is located closer to the leeward side of the ripples. The remaining bulk defects need less time for diffusion towards the windward for V and leeward side for I of the ripples, respectively.

The surface mass current investigation has been performed at two different ion incidence angles  $\theta = 0^\circ$  and  $\theta = 70^\circ$ . Based on the results obtained with TRIDER simulation (see Fig. 3.32), and their comparison with pure MH surface diffusion simulated with KMC (see Fig. 3.30), three important statements are provided:

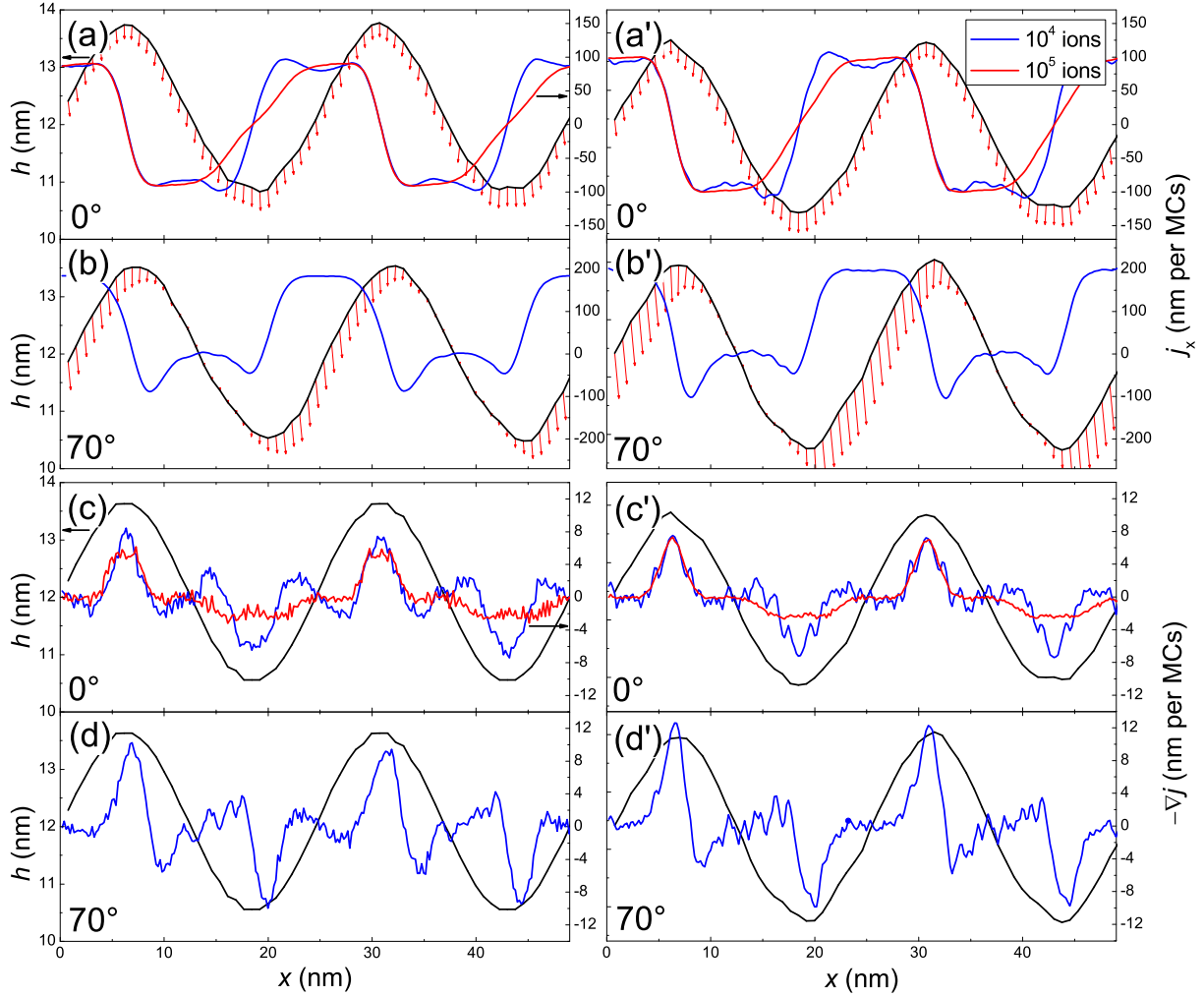


Figure 3.32.: Simulated plots of  $\vec{j}$  (a) and  $-\nabla\vec{j}$  (b). Calculation has been averaged over  $10^6$  independent KMC runs **including ion bombardment and sputtering** (left column). The red arrows mounted at the surface boundary (black line) correspond to the current vectors in (a),(b). Colored lines are  $j_x$  and  $-\nabla\vec{j}$  in (a), (b) and (c), (d) respectively. Figures (a) and (c) correspond to  $\theta = 0^\circ$ , (b) and (d) refer to irradiation at  $\theta = 70^\circ$ , both for 250 eV. Different colors denote different number of impacts: blue  $10^4$  ions and red  $10^5$  ions. The normalized simulation temperature was  $\epsilon = 1.7$ . Corresponding calculations **including ion bombardment and suppressing sputtering** are given in the right column, marked by (a'), (b'), (c') and (d').

- (i) For the pure MH diffusion case the **down-hill** surface mass current  $j_x$  was found (see Fig. 3.30a). If the surface is irradiated with ions the mass current *switches*

to an **up-hill** mode, i.e. the surface undulation growth, even under normal ion incidence (see Fig. 3.32a).

- (ii) The difference compared to the pure diffusional case, i.e. the MH diffusion of Fig. 3.30, is that values of  $j_x$  and  $-\nabla \vec{j}$  are about 2 orders of magnitude larger in Fig. 3.32. This is mainly due to the strongly enhanced surface defect density caused by ion impacts compared to the only thermally excited defects.
- (iii) The comparison of the plots in Fig. 3.32a,c indicates that both the surface current and its divergence are not constant during the simulation (blue and red curves). After  $10^5$  impacts (red curve) the asymmetry in  $j_x$  curves appears in the ripple values, which may be the reason for smoothing after longer ion irradiation.

The normal incidence ion bombardment completely changes the dynamics in comparison to the MH diffusion simulation (Fig. 3.32 vs. Fig. 3.30). Surface current vectors  $\vec{j}$  indicated with the red arrows in Fig. 3.32 are oriented always downward what confirms the mass transport from the hills to the valleys (see Fig. 3.32a). Compared to Fig. 3.30b, the function  $-\nabla \vec{j}$  shows an opposite behavior (see Fig. 3.32c). It results in the initial increase of the amplitude of the pattern, because  $-\nabla \vec{j}$  is proportional to the surface height. Longer irradiation suppresses the mass transport in the valleys creating an additional asymmetry, which finally might smoothen the surface, as expected.

At the oblique incidence angle ( $\theta = 70^\circ$ ) values of  $\vec{j}$  are almost zero at the leeward side of ripples as a consequence of the impact distribution from Fig. 3.31a. Due to a strong anisotropy in a mass balance caused by a much larger ad-atoms creation at the windward ripple side, the orientation of current vectors are tilted towards the orientation of the ion beam. The mass current  $\vec{j}$  is the highest at the highest impact density region (see Fig. 3.32b). It suggests the existence of the ripple movement along the ion beam direction. The divergence of  $\vec{j}$ , which describes the height change in time  $-\nabla \vec{j}$ , given in Fig. 3.32d, is correlated with the surface height, therefore, increase of the ripple amplitude is expected.

The suppression of sputtering Fig. 3.32a',b' provides no major changes in the surface current plots. Also the plots of  $-\nabla \vec{j}$  in Fig. 3.32c',d' do not provide any hint about a strong influence of sputtering. This result suggests that sputtering does not dominate pattern formation.

In conclusion, it has been demonstrated that by extraction of the surface current vectors and its derivatives from atomistic simulation a deeper understanding of pattern formation can be achieved. Preliminary results based on the initial sinusoidal surface provide information about curvature dependent surface parameters like the defect evolution, current vectors or the height derivative in time. The separation between MH thermal diffusion and ion induced processes provides opportunity to compare the atomistic modeling and continuum theories.

*In the beginning there was nothing,  
and it exploded.*

Terry Pratchett (1948)

# 4

## Interface mixing of bilayer interfaces

The modification of interfaces by ion beams is responsible for many physical properties, which are interesting for material science and applications. Experimental studies on ion induced grain growth [182], swift heavy ion ordering [183, 184] or interface nanoshaping [185, 186], and magnetic properties manipulation [187, 188] have been performed. Alloy formation or precipitation may occur after irradiation with low-energy ions, where the results can be understood by computer experiments [181, 189].

Several simulation techniques have been applied for modeling mechanisms of ion induced interactions at the interface. The most accurate and detailed way to describe the collision cascade is achieved by MD calculations. However, due to spatio-temporal restrictions one can only simulate small scale effects [190]. A much more efficient approach is a combination of different simulation techniques, e.g. MD with lattice KMC [181], where the information about distribution of atomic relocations calculated with MD is used as an input to KMC. Another possibility is inclusion of vacancies in the system at a depth defined by the ion projected range and applying the KMC simulation sub-sequential to the vacancy creation [86, 89, 90]. Additionally, in metals interstitial atoms induced by the collision cascade can cluster into two-dimensional structures called *dislocation loops*. This phenomenon can be described by lattice KMC simulations using the so-called trapping parameter [191] that denotes a minimum number of first-neighbor atoms required to trap interstitials.

The main aim of this work is to apply a new simulation technique called TRIDER, unifying two broadly utilized atomistic models, BCA and KMC, allowing for the full description of the radiation damage as well as investigation of the intermixing and the phase separation processes in metallic alloys. These simulation techniques necessary to understand the approach proposed here have been characterized in Chap. 2. In this chapter the multi-component KMC method of Sec. 2.3.3 will be improved by the introduction of interatomic many-body potentials.

Two systems irradiated with  $\text{He}^+$  ions are discussed:

- Al/Pb interface provides a highly immiscible type of interactions, where heterogeneous nucleation has been reported mainly for inclusion of Pb implanted into a Al lattice [192, 193]. Investigations of mixing for these materials have been mostly performed after annealing at melting temperatures, where a strong clustering of Pb in the Al layer has been observed [194].
- Pt/Co interfaces can be characterized by strong atomic self-ordering, resulting in intermetallic compound formation. Investigations focus mainly on manipulating of magnetic anisotropy of Pt/Co multilayers. In general, ion irradiation, independently on the ion species decreases or even removes the perpendicular magnetic anisotropy [195, 196].

In the present study, these two bilayer interfaces under  $\text{He}^+$  ion irradiation will be investigated at temperatures lower than the melting temperature. The analysis of ballistic and thermal interactions have been performed by the new simulation approach where BCA and KMC based models are combined.

The structure of this chapter is as follows: Sec. 4.1 describes the improvement of the simulation method, where the many-body potential of Rosato, Guillope and Legrand (RGL, [197]) to describe energetic interactions of atoms is applied. Also the method of obtaining input parameters for the simulation is characterized there. Sec. 4.3, shows simulation results. Two significantly different interfaces are presented: Al/Pb, as an example of clustering materials and Pt/Co, where the ordering to the  $\text{L1}_0$  intermetallic phase takes place. Finally in Sec. 4.4 a comparison of theoretical studies of TRIDER with TRIDYN is given.

## 4.1 Many-body interatomic potential for energies of Cellular Automata

---

In Chap. 2 the KMC simulation technique for binary systems is presented, where the NN atomic interactions are described with the Cellular Automata approximation [92]. The Ising model is the simplified CA, where the atomic energy consist of a sum of NN bond energies. Therefore, the Ising model is not using the full potential of CA and has several disadvantages, in particular:

1. Restricting to NN interactions and using the binary lattice Hamiltonian according to Eq. (2.52) to describe energetic states of the whole system allows to reproduce a binary phase diagram [198] only if it is almost symmetric. This is not the case for AlPb alloys, where asymmetry in the concentration between Al-rich and Pb-rich phase is significant [199].
2. Ising type of energetic interactions has a linear dependence over the occupation number of NN atoms which is not suited for metallic systems. One expects rather a square-root dependence as for tight-binding potentials in metals [200].

To treat the 1st case, due to the asymmetry it is necessary to assume that Hamiltonian (2.63) defining a binary alloy is equivalent to a Hamiltonian of a binary lattice gas (2.50). The drawback of this simplification is that no vacancies and interstitials can be included and atomistic kinetics is restricted to Kawasaki exchange. The transformation from the binary lattice gas Hamiltonian to the binary alloy Hamiltonian is implemented using the pairwise interaction energy in the binary system  $\varepsilon_{NN}$ , determined by a linear combination of available bond energies of the binary alloy ( $\varepsilon_{aa}$ ,  $\varepsilon_{bb}$ ,  $\varepsilon_{ab}$  and  $\varepsilon_{ba}$ ) (see Ref. [88])

$$\varepsilon_{NN} = \frac{1}{2} (\varepsilon_{aa} + \varepsilon_{bb} - \varepsilon_{ab} - \varepsilon_{ba}). \quad (4.1)$$

The unknown energies in the Eq. (4.1) are the bond energy between different components ( $\varepsilon_{ab}$  and  $\varepsilon_{ba}$ ). To fit the  $\varepsilon_{ab}$  it is necessary to find the value of  $\varepsilon_{NN}$ , which is the activation energy of the solidus of a phase diagram. It is possible to define two such energies  $\varepsilon_{NN}^a$  and  $\varepsilon_{NN}^b$  on both solidi of the phase diagram (e.g. in Al-Pb system see Fig. 4.7), thus also two different bond energies have been defined ( $\varepsilon_{ab}$  and  $\varepsilon_{ba}$ ). On the phase diagram given in Fig. 4.1-left one can assume that always one atom of type  $a$  is surrounded

## 4.1. MANY-BODY INTERATOMIC POTENTIAL FOR ENERGIES OF CELLULAR AUTOMATA

only by atoms of type  $b$  ( $a$ -rich phase), vice versa ( $b$ -rich phase). The bond energy for dissolved atom  $a$  in the  $b$ -rich phase  $E_{NN}^a$  is calculated using the activation energy of the solidus by

$$E_{NN}^a = \frac{\tau}{2} \varepsilon_{NN}^a. \quad (4.2)$$

The solidus energy is related to bond energies by Eq. (3.23) (see Ref. [81]), where

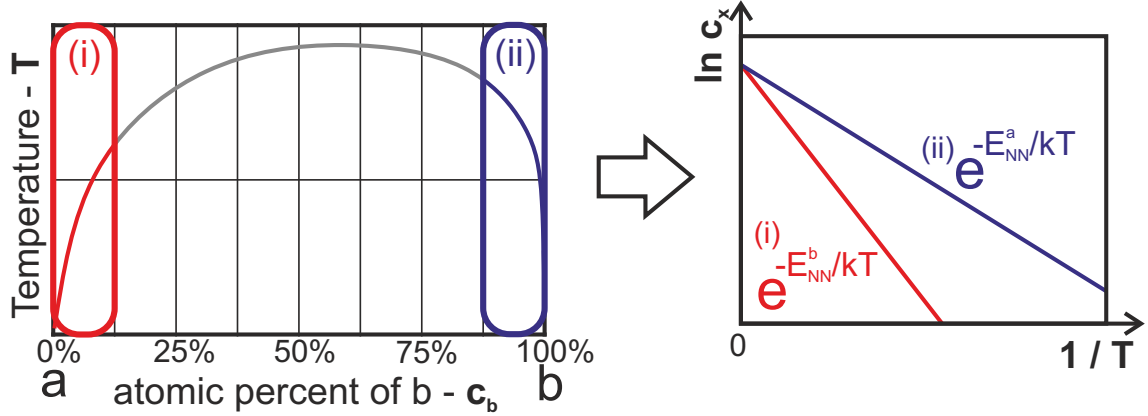


Figure 4.1.: An example of a phase diagram of immiscible alloy (left) and its solidi (i) for the  $a$ -rich phase and (ii) for the  $b$ -rich phase presented as the Arrhenius plots (right). The slope of the concentration  $\ln c_x$  determines the total bond energies of dissolved atoms  $E_{NN}^a$  and  $E_{NN}^b$ .

the bond energy is determined by the slope of the concentration  $\ln c_x$  expressed as the Arrhenius plot (see Fig. 4.1-right).

The activation energy of the solidus for atom  $a$  in the  $b$ -rich phase is calculated with the Eq. (4.1) according to

$$\varepsilon_{NN}^a = \frac{1}{2} (\varepsilon_{aa} - \varepsilon_{ab}), \quad (4.3)$$

where no bond energies  $\varepsilon_{bb}$  and  $\varepsilon_{ba}$  are expected. The activation energy of the solidus for atom  $b$  in the  $a$ -rich phase gives

$$\varepsilon_{NN}^b = \frac{1}{2} (\varepsilon_{bb} - \varepsilon_{ba}). \quad (4.4)$$

The bond energies between the same type of components  $\varepsilon_{aa}$  and  $\varepsilon_{bb}$  are calculated from their cohesive energies of these components, which in fcc lattices are  $E_c^a = 6\varepsilon_{aa}$  and  $E_c^b = 6\varepsilon_{bb}$ , respectively. Finally, the bond energies between different components are given by

$$\begin{aligned} \varepsilon_{ab} &= \frac{1}{6} E_c^a - 2\varepsilon_{NN}^a \\ \varepsilon_{ba} &= \frac{1}{6} E_c^b - 2\varepsilon_{NN}^b \end{aligned} \quad (4.5)$$

Bond energies of a fully coordinated atom (total bond energy)  $a$  in the  $b$ -rich phase and atom  $b$  in the  $a$ -rich phase are then calculated according to the equations

$$\begin{aligned} E_{tot}^{ab} &= E_c^a - 2E_{NN}^a \\ E_{tot}^{ba} &= E_c^b - 2E_{NN}^b \end{aligned} \quad (4.6)$$

respectively. Here,  $E_{NN}^a$  and  $E_{NN}^b$  are the total bond energies of dissolved atoms on the both solidi (see Fig. 4.1).

Above presented method is preferentially applied to two-component systems, or to three-component systems, where the one component has a very low total concentration. However, in the systems proposed here, a strong influence of empty sites (vacancies) on the local activation energy is expected. In order to treat this problem, a dependence of total atomic bond energy on NN occupation number has to be considered.

A tight-binding second-moment model (called also a the RGL potential [197]) is applied, where the total cohesive energy of the system of two metals [200] gives

$$E_c = \sum_i \left[ \sum_{j<i} A_{ab} e^{-p_{ab} \left( \frac{r_{ij}}{r_0^{ab}} - 1 \right)} - \left( \sum_{j<i} \xi_{ab}^2 e^{-2q_{ab} \left( \frac{r_{ij}}{r_0^{ab}} - 1 \right)} \right)^{1/2} \right]. \quad (4.7)$$

First term is a repulsive portion of the Born-Mayer pairwise interaction characterized by a parameter  $A$ . The parameter  $p$  is related to the compressibility of the bulk metal. The second term denotes the attractive band energy with effective hopping integral parameter  $\xi$ , and depending on the relative interatomic distance parameter  $q$ . The distance between atoms  $i$  and  $j$  is denoted by  $r_{ij}$ , and the NN distance is given by  $r_0^{ab}$  between interacting atomic species  $a$  and  $b$  lattice.

If atoms are fixed to a regular lattice and only the NN interaction are consider, the Eq. (4.7) reduces to

$$E_c = \sum_i E_{ab}(n_i) = \sum_i (A_{ab} n_i - \xi_{ab} \sqrt{n_i}). \quad (4.8)$$

where  $n_i$  is the NN occupation number of atom  $i$ . The energy  $E_{ab}(n)$  is the total bond energy of atom of type  $a$  surrounded by  $n$  atoms of type  $b$  and  $\eta - n$  vacancies, where  $\eta$  is the coordination number.

## 4.2 Gauging simulation parameters

---

The procedure of finding the simulation parameters specified in Sec. 4.1 can be divided into three stages:

1. Analyzing of the phase diagrams in order to calculate  $E_{NN}^a$  and  $E_{NN}^b$ .
2. Calculation of the reduced RGL potentials Eq. (4.8) for different components  $E_{ab}(n)$  and  $E_{ba}(n)$  describing only the interactions at high concentration of one component.
3. Interpolation of RGL potentials from the 2nd stage extending the rich phases of one component to the general case of arbitrary occupied NN lattice sites with the component  $a$ , the component  $b$  and the vacancies.

The treatment of the **1st stage** is different for immiscible and miscible components respectively. For immiscible materials like AlPb the bond energy for the binary lattice gas system of Al in the Pb rich phase  $E_{NN}^{Al}$  and vice-versa  $E_{NN}^{Pb}$  is calculated using the Eq. (3.23). It gives the bond energy  $E_{NN}^{Al} = 0.538$  eV of Al with all NN sites occupied by Pb atoms and the bond energy  $E_{NN}^{Pb} = 0.419$  eV of Pb with all NN sites occupied by Al atoms. Thus, the total bond energies used in the computer simulation obtained from Eq. (4.6) are  $E_{tot}^{AlPb} = 2.013$  eV and  $E_{tot}^{PbAl} = 1.151$  eV.

## 4.2. GAUGING SIMULATION PARAMETERS

In the case of CoPt interactions, the method of obtaining parameters of total atomic bond energy is similar to the Al-Pb system. However here,  $E_{NN}^a$  and  $E_{NN}^b$  of the binary system have been calculated according to transition temperature from disordered A phase to the ordered  $L1_0$  phase of a system at 50% Co content based on the phase diagram of Pt-Co (see Fig. 4.2b). The obtained values of total atomic bond energies in the binary lattice gas system are assumed to be equal for Pt and Co, therefore  $E_{NN}^{PtCo} = E_{NN}^{CoPt} = 1.3$  eV and no phase anisotropy is expected.

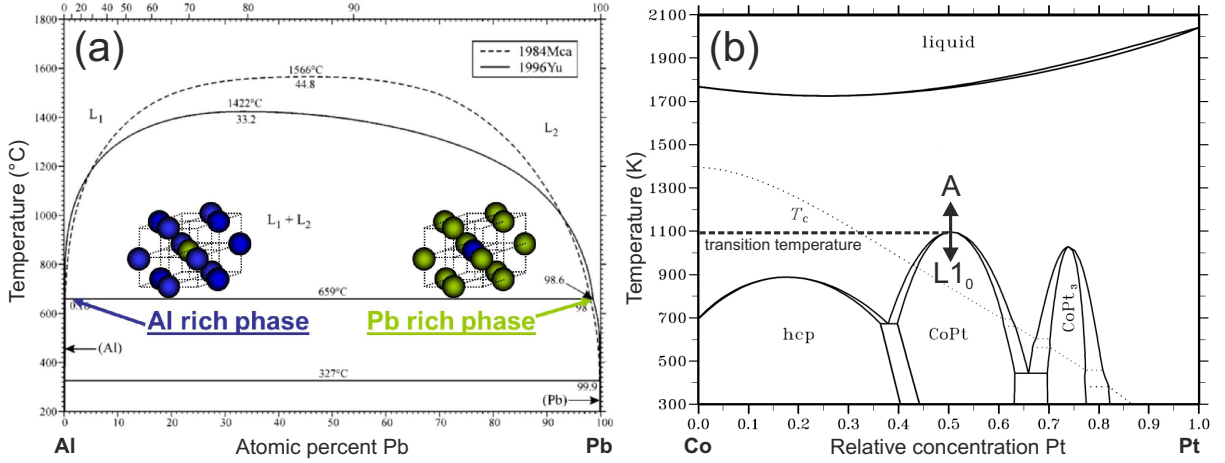


Figure 4.2.: Phase diagram for the system Al-Pb [201,202] with selected lattice configuration of Al rich and Pb rich phases (a). In (b) the phase diagram of the system Co-Pt (from Ref. [198]).

To introduce the RGL potential for pure elements of Al, Pb, Co and Pt, the literature values from Cleri *et al.* have been utilized [200]. In the **2nd stage** the interactions of different element like Al-Pb or Co-Pt have to be calculated. The RGL potential (4.8) is used in order to calculate values of  $E_{ab}(n)$  for AlPb and CoPt systems. The parameters of RGL potentials for different elements, have been calculated using a linear transformation of the parameters used in pure elements, known from the literature [200], by the ratio between the cohesive energy of atom  $a$  ( $E_c^a$ ) and the total bond energy of the fully coordinated atom of type  $a$  surrounded by atoms of type  $b$  ( $E_{tot}^{ab}$  from Eq. 4.6)<sup>1</sup>. Collected values are shown in Table 4.1. The NN occupation dependent functions  $E_{ab}(n)$  of the total bond energies used in the simulations, have been plotted in Fig. 4.3.

Table 4.1.: Simulation parameters for the tight-binding potential

	Al-Al	Pb-Pb	Al-Pb	Pb-Al	Pt-Pt	Co-Co	Pt-Co	Co-Pt
$\xi$ (eV)	1.316	0.914	0.8578	0.5281	2.506	1.907	3.634	3.05
$A$ (eV)	0.1221	0.098	0.0796	0.0566	0.242	0.189	0.3509	0.3023

The presented plots describe energetic states of pure interactions with one type of bonding only. Thus, in the **3rd stage** a combination of bonds, which occur locally, is considered. It is necessary to use a more general formula that takes into account a

<sup>1</sup>For instance, to calculate the RGL potential of Al atom surrounded by  $n$  Pb atoms  $E_{AlPb}(n)$  using Eq. (4.6), it is enough to make a linear transformation of RGL potential for Al-Al interactions  $E_{AlAl}(n)$  by a ratio  $E_c^{Al}/E_{tot}^{AlPb}$ , where  $E_c^{Al} = 3.09$  eV is the cohesive energy of Al and  $E_{tot}^{AlPb} = 2.013$  eV is the total bond energy of Al surrounded by 12 Pb NN atoms.



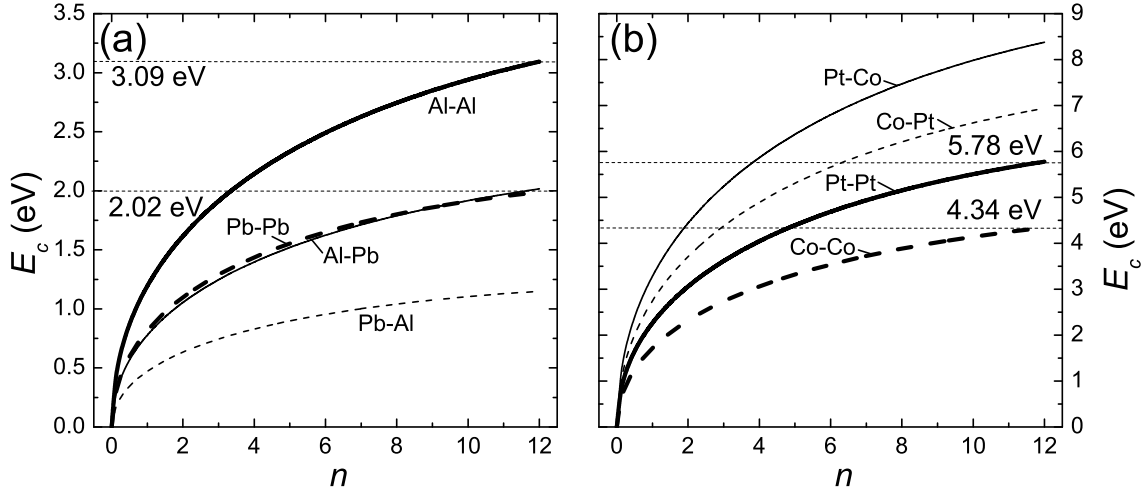


Figure 4.3.: Cohesive energy of atomic interactions as a function of the NN occupation number for the fcc lattice of Al-Pb (a) and Pt-Co (b) systems. In (a), starting from the top: Al-Al (thick solid line), Pb-Pb (thick dashed line), Al-Pb (thin solid line) and Pb-Al (thin dashed line) interactions are shown. In (b), starting from the top Pt-Co (thin solid line), Co-Pt (thin dashed line), Pt-Pt (thick solid line) and Co-Co (thick dashed line) interactions are presented. For fully coordinated configuration the cohesive energy is equal to the sublimation energy.

number and type of NN atoms in order to calculate the occupation dependent cohesive energies:

$$\begin{aligned} E_a(n_a, n_b) &= \frac{n_a}{N} \left( \xi_{aa} \sqrt{N} - A_{aa} N \right) + \frac{n_b}{N} \left( \xi_{ab} \sqrt{N} - A_{ab} N \right) \\ E_b(n_a, n_b) &= \frac{n_b}{N} \left( \xi_{bb} \sqrt{N} - A_{bb} N \right) + \frac{n_a}{N} \left( \xi_{ba} \sqrt{N} - A_{ba} N \right). \end{aligned} \quad (4.9)$$

Here, alloy components  $a$  and  $b$  have the NN occupation numbers  $n_a$  and  $n_b$ , respectively. Regarding to the sort of atoms intended for hopping, one has to use either  $E_a$  or  $E_b$  equations. The solution of equations (4.9) for the Al-Pb and the Pt-Co systems is shown in Fig. 4.4 as a contour plot. The values are calculated according to the local atomic configuration that depends on the first NN atoms. This kind of data representation has been directly converted into a look-up table and efficiently used during simulations.

Two types of atomic configurations will be as example studied here. Both configurations consisting of two layers have been used, bombarded by  $\text{He}^+$  ions at the temperature of 600 K. The system size is always  $2^8 \times 2^6 \times 2^6$  lattice units, initialized with 512000 atoms. The Al/Pb system (25.25 nm / 25.25 nm in depth) is bombarded by 150 keV  $\text{He}^+$  ions at the normal ion incidence angle. The total thickness of the bilayer system is 50.5 nm. Also for the Pt/Co system a bilayer is considered, but with the total thickness of 49 nm.

The BCA simulations require also a gauging of simulation parameters. Surface binding energy values (SBE) have to be determined in order to calculate the values of the sputtering yield. In the case of self-interactions, usually the cohesive energy is the best choice for SBE. However, for collisions between different elements, like Al with Pb, or Co with Pt, the enthalpy of formation has to be taken into account. To calculate the formation energies, a method of Miedema and Niessen [203] is used, afterwards, the result is utilized in the evaluation of SBE [204], where  $\text{SBE}_{\text{CoPt}} = 5.6$  eV. For the Al-Pb system, no formation is expected, therefore the interaction energy between Al and Pb is  $\text{SBE}_{\text{AlPb}} = 2.69$  eV.

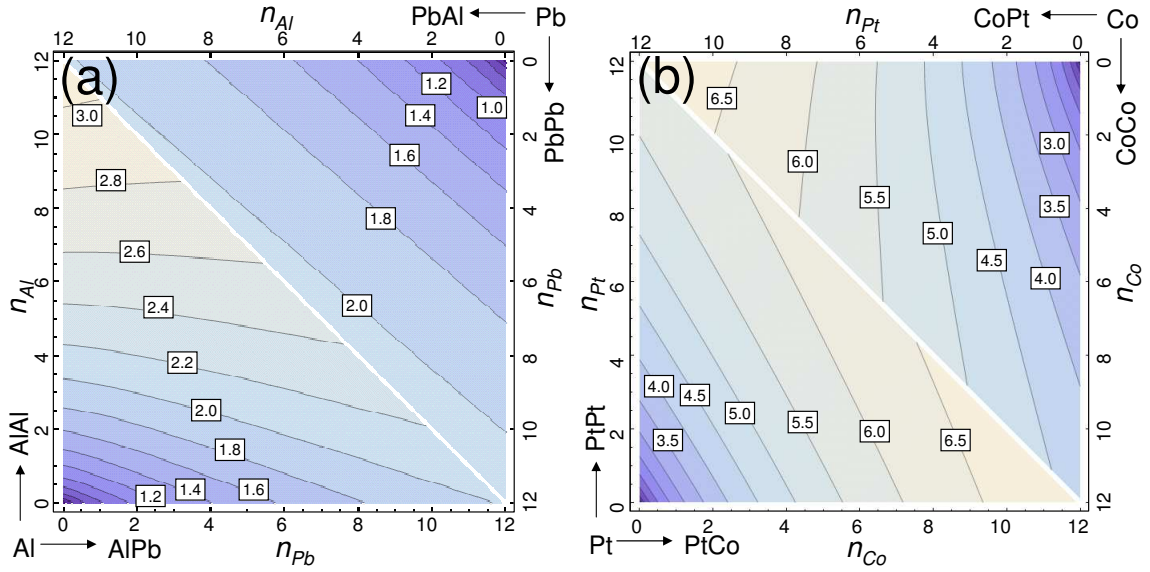


Figure 4.4.: Contour plot of the cohesive energy as the function of the NN occupation number for the Al-Pb (a) and the Pt-Co (b) system. The plots are two-dimensional extensions of one-dimensional functions presented in Fig. 4.3. E.g. the Al-Al curve in Fig. 4.3a is a cut along the abscissa of figure a. The values given in rectangles are in eV. The lower-left part of the plots denotes the energies of an Al atom for (a) and a Pt atom for (b), surrounded by  $n_{Pb}$  Pb atoms,  $n_{Al}$  Al atoms and  $12 - n_{Pb} - n_{Al}$  vacancies in (a) and by  $n_{Co}$  Co atoms,  $n_{Pt}$  Pt atoms and  $12 - n_{Co} - n_{Pt}$  vacancies in (b). Upper-right corners show the energies respectively for the configuration of a Pb atom in (a) and a Co atom in (b).

## 4.3 Simulation results

In this section, interface mixing in bimetal systems studied by TRIDYN simulation are compared with TRIDER simulations. First, the Al/Pb bimetal system with immiscible components Al and Pb is considered, where mixing leads to cluster formation. Second, the Pt/Co bimetal system forming intermetallic compound is studied, where enhanced interface mixing by high solubility of the materials followed by phase ordering is demonstrated.

### 4.3.1. Al/Pb bimetal mixing

The Al/Pb bimetal with 25.25 nm thickness of each layer of Al and Pb has been irradiated by  $\text{He}^+$  ions at the energy of 150 keV. The projected range was 690 nm, which is far beyond the interface. Therefore, almost all of the projectiles go through the simulation cell and stop deep in the bulk. Examples of single  $\text{He}^+$  and  $\text{Ar}^+$  ion incidences at a lower energy of 30 keV are shown in Fig. 4.5. The simulation has been divided into two stages (similar like in Sec. 2.4.5). In the first stage (BCA stage), ballistic displacements of atoms are simulated. It shows that the  $\text{He}^+$  damage (Fig. 4.5a) is obviously much smaller than the  $\text{Ar}^+$  damage (Fig. 4.5c) and, therefore, the number of defects after the BCA stage is much larger after  $\text{Ar}^+$  bombardment.  $\text{He}^+$  irradiation does not cause compact displacement cascades, differed from the  $\text{Ar}^+$  bombardment, which transfers enough energy to create ‘pockets’ of dense displacements. Vacancies created by displaced lattice atoms (gray dots) are usually located close to the corresponding interstitials. The BCA stage is finished when the kinetic energy of recoils drops below the displacement energy.

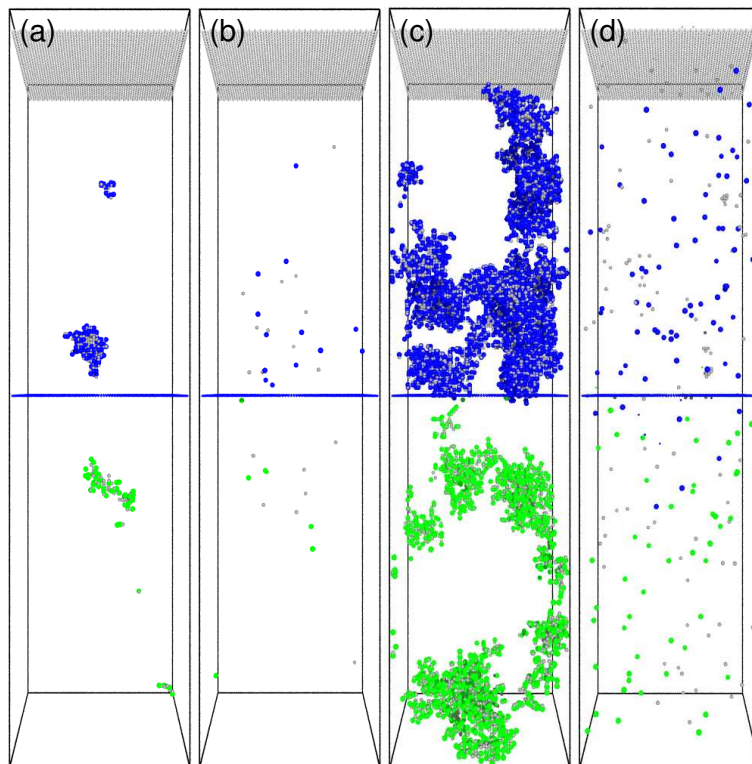


Figure 4.5.: Perspective view of the (100) Al/Pb fcc simulation cells after a single ion incidence with 30 keV ion energy for  $\text{He}^+$  (a) and (b), for  $\text{Ar}^+$  (c) and (d). Figures (a) and (c) represent the state of the system directly after the BCA stage, whereas figures (b) and (d) are snapshots after 200 MCs. Only I and V are displayed, the other atoms are made invisible. At the top of the systems the surface atoms are indicated with gray and the interface atoms are indicated in the middle with blue. Locations of interstitials are displayed in blue in the Al layer and in green in the Pb layer. Vacancies are represented by gray dots.

In the second stage (KMC stage, see Fig. 4.5b,d), the kinetics of the system is activated. At the beginning, the total number of Frenkel pairs (FPs) reduces rapidly to only a few percent compared to the number of FPs after the BCA stage. The relaxation of the system takes place by defect kinetics: (i) interstitials jump randomly interacting only with vacancies, (ii) kinetics of vacancies are determined by jump probabilities between neighboring lattice sites described in Sec. 4.1. The recombination of defects may occur simultaneously under the condition that the vacancy and the interstitial will travel a distance close enough to annihilate (see Sec. 2.4.3 for detailed description of recombination mechanism). Vacancies can nucleate to voids. Defects can travel and annihilate at the surface.

The average sputtering yield obtained for the simulation with 150 keV  $\text{He}^+$  is 0.019 Al atoms removed per one ion impact. The mean value of Pb FPs created per collision is 42. The number of FPs created in the Al layer fluctuates around 33 per incidence ion. Reported values have been registered after the BCA stage, they describe the state of the system directly after the displacement cascade. In reality, most of defects will annihilate. The average annihilation rate for both Al and Pb after 200 MCs of the KMC stage amounts to 74 FPs, i.e. only 1 FPs remains. Thus, relaxation of defects after the KMC stage results in 1 percent of preserved defects. These results agree very well with theoretical values obtained by MD studies by Betz *et al.* [104] for Al targets. All values

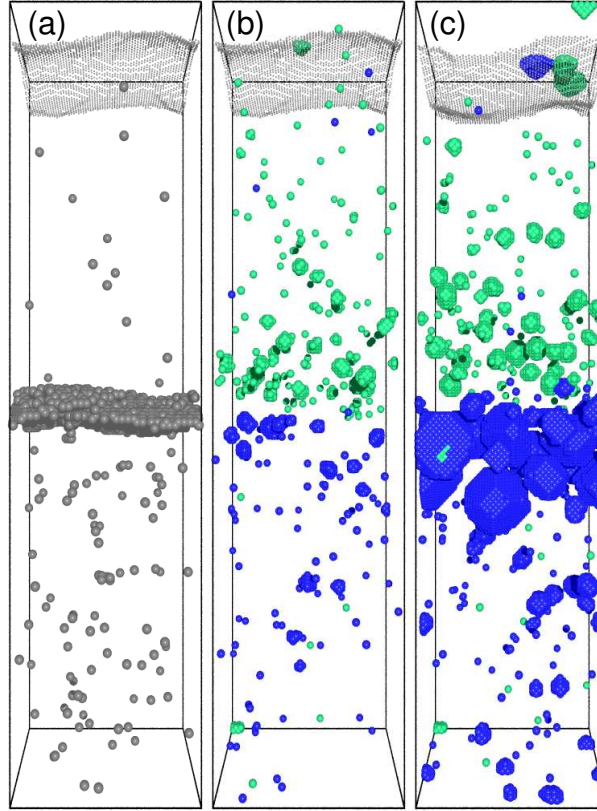


Figure 4.6.: Three-dimensional view of the simulation cell for the (100) Al/Pb bilayers, for a different visualization condition: (a) vacancy locations inside the system at the fluence of  $6 \times 10^{16} \text{ cm}^{-2}$ , where additionally the surface atoms are included, (b) and (c) monomers and clusters of Al (blue) and Pb (green) visible through transparent lattice at the fluences of  $6 \times 10^{16} \text{ cm}^{-2}$  and  $6 \times 10^{17} \text{ cm}^{-2}$ , respectively.

presented so far are valid only for the initial KMC stage after a single ion impact, i.e. before the collective mixing process starts. The mixing of interface becomes significant for the fluences larger than  $1 \times 10^{16} \text{ cm}^{-2}$ .

The distributions of elements at higher fluences are given in Fig. 4.6b-c. They show nucleation of Al and Pb atoms close to the interface in the Pb and the Al rich phase, respectively. The nucleation is caused by the phase separation due to the defect kinetics, which is a very well-known phenomenon [86, 90, 205]. The configuration of vacancies within the simulation cell has been plotted in Fig. 4.6a. There is a larger vacancy concentration at the interface. There are two reasons causing this kind of vacancy formation:

- (i) From collisional point of view, the interface between the lighter Al atoms and the heavier Pb atoms acts as a dipole of vacancy creation. There is a peak in the number of vacancies at the interface in Al, which is related with the accumulation of damage caused by Pb recoils, what is explained in more detail in Appendix A.
- (ii) Considering the relaxation mechanisms, the interface is a trap for the vacancy diffusion, because of the low bond strength between Al and Pb. Figure 4.7 shows the total bond energy of a vacancy across the interface in a fcc lattice (coordination number 12). The lowest energy is expected at the transition from Pb to Al monolayer. The vacancies will be trapped directly at the interface, where its energy is the lowest.

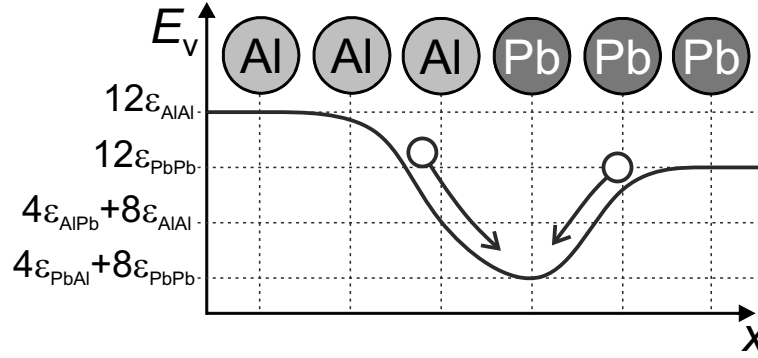


Figure 4.7.: Schematic diagram of mean bond energies across the interface in Al/Pb bilayer.

The steady-state concentration of vacancies is higher in the Pb layer than in the Al layer (see Fig. 4.6a). The same holds for vacancy creation by the BCA stage of the simulation (see Appendix A, Fig. A.2b). Additionally, in the Al layer two sinks for vacancy annihilation are present, i.e. vacancies migrate into the surface or cluster at the interface. In Pb due to the reflective boundary condition along the depth axis, the sink exists only at the interface and vacancies accumulate stronger in Pb layer.

The evolution of the Al/Pb phase separation for different fluences is shown as three-dimensional simulation snap-shots of Al/Pb cluster distributions (Fig. 4.6b-c). The mean cluster sizes increases with the fluence. It depends strongly on the solubility and, consequently, on the local concentration of defects under ion irradiation.

The state of system after the fluence of  $6 \times 10^6$  ions per  $\text{cm}^2$  is shown in 4.6c. The size of the clusters for Al is clearly much larger than the size of the Pb clusters. There are three reasons for the asymmetric distribution of clusters:

- (i) The high vacancy concentration in Pb enhances Al diffusion there, thus participate growth is accelerated.
- (ii) The higher equilibrium concentration of Al in Pb results in a higher number of diffusing species, which accelerates participate growth too.
- (iii) According the Fig. 4.7 detrapping of vacancies into the Pb layer is easier than into the Al layer due to the lower bond energy of Pb than of Al, respectively. This will also increase the vacancy concentration in Pb.

### 4.3.2. Pt/Co bimetal mixing

Pt and Co bimetals have been bombarded by 150 keV  $\text{He}^+$  ions at normal incidence. The impact energy is large enough so the maximum damage is far beyond the interface region (projected range is 500 nm). The Pt/Co interface is at the depth of 25.4 nm. The sputtering yield of the Pt is 0.02 and the average number of the FPs created by one  $\text{He}^+$  ion is 94 (46 of Pt and 48 of Co). For the ion flux used in the simulations, the mean FPs surviving the relaxation following an ion impact is  $\sim 4$ , i.e. 4.4 %.

The steady-state vacancy distribution in the system after  $3.1 \times 10^{17} \times \text{He}^+ \text{ cm}^{-2}$  impacts is indicated in Fig. 4.8a. Figure shows several significant differences compared to the Al/Pb bimetal (Fig. 4.6a), where the vacancies have been preferentially trapped at the interface and in the Pb layer. In the simulation of Pt/Co bimetal, a homogeneous

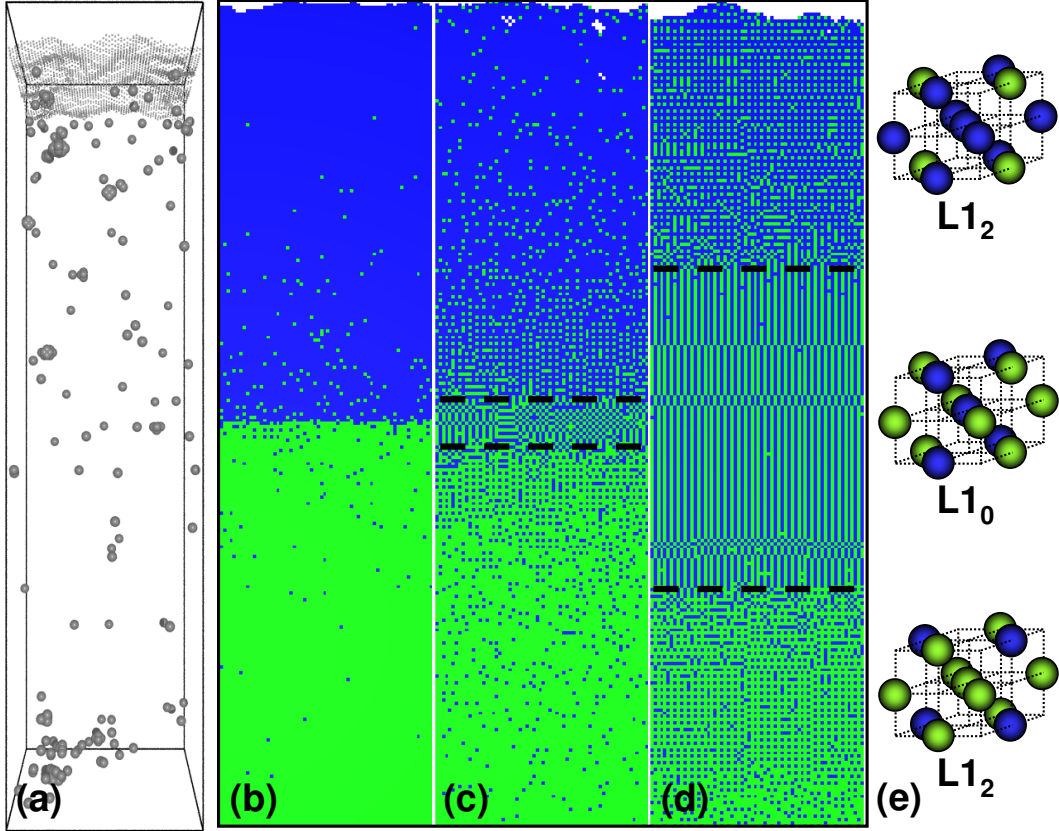


Figure 4.8.: Vacancy locations inside the Pt/Co bimetal at the fluence of  $3.1 \times 10^{17} \text{ cm}^{-2}$  (a). At the top of the simulation cell, a surface region is emphasized. Simulation slices of the chemical ordering to  $L1_0$  and  $L1_2$  formations during 150 keV  $\text{He}^+$  irradiation at 600 K temperature (b-d). Figures show 2 atomic plane cuts throughout the simulation cell in the  $[100]$  direction for different fluences: (b)  $6.3 \times 10^{15} \text{ cm}^{-2}$ , (c)  $6.3 \times 10^{16} \text{ cm}^{-2}$  and (d)  $3.1 \times 10^{17} \text{ cm}^{-2}$ . In blue Pt atoms and in green Co atoms are denoted. In (e) three different lattice occupancy configurations are highlighted: in the middle CoPt  $L1_0$ , top and bottom  $L1_2$   $\text{CoPt}_3$  and  $L1_2$   $\text{Co}_3\text{Pt}$  formations, respectively. Dashed lines show borders between  $L1_0$  and  $L1_2$  phases.

distribution over the thickness has been observed. Nevertheless, small vacancy clusters can be seen at the region up to a few mono-layers below the surface.

The simulation stages at different fluences are plotted in Fig. 4.8b-d as slices of simulation cell perpendicular to the  $[001]$  direction. They show a strong intermixing and intermetallic phase formation under irradiation of  $\text{He}^+$  ions caused by vacancy kinetics. Similar mechanisms of alloy ordering have been reported in the literature, e.g. temperature dependent order-disorder phenomena in nanoclusters [87] or irradiation of intermetallic FePd thin films [86]. Different from these former studies, here we treat both, the defect generation and kinetics, simultaneously.

Three simulation stages are outlined:

- (i) For a very low fluences (below  $6 \times 10^{15} \text{ cm}^{-2}$ ), ion induced diffusion, i.e. collisional displacement of atoms, is a dominant driving force that activates interface mixing almost without any phase ordering (Fig. 4.8b). In average, 4 vacancies per ion remain in the system after the relaxation stage. Therefore, increasing the fluence is equivalent with increasing the number of vacancies in the system.
- (ii) For the fluence of one order of magnitude larger, one can distinguish ordering

into two different atomic configurations:  $L1_0$ , when the concentration of Pt in Co approaches 50 percent, and  $L1_2$ , when the ratio between Pt and Co is about 3:1 or 1:3. Fig. 4.8c-d traces the transition from the collisional inter-mixing to the chemical ordering.

- (iii) The final state of the simulation is due to the orientation of variants in of the fcc lattice. In order to minimize the energy of the system the PtCo alloy form preferentially Co-Pt bonds rather than Co-Co and Pt-Pt bonds. Therefore, in the steady-state  $L1_0$  formation is expected. Nevertheless, due to the different concentration in depth profiles the  $L1_2$  formation is present as well.

It is possible to mark an region of the interface, where the above-named formations are clearly visible (see Fig. 4.8c-e). Whereas the  $L1_2$  formation is fully symmetric, the  $L1_0$  formation has specified orientation that creates anisotropy in the crystal. Here, mainly [010] or [001] orientation of variants have been observed. The influence of ion irradiation onto anisotropy in the crystal is not a scope of this work and will not be discussed in detail.

## 4.4 Comparison of TRIDER with TRIDYN

---

TRIDER extends the BCA method by the defect relaxation, i.e. defect kinetics in bulk and on surface, defect recombination, phase ordering and phase separation. These processes would drive the system toward equilibrium in the absence of IBS. However, if an external driving force, which induces atomic displacement is present, the system is driven towards a steady-state. In this section, the advantage of the TRIDER program compared to the binary collision simulations with the TRIDYN program will be highlighted.

The typical output of TRIDYN is a depth profile of target components at different irradiation fluences. Interface mixing induced by the ballistic displacement only, obtained with TRIDYN simulations, is plotted on the upper row of Fig. 4.9a-c and Fig. 4.10a-c. It shows an increase of the interface width with increasing ion fluence. This mechanism can be easily characterized by a 'ion-induced' diffusion, where the width of the irradiated layer is proportional to  $W \propto \sqrt{D_i \phi}$ , where the fluence  $\phi$  replaces the time in the characteristics of the diffusion equation. The ion-induced diffusion coefficient  $D_i$  exhibits the behavior described by the transport theory according to Eq. (2.32), which is temperature independent and mainly the displacement energy of target atoms is responsible for intermixing. On the other hand Eq. (2.34) takes the mean temperature of the thermal spikes into account. Therefore, the ion-induced diffusion coefficient can be corrected by the chemical interactions that are described by the mixing enthalpy  $\Delta H_{mix}$ . The exact measurement of the mean temperature of thermal spikes cannot be derived analytically. Because of many simplifications used in transport theory (see Sec. 2.1.4), e.g. isotropic distribution of the deposited energy, or empirical estimation of the thermal spike temperature, the analytical predictions of mixing properties are often questionable.

Atomistic simulations based on the BCA (TRIDYN) predict accurately the interface mixing, if the chemical interactions are not dominant. Models like TRIM or TRIDYN introduce an empirical parameter called energy threshold  $E_{thr}$ , which describes the interatomic bond strength for bulk materials and recombination of defects created in the collision cascade. Therefore,  $E_{thr}$  is usually significantly larger than the displacement energy  $E_d$  in a rigid crystal [39,206]. However, chemical driving forces are not considered in the binary models like TRIDYN.

#### 4.4. COMPARISON OF TRIDER WITH TRIDYN

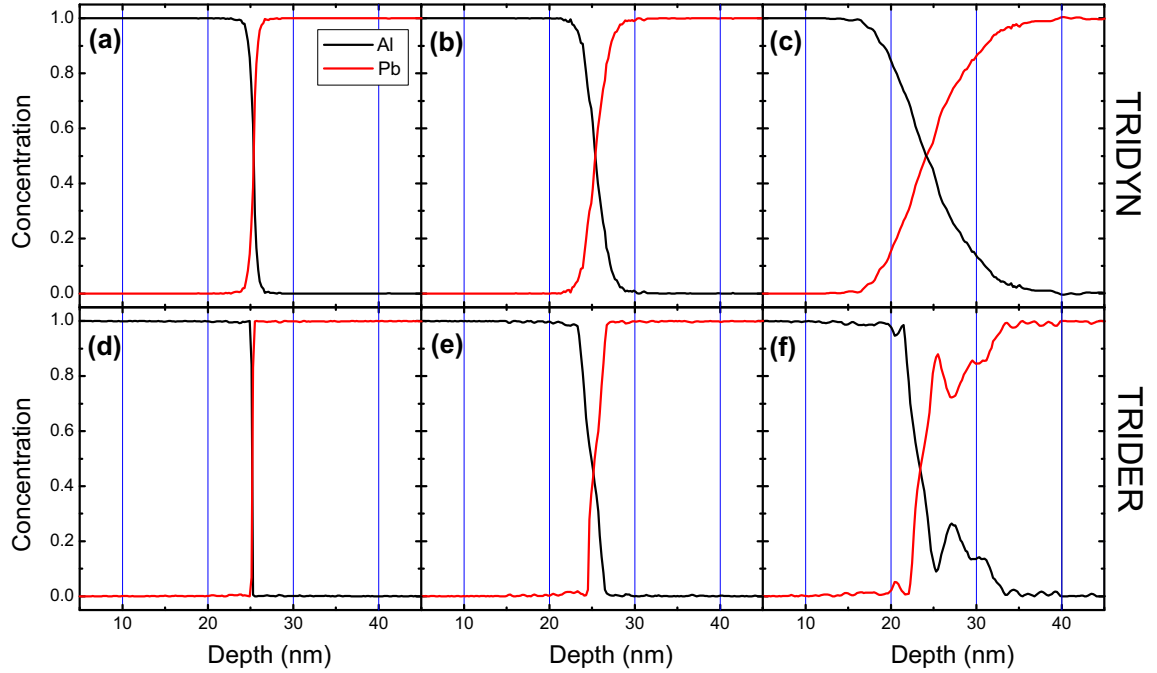


Figure 4.9.: Comparison of depth profiles after 150 keV  $\text{He}^+$  irradiation of the Al/Pb bimetal obtained from atomistic simulations with: (a-c) TRIDYN, (d-f) TRIDER. Columns are simulations for fluences:  $6 \times 10^{15} \text{ cm}^{-2}$  (left),  $6 \times 10^{16} \text{ cm}^{-2}$  (middle) and  $6 \times 10^{17} \text{ cm}^{-2}$  (right), respectively.

Input parameters used in the BCA stage of TRIDER simulations are exactly the same like for of TRIDYN simulations and have been described in Sec. 4.2. The only difference is the initial lattice configuration, which for the TRIDYN model is considered to be a one-dimensional array of atomic densities along the depth. Each element of the array corresponds to the concentration of the selected atomic species at certain depth (see Sec. 2.2.2 for details). This type of the system architecture is simple compared to the TRIDER approach, where real three-dimensional concentrations and atomic densities are calculated based on the local lattice occupancy. Therefore, in order to obtain the depth profile, an average volume of each lattice point on each plain parallel to the surface (along [100] direction) has been calculated.

The comparison between two simulation methods for the Al/Pb bimetal is shown in Fig. 4.9. Depth profiles in the upper row, which were calculated using TRIDYN are similar to TRIDER profiles, especially at low fluences. However, for  $\phi = 6 \times 10^{17} \text{ cm}^{-2}$  one can observe a few peaks around the interface region (see Fig. 4.9f). Immiscibility of the Al/Pb system is a well-known property that has been evaluated from the heat of mixing measurements [207]. The heat of mixing  $\Delta H_{mix}$  of AlPb alloy is positive for any concentration of the elements. As it has been discussed in Sec. 2.1.4, the positive  $\Delta H_{mix}$  counteracts against the mixing caused by ballistic displacement (see Fig. 4.9d,e). Additionally, due to immiscibility of Al and Pb, phase separation at the interface occurs. The constant rise of the atomic concentration of Al in the Pb rich phase and Pb in the Al rich phase close to the interface results in a cluster formation in both phases (see also Fig. 4.6). Mainly, large Al clusters are formed in the Pb layer. The secondary peaks in the depth profile for Al appear a few nm range away the first one. It is due to a secondary damage of the cluster formation next to the interface (see Fig. 4.9f). Similar effect has been observed after ion irradiation of Au nanoclusters in  $\text{SiO}_2$  [205].



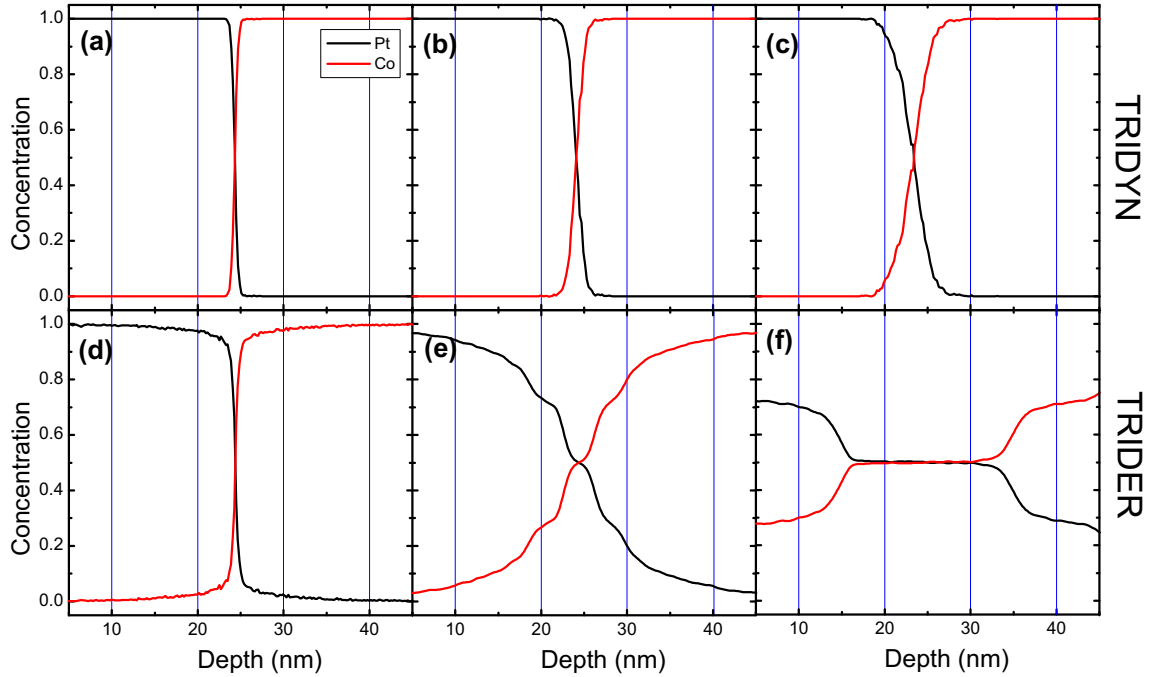


Figure 4.10.: Comparison of depth profiles after 150 keV  $\text{He}^+$  irradiation of Pt/Co bimetal obtained from atomistic simulations with: (a-c) TRIDYN, (d-f) TRIDER (analogically to Fig. 4.9). Columns are simulations for fluences:  $6.3 \times 10^{15} \text{ cm}^{-2}$  (left),  $6.3 \times 10^{16} \text{ cm}^{-2}$  (middle) and  $3.1 \times 10^{17} \text{ cm}^{-2}$  (right), respectively.

A significantly different result has been obtained for the Co/Pt bimetal. Using the TRIDER program, the interface mixing is much stronger in comparison to the results from TRIDYN (see Fig. 4.10). The differences are due to an additional driving force for mixing at the interface that constitute to the high miscibility. The TRIDER simulation stages for three different fluences are shown in Fig. 4.10d-f. Even the initial state (first column) shows a strong deviation from the purely collisional approach simulated with TRIDYN (see Fig. 4.10a,d). More clearly it is visible at the fluence of  $6.3 \times 10^{16} \text{ cm}^{-2}$ , where the intermetallic compound CoPt starts to form at about 25 nm depth. Thus, the interface region shows formation of  $L1_0$  phase (see Sec. 4.3.2 for details). At the fluence of  $3.1 \times 10^{17} \text{ cm}^{-2}$  a very well ordered step-like depth profile is shown, where the intermetallic phases are clearly separated. From the thermodynamic point of view the heat of mixing coefficient is large and negative [208] for the CoPt compound. These are favorable conditions to form the intermetallic compound at the interface. Moreover, coupling collisional and thermodynamic processes raises the magnitude of the interface mixing what was also reported by experimental study of Chappert *et al.* [209].

In Fig. 4.11 the depth profiles for the concentration obtained with simulations of TRIDYN and TRIDER at different fluences have been combined into one plot for Al/Pb bimetal and one plot for the Co/Pt system. Each depth profile has been fitted to the Eq. (2.30), which is the solution of the diffusion equation (2.28) describing the interface mixing for bilayer materials. The width of a depth profile  $Dt^2$  that is the parameter of Eq. (2.30) is given in the insets of Fig. 4.11 as a function of fluence. It confirms the observation based on the qualitative study of depth profiles that the total mixing for immiscible materials like AlPb is suppressed and for miscible materials like CoPt

<sup>2</sup>The time  $t$  defines the irradiation time, that is proportional to the fluence  $\phi$  at the flux  $j$ .

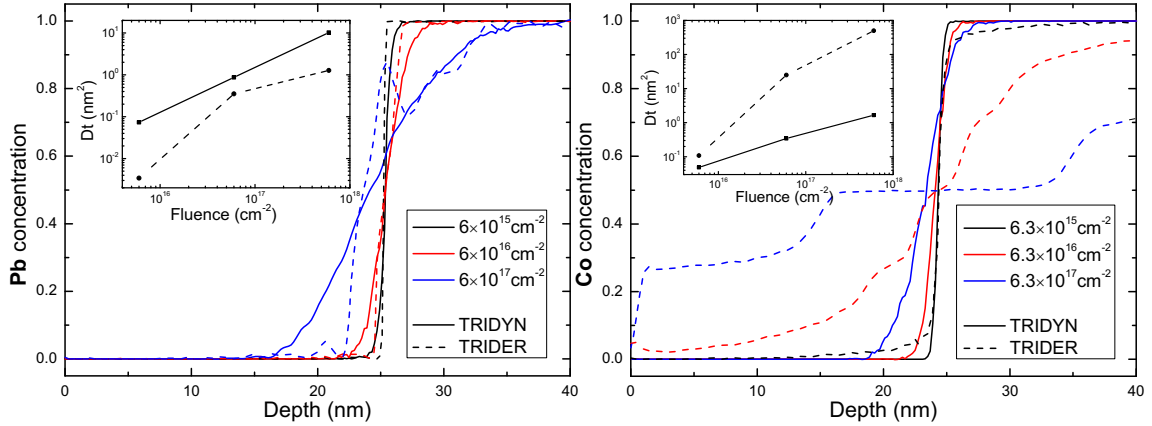


Figure 4.11.: The Pb (left) and Co (right) depth profile obtained from two models of atomistic simulation (coupling of Fig. 4.9 and 4.10). Inset shows widths of the depth profile  $Dt$  for the Pb concentration (left) and the Co concentration (right) as a functions of fluence. Solid lines indicate simulations using TRIDYN, dashed lines indicate TRIDER simulations. Different colors denote different fluences indicated in the legends.

the total mixing can be even amplified by a few orders of magnitudes, if the thermally activated kinetics of atoms is considered. A similar result for Pt/Cr/Co interfaces has been seen experimentally [210]. The formation of PtCrCo was there investigated with high-resolution transmission electron microscopy and the enhancement of mixing was confirmed by the comparison with the TRIDYN simulations.

## 4.5 Conclusions

The new simulation method unifying two computation approaches is applied to interface mixing in bimetal. It has been proved that models based on the unification BCA and KMC techniques are broadly applicable and give solutions that are in agreement with experiments. The processes, which are acting during ion irradiation, i.e. ballistic displacement as well as thermally activated migration, in many cases are mutually dependent from each other. The presented approaches open a new possibility for simulation of ion irradiation, with a detailed description of the ion-solid interactions, applicable to spatiotemporal scale of experiments. The two types of system were investigated and compared with the TRIDYN method. The results prove the importance of including the relaxation of defects in computations, what is the major improvement over the TRIDYN method. For Al/Pb bimetal the total mixing has been suppressed due to relaxation of bulk defect, whereas for Co/Pt bimetal the total mixing has been amplified.



*You climb to reach the summit,  
but once there,  
discover that all roads lead down.*

Stanisław Lem (1921 - 2006)

# 5

## Summary

The main objectives of this thesis have been the large scale atomistic, multiphysics simulations capable to reproduce and understand periodic pattern formations during ion beam irradiation. At the beginning of the thesis work, several experimental reports appeared suggesting a huge variety of patterns for different ion energies and incidence angles (e.g. [117–119]), which were inconsistent with several theoretical predictions. Thus, the formation of patterns (dots and ripples) on Si at normal incidence and incidence angles below  $50^\circ$  were often seen in experiments, but never obtained by TRIDER simulations. Only recently the crucial influence of metal impurities created in the experimental setups has been revealed. New, very clean experiments (without metal contamination of the surface) agree to a large extent with TRIDER predictions, what allows now for a detailed study of the dominating driving forces of pattern formation. Even a very low concentration of impurities can induce formation of a structure not observed under ‘clean’ conditions.

To describe periodic pattern formation the best atomistic simulation, would be molecular dynamics (MD). However, spatio-temporal scales of experiments are not accessible by MD. Atomistic KMC simulations in the framework of Solid on Solid model (i.e. describing kinetics of two-dimensional surfaces) can contribute to the general understanding only partially, because they require some phenomenological components.

In the framework of this thesis the novel program package TRIDER for simulating ion-solid interactions including relaxation processes has been developed. The full ion-induced collision cascades in matter, described by TRIM, and the subsequent relaxation of defects, treated with three-dimensional lattice KMC, are unified. By this method it is now possible to simulate ion fluences of  $10^{18} \text{ cm}^{-2}$  on irradiated surfaces of  $100 \times 100 \text{ nm}^2$ . Simulations of such fluences and areas are necessary to study the formation of periodic surface patterns under ion irradiation.

The investigation of self-organizing processes of the pattern formation using TRIDER simulations is summarized by the following major statements (*theses*):

1. TRIDER simulations result so far in the largest conformity with low energetic IBS experiments. The results of the simulation presented here allow to reproduce the recently broadly accepted ‘phase diagram’ of Madi *et al.* [147]:
  - a) No ripples predicted at ion incidence angles between  $0^\circ$  and  $50^\circ$  to the surface normal, which was for a long time in contradiction with the contaminated experiments. Only very recently, ‘clean’ experiments are consistent with our theoretical predictions, especially the ‘phase diagram’.
  - b) TRIDER simulations predict a switch from ripples orientation perpendicular to parallel with respect to the ion beam direction at incidence angle  $\theta = 80^\circ$ , which agrees with experimental studies.

2. TRIDER simulations predicts coarsening of ripples aligned perpendicular to the ion beam direction, in agreement with experiments. Other two-dimensional atomistic simulations as well as many continuum equations based on the Bradley-Harper theory cannot reproduce this type of coarsening.
3. The wavelength of ‘low-energy’ ripples on Si irradiated by Ar<sup>+</sup> ions at  $\theta > 60^\circ$  achieves a steady-state at about 30 nm [99] for both, experiments and TRIDER simulations.
4. Power law dependence of the surface roughness and the ripple wavelength as a function of ion fluence is predicted by TRIDER simulations. The growth exponent  $\beta$  is in the range of 0.29-0.38 and coarsening exponent  $l$  is between 0.08 and 0.18, which is consistent with experimental studies of Keller *et al.* [99,211].
5. TRIDER simulations reveal that sputtering is not the dominant driving force for self-organization of ripples at non-grazing ion incidences. The dominating driving force is kinetics of bulk and surface defects created by the collision cascade.
6. The increase of ion energy reduces the tendency of ripple formation, as measured by the roughness exponent  $\alpha$ . Increasing ion energy from 50 eV to 300 eV, the  $\alpha$  exponent decreases from 0.9 to 0.5.
7. As it is shown by preliminary studies, TRIDER will allow a direct comparison of the atomistic simulation with continuum theory based on the mass currents registration.
  - a) Without ion irradiation, the surface current vectors on an initially sinusoidal surface have a down-hill direction tangential to the surface. The system maintains MH smoothing behavior.
  - b) Under ion irradiation, the surface current vectors tend to point in ion beam direction.
  - c) The separation between MH diffusion and ion induced processes provides opportunity to compare the atomistic modeling and continuum theories. Utilizing results from this thesis the basis for a subsequent Ph.D. thesis, which started within the second funding project of DFG research group 845, is provided.

As a second, application of TRIDER to ion-solid interactions for interfaces of bimetals under ion irradiation are studied. It is shown that the enthalpy of mixing is a significant factor suppressing or amplifying the mixing rate at interfaces of immiscible or miscible alloys, respectively. The studies of bimetals irradiated by light ions at high energies (150 keV) are summarized by the following *theses*:

1. The interface of metal atoms for KMC has been described in two different manners:
  - a) For immiscible metals (positive enthalpy of mixing), i.e. Al/Pb, the activation energies of Al and Pb have been calculated from the relation between temperature and solubility in the rich Al and the rich Pb phases.
  - b) For intermetallic forming metals (negative enthalpy of mixing), i.e. Co/Pt, adjustment of the ordering temperature of the L1<sub>0</sub> formation has been performed.

- 
2. Analytical form of interatomic interaction in metals has been derived using RGL potential [197] for KMC simulations. It leads to a better description of interactions at surfaces and interfaces under ion irradiation.
  3. In Al/Pb bimetals irradiated by He<sup>+</sup> ions, phase separation and cluster creation in the Al rich and the Pb rich phases is predicted by TRIDER simulations. The average Al cluster size is larger than the average Pb cluster size due to 10 times larger solubility of Pb in the Al rich phase than the solubility of Al in the Pb rich phase.
  4. In Co/Pt bimetals irradiated by He<sup>+</sup> ions, the TRIDER simulations accurately predicts formation of the L1<sub>0</sub> phase with some inaccuracy regarding formation of the L1<sub>2</sub> phase.
  5. The comparison of results obtained with TRIDER and TRIDYN simulations with respect to the depth profiling of elements is provided. It shows that heat of mixing has a great influence on these profiles:
    - a) For low fluences, mixing predicted by TRIDER in Al/Pb is suppressed, and it is amplified for Pt/Co.
    - b) TRIDER simulation of high fluence irradiation provides additional information like: periodic variation of the concentration at the interface due to the cluster formation and formation of step-like concentration profiles originating from a sequence of L1<sub>0</sub> and L1<sub>2</sub> phases.

The TRIDER program package developed in the framework of this thesis provides a full description of ballistic and relaxation processes induced by ion irradiation. TRIDER accelerates simulation considerably, which can be performed alternatively, but only partially, by extremely time-consuming MD calculations. Therefore, it provides a promising tool to simulate ion beam processes in matter.





## Nuclear stopping in Al/Pb bimetal

Irradiation of Al/Pb bimetals with  $\text{He}^+$  ions reveals very interesting properties of this material. The nuclear stopping  $S_n$  of Al is much larger than that of Pb at low-energy  $\text{He}^+$  bombardment. However, above 20 keV, the nuclear stopping becomes larger for Pb (see Fig. A.1). At the ion energy used during simulations of the Al/Pb interface mixing, i.e. 150 keV, the nuclear stopping in Pb is almost two times larger than in Al.

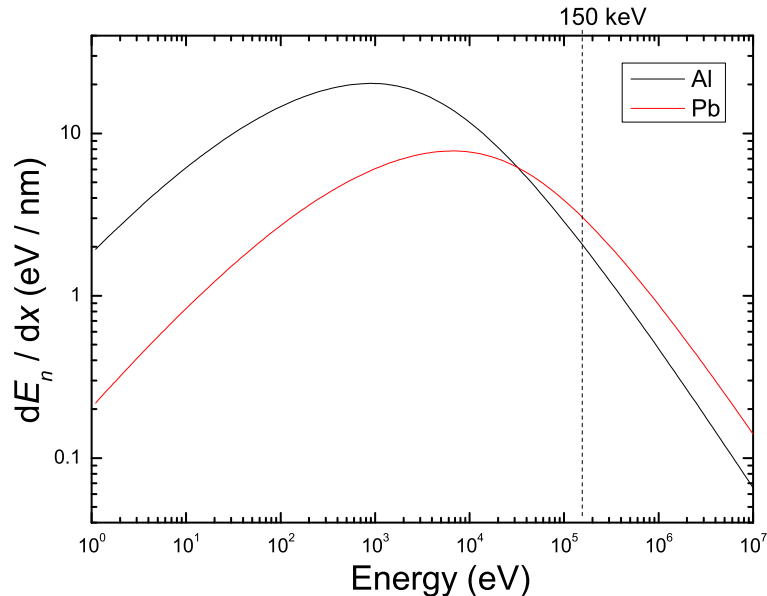


Figure A.1.: Nuclear stopping power for for  $\text{He}^+$  ions in Al (black) and in Pb (red), as predicted by transport theory (Sec. 2.1.2). With the dashed line the ion energy used in interface mixing simulations is indicated. The data are generated using the SRIM-2008 package [30].

The number of defects created within the collision cascade is correlated with the nuclear stopping power and to the energy transferred to phonons, as it is shown in Fig. A.2b. It has been calculated with TRIDYN simulation using the ‘static’ mode, i.e. without any change in concentration profiles during the simulation [72]. Higher nuclear stopping power should result in the higher defect creation. To understand the dependence of the nuclear stopping on the penetration depth of ions in Al/Pb bimetal, four different regions are described:

- (i) The nuclear stopping within the whole Al layer is constant, about 2.1 eV/nm, as predicted by the transport theory (see Fig. A.2b). The defect creation in the region near to the surface is proportional rather to the phonon energy than to the nuclear stopping power. The nuclear stopping power is assigned only to the ion



energy loss. The defects are created not only by displacements caused by the ion, but also by displacements caused by recoils. In the surface region, the collision cascade has not yet fully developed, and therefore, fewer defects are produced.

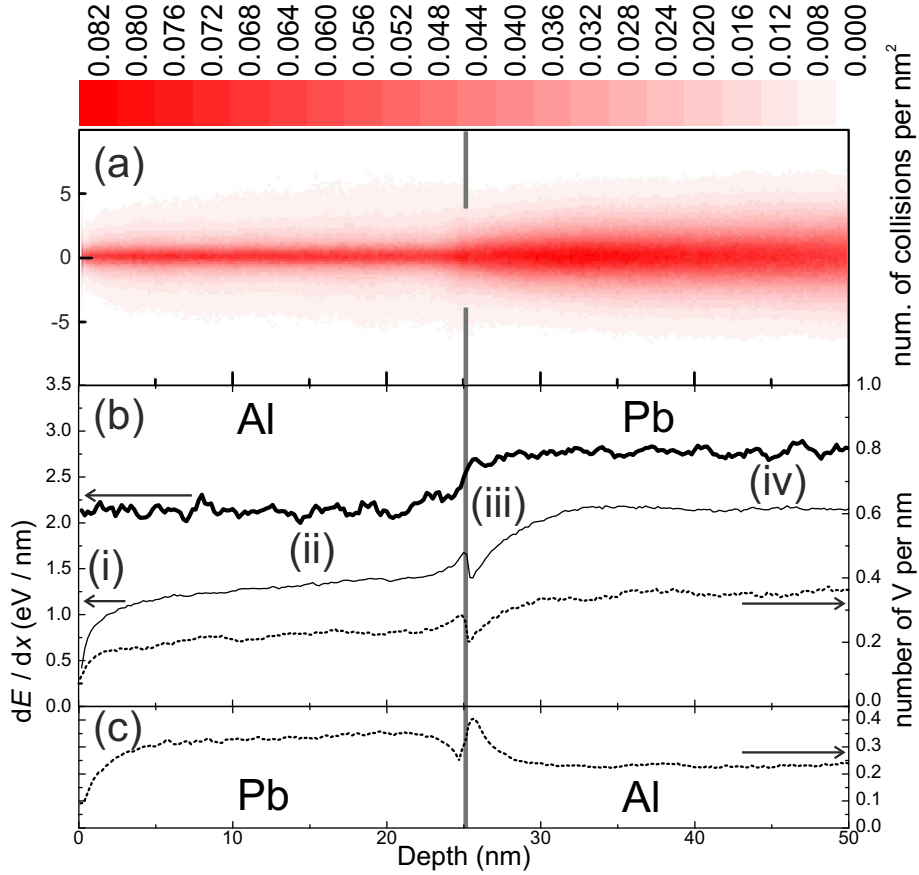


Figure A.2.: Ion trajectories plotted as two-dimensional distribution of collision events (a). Nuclear stopping (thick solid line), energy transfer to phonons (thin solid line) and number of created vacancies (dashed line) per 150 keV  $\text{He}^+$  in Al/Pb bimetal (b). The number of vacancies in Pb/Al bimetal is plotted in (c). With gray line the interface is indicated. The data are generated using the ‘static’ mode of the TRIDYN program [72].

- (ii) The trajectory for all projectiles given in Fig. A.2a becomes more and more diverged from the longitudinal direction the deeper ions penetrate into the target. The strongest divergence in Al occurs at the interface. The damage accumulated in target is proportional to the number of scatter events occurred at the given depth caused by the recoil collisions. If the trajectory diverges from the longitudinal direction, the total path length increases as well as the number of scatter events, leading to slight increase of the number of created bulk defects (Fig. A.2b).
- (iii) Directly at the interface a peak in defect distribution appears, which is lowered significantly straight after the Pb layer starts, although the nuclear stopping power in Pb is constant with about 2.8 eV/nm accordingly to the transport theory (Fig. A.1). The origin of the peak can be related to the low-energy Pb recoils, which increase the damage creation in the light Al layer due to backscatter events of Pb into Al. The depression in the defects distribution is caused by the low energetic light Al recoils, which are backreflected from the interface, creating less damage in

---

Pb at the interface. To confirm this analysis, a simulation of Pb/Al bimetal has been performed (Fig. A.2c). Here, the sequence of peak/suppressions is reversed. The peak in defect distribution obtained in the Al layer is even higher than for Al/Pb bimetal, where only the backscattered Pb recoils contributed to the damage increase in Al. On the other hand the depression in the Pb layer corresponds to lower damage production due to light Al recoils, similarly like in Al/Pb bimetal.

- (iv) The number of defects in Pb layer increases slowly with depth, similarly as it was described in point (ii), and saturates at the depth of 33 nm, where beyond the interface a new equilibrium of the collision cascade is reached.



# List of Figures

1.1.	Two types of self-organization . . . . .	1
1.2.	Two examples of self-organizing processes . . . . .	2
1.3.	Schematic plot of the one-dimensional crater topography after the impact . . . . .	4
2.1.	Schematic diagram of time-space efficiency . . . . .	7
2.2.	Scattering cross section . . . . .	10
2.3.	Schematic of a collision cascade . . . . .	12
2.4.	Nuclear stopping power plotted in reduced coordinates . . . . .	13
2.5.	Electronic stopping cross sections . . . . .	15
2.6.	Sputtering yields for Ar bombardment of Si . . . . .	16
2.7.	Schematic of ion-beam mixing processes . . . . .	18
2.8.	Ranges distributions of Ga <sup>+</sup> and He <sup>+</sup> at 30 keV Pt <sup>+</sup> calculated with SRIM . . . . .	23
2.9.	Schematic representation of simulation procedure followed in TRIDYN . . . . .	24
2.10.	Scheme of simple activation pathway in KMC . . . . .	29
2.11.	Lattice representation in KMC simulations for 1 component system . . . . .	32
2.12.	Scheme of KMC simulations for 2 component system . . . . .	33
2.13.	Variety of processes present during ion irradiation . . . . .	34
2.14.	Schematic of the surface treatment . . . . .	36
2.15.	Surface representation . . . . .	37
2.16.	Mapping from BCA to KMC configuration of defects . . . . .	38
2.17.	Schematic of a recombination procedure . . . . .	39
2.18.	Schematic flow diagram of simulation sequence . . . . .	41
2.19.	Demonstration of simulation stages with the TRIDER simulation . . . . .	42
3.1.	Variety of processes present during ion irradiation and their influence on the surface morphology . . . . .	47
3.2.	Time evolution of the average number of defects by self-irradiation of Si . . . . .	50
3.3.	Average distributions of defects over depth . . . . .	50
3.4.	I/V excess with defect relaxation . . . . .	51
3.5.	Scheme of surface crater formation by bulk defects relaxation . . . . .	52
3.6.	Defect excess by ion irradiation and defect distributions . . . . .	52
3.7.	Crater distributions of Ar <sup>+</sup> impact on Si for $\theta = 0^\circ$ . . . . .	54
3.8.	Crater distributions of Ar <sup>+</sup> impact on Si for $\theta = 30^\circ$ . . . . .	55
3.9.	Crater distributions of Ar <sup>+</sup> impact on Si for $\theta = 67^\circ$ . . . . .	56
3.10.	Crater distributions of Ar <sup>+</sup> impact on Si for $\theta = 85^\circ$ . . . . .	57
3.11.	Comparison between the simulated crater distributions and the fitted crater functions . . . . .	58
3.12.	Reconstruction of two-dimensional DoG function from two Gaussian functions . . . . .	59
3.13.	Simulated surface topographies at 0.8-1 keV Ar <sup>+</sup> irradiation of Si for different incidence angles without local-flux correction . . . . .	63
3.14.	Simulated surface topographies at 60° Ar <sup>+</sup> irradiation of Si for different ion energies without local-flux correction . . . . .	64
3.15.	Schematic plot of interface width as a function of time and square root of the height-height correlation function as a function of a spatial separation between the two points . . . . .	66

3.16. Interface width and ripple wavelength evolution for different fluxes at $\theta = 60^\circ$ without local-flux correction . . . . .	67
3.17. Interface width and ripple wavelength evolution for different fluxes at $\theta = 85^\circ$ without local-flux correction . . . . .	68
3.18. Interface width and ripple wavelength evolution for different incidence angles without local-flux correction . . . . .	69
3.19. Interface width and ripple wavelength evolution for different ion energies without local-flux correction . . . . .	69
3.20. Simulated surface topographies at 250 eV Ar <sup>+</sup> irradiation of Si for different incidence angles with local-flux correction . . . . .	71
3.21. Surface morphology evolution with fluence at 70° Ar <sup>+</sup> irradiation of Si . . . . .	71
3.22. Simulated surface pattern topographies with and without sputtering for different ion energies and incidence angle with local-flux correction . . . . .	72
3.23. Height-height correlation functions - comparison with and without sputtering . . . . .	73
3.24. Interface width and ripple wavelength evolution at different fluxes with local-flux correction . . . . .	75
3.25. Interface width and ripple wavelength evolution at different incidence angles with local-flux correction . . . . .	76
3.26. Interface width and ripple wavelength evolution for different ion energies with the local-flux correction . . . . .	76
3.27. TRIDER simulation of 250 eV Ar <sup>+</sup> irradiation of Si at 70° ion incidence angle . . . . .	78
3.28. Representation of the surface curvature $\kappa$ at the $1 + 1d$ boundary, and the $2 + 1d$ phase boundary . . . . .	80
3.29. Initial configuration of the simulation cell during investigation of the surface current as a sinus function . . . . .	82
3.30. Simulated plots of $\vec{j}$ and $-\nabla\vec{j}$ with respect to the $x$ component of $h$ without ion bombardment . . . . .	83
3.31. Plots of defects for rippled surface (250 eV Ar <sup>+</sup> , 70° ion incidence) . . . . .	84
3.32. Simulated plots of $\vec{j}$ and $-\nabla\vec{j}$ , with respect to the $x$ component of $h$ including ion bombardment, with and without sputtering . . . . .	85
4.1. A phase diagram of immiscible alloy and its solidi presented as an Arrhenius plot . . . . .	89
4.2. Phase diagram for the systems Al-Pb and Co-Pt . . . . .	91
4.3. Cohesive energy as the function of the NN occupation number for Al-Pb and Pt-Co . . . . .	92
4.4. Contour plot of the cohesive energy as a function of the NN occupation number for the Al-Pb and the Pt-Co . . . . .	93
4.5. Perspective view of Al/Pb lattice cell cells after a single ion incidence with 30 keV ion energy . . . . .	94
4.6. 3D view of Al/Pb simulation cell for the different visualization condition . . . . .	95
4.7. Mean bond energies across the interface in Al/Pb bilayer. . . . .	96
4.8. Vacancy locations inside the Pt/Co bimetal and simulation slices of chemical ordering to L1 <sub>0</sub> and L1 <sub>2</sub> . . . . .	97
4.9. Comparison of depth profiles after 150 keV He <sup>+</sup> irradiation of Al/Pb bimetals . . . . .	99

4.10. Comparison of depth profiles after 150 keV He <sup>+</sup> irradiation of Pt/Co bimetals . . . . .	100
4.11. Comparison between the Pb and Co profiles and interface width of the Pb and Co . . . . .	101
A.1. Nuclear stopping power for He <sup>+</sup> ions in Al and Pb . . . . .	107
A.2. Ion trajectories, nuclear stopping, energy to phonons and number of cre- ated vacancies in Al/Pb bimetal irradiated with He <sup>+</sup> ion . . . . .	108



# List of Tables

2.1. Comparison between TRIM and CRYSTAL-TRIM at low energies . . . . .	26
3.1. Fitting parameters obtained by 3D fitting to the Eq. (3.2) . . . . .	60
4.1. Simulation parameters for the tight-binding potential . . . . .	91





# Bibliography

- [1] P. Sutter, W. Ernst, Y. S. Choi and E. Sutter. MECHANISMS OF THERMALLY INDUCED DEWETTING OF ULTRATHIN SILICON-ON-INSULATOR. *Appl. Phys. Lett.* **88**, 141924 (2006).
- [2] R. Röntzsch. *Shape Evolution of Nanostructures by Thermal and Ion Beam Processing*. Ph.D. Thesis. TU Dresden (2007).
- [3] M. Navez, D. Chaperot and C. Sella. MICROSCOPIE ELECTRONIQUE - ETUDE DE L'ATTAQUE DU VERRE PAR BOMBARDEMENT IONIQUE. *C. R. Acad. Sci. Paris* **254**(2), 240 (1962).
- [4] R. M. Bradley and J. M. E. Harper. THEORY OF RIPPLE TOPOGRAPHY INDUCED BY ION-BOMBARDMENT. *J. Vac. Sci. Tech. A* **6**, 2390 (1988).
- [5] S. Park, B. Kahng, H. Jeong and A. L. Barabasi. DYNAMICS OF RIPPLE FORMATION IN SPUTTER EROSION: NONLINEAR PHENOMENA. *Phys. Rev. Lett.* **83**, 3486 (1999).
- [6] R. Cuerno and A. L. Barabasi. DYNAMIC SCALING OF ION-SPUTTERED SURFACES. *Phys. Rev. Lett.* **74**, 4746 (1995).
- [7] M. A. Makeev, R. Cuerno and A. L. Barabasi. MORPHOLOGY OF ION-SPUTTERED SURFACES. *Nucl. Instr. Meth. B* **197**, 185 (2002).
- [8] J. Munoz-Garcia, M. Castro and R. Cuerno. NONLINEAR RIPPLE DYNAMICS ON AMORPHOUS SURFACES PATTERNED BY ION BEAM SPUTTERING. *Phys. Rev. Lett.* **96**, 086101 (2006).
- [9] P. Sigmund. THEORY OF SPUTTERING .I. SPUTTERING YIELD OF AMORPHOUS AND POLYCRYSTALLINE TARGETS. *Phys. Rev.* **184**, 383 (1969).
- [10] A. K. Hartmann, R. Kree, U. Geyer and M. Kolbel. LONG-TIME EFFECTS IN A SIMULATION MODEL OF SPUTTER EROSION. *Phys. Rev. B* **65**, 193403 (2002).
- [11] E. Chason, W. L. Chan and M. S. Bharathi. KINETIC MONTE CARLO SIMULATIONS OF ION-INDUCED RIPPLE FORMATION: DEPENDENCE ON FLUX, TEMPERATURE, AND DEFECT CONCENTRATION IN THE LINEAR REGIME. *Phys. Rev. B* **74**, 224103 (2006).
- [12] E. O. Yewande, A. K. Hartmann and R. Kree. PROPAGATION OF RIPPLES IN MONTE CARLO MODELS OF SPUTTER-INDUCED SURFACE MORPHOLOGY. *Phys. Rev. B* **71**, 195405 (2005).
- [13] M. Moseler, P. Gumbsch, C. Casiraghi, A. C. Ferrari and J. Robertson. THE ULTRASMOOTHNESS OF DIAMOND-LIKE CARBON SURFACES. *Science* **309**, 1545 (2005).
- [14] G. Carter and V. Vishnyakov. ROUGHENING AND RIPPLE INSTABILITIES ON ION-BOMBARDED Si. *Phys. Rev. B* **54**, 17647 (1996).
- [15] P. Süle and K. H. Heinig. THE MOLECULAR DYNAMICS SIMULATION OF ION-INDUCED RIPPLE GROWTH. *J. Chem. Phys.* **131**(20), 204704 (2009).
- [16] N. Kalyanasundaram, M. Ghazisaeidi, J. B. Freund and H. T. Johnson. SINGLE IMPACT CRATER FUNCTIONS FOR ION BOMBARDMENT OF SILICON. *Appl. Phys. Lett.* **92**, 131909 (2008).

- [17] S. A. Norris, M. P. Brenner and M. J. Aziz. FROM CRATER FUNCTIONS TO PARTIAL DIFFERENTIAL EQUATIONS: A NEW APPROACH TO ION BOMBARDMENT INDUCED NONEQUILIBRIUM PATTERN FORMATION. *J. Phys. Cond. Mat.* **21**, 224017 (2009).
- [18] N. Kalyanasundaram, J. B. Freund and H. T. Johnson. A MULTISCALE CRATER FUNCTION MODEL FOR ION-INDUCED PATTERN FORMATION IN SILICON. *J. Phys. Cond. Mat.* **21**(22), 224018 (2009).
- [19] R. M. Bradley and P. D. Shipman. SPONTANEOUS PATTERN FORMATION INDUCED BY ION BOMBARDMENT OF BINARY COMPOUNDS. *Phys. Rev. Lett.* **105**, 145501 (2010).
- [20] E. M. Bringa, K. Nordlund and J. Keinonen. CRATERING-ENERGY REGIMES: FROM LINEAR COLLISION CASCADES TO HEAT SPIKES TO MACROSCOPIC IMPACTS. *Phys. Rev. B* **64**(23), 235426 (2001).
- [21] P. Huang and E. A. Carter. ADVANCES IN CORRELATED ELECTRONIC STRUCTURE METHODS FOR SOLIDS, SURFACES, AND NANOSTRUCTURES. *Annu. Rev. Phys. Chem.* **59**, 261 (2008).
- [22] R. M. Martin. *Electronic structure: Basic theory and practical methods*. Cambridge University Press (2004).
- [23] R. O. Jones and O. Gunnarsson. THE DENSITY FUNCTIONAL FORMALISM, ITS APPLICATIONS AND PROSPECTS. *Rev. Mod. Phys.* **61**, 689 (1989).
- [24] J. P. Perdew and Y. Wang. ACCURATE AND SIMPLE ANALYTIC REPRESENTATION OF THE ELECTRON-GAS CORRELATION ENERGY. *Phys. Rev. B* **45**, 5048 (1992).
- [25] S. Kurth, J. P. Perdew and P. Blaha. MOLECULAR AND SOLID-STATE TESTS OF DENSITY FUNCTIONAL APPROXIMATIONS: LSD, GGAs, AND meta-GGAs. *Int. J. Quantum Chem.* **75**, 889 (1999).
- [26] H. Gould, J. Tobochnik and W. Christian. *An introduction to computer simulation methods: Applications to physical systems - 3rd Ed.* Addison Wesley, San Francisco (2006).
- [27] L. Verlet. COMPUTER 'EXPERIMENTS' ON CLASSICAL FLUIDS. I. THERMODYNAMICAL PROPERTIES OF LENNARD-JONES MOLECULES. *Phys. Rev.* **159**, 98–103 (1967).
- [28] P.T. Cummings and S.C. Glotzer. *Inventing a new America through discovery and innovation in science, engineering and medicine: A vision for research and development in simulation-based engineering and science in the next decade*. Baltimore, Md.: World Technology Evaluation Center, Inc (2010).
- [29] J. Samela and K. Nordlund. ATOMISTIC SIMULATION OF THE TRANSITION FROM ATOMISTIC TO MACROSCOPIC CRATERING. *Phys. Rev. Lett.* **101**, 027601 (2008).
- [30] J. F. Ziegler, J. P. Biersack and U. Littmark. *Stopping power and ranges of ion in matter*. volume 1. Pergamon, New York (1985).
- [31] M. Nastasi, J. W. Mayer and J. K. Hirvonen. *Ion-solid interactions: fundamentals and applications*. volume 11. Cambridge University Press (1996).
- [32] P. Sigmund. *Particle penetration and radiation effects*. volume 151 of *Springer Series in Solid State Science*. Cambridge University Press. Cambridge (1997).
- [33] R. Smith. *Atomistic and ion collisions in solids and at surfaces*. Cambridge University Press. Cambridge (1997).

- [34] G. S. Was. *Fundamentals of radiation material science: Metals and alloys*. Springer-Verlag, Berlin Heidelberg (2007).
- [35] W. D. Wilson, L. G. Haggmark and J. P. Biersack. CALCULATIONS OF NUCLEAR STOPPING, RANGES, AND STRAGGLING IN LOW-ENERGY REGION. *Phys. Rev. B* **15**, 2458 (1977).
- [36] O. B. Firsov. A QUALITATIVE INTERPRETATION OF THE MEAN ELECTRON EXCITATION ENERGY IN ATOMIC COLLISIONS. *Sov. Phys. JETP* **6**, 534 (1959).
- [37] M. Vicanek and H. M. Urbassek. ENERGY AND ANGULAR-DISTRIBUTIONS OF SPUTTERED PARTICLES - A COMPARISON BETWEEN ANALYTICAL THEORY AND COMPUTER-SIMULATION RESULTS. *Nucl. Instr. Meth. B* **30**(4), 507–513 (1988).
- [38] J. P. Biersack and W. Eckstein. SPUTTERING STUDIES WITH THE MONTE CARLO PROGRAM TRIM.SP. *Appl. Phys. A* **34**, 73 (1984).
- [39] W. Möller, W. Eckstein and J. P. Biersack. TRIDYN - BINARY COLLISION SIMULATION OF ATOMIC COLLISIONS AND DYNAMIC COMPOSITION CHANGES IN SOLIDS. *Comput. Phys. Commun.* **51**, 355 (1988).
- [40] J. Lindhard, M. Scharff and H. E. Schiott. RANGE CONCEPTS AND HEAVY ION RANGES (NOTES ON ATOMIC COLLISIONS II). *Mat. Fys. Medd. Dan Vid. Selsk.* **33**, 3 (1963).
- [41] N. Matsunami, Y. Yamamura, Y. Itikawa, N. Itoh, Y. Kazumata, S. Miyagawa, K. Morita and R. Shimizu. ENERGY DEPENDENCE OF THE ION-INDUCED SPUTTERING YIELDS OF MONATOMIC SOLIDS. *Rad. Eff. Def. Sol.* **57**, 15 (1980).
- [42] H. Bethe. THE THEORY OF THE PASSAGE OF RAPID NEUTRON RADIATION THROUGH MATTER. *Annu. Phys.* **5**(3), 325 (1930).
- [43] F. Bloch. THE SLOW DOWN OF RAPIDLY MOVING PARTICLES IN THE THEIR PASSING THROUGH SOLID MATTER. *Annu. Phys.* **16**(3), 285 (1933).
- [44] H. Sugiyama. MODIFICATION OF LINDHARD-SCHARFF-SCHIOTT FORMULA FOR ELECTRONIC STOPPING POWER. *J. Phys. Soc. Jap.* **50**(3), 929 (1981).
- [45] R. Weissmann and P. Sigmund. SPUTTERING AND BACKSCATTERING OF LIGHT IONS BOMBARDING RANDOM TARGETS. *Radiat. Eff.* **19**, 7–14 (1973).
- [46] Y. Yamamura, C. Mossner and H. Oechsner. ANGULAR-DISTRIBUTIONS OF SPUTTERED ATOMS FROM ION-BOMBARDED SURFACES. *Rad. Eff. Def. Sol.* **105**(1-2), 31 (1987).
- [47] K. Wittmaack. ANALYTICAL DESCRIPTION OF THE SPUTTERING YIELDS OF SILICON BOMBARDED WITH NORMALLY INCIDENT IONS. *Phys. Rev. B* **68**(23), 235211 (2003).
- [48] J. Bohdanský. A UNIVERSAL RELATION FOR THE SPUTTERING YIELD OF MONATOMIC SOLIDS AT NORMAL ION INCIDENCE. *Nucl. Instr. Meth. B* **2**(1-2), 587 (1984).
- [49] N. Matsunami, Y. Yamamura, Y. Itikawa, N. Itoh, Y. Kazumata, S. Miyagawa, K. Morita, R. Shimizu and H. Tawara. ENERGY-DEPENDENCE OF THE ION-INDUCED SPUTTERING YIELDS OF MONATOMIC SOLIDS. *At. Dat. Nucl. Dat. Tabl.* **31**(1), 1 (1984).
- [50] Y. Yamamura and N. Itoh. *Sputtering Yield, in ion beam assisted film growth*. Elsevier, Amsterdam (1989).

- [51] Y. Yamamura, Y. Itikawa and N. Itoh. *Angular dependence of sputtering yields of monoatomic solids*. report IPPJ-AM-26. Institute of Plasma Physics, Nagoya University (1983).
- [52] W. Eckstein and R. Preuss. NEW FIT FORMULA FOR THE SPUTTERING YIELD. *J. Nucl. Mat.* **320**(3), 209 (2003).
- [53] W. F. van der Weg, D. Sigurd and J. W. Mayer. *Ion-beam induced intermixing in the Pd/Si system*. Applications of Ion Beams of Metals. Plenum Press, New York (1979).
- [54] S. Matteson, B. M. Paine, M. G. Grimaldi, G. Mezey and M. A. Nicolet. ION-BEAM MIXING IN AMORPHOUS-SILICON. EXPERIMENTAL INVESTIGATION. *Nucl. Instr. Meth.* **182**, 43 (1981).
- [55] H. H. Andersen. DEPTH RESOLUTION OF SPUTTER PROFILING. *Appl. Phys.* **18**(2), 131 (1979).
- [56] R. A. Swalin. *Thermodynamics of Solids*. 2nd Ed. Wiley-Interscience, New York (1972).
- [57] P. G. Schewmon. *Diffusion in Solids*. McGraw-Hill, New York (1963).
- [58] M. van Rossum, Y. T. Cheng, M. A. Nicolet and W. L. Johnson. CORRELATION BETWEEN COHESIVE ENERGY AND MIXING RATE IN ION MIXING OF METALLIC BILAYERS. *Appl. Phys. Lett.* **46**(6), 610 (1985).
- [59] F. Rossi and M. Nastasi. CASCADE STRUCTURE AND OVERLAP EFFECTS IN ION-BEAM MIXING EXPERIMENTS. *J. Appl. Phys.* **69**(3), 1310 (1991).
- [60] S. Matteson, J. Roth and M. A. Nicolet. ION-INDUCED SILICIDE FORMATION IN NIOBIUM THIN-FILMS. *Rad. Eff. Def. Sol.* **42**(3-4), 217 (1979).
- [61] J. Eckstein. *Computer simulation of ion-solid interactions*. Springer-Verlag (1991).
- [62] J. P. Biersack and L. G. Haggmark. A MONTE-CARLO COMPUTER-PROGRAM FOR THE TRANSPORT OF ENERGETIC IONS IN AMORPHOUS TARGETS. *Nucl. Instr. Meth.* **174**, 257 (1980).
- [63] M. T. Robinson. COMPUTER SIMULATION OF COLLISION CASCADES IN MONAZITE. *Phys. Rev. B* **27**, 5347 (1983).
- [64] M. Posselt and J. P. Biersack. COMPUTER SIMULATION OF ION IMPLANTATION INTO CRYSTALLINE TARGETS. *Nucl. Instr. Meth. B* **64**, 706 (1992).
- [65] H.-B. Kim, G. Hobler, A. Steiger, A. Lugstein and E. Bertagnolli. FULL THREE-DIMENSIONAL SIMULATION OF FOCUSED ION BEAM MICRO/NANOFABRICATION. *Nanotechnology* **18**(24) (2007).
- [66] I. Bizyukov, A. Mutzke, R. Schneider, A. M. Gigler and K. Krieger. MORPHOLOGY AND CHANGES OF ELEMENTAL SURFACE COMPOSITION OF TUNGSTEN BOMBARDED WITH CARBON IONS. *Nucl. Instr. Meth. B* **266**(9), 1979 (2008).
- [67] A. Mutzke, R. Schneider and I. Bizyukov. SDTrimSP-2D STUDIES OF THE INFLUENCE OF MUTUAL FLUX ARRANGEMENT ON EROSION AND DEPOSITION. *J. Nucl. Mat.* **390-91**, 115 (2009).
- [68] O. S. Oen and M. T. Robinson. COMPUTER STUDIES OF REFLECTION OF LIGHT-IONS FROM SOLIDS. *Nucl. Instr. Meth.* **132**, 647 (1976).
- [69] P. V. Ajda. IS THERE A DEPENDENCE OF DISPLACEMENT THRESHOLD ENERGY IN METALS IN ENERGY OF BOMBARDING PARTICLE. *Rad. Eff. Def. Sol.* **36**(1-2), 123 (1978).

- [70] P. Jung. RELATION BETWEEN THRESHOLD ENERGY FOR ATOMIC DISPLACEMENT IN METALS, BULK MODULUS, AND INTER-ATOMIC POTENTIAL. *Rad. Eff. Def. Sol.* **35**(3), 155 (1978).
- [71] P. Jung. AVERAGE ATOMIC-DISPLACEMENT ENERGIES OF CUBIC METALS. *Phys. Rev. B* **23**(2), 664 (1981).
- [72] W. Möller and W. Eckstein. TRIDYN - A TRIM SIMULATION CODE INCLUDING DYNAMIC COMPOSITION CHANGES. *Nucl. Instr. Meth. B* **2**, 814 (1984).
- [73] A. Mutzke and R. Schneider. SDTrimSP-2D  $a_b$ : *Simulation of Particles Bombarding on a Two Dimensional Target*. Laboratory Report. Max-Planck-Institut für Plasmaphysik, Garching (2009).
- [74] K. Gärtner, D. Stock, B. Weber, G. Betz, M. Hautala, G. Hobler, M. Hou, S. Sarite, W. Eckstein, J. J. Jimenezrodriguez, A. M. C. Perezmartin, E. P. Andriobet, V. Konoplev, A. Grasmarti, M. Posselt, M. H. Shapiro, T. A. Tombrello, H. M. Urbassek, H. Hensel, Y. Yamamura and W. Takeuchi. ROUND-ROBIN COMPUTER-SIMULATION OF ION TRANSMISSION THROUGH CRYSTALLINE LAYERS. *Nucl. Instr. Meth. B* **102**(1-4), 183 (1995).
- [75] M. Posselt and K. H. Heinig. COMPARISON OF BC-SIMULATIONS AND MD-SIMULATIONS OF LOW-ENERGY ION-IMPLANTATION. *Nucl. Instr. Meth. B* **102**(1-4), 236 (1995).
- [76] K. Nordlund. MOLECULAR DYNAMICS SIMULATION OF ION RANGES IN THE 1-100 keV ENERGY RANGE. *Comput. Mat. Sci.* **3**, 448 (1995).
- [77] G. Hobler and G. Betz. ON THE USEFUL RANGE OF APPLICATION OF MOLECULAR DYNAMICS SIMULATIONS IN THE RECOIL INTERACTION APPROXIMATION. *Nucl. Instr. Meth. B* **180**, 203 (2001).
- [78] H. Y. Chan, M. P. Srinivasan, N. J. Montgomery, C. P. A. Mulcahy, S. Biswas, H. J. L. Gossman, M. Harris, K. Nordlund, F. Benistant, C. M. Ng, D. Gui and L. Chan. APPLICATION OF MOLECULAR DYNAMICS FOR LOW-ENERGY ION IMPLANTATION IN CRYSTALLINE SILICON. *J. Vac. Sci. Tech. B* **24**(1), 462 (2006).
- [79] J. Marro, A. B. Bortz, M. H. Kalos and J. L. Lebowitz. TIME EVOLUTION OF A QUENCHED BINARY ALLOY 2. COMPUTER-SIMULATION OF A 3-DIMENSIONAL MODEL SYSTEM. *Phys. Rev. B* **12**, 2000 (1975).
- [80] A. F. Voter. CLASSICALLY EXACT OVERLAYER DYNAMICS - DIFFUSION OF RHODIUM CLUSTERS ON Rh(100). *Phys. Rev. B* **34**, 6819 (1986).
- [81] M. Strobel, K. H. Heinig and W. Möller. THREE-DIMENSIONAL DOMAIN GROWTH ON THE SIZE SCALE OF THE CAPILLARY LENGTH: EFFECTIVE GROWTH EXPONENT AND COMPARATIVE ATOMISTIC AND MEAN-FIELD SIMULATIONS. *Phys. Rev. B* **64**, 245422 (2001).
- [82] K. Binder. ORDERING OF THE FACE-CENTERED-CUBIC LATTICE WITH NEAREST-NEIGHBOR INTERACTION. *Phys. Rev. Lett.* **45**, 811 (1980).
- [83] T. A. Abinandanan, F. Haider and G. Martin. COMPUTER SIMULATIONS OF DIFFUSIONAL PHASE TRANSFORMATIONS: MONTE CARLO ALGORITHM AND APPLICATION TO PRECIPITATION OF ORDERED PHASES. *Acta Materialia* **46**, 4243 (1998).
- [84] S. J. Mitchell and D. P. Landau. PHASE SEPARATION IN A COMPRESSIBLE 2D ISING MODEL. *Phys. Rev. Lett.* **97**, 025701 (2006).

- [85] S. I. Park, B.-J. Lee and H. M. Lee. ESTIMATION OF ORDER-DISORDER TRANSITION TEMPERATURE IN Pt-Co ALLOY BY MONTE CARLO SIMULATION USING MODIFIED EMBEDDED ATOM METHOD. *Scripta Materialia* **45**, 495 (2001).
- [86] H. Bernas, J.-Ph. Attane, K.-H. Heinig, D. Halley, D. Ravelosona, A. Marty, P. Auric, C. Chappert and Y. Samson. ORDERING INTERMETALLIC ALLOYS BY ION IRRADIATION: A WAY TO TAILOR MAGNETIC MEDIA. *Phys. Rev. Lett.* **91**, 077203 (2003).
- [87] M. Müller and K. Albe. LATTICE MONTE CARLO SIMULATIONS OF FePt NANOPARTICLES: INFLUENCE OF SIZE, COMPOSITION, AND SURFACE SEGREGATION ON ORDER-DISORDER PHENOMENA. *Phys. Rev. B* **72**, 094203 (2005).
- [88] W. Schweika. *Disordered alloys - diffuse scattering and Monte Carlo simulations*. volume 141. Springer Tracts in Modern Physics, Berlin (1998).
- [89] F. Soisson. KINETIC MONTE CARLO SIMULATIONS OF RADIATION INDUCED SEGREGATION AND PRECIPITATION. *J. Nucl. Mat.* **349**, 235 (2006).
- [90] P. Novikov, K.-H. Heinig, A. Larsen and A. Dvurechenskii. SIMULATION OF ION-IRRADIATION STIMULATED Ge NANOCUSTER FORMATION IN GATE OXIDES CONTAINING GeO<sub>2</sub>. *Nucl. Instr. Meth. B* **191**, 462 (2002).
- [91] K. Binder and D.W. Heermann. *Monte Carlo simulation in statistical physics*. 2nd Ed. volume 80. Springer, Berlin (1992).
- [92] S. Wolfram. STATISTICAL MECHANICS OF CELLULAR AUTOMATA. *Rev. Mod. Phys.* **55**, 601 (1983).
- [93] K. Albe. *Computersimulationen zu Struktur und Wachstum von Bornitrid*. Ph.D. Thesis, German. TU Dresden (1998).
- [94] M. Strobel. *Modeling and Computer Simulation of Ion Beam Synthesis of Nanostructures*. Ph.D. Thesis. TU Dresden (1999).
- [95] T. Müller. *Low Energy Ion Beam Synthesis of Si Nanocrystals for Nonvolatile Memories - Modeling and Process Simulations*. Ph.D. Thesis. TU Dresden (2005).
- [96] E. Ising. BEITRAG ZUR THEORIE DES FERROMAGNETISMUS. *Z. Physik* **31**, 253 (1925).
- [97] N. Metropolis, A. W. Rosenbluth, M. N. Rosenbluth, A. H. Teller and E. Teller. EQUATION OF STATE CALCULATIONS BY FAST COMPUTING MACHINES. *J. Chem. Phys.* **21**, 1087 (1953).
- [98] G. H. Vineyard. FREQUENCY FACTORS AND ISOTOPE EFFECTS IN SOLID STATE RATE PROCESSES. *J. Phys. Chem. Solids* **3**, 121 (1957).
- [99] A. Keller, S. Rossbach, S. Facsko and W. Möller. SIMULTANEOUS FORMATION OF TWO RIPPLE MODES ON ION SPUTTERED SILICON. *Nanotechnology* **19**, 135303 (2008).
- [100] K. Kawasaki. *Kinetics of Ising models*. volume 2 of *Phase Transitions and Critical Phenomena*. Academic Press, London (1972).
- [101] Internet source [www.cosmol.com](http://www.cosmol.com). COSMOL Multiphysics modeling and simulation.
- [102] S. Garruchet and M. Perez. MODELLING THE CARBON SNOEK PEAK IN FERRITE: COUPLING MOLECULAR DYNAMICS AND KINETIC MONTE-CARLO SIMULATIONS. *Comput. Mat. Sci.* **43**, 286 (2008).

- [103] N. N. Negulyaev, V. S. Stepanyuk, W. Hergert, P. Bruno and J. Kirschner. ATOMIC-SCALE SELF-ORGANIZATION OF Fe NANOSTRIPES ON STEPPED Cu(111) SURFACES: MOLECULAR DYNAMICS AND KINETIC MONTE CARLO SIMULATIONS. *Phys. Rev. B* **77**, 085430 (2008).
- [104] G. Betz and W. Husinsky. A COMBINED MOLECULAR DYNAMICS AND KINETIC MONTE CARLO CALCULATION TO STUDY SPUTTER EROSION AND BEAM ASSISTED DEPOSITION. *Nucl. Instr. Meth. B* **193**, 352 (2002).
- [105] I. Koponen, M. Hautala and O. P. Sievanen. SIMULATIONS OF SUBMICROMETER-SCALE ROUGHENING ON ION-BOMBARDED SOLID SURFACES. *Phys. Rev. B* **54**, 13502 (1996).
- [106] B. K. Kellerman, J. A. Floro, E. Chason, D. K. Brice, S. T. Picraux and J. M. White. DEFECT PRODUCTION AND RECOMBINATION DURING LOW-ENERGY ION PROCESSING. *J. Vac. Sci. Tech. A* **13**, 972 (1995).
- [107] L. G. Shapiro and G. C. Stockman. *Computer Vision*. Prentence Hall (2001).
- [108] K. M. Klein, C. H. Park and A. F. Tasch. MODELING OF CUMULATIVE DAMAGE EFFECTS ON ION-IMPLANTATION PROFILES. *Nucl. Instr. Meth. B* **59**, 60 (1991).
- [109] S. Y. Tian, M. F. Morris, S. J. Morris, B. Obradovic, G. Wang, A. F. Tasch and C. M. Snell. A DETAILED PHYSICAL MODEL FOR ION IMPLANT INDUCED DAMAGE IN SILICON. *Ieee Trans. Elect. Dev.* **45**(6), 1226 (1998).
- [110] N. Pannier, A. Guglielmetti, L. Van Brutzel and A. Chartier. MOLECULAR DYNAMICS STUDY OF FRENKEL PAIR RECOMBINATIONS IN FLUORITE TYPE COMPOUNDS. *Nucl. Instr. Meth. B* **267**(18), 3118 (2009).
- [111] U. Birkenheuer, F. Bergner, A. Ulbricht, A. Gokhman and A. Almazouzi. *Application of rate theory modeling to cluster evolution in binary Fe-Cu alloys*. Annual Report 2007 in (Institute of Safety Research). FZD, Dresden (2008).
- [112] A. Gokhman, F. Bergner, A. Ulbricht and U. Birkenheuer. CLUSTER DYNAMICS SIMULATION OF REACTOR PRESSURE VESSEL STEELS UNDER IRRADIATION. *Def. Diff. Forum* **277**, 75 (2008).
- [113] R. Lennartz, F. Dworschak and H. Wollenberger. FRENKEL PAIR RECOMBINATION RADIUS IN COPPER AS A FUNCTION OF TEMPERATURE. *J. Phys. F* **7**(10), 2011 (1977).
- [114] N. M. Ghoniem, S. H. Tong, J. Huang, B. N. Singh and M. Wen. MECHANISMS OF DISLOCATION-DEFECT INTERACTIONS IN IRRADIATED METALS INVESTIGATED BY COMPUTER SIMULATIONS. *J. Nucl. Mat.* **307**, 843 (2002).
- [115] I. Martin-Bragado, I. Avci, N. Zographos, M. Jaraiz and P. Castrillo. FROM POINT DEFECTS TO DISLOCATION LOOPS: A COMPREHENSIVE MODELING FRAMEWORK FOR SELF-INTERSTITIAL DEFECTS IN SILICON. *Solid-State Electronics* **52**, 1430 (2008).
- [116] S. Facsko, T. Dekorsy, C. Koerdts, C. Trappe, H. Kurz, A. Vogt and H. L. Hartnagel. FORMATION OF ORDERED NANOSCALE SEMICONDUCTOR DOTS BY ION SPUTTERING. *Science* **285**, 1551 (1999).
- [117] F. Frost, B. Ziberi, T. Hoche and B. Rauschenbach. THE SHAPE AND ORDERING OF SELF-ORGANIZED NANOSTRUCTURES BY ION SPUTTERING. *Nucl. Instr. Meth. B* **216**, 9–19 (2004).



- [118] R. Gago, L. Vazquez, R. Cuerno, M. Varela, C. Ballesteros and J. M. Albella. PRODUCTION OF ORDERED SILICON NANOCRYSTALS BY LOW-ENERGY ION SPUTTERING. *Appl. Phys. Lett.* **78**(21), 3316–3318 (2001).
- [119] B. Ziberi, F. Frost and B. Rauschenbach. PATTERN TRANSITIONS ON Ge SURFACES DURING LOW-ENERGY ION BEAM EROSION. *Appl. Phys. Lett.* **88**(17), 173115 (2006).
- [120] J. Erlebacher, M. J. Aziz, E. Chason, M. B. Sinclair and J. A. Floro. SPONTANEOUS PATTERN FORMATION ON ION BOMBARDED Si(001). *Phys. Rev. Lett.* **82**, 2330 (1999).
- [121] A. D. Brown, J. Erlebacher, W. L. Chan and E. Chason. TRANSIENT TOPOGRAPHIES OF ION PATTERNED Si(111). *Phys. Rev. Lett.* **95**, 056101 (2005).
- [122] C. S. Madi, B. Davidovitch, H. B. George, S. A. Norris, M. P. Brenner and M. J. Aziz. MULTIPLE BIFURCATION TYPES AND THE LINEAR DYNAMICS OF ION SPUTTERED SURFACES. *Phys. Rev. Lett.* **101**, 246102 (2008).
- [123] T. M. Mayer, E. Chason and A. J. Howard. ROUGHENING INSTABILITY AND ION-INDUCED VISCOUS RELAXATION OF SiO<sub>2</sub> SURFACES. *J. Appl. Phys.* **76**(3), 1633–1643 (1994).
- [124] C. C. Umbach, R. L. Headrick and K. C. Chang. SPONTANEOUS NANOSCALE CORRUGATION OF ION-ERODED SiO<sub>2</sub>: THE ROLE OF ION-IRRADIATION-ENHANCED VISCOUS FLOW. *Phys. Rev. Lett.* **87**(24) (2001).
- [125] S. Habenicht, W. Bolse, K. P. Lieb, K. Reimann and U. Geyer. NANOMETER RIPPLE FORMATION AND SELF-AFFINE ROUGHENING OF ION-BEAM-ERODED GRAPHITE SURFACES. *Phys. Rev. B* **60**(4), R2200–R2203 (1999).
- [126] D. P. Datta and T. K. Chini. ATOMIC FORCE MICROSCOPY STUDY OF 60-keV Ar-ION-INDUCED RIPPLE PATTERNS ON Si(100). *Phys. Rev. B* **69**(23), 235313 (2004). 235313.
- [127] A. Karen and K. Okuno and F. Soeda and A. Ishitani. A STUDY OF THE SECONDARY-ION YIELD CHANGE ON GaAs SURFACE CAUSED BY THE O<sub>2</sub><sup>+</sup> ION-BEAM-INDUCED RIPPLING. *J. Vac. Sci. Tech. A* **9**(4), 2247–2252 (1991).
- [128] H. Hansen, A. Redinger, S. Messlinger, G. Stoian, J. Krug and T. Michely. RAPID COARSENING OF ION BEAM RIPPLE PATTERNS BY DEFECT ANNIHILATION. *Phys. Rev. Lett.* **102**, 146103 (2009).
- [129] M. Stepanova and S. K. Dew. ION BEAM SPUTTERING NANOPATTERNING OF THIN METAL FILMS: THE SYNERGISM OF KINETIC SELF-ORGANIZATION AND COARSENING. *J. Phys. Cond. Mat.* **21**, 224014 (2009).
- [130] M. V. R. Murty, T. Curcic, A. Judy, B. H. Cooper, A. R. Woll, J. D. Brock, S. Kycia and R. L. Headrick. X-RAY SCATTERING STUDY OF THE SURFACE MORPHOLOGY OF Au(111) DURING Ar<sup>+</sup> ION IRRADIATION. *Phys. Rev. Lett.* **80**(21), 4713–4716 (1998).
- [131] U. Valbusa, C. Boragno and F. B. de Mongeot. NANOSTRUCTURING SURFACES BY ION SPUTTERING. *J. Phys. Cond. Mat.* **14**(35), 8153–8175 (2002).
- [132] R. Gago, L. Vazquez, O. Plantevin, J. A. Sanchez-Garcia, M. Varela, M. C. Ballesteros, J. M. Albella and T. H. Metzger. TEMPERATURE INFLUENCE ON THE PRODUCTION OF NANODOT PATTERNS BY ION BEAM SPUTTERING OF Si(001). *Phys. Rev. B* **73**(15) (2006).

- [133] A. D. Brown and J. Erlebacher. TEMPERATURE AND FLUENCE EFFECTS ON THE EVOLUTION OF REGULAR SURFACE MORPHOLOGIES ON ION-SPUTTERED Si(111). *Phys. Rev. B* **72**(7), 075350 (2005).
- [134] H. X. Qian, W. Zhou, Y. Q. Fu, B. K. A. Ngoi and G. C. Lim. CRYSTALLOGRAPHICALLY-DEPENDENT RIPPLE FORMATION ON Sn SURFACE IRRADIATED WITH FOCUSED ION BEAM. *Appl. Surf. Sci.* **240**(1-4), 140 (2005).
- [135] B. Ziberi, F. Frost, Th. Höche and B. Rauschenbach. RIPPLE PATTERN FORMATION ON SILICON SURFACES BY LOW-ENERGY ION-BEAM EROSION: EXPERIMENT AND THEORY. *Phys. Rev. B* **72**(23), 235310 (2005).
- [136] E. Chason, T. M. Mayer, B. K. Kellerman, D. T. McIlroy and A. J. Howard. ROUGHENING INSTABILITY AND EVOLUTION OF THE Ge(001) SURFACE DURING ION SPUTTERING. *Phys. Rev. Lett.* **72**(19), 3040–3043 (1994).
- [137] G. Ehrlich and F. G. Hudda. ATOMIC VIEW OF SURFACE SELF-DIFFUSION - TUNGSTEN ON TUNGSTEN. *J. Chem. Phys.* **44**(3), 1039 (1966).
- [138] R. L. Schwoebel. STEP MOTION ON CRYSTAL SURFACES .2. *J. Appl. Phys.* **40**(2), 614 (1969).
- [139] J. Villain. CONTINUUM MODELS OF CRYSTAL-GROWTH FROM ATOMIC-BEAMS WITH AND WITHOUT DESORPTION. *J. Phys. I* **1**(1), 19–42 (1991).
- [140] J. H. Kim, M. Joe, S.-P. Kim, N.-B. Ha, K. R. Lee, B. Kahng and J.-S. Kim. PATTERN EVOLUTION ON PREVIOUSLY RIPPLED Au(001) BY CROSSING-ION-BEAM SPUTTERING. *Phys. Rev. B* **79**(20), 205403 (2009).
- [141] N. Anspach and S. J. Linz. MODELING PARTICLE REDEPOSITION IN ION-BEAM EROSION PROCESSES UNDER NORMAL INCIDENCE. *J. Stat. Mech.-Theory. E*, 06023 (2010).
- [142] C. Herring. EFFECT OF CHANGE OF SCALE ON SINTERING PHENOMENA. *J. Appl. Phys.* **21**(4), 301–303 (1950).
- [143] T. K. Chini, D. P. Datta and S. R. Bhattacharyya. RIPPLE FORMATION ON SILICON BY MEDIUM ENERGY ION BOMBARDMENT. *J. Phys. Cond. Mat.* **21**, 224004 (2009).
- [144] T. Aste and U. Valbusa. RIPPLES AND RIPPLES: FROM SANDY DESERTS TO ION-SPUTTERED SURFACES. *New J. Phys.* **7**, 122 (2005).
- [145] W. L. Chan and E. Chason. MAKING WAVES: KINETIC PROCESSES CONTROLLING SURFACE EVOLUTION DURING LOW ENERGY ION SPUTTERING. *J. Appl. Phys.* **101**(12), 121301 (2007).
- [146] J. A. Sánchez-García, L. Vazquez, R. Gago, A. Redondo-Cubero, J. M. Albella and Z. Czigany. TUNING THE SURFACE MORPHOLOGY IN SELF-ORGANIZED ION BEAM NANOPATTERNING OF Si(001) VIA METAL INCORPORATION: FROM HOLES TO DOTS. *Nanotechnology* **19**, 355306 (2008).
- [147] C. S. Madi, H. B. George and M. J. Aziz. LINEAR STABILITY AND INSTABILITY PATTERNS IN ION-SPUTTERED SILICON. *J. Phys. Cond. Mat.* **21**, 224010 (2009).
- [148] J. Erlebacher, M. J. Aziz, E. Chason, M. B. Sinclair and J. A. Floro. NON-LINEAR AMPLITUDE EVOLUTION DURING SPONTANEOUS PATTERNING OF ION-BOMBARDED Si(001). *J. Vac. Sci. Tech. A* **18**, 115 (1999).
- [149] W. W. Mullins. THEORY OF THERMAL GROOVING. *J. Appl. Phys.* **28**(3), 333–339 (1957).

- [150] F. Family and T. Vicsek. SCALING OF THE ACTIVE ZONE IN THE EDEN PROCESS ON PERCOLATION NETWORKS AND THE BALLISTIC DEPOSITION MODEL. *J. Phys. A* **18**(2), L75 (1985).
- [151] A.-L. Barabási and H. E. Stanley. *Fractal concepts in surface growth*. Cambridge University Press (1995).
- [152] G. Ódor. *Universality in nonequilibrium lattice systems*. World Scientific (2004).
- [153] C. Jayaprakash, F. Hayot and R. Pandit. UNIVERSAL PROPERTIES OF THE 2-DIMENSIONAL KURAMOTO-SIVASHINSKY EQUATION. *Phys. Rev. Lett.* **71**(1), 12–15 (1993).
- [154] J. T. Drotar, Y. P. Zhao, T. M. Lu and G. C. Wang. NUMERICAL ANALYSIS OF THE NOISY KURAMOTO-SIVASHINSKY EQUATION IN 2+1 DIMENSIONS. *Phys. Rev. E* **59**(1, Part A), 177–185 (1999).
- [155] Christoph A. Haselwandter and Dimitri D. Vvedensky. RENORMALIZATION OF STOCHASTIC LATTICE MODELS: EPITAXIAL SURFACES. *Phys. Rev. E* **77**, 061129 (2008).
- [156] M. Plischke, Z. Rácz and D. Liu. TIME-REVERSAL INVARIANCE AND UNIVERSALITY OF TWO-DIMENSIONAL GROWTH-MODELS. *Phys. Rev. B* **35**(7), 3485–3495 (1987).
- [157] G. Ódor, B. Liedke and K. H. Heinig. SURFACE PATTERN FORMATION AND SCALING DESCRIBED BY CONSERVED LATTICE GASES. *Phys. Rev. E* **81**(5), 051114 (2010).
- [158] M. Stepanova and S. K. Dew. SURFACE RELAXATION IN ION-ETCH NANOPATTERNING. *Appl. Phys. Lett.* **84**, 1374 (2004).
- [159] M. Feix, A. K. Hartmann, R. Kree, J. Munoz-Garcia and R. Cuerno. INFLUENCE OF COLLISION CASCADE STATISTICS ON PATTERN FORMATION OF ION-SPUTTERED SURFACES. *Phys. Rev. B* **71**, 125407 (2005).
- [160] S. Vauth and S. G. Mayr. ION BOMBARDMENT INDUCED SMOOTHING OF AMORPHOUS METALLIC SURFACES: EXPERIMENTS VERSUS COMPUTER SIMULATIONS. *Phys. Rev. B* **77**, 155406 (2008).
- [161] M. V. R. Murty, B. Cowles and B. H. Cooper. SURFACE SMOOTHING DURING SPUTTERING: MOBILE VACANCIES VERSUS ADATOM DETACHMENT AND DIFFUSION. *Surf. Sci.* **415**, 328 (1998).
- [162] I. Koponen, O. P. Sievanen, M. Hautala and M. Hakovirta. SIMULATIONS OF SPUTTERING INDUCED ROUGHENING AND FORMATION OF SURFACE TOPOGRAPHY IN DEPOSITION OF AMORPHOUS DIAMOND FILMS WITH MASS SEPARATED KILOELECTRONVOLT ION BEAMS. *J. Appl. Phys.* **82**, 6047 (1997).
- [163] J. Tarus, K. Nordlund, A. Kuronen and J. Keinonen. EFFECT OF SURFACE ON DEFECT CREATION BY SELF-ION BOMBARDMENT OF Si(001). *Phys. Rev. B* **58**, 9907 (1998).
- [164] R. Paruch, L. Rzeznik, M. F. Russo, B. J. Garrison and Z. Postawa. MOLECULAR DYNAMICS STUDY OF THE EFFECT OF SURFACE TOPOGRAPHY ON SPUTTERING INDUCED BY 20 keV Au-3 AND C-60 CLUSTERS. *J. Phys. Chem. C* **114**(12), 5532 (2010).
- [165] K. Nordlund, M. Ghaly, R. S. Averback, M. Caturla, T. Diaz de la Rubia and J. Tarus. DEFECT PRODUCTION IN COLLISION CASCADES IN ELEMENTAL SEMICONDUCTORS AND fcc METALS. *Phys. Rev. B* **57**, 7556 (1998).

- [166] L. Pelaz, G. H. Gilmer, M. Jaraiz, S. B. Herner, H.-J. Gossmann, D. J. Eaglesham, G. Hobler, C. S. Rafferty and J. Barbolla. MODELING OF THE ION MASS EFFECT ON TRANSIENT ENHANCED DIFFUSION: DEVIATION FROM THE " +1 " MODEL. *Appl. Phys. Lett.* **73**(10), 1421 (1998).
- [167] P. Pellegrino, P. Leveque, J. Wong-Leung, C. Jagadish and B. G. Svensson. SEPARATION OF VACANCY AND INTERSTITIAL DEPTH PROFILES IN ION-IMPLANTED SILICON: EXPERIMENTAL OBSERVATION. *Appl. Phys. Lett.* **78**(22), 3442 (2001).
- [168] M. D. Giles. TRANSIENT PHOSPHORUS DIFFUSION BELOW THE AMORPHIZATION THRESHOLD. *J. Electrochem. Soc.* **138**(4), 1160 (1991).
- [169] K.-H. Heinig and H.-U. Jäger. SIMULATIONS FOR IMPURITY GETTERING IN SILICON BY ION IMPLANTATION INDUCED DEFECTS. *Proceedings of 1st ENDEASD Workshop, Santorini/Greece*, 294 (1999).
- [170] J. A. Floro, B. K. Kellerman, E. Chason, S. T. Picraux, D. K. Brice and K. M. Horn. SURFACE DEFECT PRODUCTION ON GE(001) DURING LOW-ENERGY ION-BOMBARDMENT. *J. of Appl. Phys.* **77**(6), 2351–2357 (1995).
- [171] S. Macko, F. Frost, B. Ziberi, D. F. Forster and T. Michely. IS keV ION-INDUCED PATTERN FORMATION ON Si(001) CAUSED BY METAL IMPURITIES. *Nanotechnology* **21**(8), 085301 (2010).
- [172] Y. Zhao, G.-C. Wang and T.-M. Lu. *Characterization of amorphous and crystalline rough surface: principles and applications*. volume 37. Academic press, London (2001).
- [173] Y. Kuramoto and T. Tsuzuki. PERSISTENT PROPAGATION OF CONCENTRATION WAVES IN DISSIPATIVE MEDIA FAR FROM THERMAL EQUILIBRIUM. *Prog. Theor. Phys.* **55**(2), 356 (1976).
- [174] G. I. Sivashinsky. SELF-TURBULIZATION OF A LAMINAR FLAME. *Acta Astronautica* **6**(5-6), 569 (1979).
- [175] S. Facsko, T. Bobek, A. Stahl, H. Kurz and T. Dekorsy. DISSIPATIVE CONTINUUM MODEL FOR SELF-ORGANIZED PATTERN FORMATION DURING ION-BEAM EROSION. *Phys. Rev. B* **69**(15), 153412 (2004).
- [176] J. W. Gibbs. *On the equilibrium of heterogeneous substances*. dans Transactions of the Connecticut Academy of Arts and Sciences (1878).
- [177] J. J. Thomson. *Application of dynamics to Physics and Chemistry*. volume 5. Macmillan and Co, London (1888).
- [178] L. D. Landau and E. M. Lifshitz. *Statistische physik*. volume 5 of *Lehrbuch der Theoretischen Physik*. Akademie-Verlag, Berlin (1966).
- [179] [http://en.wikipedia.org/wiki/File:Minimal\\_surface\\_curvature\\_planes-en.svg](http://en.wikipedia.org/wiki/File:Minimal_surface_curvature_planes-en.svg).
- [180] B. Li. HIGH-ORDER SURFACE RELAXATION VERSUS THE EHRlich-SCHWOEBEL EFFECT. *Nonlinearity* **19**(11), 2581–2603 (2006).
- [181] R. A. Enrique, K. Nordlund, R. S. Averback and P. Bellon. SIMULATIONS OF DYNAMICAL STABILIZATION OF Ag-Cu NANOCOMPOSITES BY ION-BEAM PROCESSING. *J. Appl. Phys.* **93**, 2917 (2003).
- [182] D. E. Alexander, G. S. Was and L. E. Rehn. THE HEAT-OF-MIXING EFFECT ON ION-INDUCED GRAIN-GROWTH. *J. Appl. Phys.* **70**, 1252 (1991).

- [183] T. Som, B. Satpati, P. V. Satyam, D. Kabiraj, P. Ayyub, S. Ghosh, A. Gupta, B. N. Dev and D. K. Avasthi. SWIFT HEAVY ION INDUCED INTERFACE MODIFICATION IN Ni/Ge. *Nucl. Instr. Meth. B* **212**, 206 (2003).
- [184] S. K. Srivastava, R. Kumar, A. Gupta, R. S. Patel, A. K. Majumdar and D. K. Avasthi. SWIFT HEAVY ION INDUCED MIXING IN Fe/Ni MULTILAYER. *Nucl. Instr. Meth. B* **243**, 304 (2006).
- [185] M. Kac, M. Toulemonde, J. Jaworski, J. Juraszek, R. Kruk, S. Protsenko, V. Tokman and M. Marszalek. SWIFT HEAVY-ION MODIFICATION OF THE INTERFACE STRUCTURE IN Fe/Cr MULTILAYERS. *Vacuum* **78**, 661 (2005).
- [186] W. Bolse and J. Wiesner. DECORATION OF SWIFT HEAVY ION TRACKS IN NICKEL-OXIDE WITH GOLD ATOMS. *Nucl. Instr. Meth. B* **218**, 479 (2004).
- [187] J. Fassbender, J. Grenzer, O. Roshchupkina, Y. Choi, J. S. Jiang and S. D. Bader. THE EFFECT OF ION IRRADIATION AND ANNEALING ON EXCHANGE SPRING MAGNETS. *J. Appl. Phys.* **105**, 023902 (2009).
- [188] J. Jaworowicz, A. Maziewski, P. Mazalski, M. Kisielewski, I. Sveklo, M. Tekielak, V. Zablotskii, J. Ferre, N. Vernier, A. Mougin, A. Henschke and J. Fassbender. SPIN REORIENTATION TRANSITIONS IN Pt/Co/Pt FILMS UNDER LOW DOSE Ga<sup>+</sup> ION IRRADIATION. *Appl. Phys. Lett.* **95**, 022502 (2009).
- [189] S. Kavita, V. R. Reddy, S. Amirthapandian, A. Gupta and B. K. Panigrahi. Si<sup>+</sup> ION IRRADIATION IN A Co/Pt MULTILAYER SYSTEM. *J. Phys. Cond. Mat.* **21**, 096003 (2009).
- [190] P. Süle and M. Menyhárd. STRONG MASS EFFECT ON ION-BEAM MIXING IN METAL BILAYERS: A BALLISTIC PICTURE. *Phys. Rev. B* **71**, 113413 (2005).
- [191] P. Krasnochtchekov, R. S. Averback and P. Bellon. HOMOGENEOUS PHASE SEPARATION IN BINARY ALLOYS UNDER ION IRRADIATION CONDITIONS: ROLE OF INTERSTITIAL ATOMS. *Phys. Rev. B* **75**, 144107 (2007).
- [192] A. Johansen, E. Johnson, L. Sarhoh-Kristensen, S. Steenstrup, L. Yu and K. K. Bourdelle. DIFFUSION BEHAVIOR OF LEAD IMPLANTED INTO ALUMINUM. *Surf. Coat. Tech.* **51**, 461 (1992).
- [193] E. Johnson, H. H. Andersen and U. Dahmen. NANOSCALE LEAD AND NOBLE GAS INCLUSIONS IN ALUMINUM: STRUCTURES AND PROPERTIES. *Micros. Res. Tech.* **64**, 356 (2004).
- [194] P. Subramanyam and W. Reif. PHENOMENA AND MICROSTRUCTURE AT THE ALUMINUM LEAD INTERFACE. *J. Mat. Sci.* **28**, 2391 (1993).
- [195] T. Devolder. LIGHT ION IRRADIATION OF Co/Pt SYSTEMS: STRUCTURAL ORIGIN OF THE DECREASE IN MAGNETIC ANISOTROPY. *Phys. Rev. B* **62**, 5794 (2000).
- [196] C. T. Rettner, S. Anders, J. E. E. Baglin, T. Thomson and B. D. Terris. CHARACTERIZATION OF THE MAGNETIC MODIFICATION OF Co/Pt MULTILAYER FILMS BY He<sup>+</sup>, Ar<sup>+</sup>, AND Ga<sup>+</sup> ION IRRADIATION. *Appl. Phys. Lett.* **80**, 279 (2002).
- [197] V. Rosato, M. Guillope and B. Legrand. THERMODYNAMICAL AND STRUCTURAL-PROPERTIES OF fcc TRANSITION-METALS USING A SIMPLE TIGHT-BINDING MODEL. *Phil. Mag. A* **59**(2), 321–336 (1989).
- [198] C. N. R. Rao and K. J. Rao. *Phase transitions in solids*. McGraw-Hill, New York (1978).

- [199] A. Landa, P. Wynblatt, D. J. Siegel, J. B. Adams, O. N. Mryasov and X. Y. Liu. DEVELOPMENT OF GLUE-TYPE POTENTIALS FOR THE Al-Pb SYSTEM: PHASE DIAGRAM CALCULATION. *Acta Materialia* **48**, 1753 (2000).
- [200] F. Cleri and V. Rosato. TIGHT-BINDING POTENTIALS FOR TRANSITION METALS AND ALLOYS. *Phys. Rev. B* **48**, 22 (1993).
- [201] A. J. McAlister. THE Al-Pb (ALUMINUM-LEAD) SYSTEM. *Bull. Alloy Phase Diagrams* **5**, 69–73 (1984).
- [202] S. K. Yu, F. Sommer and B. Predel. ISOPIESTIC MEASUREMENTS AND ASSESSMENT OF THE Al-Pb SYSTEM. *Zeitschrift Fur Metallkunde* **87**(7), 574–580 (1996).
- [203] A. R. Miedema and A. K. Niessen. THE ENTHALPY OF SOLUTION FOR SOLID BINARY-ALLOYS OF 2 4D-TRANSITION METALS. *Comput. Coupling Phase Diagrams Thermochem.* **7**, 27 (1983).
- [204] R. Kelly. ON THE PROBLEM OF WHETHER MASS OR CHEMICAL BONDING IS MORE IMPORTANT TO BOMBARDMENT-INDUCED COMPOSITIONAL CHANGES IN ALLOYS AND OXIDES. *Surf. Sci.* **100**, 85 (1980).
- [205] K.-H. Heinig, T. Muller, B. Schmidt, M. Strobel and W. Möller. INTERFACES UNDER ION IRRADIATION: GROWTH AND TAMING OF NANOSTRUCTURES. *Appl. Phys. A* **77**, 17 (2003).
- [206] W. Möller and M. Posselt. TRIDYN - FZR *User Manual*. volume 317. FZR Publication, Dresden-Rosendorf (2002).
- [207] R. Hultgren, P. D. Desai, D. Hawkins M. Gleiser and K. Kelley. *Selected values of the thermodynamics properties of binary alloys*. Wiley, New York (1973).
- [208] T. Massalski. *Binary alloy phase diagrams, 2nd ed.* Metals Information Society, Metals Park, Ohio (1990).
- [209] C. Chappert, H. Bernas, J. Ferre, V. Kottler, J. P. Jamet, Y. Chen, E. Cambril, T. Devolder, F. Rousseaux, V. Mathet and H. Launois. PLANAR PATTERNED MAGNETIC MEDIA OBTAINED BY ION IRRADIATION. *Science* **280**(5371), 1919–1922 (1998).
- [210] J. K. Tripathi, A. Kanjilal, P. Rajput, A. Gupta and T. Som. MODIFICATION OF THE MAGNETIC AND THE STRUCTURAL PROPERTIES OF Pt/Cr/Co MULTILAYERS BY He<sup>+</sup>-ION IRRADIATION. *Nucl. Instr. Meth. B* **267**(8-9), 1608–1611 (2009).
- [211] A. Keller, R. Cuerno, S. Facsko and W. Möller. ANISOTROPIC SCALING OF RIPPLE MORPHOLOGIES ON HIGH-FLUENCE SPUTTERED SILICON. *Phys. Rev. B* **79**, 115437 (2009).



# Acknowledgements

I would never be able to finish this thesis without invaluable support of several persons.

At first, I would like to thank Prof. Dr. Wolfhard Möller most of all for giving me an opportunity to research the topic of ion-solid interactions. Even as the director of the Institute of Ion Beam Physics and Material Research, he had always the time to satisfy my lacks of knowledge concerning the all details of TRIDYN, as well as many other topics in theoretical physics. His organization and planning methods will be always for me the best possible example how to deal multiple problems simultaneously within a short period of time.

Equally I want to thank for Dr. Karl-Heinz Heinig for his professional supervision, extremely interesting discussions and great theoretical support. Without his fundamental introductions into the subject of kinetic Monte-Carlo it would not be ever possible to finish this work. He was always a 'mine' of interesting ideas and he never stopped in motivations to complete at least part of them. A very good teacher, supervisor and a great colleague.

Also my great thanks for Dr. Stefan Facsko, being for me an expert in fields of ion beam sputtering and ripple formation. His experience as an experimentalist was always an indispensable ingredient defining the goal to fulfill for the simulations. In addition to that, his theoretical knowledge about continuum theory was a source of the great advantage in understanding a variety of processes occurring during ion bombardment. Thanks go to Dr. Adrian Keller for his experimental work that generated a lot of interesting structure patterns possible to reproduce (at least some of them) by simulations.

I wish to thank Prof. Dr. Eric Chason for his kind willingness to examine this work.

I am also thankful for Dr. Matthias Posselt, the leader of the theory group FWIT. He helped me a lot, explaining a plenty of important details about molecular dynamic simulations or about methodology of crystal version of TRIM. He also delivered several useful results using CRYSTAL TRIM program, which were used in this thesis.

Great thanks to the members of the whole theory department for never-ending discussions and a continuous support, as well as to the HZDR Information Technology staff for solving my technical problems connected to hardware and software issues, and for providing me an access to HZDR computing clusters *Hydra* and *Hypnos*. Special thanks to Mr. Andreas Geyer, Mr. Joachim Kreher, Dr. Matthias Schlett, Mr. Nils Schmeißer and Dr. Henrik Schulz (in alphabetical order).

I appreciate a lot the support from one of my collaborator from Hungarian Research Institute for Technical Physics and Material Science in Budapest, Dr. Géza Ódor. His knowledge about the statistical physics, the scaling theory and his commitment into our DAAD-MÖB bilateral project was a good example of the demeanor intended for such a great physicist like him. It was always a pleasure to travel to Budapest and work with him inventing new kinetic models of surface interactions. Additionally, I would like to thank to Dr. Peter Süle from the same institute for a detailed introduction into applications of molecular dynamic simulation.

The support of the bilateral German-Hungarian exchange program DAAD-MÖB (numbers of grants: D/07/00302, 37-3/2008) and from the Deutsche Forschungsgemeinschaft (DFG research group 845, project HE2137/4-1) is also acknowledged.

I also wish to thank my brother Dr. Maciej Oskar Liedke, who was helping me during these years a lot using his physical knowledge and scientific experience. Also for my



## Bibliography

---

colleagues David Friedrich, who was able to accomplish some language corrections of this thesis; Satoshi Numazawa and Andreas Kranz for very interesting theoretical discussions.

Finally, special thanks go to my fiancée Agnieszka Boś, who I met for the very first time here in Germany. She gave me a lot of perspectives for the future and a great motivation to finish this work.

# Curriculum Vitae

## PERSONAL DATA

name                   Bartosz Liedke  
born                    31 July 1982 *in Białystok*  
email                   b.liedke@hzdr.de  
phone                   +49 351 260 3373

## EDUCATION

24.03.2011             Helmholtz-Zentrum Dresden-Rossendorf, Germany

### *Ph.D. thesis*

Submitting of the Ph.D. thesis to the faculty Mathematic and Natural Science of Technical University in Dresden on the subject: 'ION BEAM PROCESSING OF SURFACES AND INTERFACES - MODELING AND ATOMISTIC SIMULATIONS'.

since 11.2006         Helmholtz-Zentrum Dresden-Rossendorf, Germany

### *Doctoral study*

Investigation of ion beam processes of surfaces and interfaces using the atomistic simulation techniques in the Institute of Ion Beam Physics and Materials Research, Division of Theory (FWIT);

Supervisors: Prof. Dr. W. Möller, Dr. K.-H. Heinig, Dr. S. Facsko

02.2006 – 09.2006     Helmholtz-Zentrum Dresden-Rossendorf, Germany

### *Practice*

Development of programming package in LabView® for Magneto-Optic Kehr Effect to calibrate the machinery, measure intermetallic multilayer materials and analyze magnetic hysteresis data.  
Supervisor: Prof. Dr. J. Fassbender

24.10.2006             Technical University of Białystok, Poland

### *Master thesis*

Defense of the master study and obtaining Master Engineer Degree Certificate in Informatics on subject: 'MORPHOLOGICAL ANALYSIS OF THE STATISTICAL PARAMETERS OF THE PARTICLE OBJECTS, FOR THE IMAGES OF MAGNETIC NANOSTRUCTURES'.

Supervisor: Dr. W. Rakowski

2004 – 2005             University of Applied Science Mittweida, Germany

### *Erasmus Socrates*

One semester study on the University of Applied Science Mittweida in the field of informatics in the exchange program: Erasmus Socrates.

2001 – 2006             Technical University of Białystok, Poland

### *Master study*

Study in Informatics at Technical University of Białystok as the software developer.

1997 – 05.2001         IV Lyceum in Białystok, Poland

### *Secondary school*

Study in the secondary school IV Lyceum in Białystok finished with the matriculation.

## Bibliography

---

### SCIENTIFIC EXPERIENCE

#### *Simulation techniques*

- Application and programming with TRIM and TRIDYN models by Prof. Dr. W. Möller
- Application and programming with lattice kinetic Monte-Carlo methods (Cellular Automata, Ising Model, application of Molecular Dynamics potentials) by Dr. K.-H. Heinig
- Practice with Molecular Dynamic simulation in Hungarian Research Institute for Technical Physics and Material Science in Budapest by Dr. Peter Süle

#### *Courses*

- Quantum Mechanic on Technical University in Dresden (TU Dresden) by Prof. Dr. K. Becker, finished with the exam
- Thermodynamic and Statistical Physics on TU Dresden by Prof. Dr. R. Schmidt, finished with exam
- Solid State Physics on TU Dresden by Prof. Dr. K. Leo, finished with exam
- Ion Beam material analysis and fundamentals of ion-solid interactions in HZDR by Prof. Dr. W. Möller, finished with exam

#### *Programming techniques*

- Good programming knowledge of C++, Fortran, LabView®, Java
- Basic programming knowledge of Delphi®, JavaScript, C#, Lisp, PL SQL for Oracle, SHTML, ASP .NET, PHP, Perl, L<sup>A</sup>T<sub>E</sub>X
- Computer skills in MatLab®, Mathematica®, PovRay, RasMol, PyMol, Corel Draw, Origin, Microsoft® Office, etc.

### LANGUAGE CAPABILITIES

ENGLISH · Fluent

GERMAN · Fluent

POLISH · native language

# List of publications

## ARTICLES

- H. Schulz, G. Ódor, J. Kelling, K.-H. Heinig, **B. Liedke**, N. Schmeißer  
COMPUTING THE KPZ EQUATION USING GPU ACCELERATION. Conference publication for Innovation Information Technologies - Theory and Practice, 06.-10.09.2010, Dresden, Germany
- G. Ódor, **B. Liedke**, K.-H. Heinig  
SURFACE PATTERN FORMATION AND SCALING DESCRIBED BY CONSERVED LATTICE GASES. *Physical Review E* **81** (2010), 051114
- G. Ódor, **B. Liedke**, K.-H. Heinig  
DIRECTED D-MER DIFFUSION DESCRIBING KARDAR-PARISI-ZHANG TYPE OF SURFACE GROWTH. *Physical Review E* **81** (2010), 031112
- G. Ódor, **B. Liedke**, K.-H. Heinig  
MAPPING OF 2 + 1 DIMENSIONAL KPZ GROWTH ONTO DRIVEN LATTICE GAS MODEL OF DIMERS. *Physical Review E* **79** (2009), 021125
- J. Neidhardt, S. Mráztz, M. Schneider, Jochen, E. Strub, W. Bohne, **B. Liedke**, W. Möller, C. Mitterer  
EXPERIMENT AND SIMULATION OF THE COMPOSITIONAL EVOLUTION OF Ti-B THIN FILMS DEPOSITED BY SPUTTERING OF A COMPOUND TARGET. *Journal of Applied Physics* **104** (2008), 063304
- M. O. Liedke, **B. Liedke**, A. Keller, B. Hillebrands, A. Mücklich, S. Facsko, J. Fassbender  
INDUCED ANISOTROPIES IN EXCHANGE COUPLED SYSTEMS ON RIPPLED SUBSTRATES. *Physical Review B* **75** (2007), 220407

## CONFERENCE LECTURES AND SEMINARS

(as a first author only)

- SURFACE PATTERNING BY ION BOMBARDMENT: PREDICTIONS OF LARGE SCALE ATOMISTIC SIMULATIONS. 75th **DPG 2011**, 13.-18.03.2011, Dresden, Germany
- ION-BEAM-INDUCED INTERFACE MIXING: UNIFIED ATOMISTIC SIMULATIONS OF COLLISIONAL AND THERMAL PROCESSES. 17th **IBMM 2010**, 22.-27.08.2010, Montreal, Canada
- MULTIPHYSICS PROGRAM FOR ION-INDUCED COLLISION CASCADES AND THERMALLY ACTIVATED PHASE SEPARATION: INTERMETALLIC NANOLAYERS BY INTERFACE MIXING. **COSIRES 2010**, 19.-23.07.2010, Collegium Maximum Auditorium in Kraków, Poland
- EFFICIENT NUMERICAL STUDIES OF SCALING PROPERTIES AND PATTERN FORMATION DURING SURFACE GROWTH/EROSION BY SURFACE MAPPING ON A BINARY LATTICE GAS MODEL. **MRS 2009 Fall Meeting**, 30.11.-04.12.2009, Boston, USA
- MODELING OF ION BEAM MIXING WITH PHASE SEPARATION - SIMULATION OF DAMAGE FORMATION AND THERMALLY ACTIVATED RELAXATION. Seminar at the Department of Physics, University of Białystok, 21.11.2009, Białystok, Poland
- ION-INDUCED SURFACE PATTERN EVOLUTION IN COMPUTER SIMULATIONS WITH NEW APPROACH - UNIFICATION OF COLLISION CASCADE AND KINETIC 3D MONTE CARLO CALCULATIONS. **Nanoscale Modification of Surfaces and Thin Films**, 30.08.-03.09.2009, Rathen, Germany
- COMPETITION ION BEAM MIXING AND PHASE SEPARATION: A NOVEL PROGRAM COMBINING TRIM WITH KINETIC MONTE CARLO. **Workshop Ion Beam Physics**, 06.-07.04.2009, Jena, Germany

- ION BOMBARDMENT OF SOLIDS - UNIFIED SIMULATION OF DAMAGE FORMATION AND THERMALLY ACTIVATED RELAXATION. Seminar at MFA of KFKI of Budapest, 11.11.2008, Budapest, Hungary

### CONFERENCE POSTERS

(as a first author only)

- ION EROSION INDUCED SURFACE PATTERNING STUDIED BY COMBINED TRIM AND KINETIC MONTE-CARLO SIMULATIONS. 17th **IBMM 2010**, 22.-27.08.2010, Montreal, Canada; **Workshop Ion Beam Physics**, 29.-31.03.2010, FZD, Germany
- CLASSIFICATION OF SIMULATED SURFACE MORPHOLOGIES INDUCED BY ION IRRADIATION USING COMBINED TRIM AND KINETIC MONTE-CARLO CALCULATIONS. **MRS 2009 Fall Meeting**, 30.11.-04.12.2009, Boston, USA
- SIMULATION OF DEFECTS AND COMPOSITION AFTER  $\text{Ga}^+$  IRRADIATION OF ULTRATHIN Pt/Co/Pt FILM. 16th **IBMM 2008**, 31.08.-05.09.2008, Dresden, Germany
- SURFACE MODIFICATION USING BINARY COLLISION APPROXIMATION AND 3D LATTICE KINETIC MONTE CARLO SIMULATION. 16th **IBMM 2008**, 31.08.-05.09.2008, Dresden, Germany
- SIMULATION OF DEFECTS AND COMPOSITION AFTER IRRADIATION OF ULTRATHIN Pt/Co/Pt FILM WITH  $\text{Ga}^+$ . **Physics of Magnetism 2008**, 24.-27.06.2008, Poznań, Poland

# Versicherung

Hiermit versichere ich, dass ich die vorliegende Arbeit ohne unzulässige Hilfe Dritter und ohne Benutzung anderer als der angegebenen Hilfsmittel angefertigt habe; die aus fremden Quellen direkt oder indirekt übernommenen Gedanken sind als solche kenntlich gemacht. Die Arbeit wurde bisher weder im Inland noch im Ausland in gleicher oder ähnlicher Form einer anderen Prüfungsbehörde vorgelegt.

Ich erkenne die Promotionsordnung der Technischen Universität Dresden an.

Dresden, 24.03.2011

*Bartosz Liedke*

Diese Arbeit wurde am Helmholtz-Zentrum Dresden-Rossendorf e.V. und unter wissenschaftlicher Betreuung von Dr. Karl-Heinz Heinig, Dr. Stefan Facsko und Prof. Dr. Wolfhard Möller angefertigt. Wolfhard Möller ist Professor im Institut für Angewandte Physik der Fakultät Mathematik und Naturwissenschaften der Technischen Universität Dresden.